

University of Strathclyde
Strathclyde Institute of Pharmacy and Biomedical Sciences

Influence of Impurities on the Crystallisation of Pharmaceutical Materials

Natalia Dąbrowska

A thesis submitted to the Strathclyde Institute of Pharmacy and Biomedical Sciences in fulfilment of the requirements for the degree of Doctor of Philosophy.

2017

Table of Contents

Declarations	I
Acknowledgements	III
List of abbreviations used in the text	V
List of symbols used in the text	VII
Abstract.....	X
Conferences and Publications	XII
List of Figures	XIII
List of Tables.....	XXVI
1 Introduction	1
1.1 Project Background	1
1.2 Project Outline.....	9
1.2.1 Determination of the Effect of the Temperature Control on Crystallisation of L-Glutamic Acid	9
1.2.2 Determination of the Influence of Impurities on the Crystallisation of Pharmaceutical Materials	9
1.3 Project Management.....	11
1.4 Thesis Structure	11
2 Crystallisation Theory.....	13
2.1 Chapter Outline	13
2.2 Crystal Chemistry and Physical Properties of Organic Crystalline Materials	14
2.3 Solubility and Supersaturation.....	16
2.4 Nucleation	19
2.4.1 Primary nucleation	19
2.4.1.1 Homogeneous Nucleation	19
2.4.1.2 Heterogeneous Nucleation	23
2.4.2 Secondary Nucleation	24
2.4.3 Classical Nucleation Theory	26
2.4.3.1 Classical Nucleation Theory for Determining Nucleation Rates	27
2.4.4 Two-Step Nucleation Theory.....	34
2.4.4.1 Two-Step Nucleation Theory Literature Review	36
2.4.5 Classical Nucleation Theory and Two Step Nucleation Theory Summary.....	41

2.5	Crystal Growth	42
2.5.1	Crystal Nucleation and Growth in Presence of Impurities - Theory.....	43
2.5.2	Crystal Nucleation and Growth in Presence of Impurities – Literature Review.....	47
2.6	Chapter Summary	60
3	Investigation of the Effect of Temperature Control on Crystallisation of L-Glutamic Acid	61
3.1	Chapter Outline	61
3.2	Crystallisation Platforms	62
3.2.1	Stirred Tank Reactor.....	62
3.2.2	CoFlux Reactor	62
3.2.2.1	Heat Balance Calorimetry	63
3.2.2.2	Process enthalpy.....	64
3.2.2.3	CoFlux Valve.....	64
3.2.2.4	CoFlux setups used during the project	66
3.2.2.5	The accumulation or heat shift in the process fluid	69
3.2.3	Oscillatory Baffled Reactor.....	70
3.3	Analytical Techniques	72
3.3.1	Raman Spectroscopy.....	72
3.3.2	Laser Diffraction	74
3.3.3	X-ray Powder Diffraction.....	79
3.4	Model Compound Used In the Current Study	82
3.5	Materials and Methods	86
3.5.1	The Co-Flux Reactor Setup.....	86
3.5.2	Isolation and Characterisation of the Product.....	90
3.5.3	The Stirred Tank Reactor and Oscillatory Baffled Reactor Setups.....	91
3.5.4	Conditions for Analytical Measurements.....	92
3.5.4.1	Laser diffraction	92
3.5.4.2	X-Ray diffraction	92
3.5.4.3	Microscope images	93
3.5.4.4	Raman measurements.....	93
3.6	Results	94
3.6.1	Setup A	94
3.6.2	Setup B	105

3.7	Discussion.....	118
3.8	Conclusions.....	122
4	Chromatographic Techniques for Impurity Determination and Quantification	
	During Crystallisation Processes.....	114
4.1	Chapter Outline	114
4.2	Analytical Techniques.....	115
4.2.1	Liquid Chromatography.....	115
4.2.1.1	Normal Phase Liquid Chromatography.....	116
4.2.1.2	Reversed Phase Liquid Chromatography.....	118
4.2.1.3	Factors Determining Chromatographic Efficiency	119
4.2.2	Ion Chromatography	124
4.2.2.1	Salt formation	124
4.2.2.2	Ion Chromatography Principles	126
4.2.3	Gas Chromatography	128
4.2.4	Mass Spectrometry	128
4.2.4.1	Ion generation methods	128
4.2.4.2	Mass analysers.....	130
4.3	Model Compound	132
4.3.1	Introduction to Metformin Hydrochloride.....	132
4.3.2	Potential Impurities and their Determination	134
4.4	Materials and Methods	140
4.4.1	Liquid Chromatography - Mass Spectrometry Method Development	140
4.4.1.1	Liquid Chromatography – Mass Spectrometry Calibration Curves Preparation.....	142
4.4.2	Gas Chromatography Sample Preparation and Measurement Conditions ...	143
4.4.3	Ion Chromatography Conditions	144
4.4.3.1	Ion Chromatography Calibration Curve for Dimethylamine Preparation	144
4.4.3.2	Sample Preparation for Ion Chromatography Analysis.....	144
4.4.4	Temperature Stability Test Conditions	144
4.5	Results.....	146
4.5.1	Calibration Curves and Method Validation Results	146
4.5.1.1	Calibration curves	146
4.5.1.2	Precision studies	149
4.5.1.3	Accuracy studies	157

4.5.1.4	Column Efficiency, Peak Asymmetry and Capacity Factor Studies	163
4.5.1.5	Limit of Detection and Limit of Quantification	165
4.5.2	Stability Test Results	166
4.5.3	Results for Dimethylamine Determination	169
4.5.3.1	Gas Chromatography Results.....	169
4.5.3.2	Ion Chromatography Calibration Curve	169
4.5.3.3	Application of the Ion Chromatography Method for Dimethylamine	170
4.6	Discussion.....	172
4.7	Conclusions.....	176
5	Determination of the Effect of Ammonium Sulfate on the Nucleation Rate of Metformin Hydrochloride	177
5.1	Chapter Outline	177
5.2	Materials Used in the Study.....	178
5.2.1	Metformin Hydrochloride	178
5.2.2	Ammonium Sulfate	178
5.2.3	Solvent Choice.....	182
5.3	Equipment and Techniques Used in the Study.....	182
5.3.1	Crystallisation Platforms	182
5.3.1.1	Crystalline	182
5.3.1.2	Optimax and Easymax.....	183
5.3.2	Analytical Techniques.....	184
5.3.2.1	Scanning Electron Microscope.....	184
5.3.2.2	Time-of-Flight Secondary Ion Mass Spectrometry.....	186
5.3.2.3	Differential Scanning Calorimetry.....	187
5.3.2.4	Dynamic Light Scattering	188
5.3.2.5	Data Analysis of Autocorrelation Functions.....	191
5.4	Methods Used in the Study	193
5.4.1	Methods for Induction Time Effects	193
5.4.1.1	Induction Time Experimental Conditions.....	193
5.4.1.2	SEM Measurement Conditions	195
5.4.1.3	ToF-SIMS Sample Preparation and Measurement Conditions	195
5.4.1.4	DSC Sample Preparation and Measurement Conditions	195
5.4.1.5	DLS Sample Preparation and Measurement Conditions.....	196
5.4.1.6	Ion Chromatography Sample Preparation and Measurement Conditions	197
5.4.1.7	pH Investigation Experimental Conditions	197

5.4.1.8	The Effect of Impurity Concentration on Solubility of Metformin Hydrochloride – Experimental Conditions.....	198
5.5	Results and Discussion	200
5.5.1	Determining Solubility of Metformin Hydrochloride in Solvent System Results... ..	200
5.5.2	Induction Time Experiments	200
5.5.2.1	Results from Induction Time Experiments.....	200
5.5.2.2	Induction Time Experiments Discussion	207
5.5.3	Investigation of Impurity Concentration Effect on Induction Time	210
5.5.3.1	Results and Discussion from pH Investigation	210
5.5.3.2	Results and Discussion from Solubility Investigation.....	212
5.5.3.3	Results and Discussion from the Interfacial Energy Calculations	213
5.5.3.4	Results and Discussion from SEM Analysis	215
5.5.3.5	Results and Discussion from ToF-SIMS Analysis	217
5.5.3.6	Results and Discussion from DSC Analysis	219
5.5.3.7	Results and Discussion from Ion Chromatography Analysis	221
5.5.3.8	Results and Discussion from Dynamic Light Scattering Experiments	223
5.6	Conclusions.....	234
6	Overall Conclusions and Future Work	236
6.1	Conclusions from This Study	236
6.2	Suggestions for Future Work	237
7	Appendix	239
7.1	LC - MS Calibration Curves.....	239
7.2	Examples of Extracted Ion Chromatograms for Metformin Hydrochloride and Its Impurities.....	242
7.3	Dimethylamine Calibration Curve for Ion Chromatography	244
7.4	Ion Chromatogram Example for Dimethylamine Standard	244
7.5	Ion Chromatogram Example for Chloride and Sulfate Ions	245
7.6	Ion Chromatography Calibration Curves.....	246
7.7	Dynamic Light Scattering Parameter Tables	248
8	Bibliography.....	254

Declarations

This thesis is the result of the author's original research. It has been composed by the author and has not been previously submitted for examination which has led to the award of a degree.

The copyright of this thesis belongs to the author under the terms of the United Kingdom Copyright Acts as qualified by University of Strathclyde Regulation 3.50.

Due acknowledgement must always be made of the use of any material contained in, or derived from, this thesis.

Signed:

Date:

In loving memory of my grandfather Ryszard.

Acknowledgements

I would like to thank Professor Alastair Florence and Dr David Watson for their assistance, advice and support given throughout this research. Professor David Littlejohn and Dr Alison Nordon for their supervision and help with the CoFlux reactor project.

My special gratitude goes to Professor Chris Price, Professor Joop ter Horst, Professor Jan Sefcik, Dr Darren Edwards and other CMAC members including Dr Cameron Brown, Dr Huayiu Yang, Dr Thomas McGlone, Dr Andrea Johnston, Miss Maria Briuglia and Miss Denise Logue for their time, guidance and useful discussions. Dr Laura Palmer is thanked for providing data she obtained when investigating crystallisation of L-glutamic acid in stirred tank and oscillatory baffled reactors. Dr Jerzy Dziewierz for his expertise and help with Matlab, Dr Tong Zhang and Mr Osamah Albassam for their help with IC and LC/MS. I would like to thank Miss Eleonora Paladino for her help with ToF-SIMS sample analysing and Mr Fraser Mabbott for his help with the SEM.

AM technologies are thanked for the loan of the CoFlux reactor, Mr David Morris of AM Technology and Mr Kevin Poole of Autico are thanked for their help in setting up the reactor and on-going support. The Centre for Process Analytics and Control Technology is thanked for the use of the Kaiser MR probe and Raman spectrometer. I would like to express my gratitude to Mr Michael Ross and Dr Andrea Semiao from the Environmental Engineering Institute for Infrastructure and Environment at University of Edinburgh for their time spent running and analysing my IC samples.

This research has been possible due to the EPSRC Centre for Innovative Manufacturing in Continuous Manufacturing and Crystallisation. Funding for this research was gratefully received from the University of Strathclyde and the EPSRC. I would like to acknowledge that this work was carried out in the CMAC National Facility, housed within the University of Strathclyde's Technology and Innovation Centre, and funded with a UKRPIF (UK Research Partnership Institute Fund) capital award from the Higher Education Funding Council for England (HEFCE).

I would like to thank my parents for their love and support throughout my life and studies. Thank you both for giving me strength to reach for the stars and chase my dreams.

My heart felt regards goes to my family for their love and moral support.

To all my friends – thank you for your understanding and encouragement in my many moments of crisis. Especially Alicja and Karolina – thanks for our Skype calls that kept me sane when everything went wrong.

And last but not least I would like to thank my best friend Rachel. This journey would not be possible without your smile, support and encouragement you provided me with every day. The PhD is like a long and lonely marathon, but running it with you was so much easier. A simple “thank you” cannot show how much your friendship means to me.

List of abbreviations used in the text

Abbreviation	Meaning
AFM	Atomic Force Microscopy
APCI	Atmospheric Pressure Chemical Ionisation
API	Active Pharmaceutical Ingredient
CCD	Charge Coupled Device
CDHA	Canadian Drug and Health Agency
CNT	Classical Nucleation Theory
COBR	Continuous Oscillatory Baffled Reactor
Cryo – TEM	Cryo Transmission Electron Microscopy
CSTR	Continuous Stirred Tank Reactor
DLS	Dynamic Light Scattering
DMA	Dimethylamine
DSC	Differential Scanning Calorimetry
ECSN	Embryo Coagulation Secondary Nucleation
EI	Electron Impact Ionisation
ESI	Electrospray Ionisation
FBRM	Focused Beam Reflectance Measurement
FDA	United States Food and Administration
FT – IR	Fourier Transform Infra Red
GC	Gas Chromatography
HILIC	Hydrophilic interaction liquid chromatography
HTF	Heat Transfer Fluid
HTU	Heat Transfer Unit
IC	Ion Chromatography
ICH	International Conference for Harmonisation
ICR	Ion Cyclotron Resonance
KAP	Potassium Acid Phthalate
KDP	Potassium Dihydrogen Phosphate
LC/MS	Liquid Chromatography Mass Spectrometry

LD	Laser Diffraction
LGA	L-Glutamic Acid
LOD	Limit of Detection
LOQ	Limit of Quantification
MALDI	Matrix Assisted Laser Desorption Ionisation
MSMPR	Mixed Suspension and Mixed Product Removal
MSZW	Metastable Zone Width
NMR	Nuclear Magnetic Resonance
NTA	Nanoparticle Tracking Analysis
OBR/OBC	Oscillatory Baffled Reactor/Crystalliser
PAA	p-acetoxyacetanilide
PES	Polyethersulfone
PSD	Position Sensitive Detector
PTFE	Polytetrafluoroethylene
RDS	Relative Standard Deviation
SEM	Scanning Electron Microscopy
STR	Stirred Tank Reactor
THF	Tetrahydrofuran
ToF - SIMS	Time of Flight Secondary Ion Mass Spectrometry
UV-VIS	Ultraviolet – Visible
XRPD	X-Ray Powder Diffraction

List of symbols used in the text

Symbol	Meaning	Page
μ	Chemical Potential	4
R	Universal Gas Constant	6
T	Temperature	6
a	Standard Activity	6
S	Supersaturation	6
c	Concentration	6
G	Free Energy	8
r	Radius of the Nuclei	8
v	Molecular Volume	8
γ	Interfacial Surface Tension	8
k	Boltzmann Constant	10
J	Nucleation Rate	11
K	Nucleation Rate Constant	11
J_n	Primary Nucleation Rate	15
k'_n	Nucleation Rate Constant	15
n	Nucleation Order	15
M	Mass of Formed Nuclei	16
k_n	Mass Nucleation Rate Constant	16
α	Volume Shape Factor	16
ρ_c	Density of the Solute Crystals	16
ε	Conversion Factor	16
N_m/V	Number Density of Grown Primary Nuclei over Time	17
t_m	Time	17
P_m	Probability of the Formation of Nuclei in a Time Interval	19
N	Average number of Nuclei	19
V	Volume	19
M	Total Number of Experiments	21
M^+	Number of Experiments where Crystals Have Been Detected	21

V	Step Velocity	32
θ_{eq}	Fractional Coverage	32
α	Effectiveness Factor	32
K	Langmuir Constant	33
x	Impurity Concentration	33
G	Face Growth	33
a	Size of Growth Unit	34
σ	Relative Supersaturation	34
L	Average Spacing Between Two Active Sites	34
v	Volume per Molecule in Solid POohase	38
V	Molar Volume	38
N	Avogadro's Number	38
τ	Induction Time	43
q_{htf}	Power	52
m_{htf}	Mass Flow of Heat Tranfer Fluid	52
T_{htfout}	Temperature of Heat Transfer Fluid Leaving the Jacket	52
T_{htfin}	Temperature of Heat Transfer Fluid Entering the Jacket	52
Cp_{htf}	Specific Heat of Transfer Fluid	52
h_p	Enthalpy	52
q_s	Accumulation or Heat Shift in the Process Fluid	57
θ	Time	57
x	Dimensionless Diameter	66
r	Particle Radius	66
s	Radial Distance in the Detection Plane Measured from the Optical Axis	66
λ	Wavelength	66
F	Focal Length of the Lens	66
A	Area of Projected Sphere	66
ϑ	Scattering Angle	66
I	Light Intensity	66
W_i	Weight Distribution	67
N	Number og Particles	67

E	Flux of Incident Light per Unit Area	67
k	Constant	67
K	Constant	67
D	Particle Diameter	67
J _l	Bessel Function	67
θ	Scattering Angle	67
m	Complex Refractive Index	67
n	Positive Integer	68
d	Lattice Spacing	68
σ	Standard Deviation	120
s	Calibration Curve Slope	120
K'	Capacity Factor	121
V	Retention Volume	121
t	Retention Time	121
n	Number of Theoretical Plates	122
L	Column Length	122
α	Selectivity Parameter	123
R _s	Peak Resolution	124
T	Kinetic Energy	130
v	Ion Velocity	130
L	Flight Path Length	130
ΔH_f	Molar Heat of Fusion	188
F	Melted Fraction	188
1/F	Reciprocal of the Fraction Melted	188
A	Peak Area	188
c	Linearization factor	188
q	Scattering Vector	189
n	Refractive Index	189
Γ	Decay Rate	190
D	Diffusion coefficient	190
d _H	Hydrodynamic Diameter	191
η	Viscosity	191

Abstract

The major part of this thesis describes work done to investigate the organic and inorganic impurity content in metformin hydrochloride samples and their effect on induction time and nucleation kinetics.

Crystallisation from solution plays a significant role in the pharmaceutical, chemical and food industry, because it is widely used as a separation and purification technique. Nucleation is the first step of crystallisation, where the extremely small species called nuclei are formed in solution. This step determines the quality of a new crystalline material, however, at present the understanding of this process is relatively poor. One of the factors affecting the nucleation pathway and kinetics is the impurity content.

Impurity control in the pharmaceutical industry should be planned at the drug design stage and carried throughout the entire drug production process. Acceptable levels for impurities in drugs are defined in official regulations released by the International Conference of Harmonisation (ICH), the United States Food and Drug Administration (FDA) and the Canadian Drug and Health Agency (CDHA).

A liquid chromatography/mass spectrometry (LC/MS) method for the determination and quantification of metformin hydrochloride and five out of six known impurities was developed and validated during this project. This method was then used to determine the levels of these impurities in samples taken during the temperature stability test of metformin hydrochloride. The results revealed that the chosen model compound was relatively stable under the chosen conditions and the levels of impurities were within the acceptable levels. A separate ion chromatography method was developed for the determination of dimethylamine.

Initial experiments showed that the raw material of metformin hydrochloride contained several inorganic impurities, however, due to time limitations only ammonium sulfate was chosen as the source of sulfate ions to test their effect on nucleation rate of metformin hydrochloride. It was found that when up to 0.5 %w/w of ammonium sulfate was added to the solution it caused a decrease in nucleation rate and an increase in the average induction time. On the other hand, addition of

1.0 %w/w of ammonium sulfate had no influence on either nucleation rate or average induction time. The unexpected loss of the impurity effect was investigated further using many analytical techniques such as Scanning Electron Microscope (SEM), Time of Flight – Secondary Ion Mass Spectrometry (ToF-SIMS), Differential Scanning Calorimetry (DSC), Dynamic Light Scattering (DLS) and Ion Chromatography (IC). The results obtained did not provide a definitive answer with regard to why the highest concentration of impurity had no effect on nucleation kinetics. It was thought the effects on induction times were due interactions between sulfate and the nucleation clusters formed during crystallisation of metformin hydrochloride, however further investigation is required.

In a separate part of this project was an investigation into whether or not a batch CoFlux reactor could be used to produce a pure polymorphic form of L-glutamic acid and whether or not enthalpy measurements were an advantage of this reactor for monitoring the crystallisation. Particles obtained from crystallisation experiments in this reactor were analysed using in-situ Raman spectrometry (for several experiments) and off-line X-Ray diffraction (XRPD), laser diffraction (LD) and microscope imaging. The results obtained in the CoFlux reactor were reproducible and a narrower particle size distribution was achieved with the improved temperature control. Enthalpy measurements were not an advantage when monitoring the crystallisation of L-glutamic acid.

Conferences and Publications

Conferences:

Manufacturing the Future 2014, Glasgow, UK

Precise temperature control and use of enthalpy measurements during crystallization of L-glutamic acid in a batch CoFlux reactor, poster presentation

23rd – 24th September 2014

Publications:

1. Albassam, O., et al., *Using ion chromatography with suppressed conductivity detector for profiling of trace ionic impurities in pharmaceutical products*. In preparation, Analytical and Bioanalytical Chemistry, 2016.
2. Dabrowska, N., et al., *The effect of ammonium sulphate addition on the induction time during crystallisation of metformin hydrochloride*. In preparation, 2016.

List of Figures

Figure 1. Classical nucleation theory scheme	3
Figure 2. Non-classical nucleation theory scheme	3
Figure 3. Decision Tree for Identification and Qualification of Impurities [11].....	6
Figure 4. Thesis structure	12
Figure 5. Crystallographic axes and angles describing the seven crystal systems [5]	15
Figure 6. Arbitrary solubility diagram depicting regions of solution stability in relation to the solubility line (red line). Green dotted solubility line represents a solubility of a chosen compound in the antisolvent mixture. Supersolubility line and metastable line are also shown in the figure using consequently grey line and grey dash line. Crystallisation from an undersaturated solution (point A) will happen if one of three main pathways are followed: a. temperature change (cooling crystallisation), b. solute concentration change (evaporation) or c. solvent composition change (antisolvent crystallisation) [21].	17
Figure 7. Formation of nucleus in solution, according to Classical Nucleation Theory	20
Figure 8. A free energy diagram for nucleation (a) showing the relationship between critical free energy (a summation of the surface free energy G_s and the volume excess free energy G_v) and associated radius of the nuclei and b) the diagram showing effect of supersaturation on the critical radius and critical free energy [22]	21
Figure 9. Classification of nucleation processes [19]	24
Figure 10. Free energy pathways for homogeneous and heterogeneous nucleation [25]	24
Figure 11. An example of 80 experimental data points of induction time (left) and probability distribution of those induction times [28]	33
Figure 12. Classical Nucleation Model and Two-Step Nucleation Model crystallisation pathways. (a) solute molecules in supersaturated solution, (b) according to CNT critical nucleus is formed by adding one by one of solute molecules, (c) loose	

liquid-like cluster of solute molecules, (d) ordered crystalline nuclei and (e) final crystal [30].....	35
Figure 13. Changes in free energy according to the two-step nucleation theory [21]	35
Figure 14. A scheme showing the formation of prenucleation clusters at the dissolution stage [36].....	38
Figure 15. Photograph of glycine crystals grown from a 270 mg/ml solution in a continuously inverted vial containing a stirrer bar (incubation time 3 hours). Images were taken at time (a) 0 min, (b) 1 min, (C) 5 min and (d) 10 min after the initial crystal detection [36].....	39
Figure 16. Cryo-TEM images of nanodroplets observed in undersaturated and unfiltered solutions of (a) DL-alanine (150 mg/ml) and (b) glycine (200 mg/ml) [38]	40
Figure 17. Three types of crystal face: flat (F), kinked (K) and stepped (S) [41].....	43
Figure 18. Relationship between the relative step velocity and the dimensionless impurity concentration for different values of an effectiveness factor (α) - based on theory [43]	45
Figure 19. Habit evolution of α -glycine over time when bipyramidal seeds were grown in the presence of 1% (S)-glutamic acid (top row) and 2% (R,S)-methionine (bottom row) Two-dimensional cross sections of modified habits when bipyramidal seeds of α -glycine were grown in the presence of (S)-amino acid (1), (R)-amino acid (2), and (R,S)-amino acid (3) additives [51].	49
Figure 20. General relationships between the relevant crystallisation parameters, such as supersaturation, metastable zone width, crystal growth rate and nucleation rate [47].....	52
Figure 21. Solubility curve of potassium acid phthalate (KAP) with 10mol% addition of potassium chloride (\diamond) and nucleation curve of KAP with (\triangle) and without (\circ) the addition of potassium chloride [57]	55

Figure 22. A relationship between the interfacial energy (σ) and supersaturation (S) of pure (\diamond) and KCl doped (\circ) KAP solution [57]	56
Figure 23. Schematic diagram of the flow system applied for measuring the crystal growth [60].....	58
Figure 24. Faces of glycine crystals grown from aqueous solutions: a. with no additive, b. doped with L-leucine at concentration less than 8 mg/mL, c. doped with L-leucine at concentration greater than 8 mg/mL [60]	59
Figure 25. Photograph (a.) and a schematic diagram (b.) of CoFlux reactor. Temperature probes (T), temperature controller (TC) and valve controller (AC) are shown in a diagram.....	63
Figure 26. CoFlux reactor schematic diagram with description of main components	65
Figure 27. CoFlux reactor, initial setup (setup A).....	67
Figure 28. CoFlux reactor, second setup (setup B)	68
Figure 29. (a) The reactor scheme and (b) geometrical parameters of the oscillatory baffled crystalliser	70
Figure 30. Vortex formation produced by oscillatory flow: (a) Back stroke and (b) forward stroke.....	71
Figure 31. A schematic diagram of the continuous oscillatory baffled reactor, showing the main elements of the setup [72]	71
Figure 32. Jablonski diagram representing quantum energy transitions for Rayleigh and Raman scattering	73
Figure 33. Median, mean and mode in Gaussian and Bimodal distribution of particle sizes [80].....	75
Figure 34. Differences in diffraction patterns between a large (left) and a small particle (right) [81] [82].....	76
Figure 35. Intensity distribution of light against radial distance from centre of focal plane of lens for a typical particle (left) and schematic of detector containing a series of photosensitive rings (right) [83]	77

Figure 36. A schematic diagram showing Debye cones formed by two different crystallites presented in red and green [92]	80
Figure 37. Diagram depicting the interaction of the incoming beam with the crystal lattice: d is the lattice spacing and θ is the angle between the incident rays and the surface of the crystal.	81
Figure 38. L-glutamic acid structure.....	82
Figure 39. Scanning electron micrographs taken at 100x magnification of a) the metastable alpha (α) and b) the stable beta (β) form of LGA [62]	82
Figure 40. SEM image taken at magnification of 100x of the beta form crystals of L-glutamic acid growing out of the surface of the alpha form crystals [97].....	84
Figure 41. A technical drawing of the CoFlux reactor, setup A	87
Figure 42. A technical drawing of the CoFlux reactor, setup B.....	88
Figure 43. Crystal size distribution for L-glutamic acid crystals obtained during experiments no. C. 1.1 – 4, Mastersizer 2000	95
Figure 44. Enthalpy (red line) measured in Watts [W], temperature (black line) measured in Celsius [$^{\circ}$ C] and process power trend (blue line) measured in Watts [W] for experiment no. C.1. 4	95
Figure 45. An example of the relationship between wall and reactor temperature during crystallisation of L-glutamic acid (experiment C.1.3.)	96
Figure 46. The Raman spectra for alpha (green), beta(red) and solute(blue) form of L-glutamic acid	98
Figure 47. Raman real-time measured spectra of L-glutamic acid for dissolution stage (red plot), fully dissolved stage (blue plot) and crystallisation stage (green plot) (exp. C.1.4)	99
Figure 48. The 1 st derivative of Raman spectra of L-glutamic acid (exp. C.1.4).....	99
Figure 49. Dissolution and crystallisation profile (exp C.1.4) of L-glutamic acid based on peak @ 616 cm^{-1} (blue) for alpha form and peak @ 795 cm^{-1} (green) for beta form based on the 1 st derivative of the Raman spectra.	100
Figure 50. Dissolution and crystallisation profile of L-glutamic acid from experiment C.1.4 based on the 1 st derivative spectra for the alpha form at 663 cm^{-1} (blue	

plot), for the beta form at 797 cm ⁻¹ (green plot) and for the solution at 872 cm ⁻¹ (red plot).	101
Figure 51. The 1 st derivative of the Raman spectra of L-glutamic acid, showing changes in the intensities of the alpha and beta peaks over time	102
Figure 52. Raman dissolution and crystallisation profile (exp C.1.4) of L-glutamic acid, based on the changes in the intensities of alpha (at 1180 cm ⁻¹) – green plot and beta (at 1126 cm ⁻¹) – blue plot characteristic peaks.	102
Figure 53. XRPD pattern for the raw material (red plot), crystallisation product (black plot), alpha (green plot) and beta (blue plot) form of L-glutamic acid (experiment no. C.1.4)	103
Figure 54. Microscope image of prismatic shape of the alpha crystals obtained during the experiment C.1.4 – magnification 4x.....	104
Figure 55. XRPD pattern for crystallisation product (black plot), alpha (blue plot) and beta (red plot) form of L-glutamic acid (experiment no. C.2.3).....	106
Figure 56. Microscope image – magnification 10x, exp. C.2.1	106
Figure 57. Crystal size distribution for L-glutamic acid crystals obtained during experiments no. C.2.6 – 8, Mastersizer 3000	107
Figure 58. A real time accumulation or heat shift (q _s) in the process fluid [W] (blue plot) and temperature [°C] trend (black plot) for dissolution and crystallisation of L-glutamic acid, exp. C.2.2, cooling rate 0.41°C/min.....	108
Figure 59. A real time accumulation or heat shift (q _s) in the process fluid [W] (black plot) and temperature trend for heating and cooling water (blue plot), cooling rate 0.75°C/min.....	109
Figure 60. A real time accumulation or heat shift in the process fluid – q _s (blue plots) and temperature trend (black plots) for dissolution and crystallisation of L-glutamic acid, A - exp. C.2.1, B - exp. C.2.3, C - exp. C.2.5, D - exp. C.2.6, E - exp. C.2.7, F - exp. C.2.8.....	110
Figure 61. a) Raman dissolution and crystallisation profile (exp C.2.3) of L-glutamic acid, based on the 1 st derivative of the intensity changes of alpha characteristic peak at 1181 cm ⁻¹ (blue plot) and beta characteristic peak at 1126 cm ⁻¹ (green	

plot) and b) Raman dissolution and crystallisation profile (exp C.2.3) of the same compound based on the 1 st derivative of the intensity changes of alpha characteristic peak at 622 cm ⁻¹ (blue plot) and beta characteristic peak at 802 cm ⁻¹ (green plot).....	112
Figure 62. a) Zoomed in Raman crystallisation profile (exp C.2.3) based on the 1 st derivative of the intensity changes of alpha characteristic peak at 1181 cm ⁻¹ (blue plot) and beta characteristic peak at 1126 cm ⁻¹ (green plot) and b) Zoomed in Raman crystallisation profile (exp C.2.3) based on the 1 st derivative of the intensity changes of alpha characteristic peak at 622 cm ⁻¹ (blue plot) and beta characteristic peak at 802 cm ⁻¹ (green plot).....	113
Figure 63. Enthalpy (red plot), temperature (blue plot) and accumulation or heat shift (q _s) in the process fluid [W] (black plot) trend for experiment no. C.2.3.....	114
Figure 64. Raman dissolution and crystallisation profile (exp C.2.8) based on the 1 st derivative of the intensity changes of alpha characteristic peak at 1181 cm ⁻¹ (blue plot) and beta characteristic peak at 1126 cm ⁻¹ (green plot).....	115
Figure 65. Zoomed in Raman crystallisation profile (exp C.2.8) based on the 1 st derivative of the intensity changes of alpha characteristic peak at 1181 cm ⁻¹ (blue plot) and beta characteristic peak at 1126 cm ⁻¹ (green plot).....	116
Figure 66. Enthalpy (blue plot), temperature (black plot) and accumulation or heat shift (q _s) in the process fluid (red plot) trend for experiment no. C.2.8.....	117
Figure 67. Diagram showing how the process of the chromatographic separation [103]	115
Figure 68. Diagram showing the relationship between hydrophilic interaction liquid chromatography (HILIC) and other chromatographic techniques – reverse phase (RP-LC), normal phase (NP-LC) and ion chromatography (IC).	117
Figure 69. Differences between a normal-phase (NP) and reversed-phase (RP) structure.....	118
Figure 70. Commonly used reversed-phase stationary phases and their polarity..	119
Figure 71. A typical method validation parameters	119

Figure 72. Schematic diagram of chromatographic separation on the HPLC column: A and B are two components, V_0 is the void time	121
Figure 73. An example of asymmetric peak. In the scheme above a and b are the front and back half widths at 5% (or 10%) of peak height [105]	123
Figure 74. A schematic diagram showing the retention time (t_{R1} and t_{R2}) and the widths of peaks A and B measured at baseline (W1 and W2) as well as the widths of peaks A and B measured at 50% of peak height ($W_{0.5h1}$ and $W_{0.5h2}$). All these parameters are required to calculate the peak resolution.....	124
Figure 75. Basic principles of the ion chromatographic separation [110].....	127
Figure 76. Electrospray Ionisation (ESI) and Ion Source Overview [33].....	129
Figure 77. A chemical structure of metformin.....	132
Figure 78. Metformin synthesis route	132
Figure 79. (A) Needle shape form A crystals of metformin hydrochloride growing with the loss of (B) form B [117]	133
Figure 80. HPLC method for determination of metformin hydrochloride impurities [37]	136
Figure 81. A schematic diagram of the setup used during the temperature stability test	145
Figure 82. Metformin hydrochloride stability test results, showing the changes in its concentration over time	166
Figure 83. Stability test results, showing the changes in the impurities concentrations over time: green – (4,6-diamino-1,3,5-triazin-2-yl) guanidine, grey – melamine, yellow – cyanoguanidine, orange – 1-methylbiguanide, blue – N,N-dimethyl-1,3,5-triazine-2,4,6-triamine	167
Figure 84. An example of ion chromatogram, for dimethylamine (5.827 min) present in metformin hydrochloride sample	171
Figure 85. Potential route of formation of N,N-dimethyl-1,3,5-triazine-2,4,6-triamine	174

Figure 86. Photograph showing the colour difference between a) a freshly made sample of metformin hydrochloride and b) a sample collected at the end of the stability test.....	175
Figure 87. Molecular structure of ammonium sulfate.....	178
Figure 88. A summary of the results obtained for samples of metformin hydrochloride crystallised in three different reactors - Crystalline, OptiMax and EasyMax (sample description and experimental conditions are provided below – Table 55).	181
Figure 89. Crystalline Equipment Photograph	182
Figure 90. OptiMax reactor photograph.....	183
Figure 91. A schematic diagram of a scanning electron microscope [125]	184
Figure 92. Types of electrons ejected from the sample, when the focused electron beam hits the sample [126]	185
Figure 93. Dynamic light scattering diagram	189
Figure 94. Screenshot of the interactive curve fitting tool created by Dr. Jerzy Dziejewicz. Interactive cursors are indicated in red - corresponding with the 1 st decay, green – the 2 nd decay and blue - the 3 rd decay.	192
Figure 95. Solubility curve for pure metformin hydrochloride.....	200
Figure 96. The summary of the induction times for metformin hydrochloride samples containing different concentrations of ammonium sulfate at SS=1.5.....	201
Figure 97. Summary of all induction times obtained during all experiments carried out with unfiltered solution: [○] represents pure metformin hydrochloride samples, [○] represents metformin hydrochloride samples doped with 0.10 %w/w of ammonium sulfate, [○] 0.50 %w/w of ammonium sulfate and [○] 1.00 %w/w of ammonium sulfate.	202
Figure 98. Summary of all induction times obtained during all experiments carried out with filtered solution: [○] represents pure metformin hydrochloride samples, [○] represents metformin hydrochloride samples doped with 0.10 %w/w of ammonium sulfate, [○] 0.50 %w/w of ammonium sulfate and [○] 1.00 %w/w of ammonium sulfate	203

- Figure 99. Cumulative probability distributions of induction times for metformin hydrochloride samples: [x] pure metformin hydrochloride, [+] metformin hydrochloride doped with 0.01 %w/w ammonium sulfate, [⊕] 0.1 %w/w ammonium sulfate, [○] 0.25 %w/w ammonium sulfate, [◇] 0.5 %w/w ammonium sulfate, [□] 0.75 %w/w ammonium sulfate and [*] 1.0 %w/w ammonium sulfate. 204
- Figure 100. Cumulative probability distributions of induction times for metformin hydrochloride samples with logarithmic time scale: [x] pure metformin hydrochloride, [+] metformin hydrochloride doped with 0.01 %w/w ammonium sulfate, [⊕] 0.1 %w/w ammonium sulfate, [○] 0.25 %w/w ammonium sulfate, [◇] 0.5 %w/w ammonium sulfate, [□] 0.75 %w/w ammonium sulfate and [*] 1.0 %w/w ammonium sulfate. 204
- Figure 101. Summary of results (n=40) from fitting the ter Horst model to the cumulative probability distributions of all induction time experiments for all unfiltered conditions. In the graph blue □ represents nucleation rate - J and orange ○ represents growth time - t_g 205
- Figure 102. Summary of results from fitting the Classical Nucleation Theory model to the cumulative probability distributions of all induction time experiments for all unfiltered conditions: [●] represents pure metformin hydrochloride samples, [■] represents metformin hydrochloride samples doped with 0.10 %w/w of ammonium sulfate, [▲] 0.50 %w/w of ammonium sulfate and [✕] 1.00 %w/w of ammonium sulfate. 206
- Figure 103. Summary of results from fitting the Classical Nucleation Theory model to the cumulative probability distributions of all induction time experiments for all filtered conditions: [●] represents pure metformin hydrochloride samples, [■] represents metformin hydrochloride samples doped with 0.10 %w/w of ammonium sulfate, [▲] 0.50 %w/w of ammonium sulfate and [✕] 1.00 %w/w of ammonium sulfate. 207
- Figure 104. pH investigation results showing changes with decreasing temperature in the Optimax reactor during crystallisation of metformin hydrochloride. Green

represents pure metformin hydrochloride samples, orange represents metformin hydrochloride samples doped with 0.01 %w/w of ammonium sulfate, grey samples doped with 0.10 %w/w of ammonium sulfate, yellow samples doped with 0.50% of ammonium sulfate and blue samples doped with 1.00 %w/w of ammonium sulfate.....	211
Figure 105. Solubility curves obtained in the Crystalline platform for all unfiltered experiments with pure metformin (blue) and metformin doped with different ammonium sulfate concentrations: 0.01 %w/w (purple), 0.1 %w/w (grey), 0.5 %w/w(green) and 1.0 %w/w (red).....	212
Figure 106. Graph showing results obtained for the interfacial energy determination for pure metformin hydrochloride (blue) and metformin hydrochloride doped with 0.1 %w/w (orange), 0.5 %w/w (grey) and 1.0 (yellow) %w/w ammonium sulfate.....	214
Figure 107. SEM image taken at (a) 1119x magnification of recrystallised metformin (b) 205x magnification of the metformin raw material (c) 766x magnification of metformin crystals produced in the presence of 0.1 %w/w ammonium sulfate (d) 1110x magnification of metformin crystals produced in the presence of 0.5 %w/w ammonium sulfate (e) 1119x magnification of metformin crystals produced in the presence of 1.0 %w/w ammonium sulfate	216
Figure 108. Results obtained from TOF-SIMS showing the increase in the peak area corresponding to ammonium sulfate in the crystals produced when the doping concentration was increased – highlighted in red.....	217
Figure 109. Peak area results from TOF-SIMS for the ammonium sulfate standard and the metformin crystals doped with 0.1, 0.5 and 1.0 %w/w ammonium sulfate in the solution	218
Figure 110. Thermal traces for metformin hydrochloride raw material (blue), pure material (red), sample containing 0.1 %w/w of ammonium sulfate (grey), 0.5 %w/w of ammonium sulfate (yellow) and 1.0 %w/w of ammonium sulfate (green), 10°C/min cooling rate.....	219

Figure 111. Thermal traces for metformin hydrochloride raw material (blue), pure material (red), sample containing 0.1 %w/w of ammonium sulfate (grey), 0.5 %w/w of ammonium sulfate (yellow) and 1.0 %w/w of ammonium sulfate (green), 1°C/min cooling rate: a) full profile and b) zoomed in profile	220
Figure 112. Results from ion chromatography showing the concentration of chloride(grey) and sulfate (yellow) in the metformin hydrochloride crystals produced under different doping concentrations of ammonium sulfate (0.01, 0.1, 0.25, 0.5, 0.75, 1.0 %w/w) as well as blank distilled water and blank solvent	221
Figure 113. Results from ion chromatography showing the concentration of chloride (red) and sulfate (blue) in the metformin hydrochloride filtrate produced under different doping concentrations of ammonium sulfate (0.01, 0.1, 0.25, 0.5, 0.75, 1.0 %w/w)	222
Figure 114. Autocorrelation functions from dynamic light scattering measurements (angle 173°) for undersaturated solution of metformin hydrochloride (SS=0.9) first (a) and second experimental run (b)	224
Figure 115. Mean count rate recorded in kilo counts per second for each impurity concentration during the dynamic light scattering measurements for undersaturated solution of metformin hydrochloride (SS=0.9) for repetition 1 (blue) and repetition 2 (orange).	225
Figure 116. Autocorrelation functions from dynamic light scattering measurements (angle 173°) for unfiltered supersaturated solution of metformin hydrochloride (SS=1.55) first (a) and second experimental run (b)	226
Figure 117. Mean count rate recorded in kilo counts per second for each impurity concentration during the dynamic light scattering measurements for supersaturated solution of metformin hydrochloride (SS=1.55) for repetition 1 (blue) and repetition 2 (orange).	227
Figure 118. Autocorrelation functions from dynamic light scattering measurements (angle 173°) for filtered supersaturated solution of metformin hydrochloride (SS=1.55) first (a) and second experimental run (b)	228

Figure 119. Mean count rate recorded in kilo counts per second for each impurity concentration during the dynamic light scattering measurements for supersaturated solution of metformin hydrochloride (SS=1.55) for repetition 1 (blue) and repetition 2 (orange).	229
Figure 120. Average Diameter (nm) from 2nd Decay vs. Impurity Concentration for undersaturated solution of metformin hydrochloride (SS=0.9): pure metformin hydrochloride (light blue), samples doped with 0.01 %w/w of ammonium sulfate (orange), 0.1 %w/w (grey), 0.5 %w/w (yellow) and 1.0 %w/w (dark blue).	230
Figure 121. Average Diameter (nm) from 2nd Decay vs. Impurity Concentration for unfiltered supersaturated solution of metformin hydrochloride (SS=1.55): pure metformin hydrochloride (light blue), samples doped with 0.01 %w/w of ammonium sulfate (orange), 0.1 %w/w (grey), 0.5 %w/w (yellow) and 1.0 %w/w (dark blue).	231
Figure 122. Average Diameter (nm) from 2nd Decay vs. Impurity Concentration for filtered supersaturated solution of metformin hydrochloride (SS=1.55). The y-axis is presented in logarithmic scale: pure metformin hydrochloride (light blue), samples doped with 0.1 %w/w (grey) of ammonium sulfate 0.5 %w/w (yellow) and 1.0 %w/w (dark blue).	231
Figure 123. LC - MS calibration curve for metformin hydrochloride.....	239
Figure 124. LC - MS calibration curve for melamine.....	239
Figure 125. LC - MS calibration curve for 1-methylbiguanide	240
Figure 126. LC - MS calibration curve for cyanoguanidine	240
Figure 127. LC - MS calibration curve for (4,6-diamino-1,3,5-triazine-2-yl)-guanidine	241
Figure 128. LC - MS calibration curve for N,N-dimethyl-1,3,5-triazine-2,4,6-triamine	241
Figure 129. Extracted Ion Chromatogram of Metformin Hydrochloride at concentration of 5 mg/mL	242
Figure 130. Extracted Ion Chromatogram of Cyanoguanidine at concentration of 550 ng/mL	242

Figure 131. Extracted Ion Chromatogram for (4,6-diamino-1,3,5-triazine-2-yl)- guanidine at concentration of 10 ng/mL	242
Figure 132. Extracted Ion Chromatogram of N,N-dimethyl-1,3,5-triazine-2,4,6- triamine at concentration of 10 ng/mL.....	243
Figure 133. Extracted Ion Chromatogram for Melamine at concentration of 10 ng/mL	243
Figure 134. Extracted Ion Chromatogram for 1-methylbiguanide at concentration of 10 ng/mL	243
Figure 135. Calibration curve for dimethylamine	244
Figure 136. An example of ion chromatogram, for 15 µg/mL dimethylamine standard solution.....	244
Figure 137. An example of ion chromatogram, for 0.1% w/w ammonium sulfate crystals from the re-crystallised sample	245
Figure 138. Ion chromatography calibration curve for sulfate anions showing the equation of the line.....	246
Figure 139. Ion chromatography calibration curve for chloride anions in the filtrate showing the equation of the line	246
Figure 140. Ion chromatography calibration curve for chloride anions in the crystals showing the equation of the line	247

List of Tables

Table 1. Thresholds given in the guidelines for reporting, qualification and quantification of impurities in drugs [11]	5
Table 2. Classes of Impurities.....	7
Table 3. Experimental conditions –for crystallisation of LGA in a CoFlux reactor, setup A and B	90
Table 4. Experimental conditions – stirred tank reactor	91
Table 5. Experimental conditions - OBR.....	92
Table 6. Results of the analysis of the obtained product in the CoFlux reactor.....	94
Table 7. Results of the analysis of the obtained product in the CoFlux reactor, setup B.....	105
Table 8. Comparison of the results obtained during measurements of the particle size carried out in the two different Malvern MasterSizer units.....	107
Table 9. Comparison of the results obtained during experiments in stirred tank reactor and oscillatory baffled reactor	120
Table 10. Comparison of the results obtained during experiments in CoFlux reactor.....	121
Table 11. Final comparison of the results obtained using two different CoFlux setups (A and B).....	125
Table 12. Potential impurities in metformin hydrochloride samples.....	135
Table 13. LC/MS method gradient program	141
Table 14. MS detector optimisation parameters, with final values highlighted in green	141
Table 15. Retention times for metformin hydrochloride and its impurities	142
Table 16. Calibration curve results of metformin hydrochloride, including regression coefficient and the equation.....	146
Table 17. Calibration curve results of melamine, including regression coefficient and the equation.....	146
Table 18. Calibration curve results of 1-methylbiguanide, including regression coefficient and the equation.....	147

Table 19. Calibration curve results of (4,6-diamino-1,3,5-triazin-2-yl) guanidine, including regression coefficient and the equation	147
Table 20. Calibration curve results of N,N-dimethyl-1,3,5-triazine-2,4,6-triamine, including regression coefficient and the equation	148
Table 21. Calibration curve results of cyanoguanidine, including regression coefficient and the equation	148
Table 22. Demonstration of the precision of the LC/MS method for metformin hydrochloride as shown by the results on 6 replicate injections of one solution of 15 µg/mL concentration	149
Table 23. Demonstration of the precision of the LC/MS method for metformin hydrochloride as shown by the results on 6 replicate injections of one solution of 10 µg/mL concentration	149
Table 24. Demonstration of the precision of the LC/MS method for metformin hydrochloride as shown by the results on 6 replicate injections of one solution of 5 µg/mL concentration	150
Table 25. Demonstration of the precision of the LC/MS method for melamine as shown by the results on 6 replicate injections of one solution of 25 ng/mL concentration	150
Table 26. Demonstration of the precision of the LC/MS method for melamine as shown by the results on 6 replicate injections of one solution of 5 ng/mL concentration	151
Table 27. Demonstration of the precision of the LC/MS method for melamine as shown by the results on 6 replicate injections of one solution of 1 ng/mL concentration	151
Table 28. Demonstration of the precision of the LC/MS method for 1-methylbiguanide as shown by the results on 6 replicate injections of one solution of 25 ng/mL concentration	152
Table 29. Demonstration of the precision of the LC/MS method for 1-methylbiguanide as shown by the results on 6 replicate injections of one solution of 5 ng/mL concentration	152

Table 30. Demonstration of the precision of the LC/MS method for 1-methylbiguanide as shown by the results on 6 replicate injections of one solution of 1 ng/mL concentration	152
Table 31. Demonstration of the precision of the LC/MS method for (4,6-diamino-1,3,5-triazin-2-yl) guanidine as shown by the results on 6 replicate injections of one solution of 25 ng/mL concentration	153
Table 32. Demonstration of the precision of the LC/MS method for (4,6-diamino-1,3,5-triazin-2-yl) guanidine as shown by the results on 6 replicate injections of one solution of 5 ng/mL concentration	153
Table 33. Demonstration of the precision of the LC/MS method for (4,6-diamino-1,3,5-triazin-2-yl) guanidine as shown by the results on 6 replicate injections of one solution of 1 ng/mL concentration	154
Table 34. Demonstration of the precision of the LC/MS method for N,N-dimethyl-1,3,5-triazine-2,4,6-triamine as shown by the results on 6 replicate injections of one solution of 25 ng/mL concentration	154
Table 35. Demonstration of the precision of the LC/MS method for N,N-dimethyl-1,3,5-triazine-2,4,6-triamine as shown by the results on 6 replicate injections of one solution of 5 ng/mL concentration	155
Table 36. Demonstration of the precision of the LC/MS method for N,N-dimethyl-1,3,5-triazine-2,4,6-triamine as shown by the results on 6 replicate injections of one solution of 1 ng/mL concentration	155
Table 37. Demonstration of the precision of the LC/MS method for cyanoguanidine as shown by the results on 6 replicate injections of one solution of 550 ng/mL concentration	156
Table 38. Demonstration of the precision of the LC/MS method for cyanoguanidine as shown by the results on 6 replicate injections of one solution of 250 ng/mL concentration	156
Table 39. Demonstration of the precision of the LC/MS method for cyanoguanidine as shown by the results on 6 replicate injections of one solution of 50 ng/mL concentration	156

Table 40. Demonstration of the accuracy of the LC/MS method for metformin hydrochloride as shown by the results on 6 replicate injections of three solutions of 15, 10 and 5 µg/mL concentrations respectively	157
Table 41. Demonstration of the accuracy of the LC/MS method for melamine as shown by the results on 6 replicate injections of three solutions of 25, 5 and 1 ng/mL concentrations respectively.....	158
Table 42. Demonstration of the accuracy of the LC/MS method for 1-methylbiguanide as shown by the results on 6 replicate injections of three solutions of 25, 5 and 1 ng/mL concentrations respectively.....	159
Table 43. Demonstration of the accuracy of the LC/MS method for (4,6-diamino-1,3,5-triazin-2-yl) guanidine as shown by the results on 6 replicate injections of three solutions of 25, 5 and 1 ng/mL concentrations respectively	160
Table 44. Demonstration of the accuracy of the LC/MS method for N,N-dimethyl-1,3,5-triazine-2,4,6-triamine as shown by the results on 6 replicate injections of three solutions of 25, 5 and 1 ng/mL concentrations respectively	161
Table 45. Demonstration of the accuracy of the LC/MS method for cyanoguanidine as shown by the results on 6 replicate injections of three solutions of 550, 250 and 50 ng/mL concentrations respectively.....	162
Table 46. Capacity factors for all individual compounds.....	163
Table 47. Summary of two validation parameters: peak asymmetry and column efficiency for all analysed compounds.....	164
Table 48. Limit of Detection and Limit of Quantification for all individual compounds.....	165
Table 49. Relative impurity concentrations (%w/w relative to metformin hydrochloride) in the initial solution (t=0) and final solution (t=241 hr).....	168
Table 50. Calibration curve results for dimethylamine.....	170
Table 51. Gradient program and measurement conditions for Ion Chromatography	179
Table 52. Sample description and experimental conditions.....	180
Table 53. Experimental Conditions for Induction Time Experiments	194

Table 54. DLS experimental conditions summary.....	196
Table 55. Concentrations used in solubility study of metformin hydrochloride.....	198
Table 56. The comparison of the nucleation rate values obtained from the two studied models - Classical Nucleation Theory and ter Horst Model, for the experiments, where supersaturation of 1.55 was chosen.	209
Table 57. SS=0.9 Unfiltered.....	248
Table 58. SS=0.9 Repetition Unfiltered.....	249
Table 59. SS=1.55 Unfiltered.....	250
Table 60. SS=1.55 Repetition Unfiltered.....	251
Table 61. SS=1.55 Filtered.....	252
Table 62. SS=1.55 Repetition Unfiltered.....	253

1 Introduction

1.1 Project Background

Crystallisation is a process which can be used as a natural or artificial way of forming solid particles. In the chemical and pharmaceutical industry crystallisation is widely used to produce drugs, dyes, pesticides, etc. At present, more than 90% of active pharmaceutical ingredients (APIs) are produced through crystallisation, as a final step of API formation [1].

Crystallisation can also be used as a chemical solid-liquid separation technique, where the process is used to purify the product – therefore crystallisation is an aspect of precipitation. It is achieved through varying the solubility conditions of the solute in the specific solvent and does not occur as a result of a chemical reaction like other precipitation processes. [2].

There are a few essential key aspects [3] that have to be considered while designing a successful crystallisation process:

- 1) Solubility – the solubility of the compound is defined as the maximum amount of solute that can exist at equilibrium under given conditions in a certain solvent. Usually the solubility increases with temperature and is highly dependent on the solvent composition [4]. The driving force for the crystallisation is the supersaturation, which can be described as a state of a solution that contains more dissolved solid than represented by the equilibrium saturation [5]. Supersaturation is a necessary condition for nucleation to take place [6].
- 2) Metastable zone width – the beginning of the crystallisation is dependent on the cooling rate, because the width of the metastable zone depends on this parameter. As the cooling rate increases, the metastable zone width widens, so the position of the optimum supersaturation level changes. Therefore, choosing the best possible cooling profile is crucial. The best way is to use a parabolic cooling profile, which provides better control of nucleation and

constant crystal growth, however this kind of cooling profile is quite often unreachable. In practice a linear cooling profile is most often used [7].

- 3) Nucleation characteristics – determining parameters such as nucleation rate or nucleation induction time provides information about timescales of nucleation and the behaviour of the chosen compound under certain conditions [3].
- 4) Crystal growth characteristics – parameter crucial especially when a particular size distribution is required – for seed production or in order to improve downstream processes, such as filtration [3].
- 5) Hydrodynamics of crystal suspension – the behaviour of the slurry will have a significant effect on downstream processes, so it is essential to provide this information at the stage of designing the crystallisation unit operation [3].

Crystal properties depend on thermodynamic conditions and the kinetics of the nucleation and growth processes. Nucleation happens when the supersaturated solution which is not at equilibrium crystallises in order to reach equilibrium. At this stage the solution contains extremely small species – nuclei, which initiate the crystal growth. Molecules prefer to cluster in a supersaturated solution and continue to grow rather than dissolve [4].

Nucleation can be divided into two classes – primary and secondary nucleation. Primary nucleation occurs when no crystalline matter exists in the supersaturated solution, and secondary nucleation is when nuclei are generated in the vicinity of crystals already present in a supersaturated solution. Primary nucleation can be distinguished into two classes – homogenous (spontaneous) and heterogeneous (induced by foreign particles). Two theories describe nucleation – according to the classical nucleation theory the nuclei are miniature crystals, nearly perfect in form, according to non-classical nucleation theory the nuclei are diffuse bodies with molecules or solvated ions in a state not too different from the bulk solution, with no clearly defined surface (Figure 1 and Figure 2) [5] [4] [6].

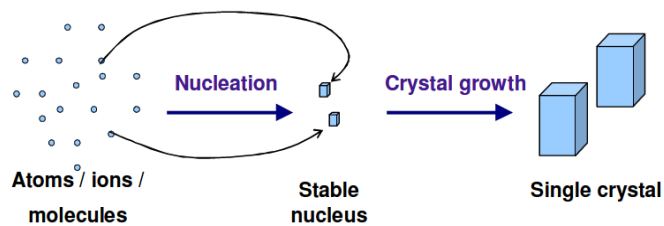


Figure 1. Classical nucleation theory scheme

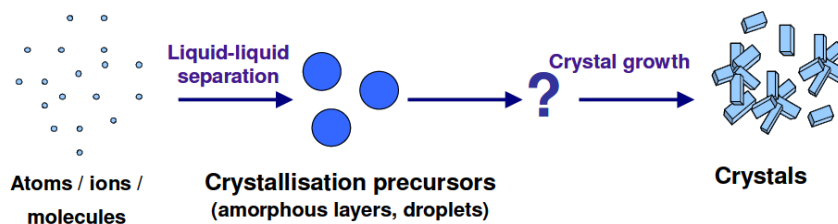


Figure 2. Non-classical nucleation theory scheme

As mentioned above the second step in the crystallisation process is crystal growth. This step determines the crystals' size. Solute molecules diffuse through the liquid phase to approach the crystal face, which results in layer-by-layer growth of the crystals [6]. Two processes are observed during the crystal growth – the first one is mass transport of the solute by diffusion to the crystal face, and the second one is a surface integration of the material into the crystal lattice – adsorption onto the crystal surface and then addition to the lattice (solvation shell is lost) [4].

The ability of a compound to adopt different crystalline arrangements is described as polymorphism. The major polymorphic form produced during the crystallisation is dependent on the system parameters: solvent choice, temperature range, mixing speed, impurities present and supersaturation level. The supersaturation level is a parameter which plays the most important role, because the nucleation and growth kinetics are supersaturation dependent [8]. Different polymorphic forms show different physical properties such as shape, morphology, solubility, density or colour. Different properties can emerge from different polymorphs, so the proper polymorphic form is vital in the pharmaceutical industry. The transformation of

polymorphs is a problem for the pharmaceutical industry, because the different physical properties of different polymorphic forms affect the product properties such as the bioavailability, shelf life, compactness etc. of a drug compound. The control of the formation of polymorphs during crystallisation is a crucial point of the process [9].

The impurities in pharmaceuticals are unwanted chemicals that arise from the synthetic route and remain with the active pharmaceutical ingredients, develop during formulation or arise during aging and formulation of drugs. The presence of impurities in drugs may significantly change product quality and safety, therefore production of pure (including the control of polymorphic form presence) products is especially important in drug manufacture, where the patient may be potentially at risk.

Impurity control in drugs should be considered at the drug design stage and should be carried on throughout the entire drug production process. Procedures of determination, quantification and control of impurities are included in official regulations released by International Conference of Harmonization, the United States Food and Drug Administration (FDA) and the Canadian Drug and Health Agency (CDHA) [10].

In general, impurities present in excess of 0.1% (w/w) should be identified and quantified. Identification of impurities below this level is not necessary, however if the potential impurities are expected to be unusually toxic they also should be identified and quantified. The impurity guidelines have been published by the International Conference on Harmonisation (ICH) [11]. This guideline defines methods for analysis of impurities in new drug substances, new drug products, residual solvents and microbiological impurities for registration of pharmaceuticals for human use. Thresholds for the impurities are given in the guidelines for reporting, qualification and identification of impurities and are presented in Table 1.

Table 1. Thresholds given in the guidelines for reporting, qualification and quantification of impurities in drugs [11]

Maximum daily dose ^a	Reporting threshold ^{b,c}	Identification threshold ^c	Qualification threshold
≤2g/day	0.05%	0.1% or 1mg per day intake	0.15% or 1mg per day intake
>2g/day	0.03%	0.05%	0.05%

- a. The amount of drug substance administered per day
- b. Higher reporting thresholds should be scientifically justified
- c. Lower thresholds can be appropriate if the impurity is unusually toxic

ICH guidelines also provide a decision tree for identification and qualification of impurities, which is shown below in Figure 3.

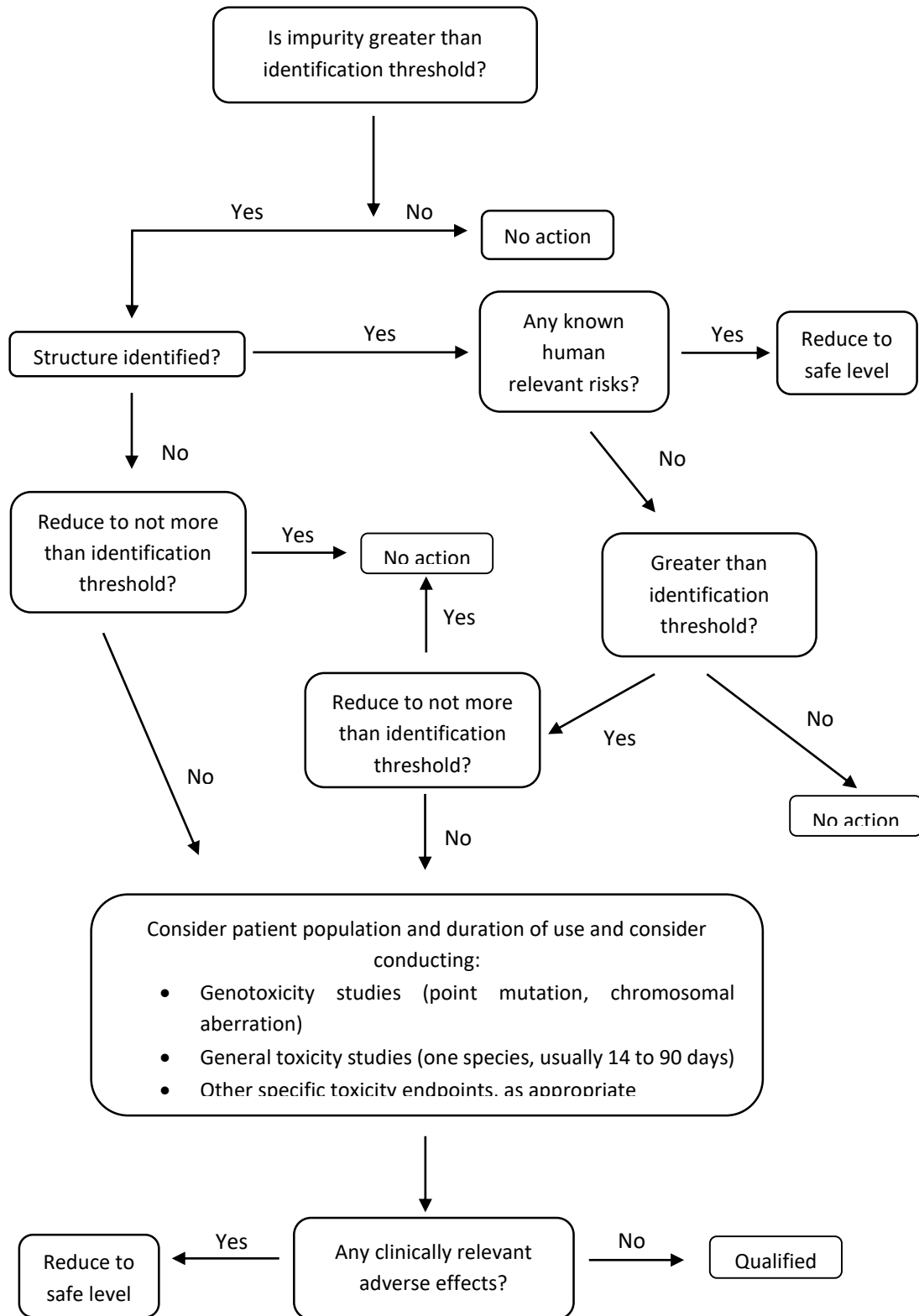


Figure 3. Decision Tree for Identification and Qualification of Impurities [11]

The ICH guideline also contains classification of impurities. According to this document, impurities can be classified into 3 categories – organic, inorganic and residual solvents. Most of them can be related to the synthetic route of manufacturing process. Typical sources of impurities are:

- intermediates generated during synthesis,
- products or residuals from incomplete reactions during the synthesis,
- products of overreaction or side-reactions,
- impurities from solvents, reagents or starting material,
- impurities from catalysts, inorganic impurities
- degradation products [12].

A more detailed characterisation of the types of impurities is shown in Table 2.

Table 2. Classes of Impurities

Organic impurities	Inorganic impurities	Residual solvents
Organic impurities can appear during the manufacturing process and/or storage. This group of impurities include: starting materials, by-products, intermediates, degradation products, reagents, ligands and catalysts.	Inorganic impurities may be produced during the manufacturing process. This group includes: reagents, ligands and catalysts, heavy metals or other residual metals, inorganic salts, other materials such as filter aids, charcoal etc.	This group contains all organic and inorganic liquids used during the manufacturing.

The determination and identification of drug impurities should be a crucial stage of every manufacturing process, especially when the impurity could potentially be toxic. British, European, United States and Indian Pharmacopoeia [10] provide not only limits of acceptable levels of impurities, but also a list of analytical techniques, that should be used for isolation and characterization of impurities in pharmaceuticals. Both chromatographic and spectroscopic techniques can be used in order to determine and quantify the impurity level. The fundamental criteria for the choice of

analytical technique is the ability to differentiate between the compounds of interest. Spectroscopic techniques are more useful for determining isolated compounds/impurities - however the limitation of techniques such as ultraviolet (UV) spectroscopy or Infrared spectroscopy is their ability to detect low amounts of impurity. Nuclear Magnetic Resonance (NMR) or Mass Spectrometry (MS) can be classed as very sensitive techniques, however costs of using these techniques is relatively high. When impurities are not isolated, chromatographic techniques are the first choice for their detection. Gas chromatography is especially useful for volatile organic compounds, while liquid chromatography can be applied to a wide range of organic impurities – high sensitivity and robustness of this technique have been achieved by the use of a variety of detectors – UV, fluorescence, electrochemical, MS, etc. [13] [12]. Currently chromatography is the most commonly used in monitoring the drug substance and its impurities and applications of liquid chromatography for this purpose are widely reported in the literature. A review published by Rao and Nagaraju [12] reports that over 450 papers describing chromatographic methods for determination of impurities were published in the time period from 1995 to 2001 and this total is still increasing.

1.2 Project Outline

1.2.1 Determination of the Effect of the Temperature Control on Crystallisation of L-Glutamic Acid

Work was carried out in order to investigate the effect of an improved temperature control on crystallisation of L-Glutamic Acid using a Coflux reactor. L-Glutamic Acid was chosen as a model compound, due to extensive literature available and therefore better opportunity to compare the results obtained with those present in the literature. A series of cooling crystallisations of this model compound were carried out in order to evaluate the performance of a batch CoFlux reactor in relation to polymorphic forms being produced, crystal size and crystal distribution. Obtained results were then compared with the results obtained by Dr Laura Palmer [14] for stirred tank reactor and oscillatory baffled crystalliser reactor.

An additional aim of this work was to assess if enthalpy measurement was an advantage of this reactor for monitoring the crystallisation of this compound.

Experimental conditions along with experimental results are presented in Chapter 3. It should be noted that the work described here was performed under supervision of Professor David Littlejohn and Dr Alison Nordon from the Pure and Applied Chemistry Department at University of Strathclyde.

1.2.2 Determination of the Influence of Impurities on the Crystallisation of Pharmaceutical Materials

Metformin hydrochloride (anti-hyperglycemic agent and the first line drug choice for the treatment of type II diabetes) is the active pharmaceutical ingredient chosen for this project. The reason behind is that the effect of inorganic impurities was to be investigated throughout the project and therefore metformin hydrochloride as an ionic compound was a suitable choice.

The first step of this project was to develop a quick quantitative and qualitative chromatographic method to identify and determine the impurities in metformin hydrochloride samples – for organic impurities high resolution liquid chromatography coupled with mass spectrometry was used, while for inorganic

impurities an ion chromatography method with conductometric detection was developed.

In the current work accelerated degradation experiments were also undertaken for metformin hydrochloride in order to find out which organic impurities arose from the synthetic route and which arose from the degradation of the API.

Initial analysis of metformin samples using ion chromatography revealed that sulfate amongst others was present as an inorganic impurity. The compound ammonium sulfate was chosen as the source of sulfate anions for further investigation into the effect that sulfate levels have on the nucleation rate. Small scale reactor – a Crystalline reactor – was chosen in order to minimise the costs of the experiments carried out throughout the project. Two unrelated models were applied to the obtained data - ter Horst model and Classical Nucleation Theory - in order to obtain nucleation rates. Both models are described in Chapter 2 and the results are presented and discussed in Chapter 5.

The focus on inorganic impurities was dictated mainly by a nature of the model compound, however a high cost of organic impurities was the reason for elimination the investigation of the effect of these impurities on nucleation rate.

One of the aims of this project was to provide enough information about the impurities present and their effects on the continuous crystallisation environment to simplify the design of the crystallisation process, in case the continuous campaign for metformin hydrochloride will be taking place in the future. The following problem statements were addressed during this project:

- Growth and habit control: where the effect of impurities in the system has an effect and hence must be understood if continuous crystallisation is to be implemented.
- Particle attributes and performance: any impurities, at any concentration within the system can influence the particle attributes and in turn the performance of the crystals being produced.

- Process understanding: through monitoring the changes in impurities throughout continuous crystallisation, a deeper understanding of their influence on the entire process can be achieved.

This part of the entire project was carried out under supervision of Dr David Watson and Professor Alastair Florence from Strathclyde Institute of Pharmacy & Biomedical Sciences at University of Strathclyde.

1.3 Project Management

As mentioned above this PhD project was undertaken in two different departments - Pure and Applied Chemistry Department and Strathclyde Institute of Pharmacy & Biomedical Sciences, under two different supervisions due to unforeseen circumstances. For these reason, there were a number of experiments that could not be carried out or repeated due to time limitations.

It also needs to be noted, that numerous facility's availability difficulties were faced during this project – the lab closure for nearly 6 months caused a delay in project progress.

1.4 Thesis Structure

This thesis is split into 6 chapters. Chapter 1 introduces the project background and project aims and objectives. In Chapter 2 crystallisation theory background is provided, including classical and two-step nucleation theories. Chapter 3 covers the theory and setup of the CoFlux reactor as well as the methods that were implemented. Chapter 4 provides a theoretical background to crystallisation techniques and describes the methods and compounds used in this study. Chapter 5 details the experimental and data analysis work carried out to determine the effect of the ammonium sulfate on the nucleation rate of metformin hydrochloride. Chapter 6 presents the overall conclusions drawn from this work, as well as suggestions for future work. The structure is shown below:

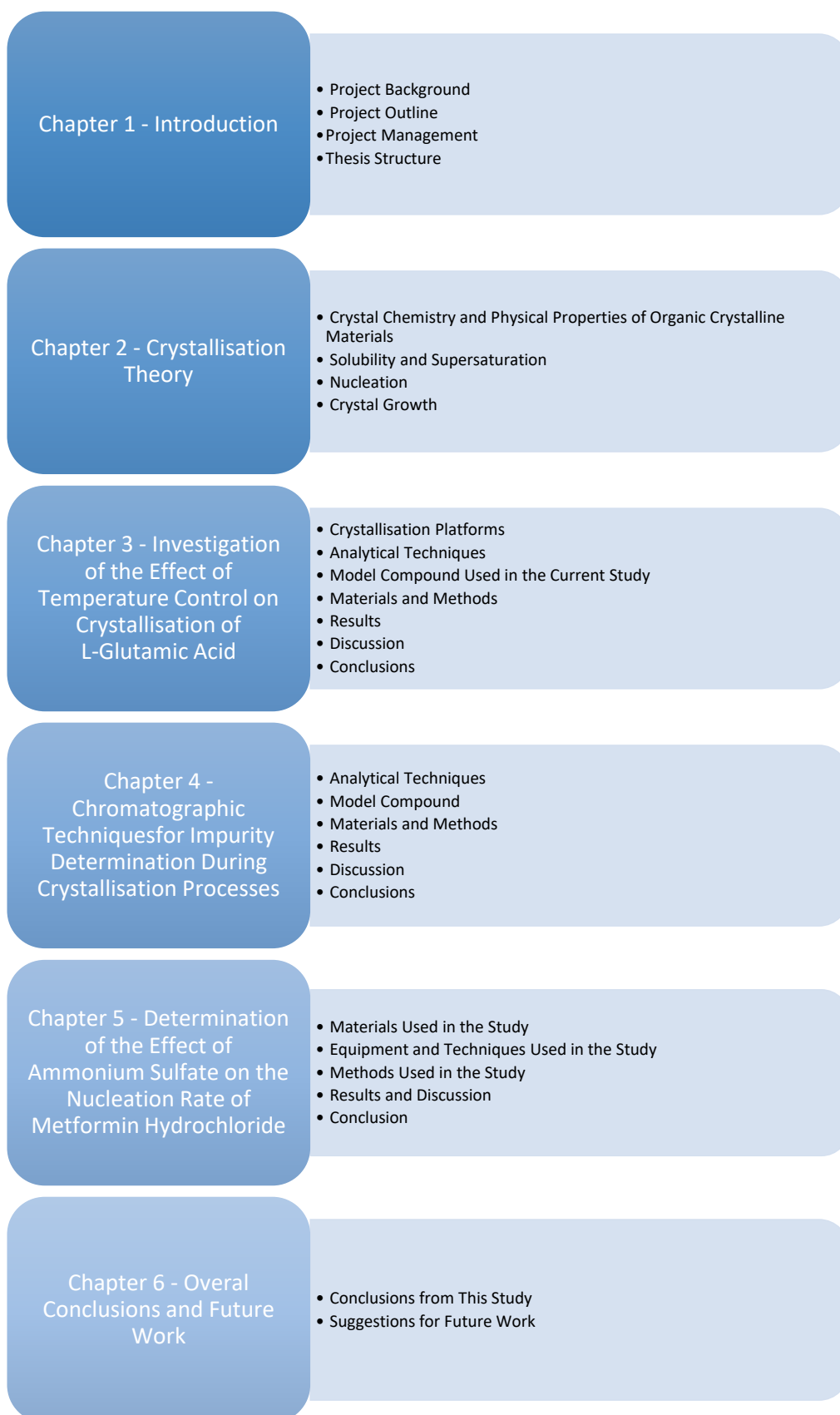


Figure 4. Thesis structure

2 Crystallisation Theory

2.1 Chapter Outline

This chapter aims to cover the background theory on crystallisation, with focus on nucleation as well as provide a literature review on different aspects of nucleation and crystallisation.

Chapter delivers a brief familiarisation with crystal chemistry and physical properties of organic crystalline materials and provides a detailed description of the crystallisation driving force – supersaturation. In the subsequent sections nucleation process is discussed in detail, providing information about classification of nucleation processes, energy barriers needed to be overcome during these processes as well as two approaches describing the nucleation step – classical nucleation theory and a non-classical, two-step mechanism. A theoretical background and a literature review on crystal nucleation and growth in presence of impurities is also included in this chapter.

2.2 Crystal Chemistry and Physical Properties of Organic Crystalline Materials

There are three general states of matter – gaseous, liquid and solid – and each of them represents different degrees of atomic or molecular mobility. In the gaseous state molecules are well separated, with no regular arrangement and they move freely at high speeds. This state is easily compressed and exhibits a low viscosity. In the liquid state the molecules are loosely packed and constantly moving, the viscosity of liquids is much higher than gases and therefore they can be less easily compressed. The state of the most restricted molecular motion is the solid state. For this state, molecular motion is narrowed to an oscillation about a fixed position. The structure of the solid state is well defined and the material is not compressible [4] [5] [6].

There are two types of solid – crystalline and amorphous, where the crystalline material consists of atoms, ions and molecules arranged in definite and repeating three-dimensional patterns (known as a lattice) and this is what differentiates it from the amorphous material [5]. The model crystal comprises a rigid lattice of ions, atoms or molecules, the location of which are characteristic of the substance. Due to its well defined internal structure crystals have a characteristic shape [4] [5]. The angles between two corresponding faces of a given substance remain constant independently of the relative size of the individual faces – these angles along with the crystal dimensions define the crystal structure.

Relatively often, crystals are to some degree symmetrical, and therefore this fact can be used as a means of crystal classification. There are three elements of symmetry that should be considered when defining crystal symmetry:

- a centre of symmetry,
- an axis of symmetry and
- a plane of symmetry [4] [5].

Those elements of symmetry can form 32 possible combinations – so called classes or point groups. These 32 classes are grouped into 7 systems characterised by the angles between their x , y and z axes and the length of axes (the directions of the axes are shown below in Figure 5).

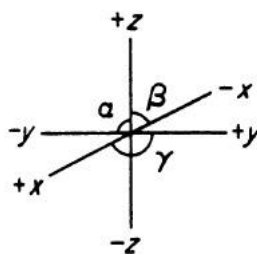


Figure 5. Crystallographic axes and angles describing the seven crystal systems [5]

As it can be seen from the figure above α is the angle between y and z axes, β is the angle between x and z axes and γ is the angle between x and y axes [5].

Miller indices (hkl) define directional and planar orientation within a crystal lattice. They can refer to a specific crystal face, a direction, a set of faces, or a set of directions.

Crystal habit (known also as morphology) is the shape a crystal adopts in relation to its internal structure. However, it needs to be noted that the presence of the solvent or impurities may have a significant effect on crystal's morphology [4] [5].

The ability of a compound to adopt different crystalline arrangements is described as polymorphism. The major polymorphic form produced during the crystallisation is dependent on the system parameters: solvent choice, temperature range, mixing speed, impurities present and supersaturation level. The supersaturation level is a parameter which plays the most important role, because the nucleation and growth kinetics are supersaturation dependent [8]. Different polymorphic forms show different physical properties such as shape, morphology, solubility, density or colour. Different properties can emerge from different polymorphs, so the proper polymorphic form plays a significant role in the pharmaceutical industry. The transformation of polymorphs is a big problem for the pharmaceutical industry, because different physical properties of different polymorphic forms effect the product properties such as the bioavailability, shelf life, compactness etc. of a drug compound. That is why the control of the formation of polymorphs during crystallisation is a crucial point of the process [9]. Production of the pure (also in case of polymorphic form presence) products is especially important in drug manufacture, where the patient may be potentially at risk [6].

2.3 Solubility and Supersaturation

Solubility is defined as the amount of a substance that will dissolve in a given amount of a particular solvent, under given conditions of temperature, pressure or pH. Solubility is a quantitative term and is usually defined as mass of solute per volume of solvent (for example grams per Litre (g/L)) or mass of solute per mass of solvent (for example grams per kilogram (g/kg)).

A solution is saturated when the chemical potentials of the solute in solution ($\mu_{solution}$) and the solid phase (μ_{solid}) are equal and therefore the potential change ($\Delta\mu$) is zero (Equation 1). It means that no more solute can be dissolved in the system [15].

Equation 1

$$\Delta\mu = \mu_{solution} - \mu_{solid} = 0$$

A solution is supersaturated when the difference in the chemical potentials is positive - the concentration of solute in solution exceeds its thermodynamic solubility limit. When the chemical potential difference is negative then the solution is undersaturated [16].

A typical solubility curve is shown in Figure 6. This curve can be divided into three separated regions:

- the undersaturated (stable) region, where crystals present in the solution will dissolve, due to lack of crystallisation driving force. Crystallisation from an undersaturated solution (point A in Figure 6) will happen if one of three main pathways are followed (shown in Figure 6 as a, b and c): temperature change (cooling crystallisation), solute concentration change (evaporation) or solvent composition change (antisolvent crystallisation).
- the metastable region is where nucleation will take place but only under kinetic control and where crystals will grow. The metastable zone shows the allowed level of supersaturation for the process and always occurs between the labile and undersaturated region [17] [18]. The width of the metastable zone is kinetically described and controlled [19]. Both the supersolubility line

position and the metastable zone width depend on the rate of generating supersaturation, the type and intensity of mixing, reactor type, sample preparation and the presence of impurities. The product properties such as crystal size, crystal size distribution and polymorphic form strongly depend on the metastable zone width (metastable zone width has a strong impact on nucleation) [20].

- the supersaturated region (labile) region, where crystals will nucleate spontaneously and nucleation is not controlled.

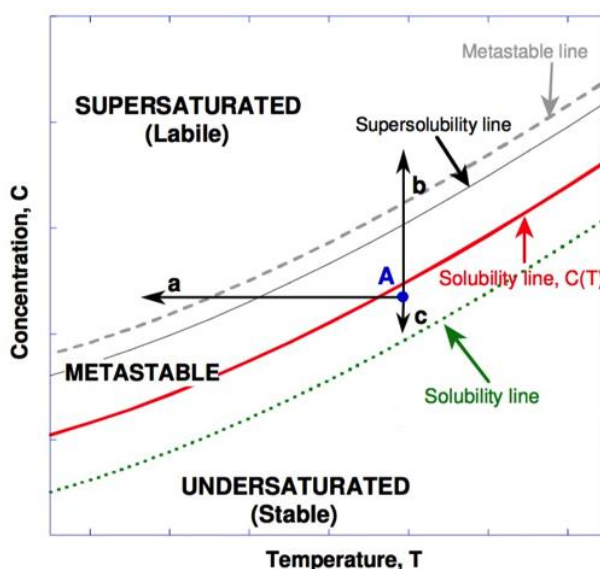


Figure 6. Arbitrary solubility diagram depicting regions of solution stability in relation to the solubility line (red line). Green dotted solubility line represents a solubility of a chosen compound in the antisolvent mixture. Supersolubility line and metastable line are also shown in the figure using consequently grey line and grey dash line. Crystallisation from an undersaturated solution (point A) will happen if one of three main pathways are followed: a. temperature change (cooling crystallisation), b. solute concentration change (evaporation) or c. solvent composition change (antisolvent crystallisation) [21].

Chemical potential, μ , can be expressed in terms of standard potential, μ_0 , and standard activity, a , as shown in Equation 2, where R is the universal gas constant and T is the absolute temperature.

Equation 2

$$\mu = \mu_0 + RT \ln a$$

If a is the standard activity of the solution phase and a^* is the standard activity of the crystalline phase, Equation 1 can be transformed:

Equation 3

$$\frac{\Delta\mu}{RT} = \ln\left(\frac{a}{a^*}\right) = \ln S$$

where $\Delta\mu$ is the difference in chemical potentials and S is fundamental supersaturation. This way of defining the supersaturation is not useful in real life, because chemical potentials and standard activities are often not known. Assuming that the solution is ideal (standard activities remain constant) it is possible to define the supersaturation in terms of concentration as shown in Equation 4.

Equation 4

$$\ln S = \ln \frac{c}{c^*} \quad \text{hence} \quad S = \frac{c}{c^*}$$

Where S is fundamental supersaturation, c is actual solute concentration and c^* is the equilibrium concentration. Supersaturation depends on temperature, therefore needs to be stated with respect to a chosen temperature [19].

2.4 Nucleation

2.4.1 Primary nucleation

2.4.1.1 *Homogeneous Nucleation*

Supersaturated solutions are not at equilibrium, so they attain greater stability through crystallisation. Nucleation is the first stage of crystallisation. When a new solid phase is created from a homogeneous solution, without foreign species or crystals present, the process is called homogeneous nucleation. There is a similarity between nucleation and chemical reaction in that they both have an activation energy barrier to overcome. The 'transition state' for nucleation is a cluster of few tens of units (atoms, ions, molecules) held together by weak intramolecular forces. The smallest amount of new solid phase that can exist in solution without complete dissolution is called a crystal nucleus [16]. There is a limited number of techniques that allow nucleation to be studied and consequently an accurate description of the process has not been developed [22].

Classical Nucleation Theory (CNT) is the simplest and most commonly used theory to describe the nucleation process. It uses the analogy of nucleation from supersaturated solution or melt to the condensation of vapour to liquid. This makes it possible to use the same principles in condensation theory, however it was necessary to make assumptions to simplify the CNT model. Unfortunately, those assumptions lead to restrictions in its application [22].

The first thermodynamic description of crystallisation was developed by Gibbs, in the 19th century [22]. He described a saturated solution as a state where clusters of solute molecules constantly aggregate and dissolve. In a supersaturated solution aggregation becomes more favourable and hence three-dimensional nucleation is possible. The creation of new surface has an energy penalty associated with it. Formation of a new three-dimensional structure is shown in Figure 7.

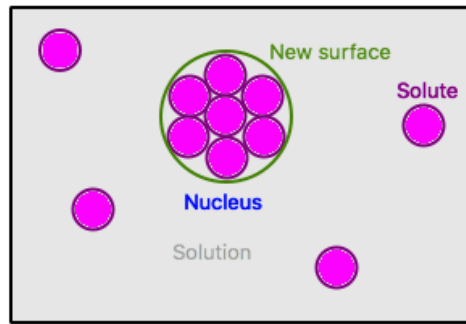


Figure 7. Formation of nucleus in solution, according to Classical Nucleation Theory

Not all new three-dimensional clusters will become stable and continue to grow into a crystal – this process is driven by the energy associated with its formation and growth. The free energy change (ΔG) required for cluster formation is the summation of the surface excess free energy G_s and the volume excess free energy G_v (see Equation 5).

Equation 5

$$\Delta G = G_s + G_v$$

The surface excess free energy and the volume excess free energy are defined as follows (Equation 6 and Equation 7):

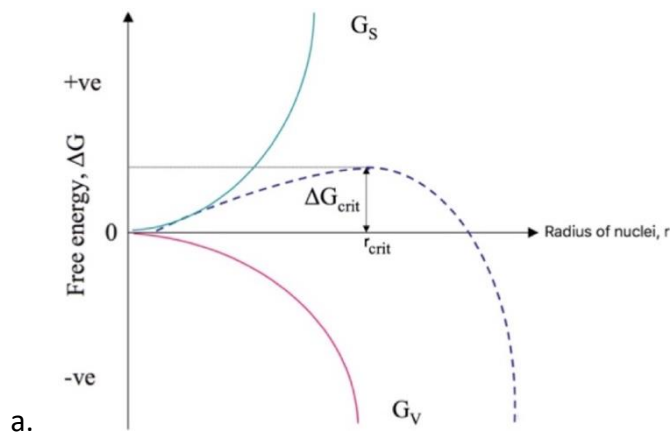
Equation 6

$$G_s = 4\pi r^2 \gamma$$

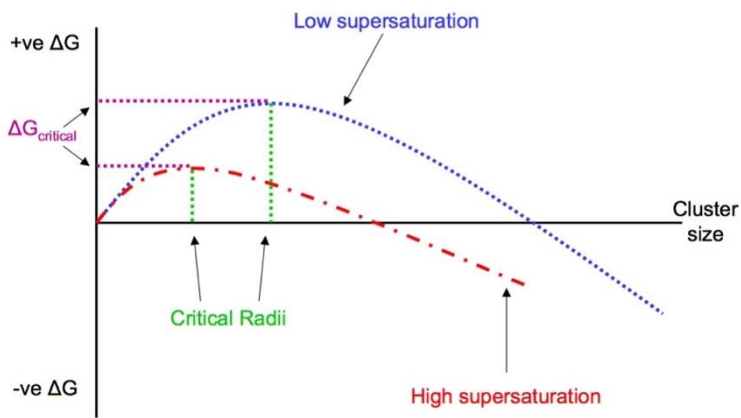
Equation 7

$$G_v = \frac{-4\pi r^3 \Delta\mu}{3v}$$

where r is the radius of the nuclei, $\Delta\mu$ is the difference in chemical potentials, v is the molecular volume and γ is the interfacial surface tension. Figure 8 shows the competing forces of the surface excess free energy and the volume excess free energy.



a.



b.

Figure 8. A free energy diagram for nucleation (a) showing the relationship between critical free energy (a summation of the surface free energy G_s and the volume excess free energy G_v) and associated radius of the nuclei and b) the diagram showing effect of supersaturation on the critical radius and critical free energy [22]

As can be seen from Figure 8a, increasing the radius of nuclei has the opposite effect on surface excess energy and volume excess energy – the first one increases with the increase of the radius of nuclei whilst the volume excess energy decreases. The total free energy curve is shown as the blue dashed line in Figure 8. The maximum of the free energy curve defines the critical point, at which the radius of the nucleus is large enough for nucleation to begin. Above the critical size of the nucleus, r_{crit} , growth becomes energetically favourable, therefore crystallisation can occur [22].

In order to calculate the critical free energy for a three-dimensional nucleus, the first derivative of the free energy function needs to be set equal to zero – the critical point

is the maximum of the function, so its first derivative at this point will equal zero – see Equation 8. Those mathematical operations will yield an equation for the critical radius, r_{crit} - Equation 9 – which when inserted into Equation 8 will result in an expression describing the critical free energy given in Equation 10.

Equation 8

$$\Delta G = \frac{-4\pi r^3 \Delta\mu}{3v} + 4\pi r^2 \gamma$$

$$\frac{d\Delta G}{dr} = \frac{-4\pi r^2 \Delta\mu}{v} + 8\pi r \gamma = 0$$

Equation 9

$$r_{crit} = \frac{2v\gamma}{\Delta\mu}$$

Equation 10

$$\Delta G_{crit} = \frac{16\pi\gamma^3 v^2}{3\Delta\mu^2}$$

Equation 10 can be expressed in terms of supersaturation by using Equation 3 to replace $\Delta\mu$ with supersaturation. The critical free energy of the critical nucleus as a function of supersaturation is shown below - Equation 11.

Equation 11

$$\Delta G_{crit} = \frac{16\pi\gamma^3 v^2}{3(kT \ln S)^2}$$

As mentioned before S is the fundamental supersaturation, T is temperature and k is the Boltzmann constant (1.38×10^{-23} J/K). The universal gas constant (R) has been replaced by Boltzmann constant, because the object of study changed from molecules to particles [22].

Equation 11 shows that supersaturation plays a significant role in defining the critical free energy of the nuclei. The higher the supersaturation, the lower the energy barrier becomes and the critical radius decreases. The effect of supersaturation on the critical radius is depicted in Figure 8b. At high enough supersaturation nucleation will become a spontaneous process [16].

Classical nucleation theory determines the nucleation rate in the form of the Arrhenius reaction rate equation shown in Equation 12:

Equation 12

$$J = Ke^{\left(\frac{-\Delta G_{crit}}{kT}\right)}$$

where J is the nucleation rate equal to the number of nuclei formed per unit time per unit volume, K is the nucleation rate constant - and ΔG_{crit} is the critical free energy. For homogenous nucleation the nucleation rate originates from the frequency of molecular collisions, however in reality its value is very difficult to determine – molecular mobility changes significantly with temperature and the nucleation rate is strongly temperature dependent [22] [23] [24].

2.4.1.2 *Heterogeneous Nucleation*

Homogenous nucleation in reality is almost impossible to achieve – a system theoretically treated as homogenous under closer examination is found to be heterogeneous – nucleation has been induced by foreign particles present in the solution, e.g. dust. Filtration can reduce the number of unwanted species in the solution, however it is very difficult to eliminate all of them. Equipment surfaces are impossible to eliminate and their surface behaviour is difficult to predict and control. Heterogeneous nucleation can be defined as a surface catalysed or assisted process, however it is classified as primary nucleation since it is not induced deliberately by crystals i.e. seeding. Figure 9 shows the classification of nucleation processes.

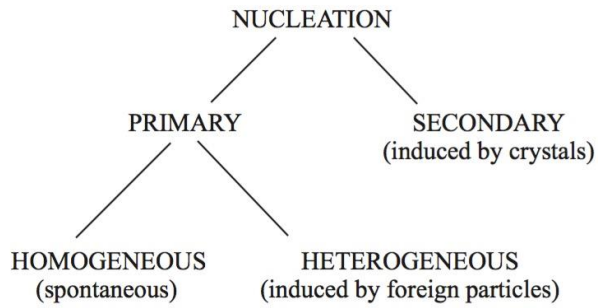


Figure 9. Classification of nucleation processes [19]

The presence of foreign particles will allow the crystallising compound to absorb and therefore lower the value of critical free energy as can be seen from Figure 10.

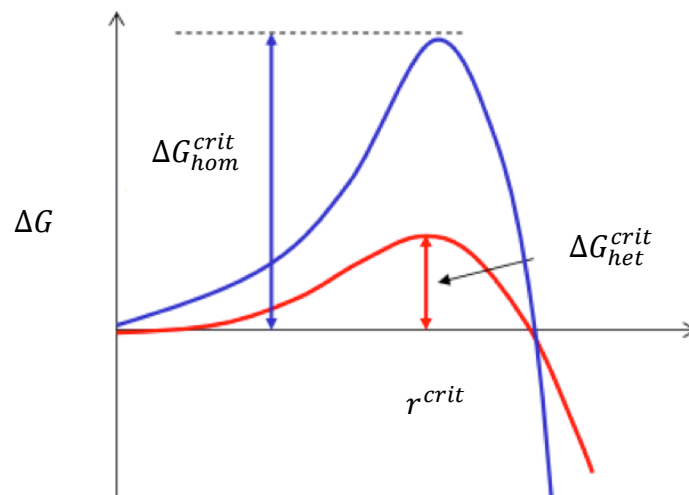


Figure 10. Free energy pathways for homogeneous and heterogeneous nucleation [25]

2.4.2 Secondary Nucleation

Secondary nucleation is the dominant nucleation mechanism in industrial crystallisers. A supersaturated solution will tend to nucleate more likely in the presence of the solute's crystal [4] [5] [6] [26]. The literature provides an evidence of a few secondary nucleation modes, such as:

- initial breeding,
- needle breeding,
- polycrystalline breeding,

- shear nucleation and
- contact nucleation [5].

In general, it can be said that the nuclei are formed from the solution layer adjacent to the surface or originate from crystal [26].

An adsorbed solute layer (not yet in crystalline form) located close to the crystal surface can be displaced and therefore provide a source of the secondary nuclei. A potential mechanism for this process is provided by the embryo coagulation secondary nucleation (ECSN) theory. According to it, the seed crystals interact with the solute clusters (embryos) present in the boundary layer through the van der Waals forces. If the concentration of the solute clusters is high, the rapid coagulation is observed and therefore the nuclei reaches the size greater than the critical size, consequently leading to nucleation [26].

Contact nucleation is another mode of secondary nucleation, where the nuclei originates from the solution. The secondary nuclei are then a result of a crystal-crystal collision or crystal-agitator collision. It has been reported that crystal-agitator collision is possible only for crystals able to penetrate the fluid boundary layer around the blade – the speed of the agitator and the relative hardness of the contacting bodies are the parameters that will affect the effectiveness of the secondary nucleation. The ‘survival theory’ based on the Gibbs-Thomson effect should also be mentioned here – microcrystals in supersaturated solutions will tend to dissolve unlike microcrystals. According to this theory, any crystalline fragments smaller than 1 μm will not survive in the agitated crystalliser [5] [26].

There are three mechanisms of generating secondary nuclei from the crystal: initial breeding, needle breeding and attrition. Generating secondary nuclei from the crystal is called seeding and it is a process widely used in industrial crystallisation, as an approach allowing control over crystal size and distribution. Initial breeding should be used when fines on the seed crystal’s surface get displaced and become nuclei. However, this mode of seeding is not very efficient – the number of fines is finite, so seeds will not work as a continuous source of secondary nuclei. Needles, at high

supersaturation, grow over the crystal surface and afterwards detach from the main crystal (due to mechanical forces) and grow as independent crystals. Because, the high supersaturation is required, this kind of breeding is not widely used in industrial crystallisers. The last mode of originating secondary nuclei is attrition. Attrition is a process, where the collision of crystals with each other or other objects causes the removal of fragments of the parent crystal (seed). Those fragments can consequently act as nuclei and relatively often this route is chosen for secondary nucleation in industrial crystallisers [5] [26].

2.4.3 Classical Nucleation Theory

Classical Nucleation Theory (CNT) is the simplest and most commonly used theory to describe the nucleation process. The theory states that nucleation is analogous to the condensation of vapour in to liquid. This makes it possible to use the same principles as in condensation theory, however it was necessary to make major assumptions to simplify the CNT model. Unfortunately, those assumptions lead to restrictions in its application [22]. Five main assumptions connected with classical nucleation theory are listed:

- Spherical droplet model of clusters is applied – droplet density is constant and does not depend on their size. Density of those included in clusters is the same as the density of the bulk supersaturated solution. This assumption implies that units (molecules, atoms) are adding one by one in order.
- Surface tension of the nuclei is size and temperature independent.
- Clusters of molecules do not interact with other nuclei and it is assumed that crystals are at rest and do not undergo any type of motion.
- System is assumed to be at steady state – nucleation rate does not depend on time.
- The clusters are incompressible and surrounded by an ideal gas of constant pressure [22].

2.4.3.1 Classical Nucleation Theory for Determining Nucleation Rates

2.4.3.1.1 Nývlt's mass based approach and Kubota's approach

A study published by Mitchell and Frawley [27] looked at nucleation kinetics during batch cooling crystallisation of paracetamol-ethanol solutions. The aim of this research was to estimate the nucleation kinetics based on the metastable zone width (MSZW). Authors employed two theoretical approaches – Nývlt's mass based approach and Kubota's approach, which includes number density.

Nývlt's model assumes that the nucleation rate at the beginning of nucleation corresponds to the supersaturation rate only for a limited period of time, hence the primary nucleation rate - J_n , can be expressed as a function of supersaturation S (Equation 13):

Equation 13

$$J_n = k'_n(S)^n$$

k'_n is the nucleation rate constant, S is the supersaturation and n is the nucleation order. If cooling crystallisation is chosen as the crystallisation method, then supersaturation can be described as a function of the cooling rate R (Equation 14). In the equation below dS^*/dT is the slope of the solubility curve for a given temperature.

Equation 14

$$\frac{dS}{dt} = R \frac{dS^*}{dT}$$

The maximum supercooling, ΔT_{max} , and the maximum supersaturation, S_{max} , at the beginning of the nucleation are given as follows:

Equation 15

$$\Delta T_{max} = T^* - T_{nuc}$$

Equation 16

$$S = \Delta T_{max} \frac{dS^*}{dT}$$

As mentioned before the nucleation rate relates to the supersaturation rate at the beginning of nucleation only, so the mass of formed nuclei can be linked with the number of nuclei formed as it has been shown in Equation 17 below:

Equation 17

$$\frac{dM}{dt} = k'_n \alpha \rho_c r^3 S^m = k_n S^m$$

where M is the mass of formed nuclei, k_n is the mass nucleation rate constant, α is the volume shape factor and ρ_c is the density of the solute crystals. Combining Equation 14, Equation 16 and Equation 17 results in Equation 18, which includes ε - a conversion factor for the concentration change caused by the formation of hydrates/solvates (the original application of Nývlt's theory):

Equation 18

$$k_n S^m = k_n \left[\frac{dc^*}{dT} \Delta T_{max} \right]^m = R \left(\frac{dS^*}{dT} \right) \varepsilon$$

Conversion factor, ε , can be defined as:

Equation 19

$$\varepsilon = \frac{R_h}{[1 - c(R_h - 1)]^2}$$

In the equation above R_h is the ratio of the molecular masses of the hydrate to that of the anhydrate, while c is the solution concentration represented by the mass of anhydrate per unit mass of solvent. The authors were using paracetamol as their

model compound, which does not form hydrates or solvates, so R_h equals 1 and hence ε equals 1 too. By rearranging Equation 18 and taking the logarithm of both sides, Equation 20 is obtained and can be fitted to a logarithmic plot of the cooling rate, $\ln R$, versus the metastable zone width, $\ln(\Delta T_{max})$ for a given temperature.

Equation 20

$$\log R = m \log(\Delta T_{max}) + \log k_n + (m - 1) \log \left(\frac{dS^*}{dT} \right)$$

The result of this plot should be a straight line, where the slope corresponds to the apparent nucleation order, m , and the intercept corresponds to the mass nucleation rate constant – k_n .

Kubota's model assumes that the metastable zone width correlates to the point at which a fixed, but unknown value of the number density of grown nuclei is achieved. If the solubility of the studied compound is linear ($dS^*/dT = \text{constant}$), the supersaturation (S) in Equation 13 can be replaced by the supercooling (ΔT), defined by Equation 16 and therefore the primary nucleation rate can be evaluated as follows:

Equation 21

$$J_n = k_n (\Delta T)^n$$

where $k_n = k'_n (dc^*/dT)^n$. Integration of the nucleation rate ($J_n = d(N/V)/dt$) yields Equation 22 - based on which the number density N_m/V of grown primary nuclei over time, t_m can be calculated.

Equation 22

$$\frac{N_m}{V} = \int_0^{N_m} d \left(\frac{N}{V} \right) = \int_0^{t_m} J_n dt$$

When the cooling rate, R , is constant ($R=d(\Delta T)/dt$), Equation 22 gives:

Equation 23

$$\frac{N_m}{V} = \int_0^{\Delta T_m} \frac{J_n}{R} d(\Delta T_m)$$

In the Equation 23 ΔT_m is the metastable zone width. At this supercooling the density of primary grown nuclei reaches a fixed, but unknown value – N_m/V . At a constant mass nucleation rate constant, inserting Equation 20 and integrating Equation 23, the equation defining the MSZW can be written as follows:

Equation 24

$$\Delta T_m = \left[\left(\frac{N_m}{k_n V} \right) (n + 1) \right]^{1/(n+1)} R^{1/(n+1)}$$

Taking the logarithm of both sides of Equation 24, results in a new equation, which can be fitted with a straight line where $(\ln(\Delta T_m))$ is plotted against the cooling rate, $\ln R$, for a given concentration. The slope of this line corresponds to the nucleation order, and the intercept of the trendline corresponds to the expression $(N_m/k_n V)$.

Kubota's model redefined the induction time, t_{ind} , as the time required for the number density of primary grown crystals (N_m/V) to achieve a fixed value. If primary nucleation is described as shown in Equation 20, the number density of primary grown crystals can be evaluated as follows:

Equation 25

$$\frac{N_m}{V} = \int_0^{t_{ind}} J_n dt = \int_0^{t_{ind}} k_n (\Delta T)^n dt$$

The authors used an isothermal way of conducting experiments, hence the supercooling is constant and Equation 25 yields Equation 26:

Equation 26

$$\frac{N_m}{V} = k_n (\Delta T)^n t_{ind}$$

which when rearranged again yields an expression describing the induction time as a function of the degree of supercooling - ΔT – Equation 27.

Equation 27

$$t_{ind} = \left(\frac{N_m}{k_n V} \right) (\Delta T)^{-n}$$

Both the expression ($N_m/k_n V$) and the exponent n , are the same as those in Equation 24 and Equation 25, which proves that model the proposed by Kubota shows the connection between the metastable zone width and the nucleation induction time.

2.4.3.1.2 Crystal Nucleation Rates from Probability Distributions of Induction Times

The Poisson distribution describes the probability of the formation of nuclei in a time interval (P_m). In the equation below (Equation 28) N is the average number of nuclei that form in the time interval (t_i) and volume (V) [28].

Equation 28

$$P_m = \frac{N^m}{m!} \exp(-N)$$

Based on Equation 28 it is possible to produce an equation that described the probability that no nuclei will be formed (Equation 29).

Equation 29

$$P_0 = \exp(-N)$$

The probability that at least one nucleus will be formed can be described as follows (Equation 30):

Equation 30

$$P_{\geq 1} = 1 - P_0 = 1 - \exp(-N)$$

The number of nuclei is related to the stationary nucleation rate (J) in the following way (Equation 31):

Equation 31

$$N = JVt_j$$

Combining all the equations above provides enough information to form the equation that describes the probability $P^*(t_j)$ that at least one nucleus will be formed in time interval t_j (Equation 32).

Equation 32

$$P^*(t_j) = 1 - \exp(-JVt_j)$$

The induction time probability $P(t)$ to detect crystals at time t (time of detection $t_j = t - t_g$, where t_g is growth time and $t \geq t_g$) is given below (Equation 33). This equation is used to fit to the experimental probability distribution.

Equation 33

$$P(t) = 1 - \exp(-JV(t - t_g))$$

The experimental probability distribution at constant conditions – supersaturation, volume and temperature - is determined using the equation (Equation 34):

Equation 34

$$P(t) = \frac{M^+(t)}{M}$$

Where M is the total number of experiments and $M^+(t)$ is the number of experiments where crystals have been detected. Combination of Equation 33 and Equation 34 allows the nucleation rate (J) and growth time (t_g) to be determined [28]. Figure 11 shows an example of experimental data (left graph) and its fit to the model (right graph).

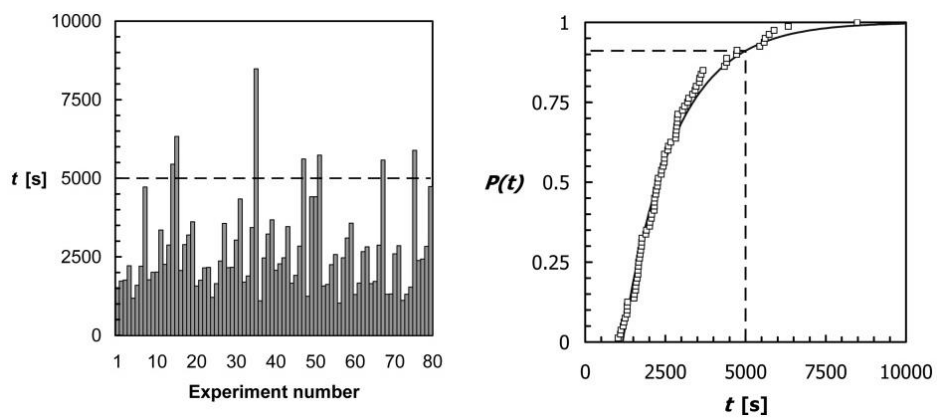


Figure 11. An example of 80 experimental data points of induction time (left) and probability distribution of those induction times [28]

For the simplicity, the model described in this section is referred to as ter Horst model throughout this thesis.

2.4.4 Two-Step Nucleation Theory

Classical nucleation theory (CNT), developed in the 19th century, is the mathematical model frequently used to describe the crystal nucleation process. Comparison of the predicted and measured nucleation rates, based on CNT, shows differences reaching several orders of magnitude. The main disagreement between theory and practise lies in the assumption that the nucleation rate is independent of temperature. A good example to illustrate this, is the nucleation of water – theory correctly predicts the dependence of the nucleation rate on supersaturation, however only at a temperature of 259K does the experimental data agree with the predicted value. The same disagreement has been observed with pentan-1-ol, where the nucleation rate based on experimental data is four times higher than the nucleation rate predicted by the CNT model [22] [29].

Another assumption of classical nucleation theory is that the system is at steady state or in other words the size distribution does not change over time. Drenth and Haas [30] carried out lysozyme crystallisation in order to investigate the nucleation induction time by recording the NMR spectra of the crystallising solution as a function of time. They observed that there was a significant delay in induction time before the first nuclei appear and that the induction time strongly depended on the supersaturation of the solution. The fact that there was a delay in the induction time for the first nuclei to appear proved that the system was not at steady state and therefore refutes the classical nucleation assumption.

Disagreements between the predicted and measured values for a simple single-component system showed that the reliability of this theory for more complex systems is very questionable, due to the fact that this theory is oversimplified for this type of system [31].

Non-classical, two-step nucleation theory is another way to describe crystal nucleation in solution. Figure 12 shows the basic summary of the two-step nucleation model; the classical model is included in this figure for comparison. This theory assumes density fluctuations, which cause the formation of a new liquid-like phase - Figure 12(c).

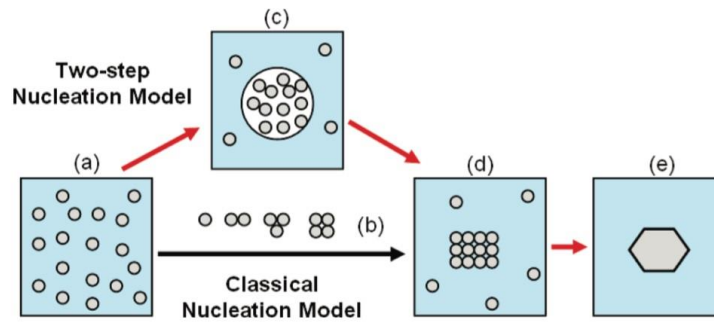


Figure 12. Classical Nucleation Model and Two-Step Nucleation Model crystallisation pathways. (a) solute molecules in supersaturated solution, (b) according to CNT critical nucleus is formed by adding one by one of solute molecules, (c) loose liquid-like cluster of solute molecules, (d) ordered crystalline nuclei and (e) final crystal [30].

Formation of this new phase – the first step of a nucleation process – decreases the free energy of the system – changes in free energy are depicted in Figure 13.

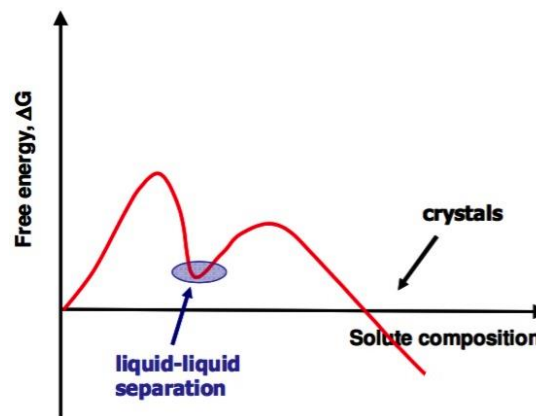


Figure 13. Changes in free energy according to the two-step nucleation theory [21]

During the second step of crystallisation, crystals are formed through a series of complicated process, such as liquid droplet coalescence, aggregation, surface to volume nucleation and eventually crystal growth - Figure 12(d) and (e) [30].

As can be seen from Figure 12 the main difference between CNT and two-step theory is the formation of the intermediate product – liquid-like droplets, so-called nanodroplet species. Their real nature, shape and the way they are formed is not known at present, however, it is believed that if solute molecules present in

supersaturated solution come within close proximity, they will create nanodroplets of higher concentration than the bulk solution. When the cluster reaches a large enough size the crystal nuclei form [22]. Fully understanding the creation of these nanodroplets would improve the understanding of the nucleation process and as a consequence develop better control over crystallisation.

2.4.4.1 Two-Step Nucleation Theory Literature Review

Due to the lack of tools for analysing the detailed behaviour of solutions at the molecular level computer simulations are implemented. The first computer simulation was published by ten Wolde and Frenkel [32]. Authors used the Monte Carlo method in order to develop a simulation which allows the calculation of the free energy barrier against formation of a critical nucleus as a function of critical nucleus size. The results showed that the critical point was achieved via the formation of a liquid-like droplet. Formation of the droplet caused density fluctuations and therefore affected the crystallisation pathway. When the system crystallised involving these droplets, the free energy barrier was lowered and consequently the nucleation rate was increased by a factor of 10^{13} [32] [25].

In 2006 Marian Sedlak published a series of three papers where the phenomenon of forming large-scale supramolecular structures in solutions containing low molecular mass compounds was studied. In his first paper [33] the main focus was on applying static and dynamic light scattering to investigate the presence of prenucleation clusters in liquid mixtures, low mass electrolytes and nonelectrolytes. An uneven distribution of solute in the solution was observed with regions of low and high concentration being detected. Where the higher solute concentration was used, the density of those regions was higher than the density of the rest of the solution and based on detailed light scattering analysis the formed species were called 'close-to-spherical discrete domains'. The size distribution of the nanospecies was described as broad, with an average size of around a few hundred nanometres. It was found that the domains had higher solute concentration than the bulk solution and their size increased with decreased sample dilution.

The second paper published by Sedlak [34] focused on the kinetics of the cluster formation and their long-term stability. It was possible to carry out real-time monitoring of liquid mixtures; if the monitored samples were solutions of solid samples the real-time monitoring was possible only if the structure formation was notably slower than the dissolution process. It was found that the time scale required for the cluster to form varied from minutes to a few weeks. Due to the growth of the clusters, the scattering intensity was increasing over time. For all the solutions studied it was found that the growth of the clusters was generally accompanied by an increase in diameter and broadening of the size distribution. The long-term stability test revealed that the formed nanostructures remained stable for up to 15 months.

In his final paper [35] Sedlak investigated the solute – solvent interactions and their potential responsibility for solute association. The main assumption made in the paper was that submicron-sized domains form in the solution as an effect of hydrogen bonds occurring between solute and solvent molecules. It was observed that clustering was more likely to occur if the solvent had a tendency to create networks. Comparison of methanol and water showed that clusters occurred only in water but not in methanol. It is well known that hydrogen bonding forms in liquid water as the hydrogen atoms of one water molecule are attracted towards the oxygen atom of a neighbouring water molecule, therefore an extensive solvent networks are formed. It was observed that molecules having a dipole were more likely to cluster, which was confirmed while analysing several polar and non-polar molecules – only polar compounds demonstrated the clustering phenomenon. Further investigation revealed that the polarity of the molecule was a necessary condition, but not enough for the molecule to cluster – some of the highly polarised substances used did not cluster. Sedlak's work was focused on explaining the clustering phenomenon based on the fundamental interactions between molecules. In a paper published by Jawor – Baczynska et al. [36] the authors present a study where an investigation into the potential formation of nanodroplet intermediate species during the dissolution stage was carried out. According to the two-step

nucleation theory disordered molecular clusters present in the solution act as nucleation precursors. Their presence in the solution after dissolving crystals would prove the reversibility of the nanodroplet formation process.

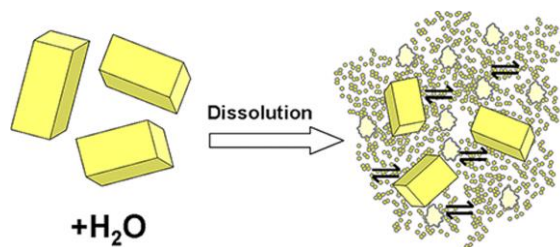


Figure 14. A scheme showing the formation of prenucleation clusters at the dissolution stage [36].

Glycine in water was chosen as the model system in this study and the following techniques were used to analyse the resultant solution: small-angle X-ray scattering, dynamic light scattering and nanoparticle tracking analysis. The presence of nanodroplets was observed at the dissolution stage, with a mean diameter of roughly 250 nm when the glycine concentration was close to saturated. The glycine-rich nanoparticles persisted in the solution containing excess glycine crystals with an equilibrium number concentration of 10^9 per ml. When nanofiltered (low population of nanodroplets) and unfiltered (high population of nanodroplets) quiescent supersaturated ($SS=1.1$) solutions were left without agitation, it took approximately 30 hours for only a single glycine crystal to form in both cases. The crystallisation time was significantly reduced when a small stirrer bar was used in order to gently mix the solution inside the vial – thousands of microcrystals were formed after an incubation time of 3 to 5 hours (Figure 15).

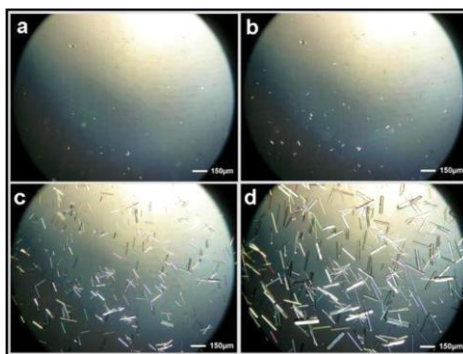


Figure 15. Photograph of glycine crystals grown from a 270 mg/ml solution in a continuously inverted vial containing a stirrer bar (incubation time 3 hours). Images were taken at time (a) 0 min, (b) 1 min, (c) 5 min and (d) 10 min after the initial crystal detection [36]

Explanations for this behaviour such as it being due to secondary nucleation, glass splinters, scratches on the vial or bubble formation were eliminated via control experiments. The authors analysed the glycine solution just prior to the appearance of the microcrystals and detected a subpopulation of large nanodroplets with diameters greater than 750 nm, which were not observed in the quiescent solution. It was believed that these large nanodroplets, formed prior to nucleation create a new crystallisation pathway, which can successfully lead to nucleation but only if a critical mass of glycine within the nanodroplets was achieved.

In the next paper [37] Jawor-Baczynska et al. studied two amino acids – glycine and DL-alanine – in supersaturated and undersaturated aqueous solutions using, Brownian Microscopy/Nanoparticle Tracking Analysis, Dynamic Light Scattering (DLS) and Cryogenic Transmission Electron Microscopy (Cryo-TEM). It is generally assumed that solutions of highly soluble compounds, such as small amino acids, are homogenous systems with only a small degree of internal structure, such as molecular clusters or hydration shells. According to previous studies, nanodroplets were detected in supersaturated solutions of these two amino acids. The work carried out by Jawor-Baczynska et al. revealed the presence of the mesospecies in solution, where the solute concentration was well below the saturated concentration. Detected nanodroplets were found to have a diameter in the range of 100 to 300 nm and the size distribution broadened towards larger diameters with

increasing concentration. It has been observed that mesospecies do not form a separated phase and authors described them as ‘thermodynamically stable mesostructured liquids containing solute-rich domains dispersed within the bulk solute solution’. High-resolution Cryo-TEM analysis revealed the presence of colloidal scale objects, which were not observed in blank water samples. For both systems, glycine and DL-alanine solutions, the detected species were 300 to 400 nm in diameter. These results agree with the data obtained using DLS and NTA, so they are likely to be the same species as those detected using the light scattering techniques. Electron diffraction patterns obtained for undersaturated amino acid solutions showed that the species were amorphous structures, which was confirmed by Cryo-TEM visualisation (Figure 16).

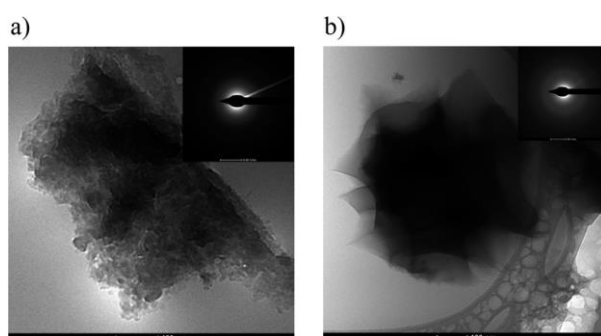


Figure 16. Cryo-TEM images of nanodroplets observed in undersaturated and unfiltered solutions of (a) DL-alanine (150 mg/ml) and (b) glycine (200 mg/ml) [38]

Filtration of amino acid solutions using PTFE 100 nm syringe filters revealed differences in the mesospecies properties – glycine nanodroplets easily passed through the filter and therefore it can be said they have more liquid-like properties and a less dense structure than DL-alanine – this amino acid tended to bind with the filter, in other words they had more solid-like properties. Filtration successfully removed the nanodroplets, however, it was noted that agitation caused a reappearance of the mesospecies in the solution.

In the final paper published by Jawor-Baczynska et al. [38] authors present work where the formation of mesostructured solutions in DL-valine-water-2-propanol

mixtures was analysed as well as the crystallisation of DL-valine from those solutions. Dynamic Light Scattering and Brownian microscopy were used in order to analyse saturated and undersaturated solutions of DL-valine; similar nanodroplets to those observed in aqueous glycine and DL-alanine solutions [37] were detected in the optically clear solution. Prenucleation clusters of DL-valine with a mean hydrodynamic diameter of approximately 200 nm and a narrow size distribution were formed during the slow cooling process. When solutions of the same composition were prepared via rapid isothermal mixing of aqueous DL-valine solution with 2-propanol, it was found that the formed mesospecies were significantly larger in diameter than those detected in the slow cooled solutions. The presence of larger nanospecies decreased the nucleation time in comparison to solutions containing smaller clusters. Nucleation times as well as the cluster sizes were strongly dependent on the mixing conditions. Based on further investigation of those clusters, the authors proposed that mesoscale clusters above a critical size could be the location of productive nucleation events. Two types of clusters were detected in DL-valine solutions using dynamic light scattering technique (DLS) – molecular clusters (diameters of 1-2 nm) and solute-rich prenucleation clusters (diameters of hundreds of nanometers). Rapid cooling caused two orders of magnitude decrease in induction time. Shorter induction time and larger prenucleation clusters in rapidly cooled solution can be coupled together to play a key role in the nucleation process.

2.4.5 Classical Nucleation Theory and Two Step Nucleation Theory Summary

The main shortcomings coming from the Classical Nucleation Theory were presented in section 2.4.4. This theory of nucleation can be also described as a direct pathway of nucleation, where the molecules immediately group together in the right order to form a crystal [39]. CNT provides a platform to start with, however this model fails to provide understanding of nucleation rates (the prediction is orders of magnitude higher than the experimental value) or the role of stable and unstable potential phases present in the solution [40].

The two-step nucleation theory assumes the formation of the intermediate nanospecies during the nucleation process. Once the clusters of a sufficient size are formed, in the second step the reorganisation of the clusters into ordered structure is taking place. The second stage is defined as rate-determining step – it has been observed that the nucleation takes longer for more complex molecules than for the simple ones, as it becomes more difficult to arrange into an ordered structure forming a crystal lattice (due to its conformational flexibility) [25].

Initially two step nucleation theory was studied only for proteins, however more and more extensive studies proved that this theory may be true for other materials – organic, inorganic and colloids [25] [39] [40].

However, it has to be noted that nucleation is still not fully understood and further work is needed in order to confirm the truth value of the theories described above.

2.5 Crystal Growth

Crystal growth is the second stage in the crystallisation process, which determines the final crystal size. Growth can be achieved when the flux of growth units surpasses the equilibrium stage, so the number of growth units attaching to the surface is greater than the number of units leaving. How quickly the surface will grow (growth rate) depends on many factors and will highly depend on the strength and number of interactions between the surface and the growth unit [16].

The exact mechanism of crystal growth is not known and there are numerous theories trying to explain this process. In general, crystal growth can be described by the following steps:

- 1) diffusion of the solute molecules to the liquid phase in order to approach the crystal face – mass transport of solute,
- 2) reorganisation of the growth units,
- 3) adsorption of the growth units – molecules when adsorbed onto the crystal face makes the molecule part of its solvation shape and therefore is added into the lattice where it loses the rest of its shape - layer-by-layer growth of the crystal [6].

The interactions at the surface depend on the underlying packing of the molecules in the crystal lattice and it is observed that the crystal will grow in a fashion that maximises the intramolecular interactions.

There are three types of crystal face: flat (F), kinked (K) and stepped (S). All three types are depicted in Figure 17.

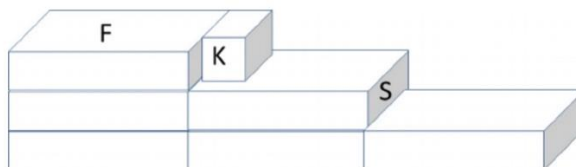


Figure 17. Three types of crystal face: flat (F), kinked (K) and stepped (S) [41]

The crystal will be bounded only to the flat faces (F) when the additional growth units are adsorbed, however those faces are marked by low binding properties – the molecular interactions will not be very strong (only one interaction site) and the growth units will tend to desorb. The other two crystal faces – kinked (K) and stepped (S) have respectively three and two interaction sites, hence they are more favourable for the growth unit to be attached to.

The more sites for interactions, the faster the surface will grow, which means that different crystal faces will have different growth rates. The surface growing the slowest determines the crystal habit, so the studies on the prediction of the crystal shape focus on the mechanism of flat surface growth [4].

2.5.1 Crystal Nucleation and Growth in Presence of Impurities - Theory

The first classical model that explains the impact of impurities on crystal growth was proposed by Cabrera and Vermilyea [42] in 1958. Their model suggested that impurities are adsorbed onto steps or terraces of growing crystals and act as local pinning points - impurities immobilized on the terraces cannot be passed by a straight growing step. Subsequently growing steps need to be squeezed through the impurities pinning points, which results in decreasing the step growing velocity in comparison to straight steps growing.

Kubota and Mullin [43] in 1995 published a paper describing a kinetic model for crystal growth from aqueous solution in the presence of impurities. They based their model on the following expression suggested by Davey and Mullin:

Equation 35

$$\frac{V}{V_0} = 1 - \theta_{eq}$$

In the equation above V is the step velocity, V_0 is the step velocity in a pure system and θ_{eq} is the fractional coverage by adsorbed impurities on the surface. Equation 35 shows that in the presence of impurities the diffusion rate of growth units to the steps is being reduced. The relative velocity (V/V_0) is zero when the fractional coverage is 1. However, full coverage does not have to be caused by the presence of the impurities of interest - presence of macro-molecules, organic compounds, metallic ions etc. can increase the coverage of sites available for absorption and decrease the value of the relative velocity. How well the impurity will suppress the crystal growth depends on the impurity properties such as size, shape or orientation of the impurity molecules (a stereochemical effect). To fully describe the effect that an impurity has on crystal growth it is necessary to consider two parameters – an absorption factor (θ_{eq}) and an effectiveness factor (α) – see Equation 36.

Equation 36

$$\frac{V}{V_0} = 1 - \alpha\theta_{eq}$$

The relation between the relative step velocity and the concentration of the impurity in the solution (x) can be expressed using the Langmuir isotherm (Equation 37). In the equation below K is the Langmuir constant.

Equation 37

$$\theta_{eq} = Kx/(1 + Kx)$$

Combination of Equation 36 and Equation 37 gives the equation that describes the relative step velocity as a function of the impurity concentration (Equation 38).

Equation 38

$$V/V_0 = 1 - [\alpha Kx/(1 + Kx)]$$

Assuming that the relative step velocity is proportional to the relative face growth rate G/G_0 the equation above can be written as follows:

Equation 39

$$G/G_0 = 1 - [(\alpha Kx/1 + Kx)]$$

Equation 38 provides a theoretical relationship between the relative step velocity and the dimensionless impurity concentration for different values of α (Figure 18).

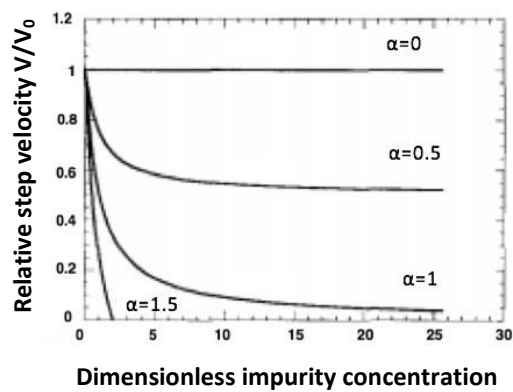


Figure 18. Relationship between the relative step velocity and the dimensionless impurity concentration for different values of an effectiveness factor (α) - based on theory [43]

In 1997 Kubota, Yokota and Mullin [44] described the rate of crystal growth in solution in the presence of impurity as a function of supersaturation. The equations presented were proposed for constant impurity content and constant temperature. The relative velocity can be defined using two factors – an absorption factor (θ_{eq}) and an effectiveness factor (α) as has been described before [43] - Equation 36. The authors defined the impurity effectiveness factor by the critical radius of the two-dimensional nucleus and the average spacing between two active sites (L) as shown in Equation 40.

Equation 40

$$\alpha = \frac{\gamma a}{kT\sigma L}$$

In the equation above γ is the edge free energy, a is the size of a growth unit, k is the Boltzmann constant and σ is the relative supersaturation. L depends on the adsorption characteristics of the impurity. Using this definition of the effectiveness factor, Equation 38 and Equation 39 become:

Equation 41

$$\frac{V}{V_0} = 1 - \left(\frac{\gamma a}{kT\sigma L} \right) \left(\frac{Kx}{1 + Kx} \right)$$

Equation 42

$$\frac{G}{G_0} = 1 - \left(\frac{\gamma a}{kT\sigma L} \right) \left(\frac{Kx}{1 + Kx} \right)$$

At constant temperature and constant impurity concentration it is possible to convert Equation 42 and define the relative growth rate as a function of supersaturation – see Equation 43 below.

Equation 43

$$\frac{G}{G_0} = 1 - \left(\frac{S}{S_c}\right)^{-1}$$

S_c is the critical relative supersaturation (below which the face growth is zero) and is defined by Equation 44:

Equation 44

$$S_c = \frac{\gamma\alpha Kx}{kTL(1 + Kx)}$$

2.5.2 Crystal Nucleation and Growth in Presence of Impurities – Literature Review

The section above shows the theoretical approach. The following examples describe the literature discussing the effect of impurities on the crystallisation process.

The presence of impurities can affect nucleation kinetics and crystal growth. The explanation of this effect on nucleation kinetics is very difficult, due to poor understanding of nucleation itself. It has been reported that the presence of foreign particles increases the chances of a nucleation event occurring – foreign particles can work as additional active nucleation centres or may reduce interfacial tension [45]. Gahn and Mersmann [46] have observed the opposite effect of the impurity presence on nucleation – in their study impurities caused a reduction in nucleation rate, by lowering the number of active growth sites.

Computational modelling of crystallisation processes provides an explanation for changes in crystal shape, which is a result of impurities adsorbing onto specific crystal faces – if the adsorption of the impurities is permanent, the foreign particles will be built-in the crystal lattice and therefore will change crystal shape. Impurities will be more likely to adsorb on surfaces where the free adsorption energy is at a maximum [47].

Initial investigations of the effect of impurities on crystal growth during both batch and continuous crystallisation did not provide a clear answer to this question. It has

been observed that initial addition of impurities lead to an increase in crystal growth, however further increase of impurity concentration reversed the positive effect and caused a decrease [48] [49].

Studies of the influence of impurities on crystallisation kinetics have been undertaken for many different groups of compounds – inorganic compounds, drugs, sugars, etc. - examples of which are presented below.

Belhamri and Mathlouthi [50] studied the effect of hydrophilic impurities, such as oligosaccharides and polysaccharides on the crystal growth of sucrose. It has been found that especially low molecular mass impurities – oligosaccharides have a negative effect on sucrose crystal growth. This is caused by the high affinity of the oligosaccharides for specific active faces of sucrose crystals having the same conformation as the oligosaccharides. In turn this blocks some of the faces of the crystal that were before encouraged to grow and hence alters the crystal shape.

The work published by Sultana and Jensen [51] is one of very few examples present in literature, where the effect of impurities has been investigated during continuous crystallisation. The authors used a continuous microfluidic system for seeded crystallisation of glycine in the presence of glutamic acid and methionine. α -glycine was chosen as their model system, due to well established knowledge about the modifications of its crystal habit. Figure 19a shows the changes in its crystal habit in the presence of (S)-glutamic acid (top row) and (R,S)-methionine (bottom row), while Figure 19b shows two-dimensional cross sections of the modified habits of α -glycine crystals.

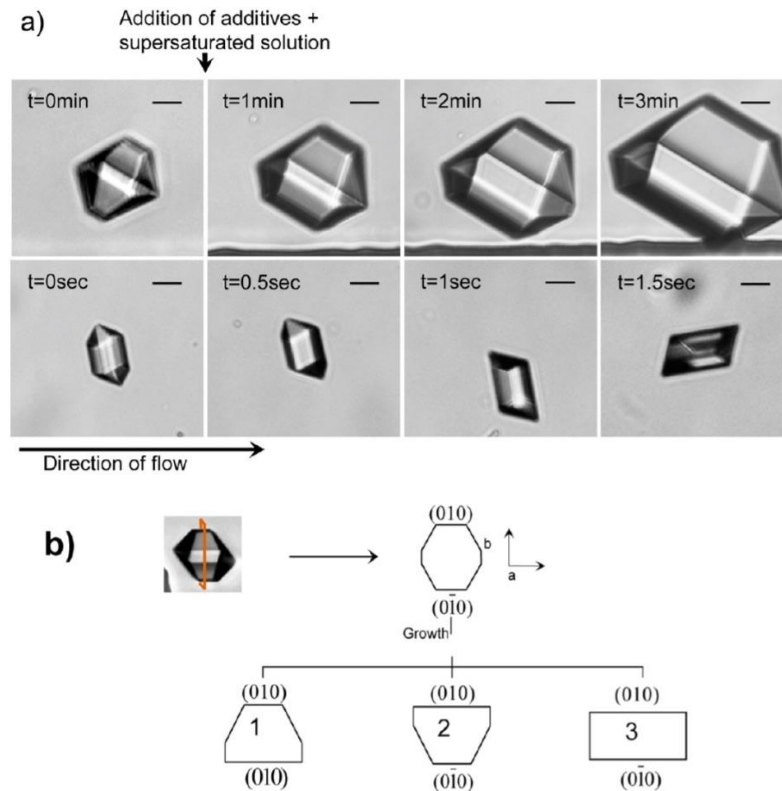


Figure 19. Habit evolution of α -glycine over time when bipyramidal seeds were grown in the presence of 1% (S)-glutamic acid (top row) and 2% (R,S)-methionine (bottom row) Two-dimensional cross sections of modified habits when bipyramidal seeds of α -glycine were grown in the presence of (S)-amino acid (1), (R)-amino acid (2), and (R,S)-amino acid (3) additives [51].

It can be seen that (S)-glutamic acid decreased the growth rate of face (010), but also had an effect on the growth rates of other faces. (R,S)-methionine had the same effect on (010) faces, but in the presence of this impurity the crystals reoriented and displayed their larger faces. The work presented here is a good example of the effect of impurities on crystal growth and shows the importance of understanding the effects that impurities may have on crystal kinetics. This knowledge would be extremely beneficial when designing a continuous crystallisation method – impurities brought into the system at an early stage of crystallisation will be carried through the entire process and influence the final product. Lack of necessary knowledge about impurities may cause termination of the process and therefore loss of time and money.

Shanmugham et al. [52] studied the effect of soluble impurities (potassium carbonate, potassium sulfate, potassium oxalate, sodium borate and potassium chromate) on nucleation rates for potassium dihydrogen orthophosphate during crystallisation experiments. Natural cooling was applied to achieve a desired supersaturation. Authors defined the interfacial tension as a crucial parameter that should be used in order to compare the nucleation theory with experimental results. Equations well known from Classical Nucleation Theory were applied to calculate the energy of formation and critical radius of the nuclei and the interfacial tension. The transformation of the Arrhenius equation (Equation 12) the equation for the free energy of formation of the nucleus (Equation 10) and the assumption that the frequency of formation of nuclei is inversely proportional to the induction period led to the final equation used in this study:

Equation 45

$$\ln\tau = B + \frac{16\pi\gamma^3v^2}{3R^3T^3\ln^2S}$$

where γ is the interfacial tension, v is the volume per molecule in solid phase, R is the universal gas constant, T is the temperature and S is the supersaturation.

The relationship between $\ln\tau$ and $1/\ln^2S$ is expected to be a straight line with a slope (m) of:

Equation 46

$$m = \frac{16\pi\gamma^3V^2N}{3R^3T^3}$$

where V is the molar volume of crystal and N is Avogadro's number.

The interfacial tension was therefore calculated from Equation 47, whereas the energy of formation of a critical nucleus was estimated using Equation 48.

Equation 47

$$\gamma = RT \left[\frac{3m}{16\pi V^2 N} \right]^{1/3}$$

Equation 48

$$\Delta G = \frac{RTm}{\ln^2 S}$$

Experiments have shown that the presence of impurities that have a common ion with the crystallising material, decrease the induction time. However, the same effect was observed for all the divalent anionic impurities considered in this study. Sodium borate increased the growth rate of potassium dihydrogen orthophosphate. Calculations were carried out to estimate the interfacial tension, the energy of formation and the critical radius of the nucleus showed that the values of these listed parameters decreased in the presence of the impurities.

A paper published by Rauls and co-workers [53] described the influence of impurities on the crystallisation kinetics of ammonium sulfate. The experiments were carried out in an MSMPR (mixed-suspension, mixed-product-removal) crystalliser and the impurities that were added were aluminium sulfate and two azo dyes – amaranth and fuchsine.

The authors observed that the kinetic coefficients for crystal growth were reduced – at all of the impurity levels – which can be explained by their adsorption on to the crystal surfaces and hence suppressing nucleation. This effect can be compensated at low impurity levels by increasing the supersaturation or metastable zone width, which affects larger crystals present in the system. The higher the impurity concentration level, the higher the surface coverage of the crystals which causes a high rise in supersaturation rate (compare to the metastable zone width increase) and by increasing the nucleation rates, the growth of the smaller crystals is triggered. It has also been reported that increasing the supersaturation caused an increase or stabilisation of the crystal growth rates.

Figure 20 shows the relevant relationships between the crystallisation parameters.

The following conclusions can be drawn:

- the presence of impurities in the system causes a widening of the metastable zone width;
- the nucleation rate is reduced due to suppression of secondary nucleation – adsorption sites blocked by impurities;
- supersaturation increases linearly with impurity concentration;
- crystal growth rate increases up to a critical point, above which the positive effect of the impurity is reversed.

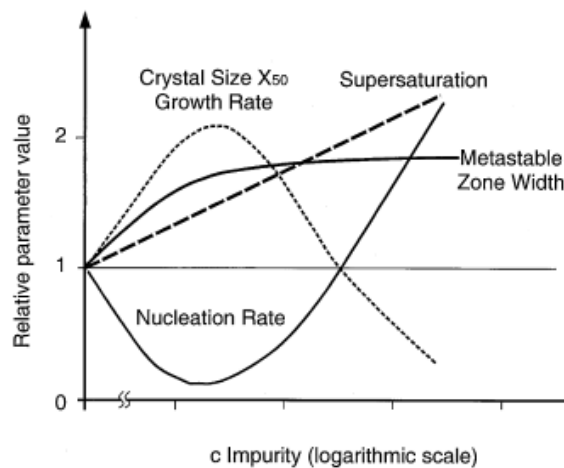


Figure 20. General relationships between the relevant crystallisation parameters, such as supersaturation, metastable zone width, crystal growth rate and nucleation rate [47]

Six structurally similar additives of paracetamol are known to inhibit growth rates and nucleation of paracetamol. These are namely acetanilide, *p*-acetoxyacetanilide (PAA), orthocetamol, methylparaben, *p*-acetoxybenzoic acid (PABA) and metacetamol. The study of PAA on paracetamol crystallisation has been the most widely investigated of all of these.

Prasad et al. [54] carried out work to examine the effect of the presence of *p*-acetoxyacetanilide (PAA) on the crystallisation of paracetamol. PAA is one out of the six structurally similar impurities of paracetamol and its effect on induction time

and crystal habit of the paracetamol system has been studied in detail. During the experiments it was found that the induction time, defined as the time period between the time when a constant supersaturation is achieved and the time when crystals are detected, increased with the increase of PAA concentration. Potential crystal habit changes were investigated using scanning electron microscopy (SEM) and the crystals changed from columnar for pure crystals (dominant (110)) to plate-like crystals (dominant (001)) at higher supersaturation levels. Addition of p-acetoxyacetanilide led to columnar crystal formation with an aspect ratio that varied with impurity level and supersaturation. Authors report that in previous investigations PAA worked as a nucleation inhibitor, mainly stopping the (110) faces. This occurred because of the structural similarity of PAA to paracetamol and hence it was simpler to adsorb at the growing interface. A significant change was observed in the surface free energy values – from 1.8 mJ/m² for the pure system to 4.9 mJ/m² for the system containing 6.02 (%w/w) of p-acetoxyacetanilide. Authors suggested that this change could be related to an increase in the size of the critical nucleus and a decrease in the nucleation rate.

Thomson et al. [55] carried out work to study the influence that two structurally similar additives to paracetamol had on the crystal morphology. Atomic force microscopy (AFM) and scanning electron microscopy (SEM) were used to analyse the samples' morphology. The (001) face of the crystal was the focus for *in situ* investigations of additive effects on the morphology and growth rate of the steps.

The habit of crystals grown with 4 mol% of acetanilide, were shown via SEM to be similar to that of pure paracetamol despite their size being much smaller in comparison. When AFM was carried out on these samples, it was found that the crystal surface had thin, branched terraces compared to the curved or straight edges observed for pure paracetamol. It was proposed that this stepped nature of the surface could be attributed to the 'pinning' of the steps by molecules of acetanilide. When the paracetamol was exposed to 4 mol% of metacetamol during crystallisation, SEM revealed that they exhibited a columnar habit unlike the tabular one for pure paracetamol and paracetamol spiked with 4 mol% acetanilide. The aspect ratio of

these crystals was more affected by this impurity – 7.33 compared with 1.2 for pure paracetamol. It was also found via AFM that the presence of metacetamol greatly increased the number of defects on the crystal surface compared to the acetanilide impurity.

When metacetamol was added, the step growth rate was found to be from 19.0 to 37.8 nm/s. Therefore, AFM and SEM have been proved to give insight into the effect that impurities have on the crystal surface, despite only focusing on the behaviour of one crystal face.

In 2002 Jiban Podder [56] published a paper about the effect of impurities on the growth and nucleation of potassium dihydrogen phosphate (KDP), which is a well-recognised non-linear optical material widely used in solid state laser source devices. The author chose two impurities - urea and potassium chloride (KCl) – in order to study their effect on the growth and nucleation kinetics as well as the morphology and mechanical, structural and optical properties. Slow cooling crystallisation was used as the crystallisation method. A general observation was that urea had a stronger effect on the crystallisation kinetics and KDP crystal features - it has been observed, using Fourier transform infrared spectroscopy (FT-IR), that only urea crystallised out with KDP, as an element of its crystal lattice. The presence of urea had a strong positive effect on the growth rate (KCl also increased the growth rate, but to a lesser extent) as well as increasing the hardness of the crystals. The study showed that using KCl as an impurity improved the optical quality of the crystals. To conclude, crystals produced in the presence of urea or potassium chloride demonstrated better non-linear optical properties and therefore this is an example where impurities yield a positive effect.

The effect of potassium chloride (10mol%) on the crystallisation of potassium acid phthalate (KAP) was studied by Rahman and Rahman [57]. The authors applied classical nucleation theory in order to determine the induction period, the interfacial energy and the energy of formation of the critical nucleus. X-Ray Diffraction (XRD), Fourier transform infrared spectroscopy (FT-IR) and UV-VIS spectroscopy were used to investigate the structural and optical properties of the obtained crystals.

The addition of KCl increased the metastable zone width, however it was not the only positive effect. It was believed that the presence of KCl in solution reduced the negative effect of trivalent ions, such as Cr^{3+} , Fe^{3+} and Al^{3+} , on the crystal growth. Figure 21 shows the solubility and metastable zone width of KAP with and without the addition of potassium chloride.

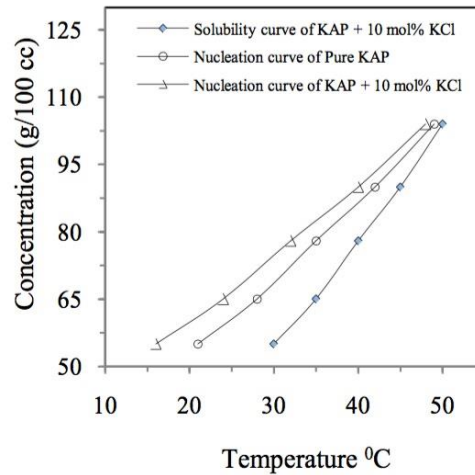


Figure 21. Solubility curve of potassium acid phthalate (KAP) with 10mol% addition of potassium chloride (\diamond) and nucleation curve of KAP with (\triangle) and without (\circ) the addition of potassium chloride [57]

Next, the effect of KCl addition on the interfacial energy (σ) and the energy of formation of critical nuclei (ΔG_{crit}) was investigated. The interfacial energy was calculated from the induction period, based on Equation 49 below:

Equation 49

$$\sigma = \left(\frac{3R^3 T^3 m}{16\pi v^2 N_A} \right)^{1/3}$$

where R is the universal gas constant, T is the temperature, m is the slope evaluated from the straight line fit for the natural logarithm of induction time (τ) - $\ln \tau$ against $1/(\ln S)^2$, where S is the supersaturation, and N_A is Avogadro's number.

The energy of formation of the critical nuclei was calculated from Equation 50.

Equation 50

$$\Delta G_{crit} = \frac{RTm}{(\ln S)^2}$$

There was no significant effect on the energy of formation of the critical nuclei, but as can be seen in Figure 22, the effect of KCl on the interfacial energy was significant – energy notably increased.

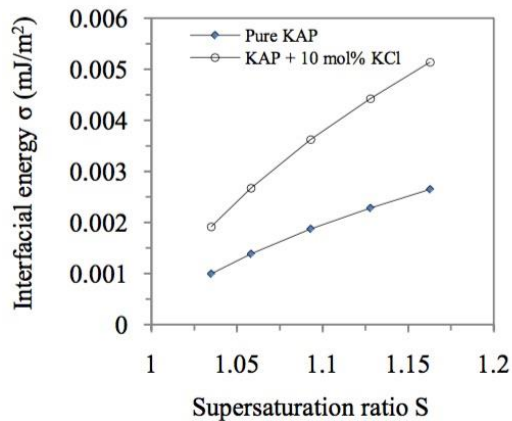


Figure 22. A relationship between the interfacial energy (σ) and supersaturation (S) of pure (\diamond) and KCl doped (\circ) KAP solution [57]

Based on XRD results it can be said that KCl was being incorporated into the KAP crystal lattice. According to UV/VIS spectra analysis, spiking the solution with KCl improved the transmission capability of the KAP crystals.

Zhang et al. [58] carried out work to study the influence of malic acid on the crystallisation of zinc lactate. Authors observed that addition of 5.85 (%w/w) malic acid caused an increase in the solubility of zinc lactate in comparison to the solubility of the pure system. The positive effect of malic acid on the solubility of zinc lactate can be explained by the pH change and the formation of metal-organic complexes in the solution. The nucleation induction time was prolonged when malic acid was present in the solution.

A study, published by Peng et al. [59], presented the effect of the chloride ion (Cl^-) and the sulfate ion (SO_4^{2-}) on the solubility, metastable zone width and nucleation kinetics of borax decahydrate. Two methods were used with the intention of determining these crystallisation parameters. For the solubility and metastable zone width measurements, a polythermal crystallisation was applied, while for the induction time measurements an isothermal approach was used. It has been observed that both studied anions increased the metastable zone width. Applying an isothermal crystallisation lead to two different nucleation mechanisms – homogeneous nucleation for high supersaturation ($S > 1.3$) and heterogeneous nucleation for low supersaturation ($S < 1.25$). The presence of chloride and sulfate ions caused the prolonged induction time, which meant that addition of impurities inhibited the nucleation. Interfacial energy values, calculated from the isothermal method were lower than those calculated from the polythermal method – in this case $\ln S$ (where S is supersaturation) was calculated based on the solute concentration instead of the activity.

Nucleation kinetic parameters – nucleation order, interfacial energy, kinetic constant and the nucleation constant – were calculated using two approaches - Nývlt'-like equation and the Classical Three-Dimensional Nucleation Theory approach.

The two studied anions had no effect on the nucleation order. A positive effect on the interfacial energy was observed – higher concentration of impurity, had a stronger effect. The nucleation rate constant increased with the increase in the saturation temperature, but the kinetic constant was independent of temperature.

Li et. al [60] studied the effect of α -amino acids on the nucleation and morphology of glycine crystals. Authors carried out batch experiments, where a supersaturated solution was cooled down from around 80°C to room temperature and left unstirred to crystallise. The effect of the following α -amino acids (“tailor-made” additives) was studied: L-alanine, L-valine, L-leucine, L-phenylalanine, L-serine and L-histidine. There was no significant effect of most of these impurities, therefore the authors focused on the effect of L-leucine. When the crystal growth was studied authors used the flow system, which is depicted in Figure 23.

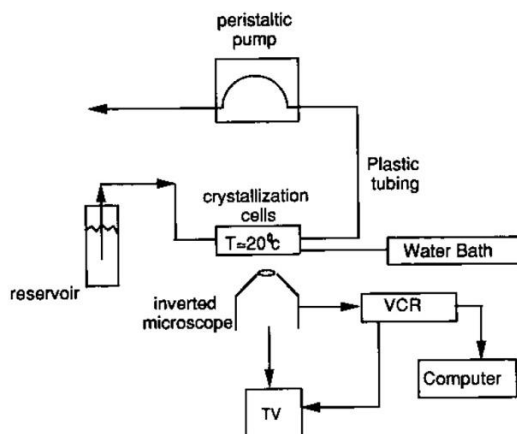


Figure 23. Schematic diagram of the flow system applied for measuring the crystal growth [60]

An inverted microscope was used to monitor the increase of crystal size and UV spectrophotometry and high pressure liquid chromatography were used for glycine concentration measurements. It was observed from crystal growth experiments that L-leucine had a tendency to adsorb onto the $(0\bar{1}0)$ face of glycine crystals and therefore reduced the growth of this face and changed the morphology of glycine crystals. The addition of L-leucine below the critical concentration (8 mg/ml) caused the reduction of the growth of face $(0\bar{1}0)$ and hence the morphology of glycine crystals changed from bipyramidal to pyramidal. More than 8 mg/ml of L-leucine added to glycine solution triggered the dimerization of glycine and thus the growth of the (010) , (001) and $(01\bar{1})$ faces increased. Potentially it could be explained by multilayers adsorption of L-leucine on glycine $(0\bar{1}0)$ face and in this way the oriented nucleation and growth of glycine twin crystal template was provided. Changes in glycine crystal's morphology in presence of different amount of L-leucine are depicted in Figure 24.

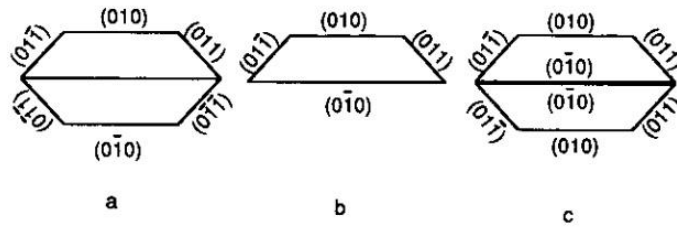


Figure 24. Faces of glycine crystals grown from aqueous solutions: a. with no additive, b. doped with L-leucine at concentration less than 8 mg/mL, c. doped with L-leucine at concentration greater than 8 mg/mL [60]

The induction time measurements can be used not only to determine the nucleation rates during the primary nucleation experiments, but also can be applied to the experiment where the secondary nucleation mechanism was observed. The induction time is then determined by the growth rate of the seeds only. In order to study these two processes separately – nucleation and growth two sets of induction time experiments should be carried out – for seeded and unseeded system. This type of experiment allows studying the effect of additives on primary nucleation during precipitation. Van der Leeden, Kashchiev and van Rosmalen [61] published a study on the effect of the addition of a copolymer of maleic acid and vinyl sulfonic acid (PMA-PVS) on the nucleation and growth rates of barium sulfate. Authors observed that the induction time is supersaturation and seed number density dependent as well as the presence of the additive depended. It was revealed that the presence of PMA-PVS copolymer caused a decrease in the growth rate of barium sulfate crystals, however at the same time the nucleation rate increased.

2.6 Chapter Summary

The main aspects of crystallisation theory, related to this project, were presented in this chapter. It was shown, throughout this chapter, that there are many essential key aspects that have to be considered while designing a successful crystallisation process, such as: solubility, supersaturation, metastable zone width, nucleation characteristics and crystal growth characteristics.

Presented literature review on two nucleation theories – Classical Nucleation Theory and Two-step Nucleation Theory showed that at the moment, nucleation is not a fully understood process and further investigation is required in order to explain the crystal formation mechanism.

The literature review on crystal nucleation and growth in presence of impurities revealed that the main focus is on the effect of impurities on crystal growth rather than nucleation rates, even so these two parameters are related. There is also a lack of interest in investigating the effect of inorganic impurities on crystallisation of organic materials – the observed trend is to investigate the effect of organic impurities (by-products, intermediates, degradation products) on crystallisation parameters.

3 Investigation of the Effect of Temperature Control on Crystallisation of L-Glutamic Acid

3.1 Chapter Outline

This chapter outlines all experimental work and results carried out in the CoFlux reactor. L-glutamic acid in aqueous solution was studied under different concentrations and cooling rate conditions using two different reactor setups. The reason behind choosing L-glutamic acid for this study was that this compound is a well-studied molecule and large amount of data was available for comparison.

Crystals obtained from those experiments were analysed using different analytical techniques:

- 1) X-Ray Powder Diffraction
- 2) Microscope Imaging
- 3) Laser diffraction
- 4) Raman spectrometry.

These techniques were used to compare the crystal features (polymorph, particle size) to the results obtained for L-glutamic acid using other reactor types – batch oscillatory baffled reactor (OBR) and stirred tank reactor (STR). It is believed that the Coflux reactor provides a better temperature control, therefore a better control over the entire crystallisation process could be achieved. It can result in elimination of unwanted polymorphic forms and hence lead to production of pure product in terms of polymorphs.

Another aim of this project was to assess if enthalpy measurement was an advantage of the CoFlux reactor for monitoring the crystallisation of L-glutamic acid from water. This chapter contains a section providing a theoretical background about crystallisation platforms and analytical techniques used for this study (sections 3.2 and 3.3) followed by section describing experimental conditions (section 3.4 and 3.5) and section presenting results and discussion (section 3.6 and 3.7).

3.2 Crystallisation Platforms

In this section three types of the reactors will be described. There are more types, but only three of them were used in this project and hence require further description.

3.2.1 Stirred Tank Reactor

The batch reactor is widely used in the fine chemical and pharmaceutical industries, where reactants are converted to products in a single batch cycle. This kind of reactor can be used for a variety of process operations such as dissolution, distillation, product mixing, chemical reactions, crystallisation, liquid/liquid extraction and polymerisation.

Because the process parameters change over time the system does not achieve steady state, so the process control is really time-dependent. Conventional batch reactors are characterized by slow response to heat load changes. To achieve good temperature control in conventional jacketed reactors, two factors have to be considered – the temperature control system has to be able to react to the bulk temperature changes and keep the temperature at the desired value. Secondly, the wall temperature has to be set at the level which does not change the product properties. The jacket temperature is not a good indicator of the internal wall temperature [62]. This lack of the uniformity within a reactor can cause changes in the product properties including polymorphic composition [63].

There is also a problem with the scaling up this technology from lab to industrial scale, which is a result of the complexity of the parameters involved [64].

3.2.2 CoFlux Reactor

Changes caused by fluctuations in the temperature may significantly affect the chemical and physical properties of the materials produced in the reactor. Ashe and Morris from AM Technology designed a CoFlux reactor which allows users to have better control over the jacket temperature and the heated surface area. The CoFlux

has an innovative jacket, consisting of a system of coils and plates around a glass vessel, which allows for dynamic temperature control (Figure 25).

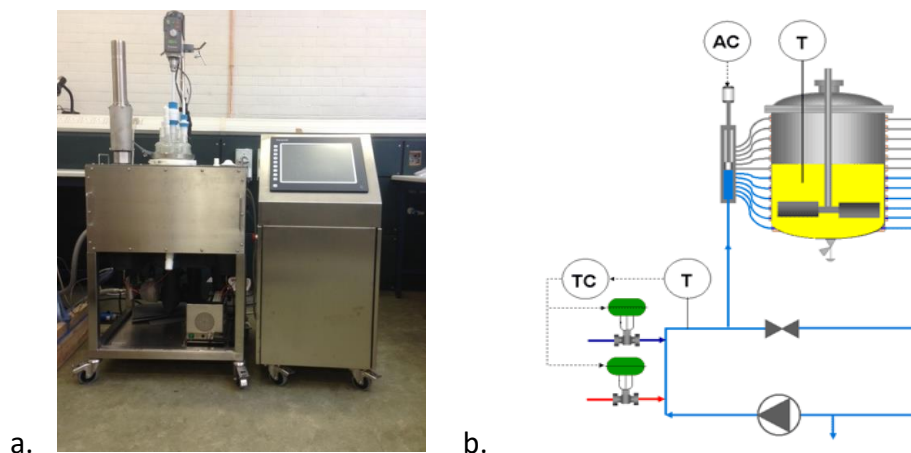


Figure 25. Photograph (a.) and a schematic diagram (b.) of CoFlux reactor. Temperature probes (T), temperature controller (TC) and valve controller (AC) are shown in a diagram.

3.2.2.1 Heat Balance Calorimetry

Although different calorimetric techniques can be used with constant flux control, the preferred method is heat balance calorimetry. It is a fast, sensitive, accurate and simple method to use with constant flux control. The measurements used are:

- Accumulation - heat shifts due to changes in the system temperature,
- Heat balance - heat entering or leaving the system with the heat transfer fluid.

In addition to these, a number of other factors need to be taken into account of such as heat losses to the environment, agitator energy and enthalpy shifts in the vessel jacket.

Enthalpy is the cumulative value of power and is measured in Joules. It is used to monitor reaction efficiency, identify reaction endpoints or for timing of critical process decisions. It also performs a valuable safety function for strong exotherms since it can detect accumulation of unreacted material. Since enthalpy is measured over longer time frames it can deliver very accurate data [2].

3.2.2.2 Process enthalpy

Signals from the reactor are used to determine the power added or removed from the process by the heat transfer fluid, which describes the equation below (Equation 51 and Equation 52).

Equation 51

$$q_{htf} = m_{htf}Cp_{htf}(T_{htfin} - T_{htfout}) \\ \pm (\text{adjustments for the other system factors}) [W]$$

where T_{htfin} is temperature of heat transfer fluid entering the jacket in Kelvins, T_{htfout} is temperature of heat transfer fluid leaving the jacket in Kelvins, m_{htf} is mass flow of heat transfer fluid in kilograms per second and Cp_{htf} is specific heat of transfer fluid in kilojoules per kilogram times Kelvin. The enthalpy can be measured from the power readings is shown in Equation 52:

Equation 52

$$h_p = \int q_{htf} \pm (\text{adjustments for other system factors}) [J]$$

where q_{htf} is the power measured in the heat transfer fluid in Watts.

3.2.2.3 CoFlux Valve

Unlike traditional jacketed reactors which control the process temperature by either varying the flow rate or temperature of the heat transfer fluid; the CoFlux system controls the process temperature by effectively varying the heat transfer area shown in Figure 26.

Symbol	Description
TC	Temperature controller
T_p	Temperature of the process material [K]
T_{htfin}	Temperature of heat transfer fluid entering the jacket
T_{htfout}	Temperature of heat transfer fluid leaving the jacket
m_{htf}	Mass flow of heat transfer fluid
T_e	Temperature of ambient air
E_a	Electrical power drawn by agitator
θ	Time
S	Agitator speed
τ	Agitator torque
Z	Fraction of jacket in service

Figure 26. CoFlux reactor schematic diagram with description of main components

This is achieved by varying the number of cooling coils which are in operation at any given time. This has a number of advantages over traditional techniques. The CoFlux jacket distributes the heating/cooling energy much more evenly and gives faster, more stable and much more accurate temperature control. The elimination of any hot or cold spots minimises the thermal degradation of the process fluid. As we have seen from the results obtained in our experiments, this has many benefits for crystallisation. In crystallisation processes localised cold spots can cause a nucleation and crystallisation in small localised areas, resulting in lower yields – due to fouling,

a large range of particle sizes and secondary nucleation. Two of the major advantages of the CoFlux design are much better distribution of the heating and cooling resulting in better control of the reactor wall temperature and ultimately greatly improved process temperature control. The effects of this on the process can be seen in the experimental results obtained by Allan et al. [65] [66]. The CoFlux reactor has many advantages over conventional batch reactors and they are summarised here:

- improved yield through better temperature control - due to the short residence time of the heat medium in the CoFlux jacket (less than 3 seconds), the dynamic control of the reactor is simple. The CoFlux reactor responds faster to temperature changes. Control of temperature in a 5000 L CoFlux reactor is comparable to the control of 1 L lab reactor (STR);
- reduces energy consumption - with the CoFlux reactor flow is reduced by about 90% and the pressure by > 90% while maintaining high rates of heat transfer - this greatly improves energy efficiency;
- improved crystallisation control with direct measurement of the power of the process (W), enthalpy (J), the U-value and temperature (K) of the wall [65] [66] [67].

3.2.2.4 CoFlux setups used during the project

For the initial set of experiments, the heat transfer fluid (HTF) was transferred once through the jacket before the fluid was returned to the heat transfer unit (HTU). The diagram below illustrates this arrangement (Figure 25).

KEY:

1. Jacket heater/cooler elements
2. Constant flux valve
3. Heat transfer fluid inlet header
4. Heat transfer fluid booster pump
5. Heater/chiller unit

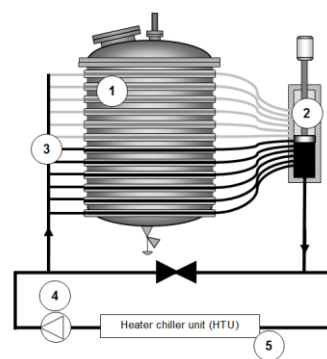


Figure 27. CoFlux reactor, initial setup (setup A)

Although the CoFlux jacket is designed to provide good distribution of the heating/cooling fluid across the heat transfer surface area, the actual temperature of the HTF is under the control of the HTU. This can have disadvantages for processes such as crystallisation. For processes requiring rapid cooling rates this is normally achieved by ramping down the HTU. This creates a differential temperature between the jacket and the process, which consequently cools the process fluid at a similar rate to the HTU. The problem with this method is that a large differential temperature is often present between the cooling jacket and the process and the amount of energy available from the cooling jacket can exceed the desired amount for some phases of the crystallisation process. This can cause a number of problems, such as nucleation and crystallisation in a small localised surface area, resulting in lower yields, large ranges of particle sizes and secondary nucleation. In such circumstances to prevent this from occurring the HTU must rapidly reduce the amount of energy available in the jacket. In order to do this the HTU must change the temperature of the entire contents of the jacket, the associated interconnecting pipework and the HTU internal system. Even at the scale that was worked at in the current study this involved changing the temperature of several litres of heat transfer fluid which can take several minutes. On larger systems this takes much longer. In the time it takes to do this the available energy in the jacket can have affected the process in an adverse way. However, such scenarios can be virtually eliminated by

the introduction of a second control valve controlling the temperature of a temperate loop.

During the second phase of experiments, a temperate temperature loop was added to the heat transfer pipework. The diagram below illustrates this arrangement (Figure 27).

KEY:

1. Jacket heater/cooler elements
2. Constant flux valve
3. Heat transfer fluid inlet header
4. Heat transfer fluid temperate loop pump
5. Heater/chiller unit
6. Static mixer
7. Temperate loop control valve

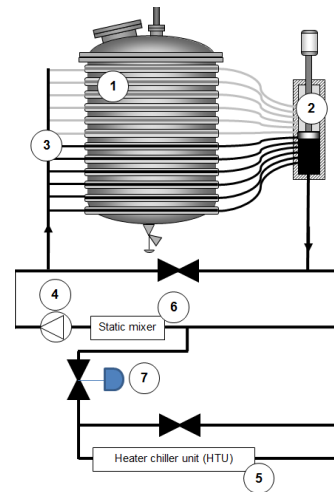


Figure 28. CoFlux reactor, second setup (setup B)

With this arrangement the temperature in the temperate loop is controlled by the temperate loop control valve (7). The CoFlux valve (2) continues to control the process temperature. The temperature of the heat transfer fluid supplied by the HTU (5) can be much hotter or colder than the temperate loop. By using a static mixer, the very hot or cold fluid introduced into the temperate loop is quickly mixed into the fluid in the temperate loop and as a consequence a much less harsh heating or cooling effect is generated and hot and cold spots are eliminated. Compared with the first setup (where the HTF was transferred once through the jacket before being returned to the HTU) the inventory of heat transfer fluid in the temperate loop is very small and consequently the temperature can be controlled very quickly and very precisely. The experiments operated with the temperate loop during the cooling phase at a constant differential temperature of 20°C below the process set point. The HTU set point was set at -5°C. This gave a very strong cooling rate initially, but as the reactor

approached the process set point the system stabilized and cooled the process at a constant differential temperature of 0°C. Once the reactor was within 1°C of the process set point, the temperate loop valve (7) was instructed to close fully. Thus, the only energy now available to the process is that contained within the temperate loop. During this time the experimental data show that crystallisation is taking place. The data also show that the reactor wall temperature reduces until it is at the same temperature as the process (all the available energy has been used up). This method of control is an ideal arrangement for crystallisation processes as it can quickly moderate the available energy in the jacket and this method also ensures that the heat transfer fluid entering the jacket is well mixed and essentially all at the current desired temperature. The major benefit of operating in this way is that it can prevent localized crystallisation - encrustation, and thus improve yields and reduce particle size distribution.

3.2.2.5 *The accumulation or heat shift in the process fluid*

During the second phase of experiments, an additional parameter was measured – q_s . The q_s parameter can be described as the accumulation or heat shift in the process fluid and is driven by the rate of change of the process temperature. When this is zero no energy is entering or leaving the system, via the jacket and no energy is being generated or absorbed by the process. The equation describing how the parameter is calculated is shown below (Equation 53):

Equation 53

$$q_s = \frac{m_p C_{p_p} dT_p}{d\theta} [W]$$

where T_p is the temperature of the process fluid in Kelvins, m_p is the mass of the process fluid in kilograms, C_{p_p} is the specific heat of the process fluid in kilojoules per kilogram times Kelvins and θ is the time in seconds.

Constant values were provided for m_p (3.4) and C_{p_p} (4080), hence the important variable is the rate of change of temperature $dT_p/d\theta$.

3.2.3 Oscillatory Baffled Reactor

The oscillatory baffled reactor (OBR) is a recent development in technology, which permits processes to run continuously under close to plug flow conditions where the material is being transported through the reactor under laminar flow. Figure 29(a) shows a typical design of the oscillatory baffled crystalliser – a tube (10-150 mm internal diameter (D)) in which orifice plates are spaced equally. The oscillation is produced by a reciprocating pump or piston located at one end of the tube [68].

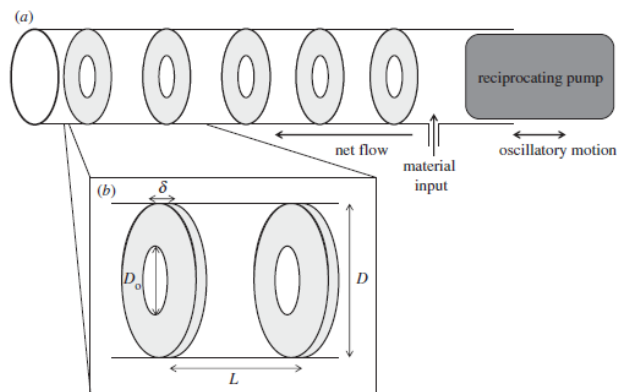


Figure 29. (a) The reactor scheme and (b) geometrical parameters of the oscillatory baffled crystalliser

Mixing in this type of the reactor is obtained by oscillating the fluid, leading to the creation of eddies which are vortices generated when the flow and baffles interact [69] – see Figure 30. Each inter-baffle zone can then be treated as a continuously stirred tank reactor (CSTR), so the OBR can be described as a finite number of CSTRs connected in series. Control of the mixing intensity in the OBR is possible by changing the oscillating conditions – frequency and amplitude, whereas in a conventional tubular reactor the mixing intensity is controlled by changing the flow rate [68].

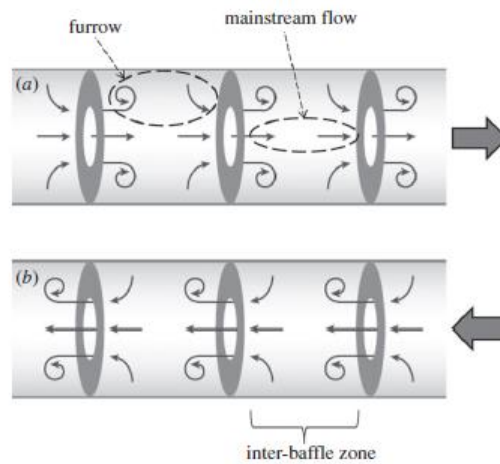


Figure 30. Vortex formation produced by oscillatory flow: (a) Back stroke and (b) forward stroke

This kind of oscillatory mixing is more efficient than internal mixing, which causes the product obtained in a batch OBR to have better quality and better consistency in terms of particle features than those obtained in a conventional stirred tank reactor [70] [71].

The oscillatory baffled reactor can work in a continuous setup – continuous oscillatory baffled reactor (COBR). This type of system contains several glass sections (OBRs) all under different temperatures. The principle of operation of COBR is the same as for OBR. Figure 31 shows a schematic diagram of COBR.

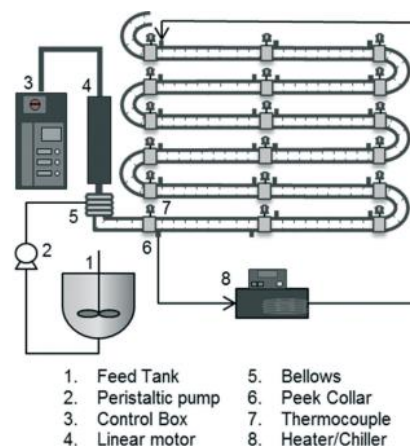


Figure 31. A schematic diagram of the continuous oscillatory baffled reactor, showing the main elements of the setup [72]

3.3 Analytical Techniques

3.3.1 Raman Spectroscopy

Raman spectroscopy has been known since 1928. In 1930, Sir Chandrasekhar Venkata Raman was awarded the Nobel Prize for his work on the scattering of light and the discovery of the phenomenon, and hence it was named after him. Raman spectroscopy (as well as infrared absorption spectroscopy) is a technique used to study vibrational spectra of materials and is a complementary technique to infrared spectroscopy [73] [74].

Raman spectroscopy focuses on the scattering of light from a particular molecule. There are two types of light scattering:

- elastic – where the scattered radiation is at the same frequency as the incident radiation (Rayleigh scattering)
- inelastic – where the scattered radiation is at a different frequency, which means that the energy was transferred between the light quanta and the material (Stokes and anti-Stokes scattering) [75].

A Raman spectrum can be described as scattered intensity plotted against energy and peaks observed in the spectrum correspond to an energy or Raman shift from the incident radiation energy. The light source is normally a laser of visible or near infrared monochromatic radiation. The scattered radiation collected by a spectrometer gives three different types of signal: Stokes, anti-Stokes and Rayleigh lines. Raman scattering is inelastic: the total photon plus molecular energy is conserved but the vibrational energy changes and frequency shifts occur in the scattered radiation [76].

Figure 32 below illustrates the types of bands observed in the Raman spectrum.

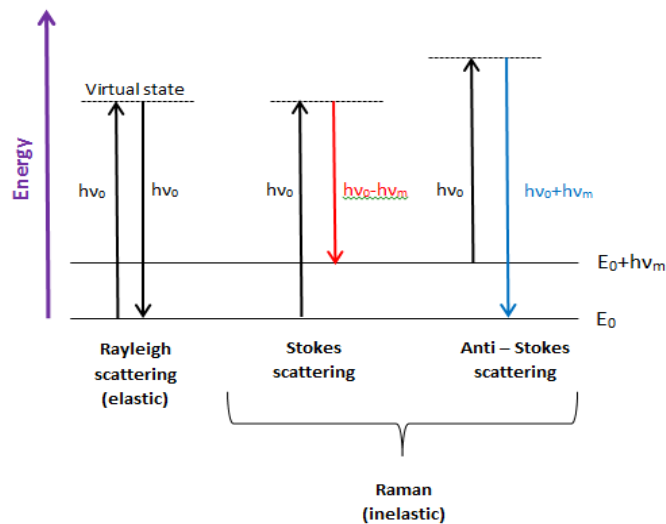


Figure 32. Jablonski diagram representing quantum energy transitions for Rayleigh and Raman scattering

As mentioned before, in the Raman spectrum, the following bands are observed:

- Elastic scattering is called Rayleigh scattering. In this type of scattering, a scattered photon has exact the same wavelength as the incident beam. Rayleigh scattering has the highest probability of occurring.
- When the incident radiation shifts to a lower frequency (lower energy, higher wavelength), the scattered light is called Stokes scattering. In this type of scattering, energy is transferred to the vibrational mode of the molecule which ends up in a higher vibrational energy state.
- When the incident radiation shifts to a higher frequency (higher energy, lower wavelength), the scattered light is called anti-Stokes scattering. In this type of scattering, energy is transferred from the vibrationally excited mode of the molecule, finishing in a lower vibrational energy state [77].

At room temperature most of the molecules are in the ground vibrational state ($\nu=0$) with a much lower population in the first vibrationally excited state ($\nu=1$). Since there is a much higher probability the molecule is in the ground vibrational state, the Stokes lines in the spectrum are much more intense than the anti-Stokes [77] [78] [79].

Raman spectroscopy has many advantages: ease of preparation of samples, the ability to perform measurements at higher temperatures and higher pressures, the ability to analyse all states of material: solid, liquid and gas. However, the sensitivity of the Raman measurements for gases and liquids is not very high. The main advantage of Raman is the ability to monitor processes, where water is the solvent – water gives a very weak signal during measurements in comparison with infra-red measurements. Raman spectroscopy provides information on the qualitative and quantitative composition of the sample, in a non-destructive and non-invasive way. Raman is a flexible spectroscopic tool – because of the wide range of laser wavelengths it is possible to remove the effects of fluorescence during measurements by using a near infra-red laser. In crystallization process Raman spectroscopy helps identify and can provide quantitative information on the composition of the polymorphic forms, while monitoring the formation or transformation of one form into another [77].

3.3.2 Laser Diffraction

In industrial processes in order to characterize any solid materials produced, the particle size must be obtained. In the pharmaceutical industry this property is key as the dissolution rate of a drug can be altered if the particle size is not at the desired specification. In extreme cases this can affect the bioavailability of the drug limiting the quantity of drug in solution in the intestine available for adsorption.

Particle size measurements can be represented in different ways, with the difficulty in describing this property increasing as the shape of the particles drifts further away from the classic spherical shape. Depending on the measurement technique applied, a different answer for particle size will be determined. This is due to the fact that different instrumentation will measure different intrinsic properties of the particles and hence different sizes will be reported.

When carrying out particle size measurements, the mean, mode and median particle size are significant values. The mean value is the average of all data that are collected

during the measurement and can be computed in several ways based on the calculation where there are 3 spheres with diameters of 1, 2 and 3 μm :

Equation 54

$$D[4,3] = \frac{1^4 + 2^4 + 3^4}{1^3 + 2^3 + 3^3} = 2.57\mu\text{m}$$

The $D[4,3]$ value (Equation 54) is otherwise known as the volume or mass moment mean. The $D[3,2]$ (Equation 55) representation of the particle size can also be called the surface area moment mean.

Equation 55

$$D[3,2] = \frac{1^3 + 2^3 + 3^3}{1^2 + 2^2 + 3^2} = 2.72\mu\text{m}$$

If the median value is quoted, this means that the data have been split into two halves and the median lays 50% above the lowest value and 50% below the highest value. It is however the mode that is value of the highest point in a frequency distribution curve and this is the most popular method when describing particle size.

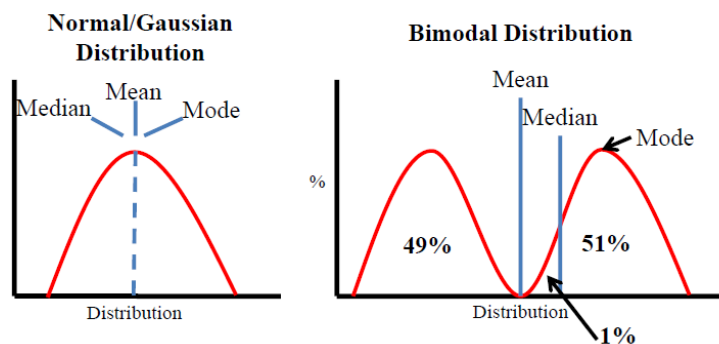


Figure 33. Median, mean and mode in Gaussian and Bimodal distribution of particle sizes [80]

The figures shown above (Figure 33) display how all of the values described previously would be positioned in such distributions. In a normal distribution all would be in the

same place, however if the shape of distribution varies then the mode, median and mean would lie in different areas of the curve.

In this project laser diffraction (LD) techniques were used for particle sizing. The theory underpinning this technique is discussed below.

Laser diffraction has many benefits for being used for particle size analysis in industry as it is fairly cheap and results are obtained quickly. This technique correlates the diffraction angle to the particle size by stating that they are inversely proportional to one another during the measurement. When a laser beam with a fixed wavelength comes into contact with a particle, a diffraction pattern is produced. It is from the properties of this pattern (such as the intensity and distance between the diffraction rings) that the particle size can be determined. If particles are larger in size, then the diffraction patterns will have a stronger and more distinctive appearance. This is due to the scattering taking place at a smaller angle to the incident beam when compared to the larger angles that arise from smaller particles [81]. Radial distance r_0 is depending on the particle size [82] (Figure 34).

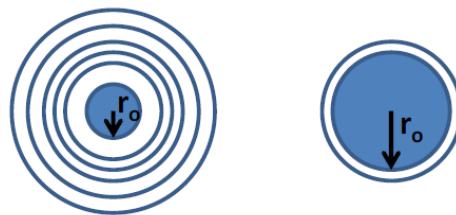


Figure 34. Differences in diffraction patterns between a large (left) and a small particle (right) [81] [82]

The data obtained is plotted as an intensity distribution of light against the radial distance from the centre of focal plane of lens (Figure 35) [83].

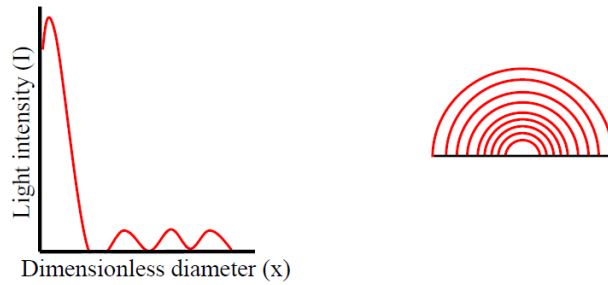


Figure 35. Intensity distribution of light against radial distance from centre of focal plane of lens for a typical particle (left) and schematic of detector containing a series of photosensitive rings (right) [83]

Conversion of the obtained scattering patterns is possible using a combination of two theories – Mie and Fraunhofer. Both theories provide different conditions under which scattering occurs, however both are based on the same assumption that measured particles are spherical. The optimum conditions for scattering occurring are listed below:

- Fraunhofer – scattering occurs if the wavelength of incident light is 5 or 6 times smaller than particle size
- Mie – scattering occurs if the ratio of particle diameter to wavelength of incident light is approximately 1 [81].

The assumption that all particles are spherical causes an error, because in reality it is almost impossible to produce spherical particles. The range of the error in comparison to different methods such as microscopy has been explored and widely reported in the literature [84] [85] [86].

The following requirements must be met to make the Fraunhofer theory valid:

- the diffracting particle has to be much larger than the wavelength of the illuminating light
- the illuminating light corresponds to a planar wave front (laser light) and the diffraction pattern is observed in the focal plane of the lens
- the intensity distribution of the illuminating light is homogeneous over the particle

- the refractive index of the particle differs sufficiently from the surrounding medium [87].

Figure 35 shows the dimensionless diameter (x) calculated using Franhofer theory. The actual equation is shown below (Equation 56).

Equation 56

$$x = \frac{2\pi rs}{\lambda F}$$

In the equation above r is the particle radius, s is the radial distance in the detection plane measured from the optical axis, λ is the wavelength of light and F is the focal length of the lens.

For a spherical particle illuminated with incident light the intensity of the scattering ring pattern is given by Equation 57:

Equation 57

$$I(\theta, x) = I_0 \frac{A^2}{\lambda^2 f^2} \left[\frac{2J_1\left(\frac{kx \sin\theta}{2}\right)}{kx \sin\theta / 2} \right]^2$$

where A is the area of projected sphere, x is the diameter and ϑ is the scattering angle. The equation above only works for a single particle. For a group of particles, the diffraction pattern becomes more complicated, which is caused by the fact that different particles scatter light at different angles. The total light energy distribution can be described in the form of a matrix (Equation 58) [88].

Equation 58

$$L(j)=W(i)T(i,j)$$

$L(j)$ is the total light energy falling on the ring, $W(i)$ is the weight fraction of the particles in the size range i , $T(i,j)$ represents the scattering matrix for spherical particles (matrix contains the coefficients to define the light energy distribution for each particle size range). The weight distribution is known as (Equation 59) [83]:

Equation 59

$$W_i = \frac{4}{3} \pi r_i^3 \rho N_i$$

where N is the number of particles and r is the particle radius.

To use Mie theory, it is necessary to know the refractive index of the solution and the particles and the coefficient of light absorptivity of the particles in the suspension. Results obtained using Mie theory are a function of the refractive index and particle size and the reflected, refracted and diffracted components of the light are included. The simplified version of Mie's theory developed in 1908 is given in the equation below (Equation 60) [81]:

Equation 60

$$I(\theta) = E\{k^2 D^4 [J_1^2] \theta^1 + [k_1 \theta]^1 + [k_2 \theta]^3 + [k_3 \theta]^5 + K^4 D^6 (m - 1)^2 \theta^6 / 8\pi\}$$

where I is the scattered light intensity, E is the flux of incident light per unit area, k and K are constants, D is the diameter of the particles, J_1 is the Bessel function, θ is scattering angle and m is the complex refractive index.

3.3.3 X-ray Powder Diffraction

X-rays are electromagnetic waves with wavelengths in the range of from 10 pm to 10 nm. X-ray powder diffraction (XRPD) is a rapid analytical technique primarily used for phase identification of a crystalline material and can provide information on unit cell dimensions. It is now a common technique for the study of crystal structures and atomic spacing [89] [90]. In the pharmaceutical industry XRPD is a widely used off-

line technique to determine the polymorphic form of an end product. Recent publications show that XRPD can be potentially used as an on-line technique to monitor the polymorphic transformation during the process [90] [91].

As mentioned above the X-Ray powder diffraction can determine the crystal structure. Different polymorphic forms have different crystal structures that result in different diffraction patterns between the polymorphic forms.

X-ray diffraction can be described as the elastic interaction of radiation with matter. The X-ray beam can be scattered only if its wavelength is the same as the interatomic distance present in the sample. The scattered photons form a series of Debye cones and are recorded by the detector (Figure 36).

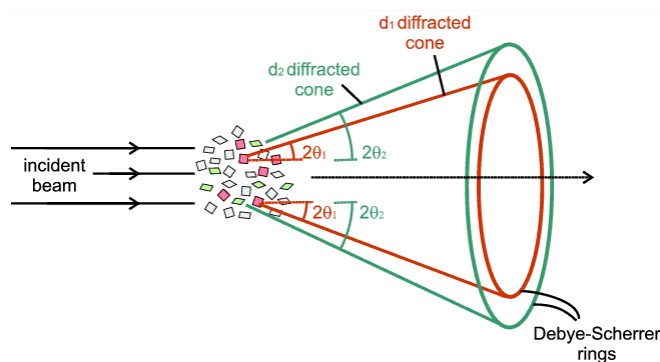


Figure 36. A schematic diagram showing Debye cones formed by two different crystallites presented in red and green [92]

X-ray diffraction is based on constructive interference of monochromatic X-rays and a crystalline sample. X-rays are generated by a cathode ray tube, filtered to produce monochromatic radiation, collimated in order to concentrate the rays, and directed toward the sample. The interaction of the incident rays with the sample produces constructive interference (and a diffracted ray) when conditions satisfy Bragg's Law. Bragg's diffraction condition is shown in the following equation (Equation 61):

Equation 61

$$n\lambda = 2d_{hkl}\sin\theta$$

where n is the positive integer, λ is the wavelength of the incident wave, d is the lattice spacing and θ is the angle between the incident rays and the surface of the crystal.

At certain distances between surfaces and for a given wavelength Bragg's law determines the angle at which the wave must fall, that there will be constructive interference (Figure 37).

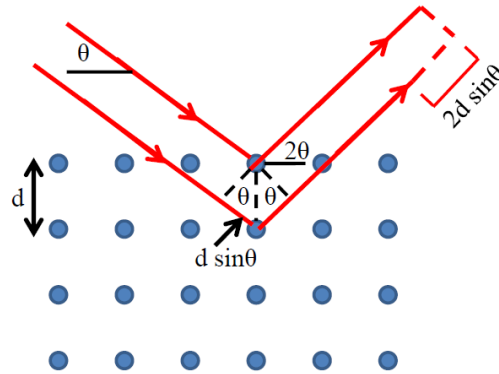


Figure 37. Diagram depicting the interaction of the incoming beam with the crystal lattice: d is the lattice spacing and θ is the angle between the incident rays and the surface of the crystal.

This means that X-rays incident on the crystal yield maxima of the diffracted radiation only at certain angles of incidence [89].

3.4 Model Compound Used In the Current Study

L-glutamic acid (Glu, $C_5H_9NO_4$) is a non-essential amino acid of molecular weight 147.13 g/mol and structure shown below (Figure 38).

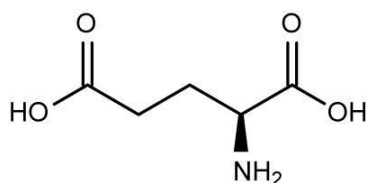


Figure 38. L-glutamic acid structure

This compound exists in two polymorphic forms – metastable alpha (α) and stable beta (β). Both of them can be characterised with space group $P2_12_12_1$, but they have different morphology. The stable form has needle-shape morphology, whereas the metastable form has prismatic-shape morphology (Figure 39) [62].

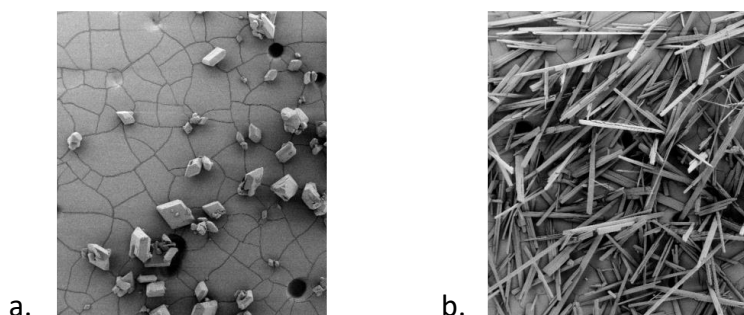


Figure 39. Scanning electron micrographs taken at 100x magnification of a) the metastable alpha (α) and b) the stable beta (β) form of LGA [62]

The aim of the work carried out by Srinivasan and co-workers [64] was to separate and control the nucleation of alpha and beta forms of L-glutamic acid (LGA). A laboratory-scale swift cooling crystallisation process was chosen for this purpose. Researchers found that induction time for the alpha form was significantly shorter than the beta form and less variation in the nucleation time occurs for alpha form. Based on this work it was possible to say that the alpha form nucleates at lower

temperatures (1-9°C), while the beta form nucleates at higher temperatures (27-34°C). The observations suggested that nucleation of the alpha and beta forms of L-glutamic acid is predominantly supersaturation dependent – at lower supersaturation only the beta form nucleates, whereas at higher supersaturation only nucleation of the alpha form is observed.

In the case of the downstream processing operations the alpha form is more preferable, because is easier to work with.

A previous study carried out by Borissova et al. [93] showed that the formation of one of the polymorphic forms was also cooling rate dependent - faster cooling rate favours the formation of the alpha form, when the slower cooling favoured the formation of the beta form. It can be explained as the alpha form nucleates first and over time crystals convert to the beta form by a solvent mediated phase transition.

Ni and colleagues [94] carried out experiments aiming to crystallise L-glutamic acid in a batch oscillatory baffled crystalliser (OBC). In a 1 L OBC L-glutamic acid solution (concentration of 45 g/L) was heated up to 80°C and then cooled down to 15°C. The main observations from their work were that they were not able to obtain alpha L-glutamic acid through elimination or reduction of the mixing intensity; the alpha form transformed to the beta form through the solution-mediation during the experiments; increasing of the cooling rate did not cause formation of the alpha form of L-glutamic acid; the only one way to produce the alpha form of L-glutamic acid was to use seeds to induce crystallisation.

Dharmayat et al. [95] studied polymorphic transformation of L-glutamic acid using on-line video microscopy and X-ray diffraction. The main purpose of their work was to compare these two techniques and assess their sensitivity. There is need of studying the mechanism of polymorphic transformation of alpha form to beta form of L-glutamic acid. As it has been mentioned before, the metastable (α) form tends to crystallise from the solution under rapid cooling conditions. The transformation of the alpha form to the stable beta (β) form takes place when the metastable crystals are placed in the saturated solution, at the temperature above 40°C. It is thought that

the solvent-mediated, monotropic transformation occurs as an effect of a dynamic process involving relevant dissolution of alpha form and growth of beta form [96]. During the experiments carried out by Dharmayat and colleagues [95] authors observed the solvent-mediated phase transformation of metastable (α) form to the stable (β) form using combined video-imaging and X-Ray diffraction. On-live video microscopy provided information based on the morphological changes of the two forms, while on-line XRPD tracked the structural differences arising from the solution. Cashell et al. [97] presented their work carried out in order to provide the evidence of the secondary nucleation of the beta form of L-glutamic acid on the surface of the metastable, alpha form. For this purpose, two analytical techniques were used – Scanning Electron Microscopy (SEM) and Raman spectroscopy. The alpha form of L-glutamic acid from was produced from L-glutamic monosodium salt monohydrate using 37% hydrochloric acid. After preparation via this method, the crystals were then recrystallized by heating to 80°C and cooling to 45°C. During the experiments, they observed that slow cooling rate with mixing during cooling favoured nucleation of the alpha L-glutamic acid form. Continuous agitation influenced the crystal size – crystals that were obtained were smaller in this case when compared to experiments without mixing. Increasing the cooling rate or resignation of mixing during cooling allows production of the beta form of L-glutamic acid. SEM images obtained during the crystallisation experiments provided an evidence of the beta form growing out of the surface of the alpha form (Figure 40).

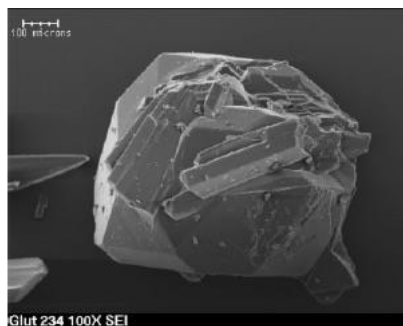


Figure 40. SEM image taken at magnification of 100x of the beta form crystals of L-glutamic acid growing out of the surface of the alpha form crystals [97]

Liang et al. [98] investigated the effect of the supersaturation on the polymorphic outcome and transformation rate of L-glutamic acid. Authors used FTIR to study the supersaturated solution in order to predict the final solid form crystallising out. The relationship between the supersaturation and polymorphic transformation was also analysed. Authors assumed that the polymorphic transformation is a result of the solution-mediated mechanism of transformation. It was proved that the crystallisation of the stable beta form is favourable at low supersaturation ($SS=0.3-0.7$), while for high supersaturation ($SS=1.0-3.0$) only alpha form was formed, which corresponds with what was reported by Srinivasan et al. [64].

In another paper, Liang et al. [99] studied the solution-mediated polymorphic transformation of L-glutamic acid using experimental and simulation approach. Experimental results revealed that the β form predominantly nucleates out from three surfaces of the α form with the corresponding probability of $(011) > (111) > (001)$. The computational simulation confirmed the experimental results, based on the adsorption energies values for these three surfaces – molecules are adsorbed most strongly on the (011) surface followed by (111) surface and the weakest adsorption energy was observed for the (001) surface. Additionally, the molecular simulation uncovers the fact, that all these surfaces have different ability to induce the polymorphic transformation – it was especially visible for the (011) surface, at which alpha L-glutamic acid was always transformed into beta L-glutamic acid.

Guggiero et al. [100] investigated another theory proposed as the explanation of the mechanism of alpha to beta polymorphic transformation of L-glutamic acid – a thermal solid-solid transformation. Using solid-state density functional theory coupled with a low-temperature single-crystal X-ray diffraction data it was possible to define the thermodynamic energetic parameters ruling the stabilization of the two polymorphs. It was revealed that the alpha form is favourable at low temperatures (<222 K), while the beta form becomes stable at ambient temperatures. In addition, Terahertz Spectroscopy was used to provide a data for quantification of polymorphic mixtures or crystal growth monitoring.

3.5 Materials and Methods

3.5.1 The Co-Flux Reactor Setup

Experiments were carried out using two different reactor setups. Setup A worked without the reactor temperature loop (Figure 41) and setup B worked with the reactor temperature loop (Figure 42). The idea of the temperature loop control was to stabilize the temperature in the jacket. The heat transfer fluid (HTF) was recirculated around the jacket and cold fluid was mixed in to change the jacket temperature. This gave a very even temperature distribution around the entire jacket.

The additional change made in setup B was real time measurement of the accumulation or heat shift in the process fluid trend measurements.

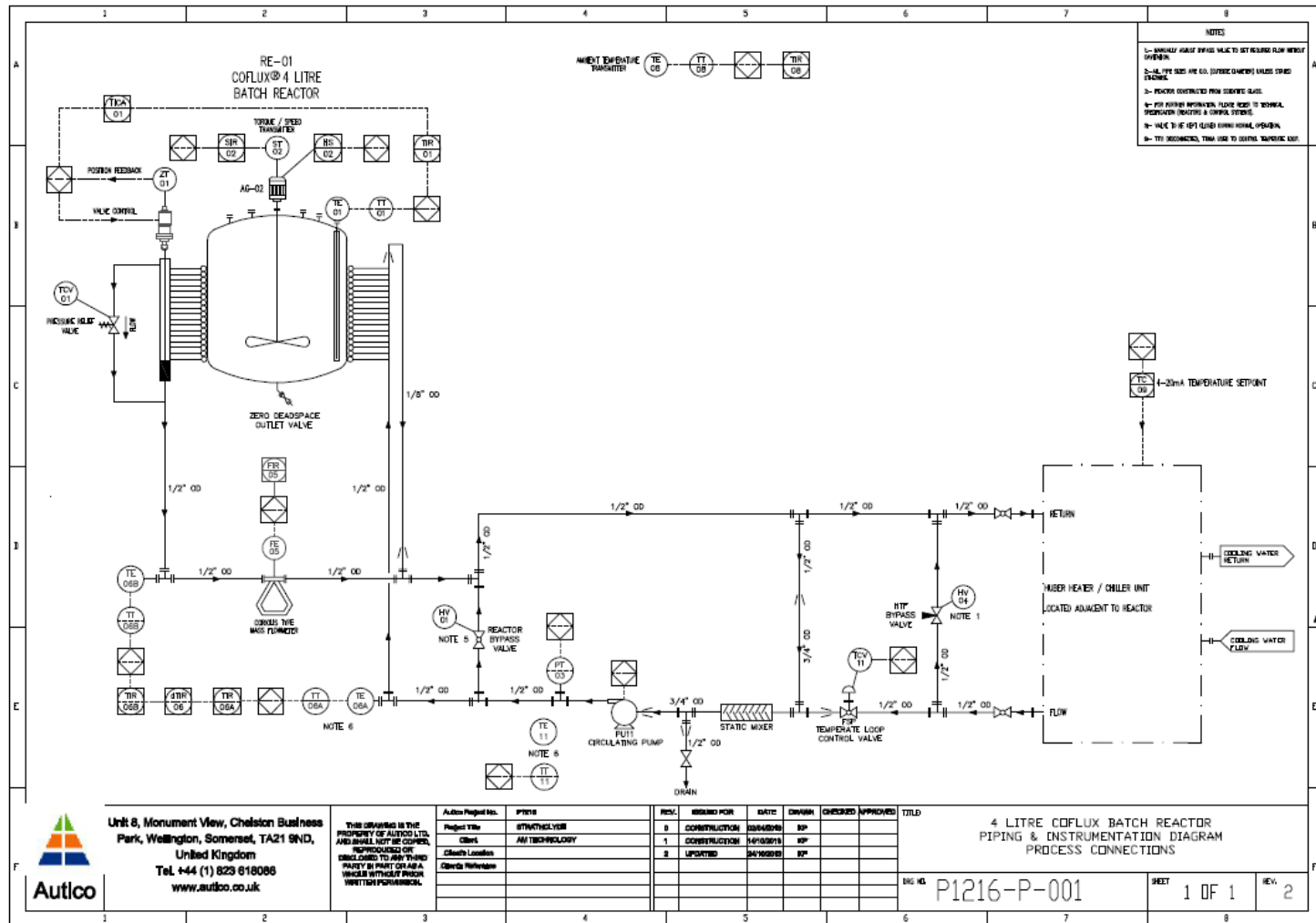


Figure 41. A technical drawing of the CoFlux reactor, setup A

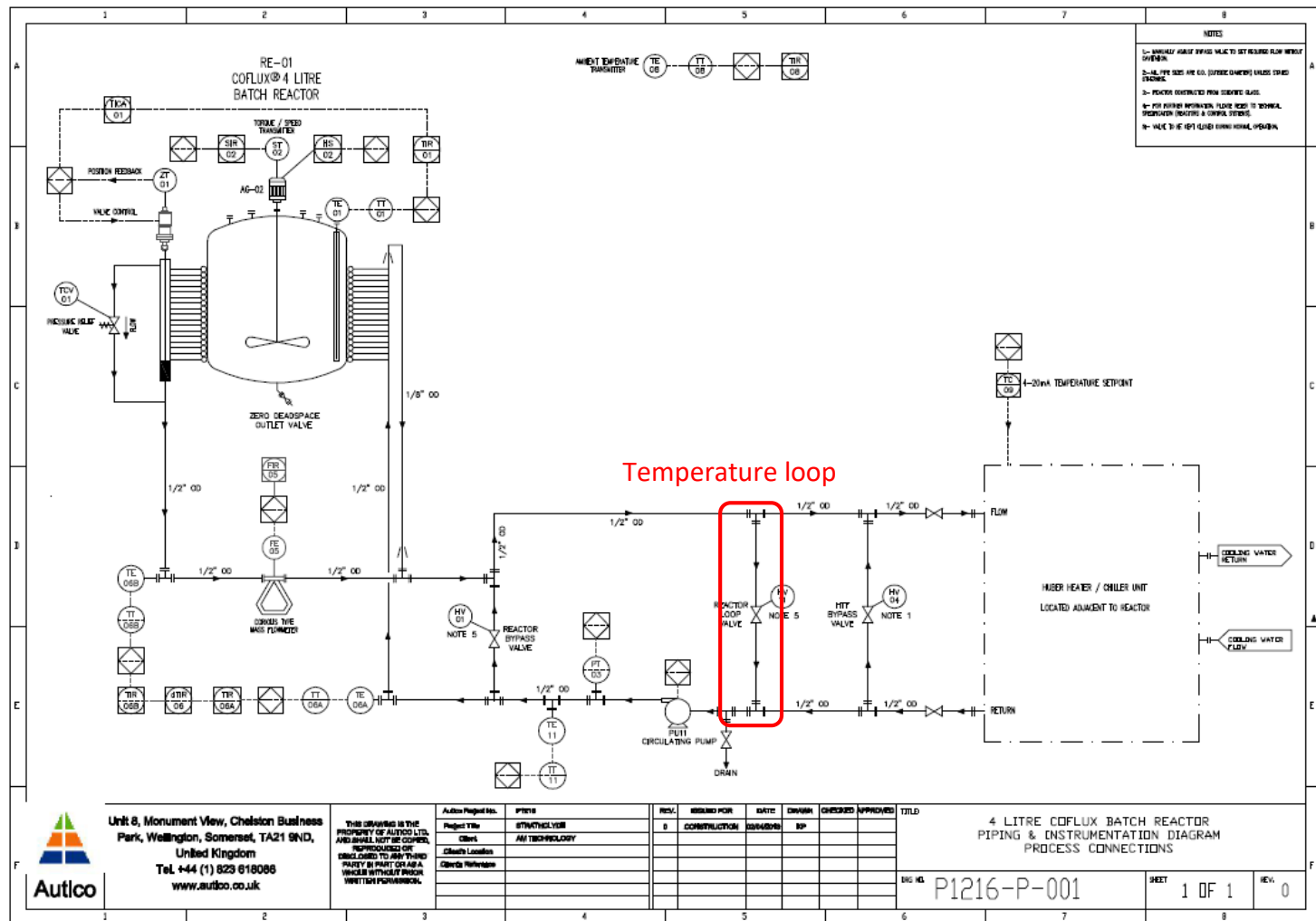


Figure 42. A technical drawing of the CoFlux reactor, setup B

Table 3 shows the experimental conditions which were used with setups A and B. The reactor consisted of a 4 L jacketed vessel fitted with a PTFE paddle impeller and the process temperature was controlled using a system of CoFlux valves. The concentration of L-glutamic acid ($\geq 98.5\%$, Sigma-Aldrich), temperature range for cooling and the agitator speed were changed across all of the experiments. The volume of the reactor content was maintained constant – at 3.4 L. The cooling rate was a major limitation of the CoFlux reactor used in the study and only rates between $0.30^{\circ}\text{C}/\text{min}$ and $0.90^{\circ}\text{C}/\text{min}$ could be set (cooling rates were strongly dependent on the reactor's cooling capacity and therefore it was almost impossible to achieve set cooling rates). These values are close to the rate of $0.5^{\circ}\text{C}/\text{min}$ used with the other reactors that have been investigated for crystallisation of LGA (see later comparison). The labelling of the experiments is as follows – C (CoFlux reactor). 1 – setup A, 2 – setup B. 1-12 (number of the experiment).

Table 3. Experimental conditions –for crystallisation of LGA in a CoFlux reactor, setup A and B

Experiment	Concentration [g/L]	Initial – final temperature [°C]	Cooling rate [°C/min]	Agitator speed [rpm]
C.1.1-2	45	80-20	0.75	150
C.1.3-4	45	80-20	0.75	250
C.1.5-6	15	65-10	0.75	150
C.1.7-8	15	65-10	0.75	250
C.1.9-10	30	75-15	0.75	150
C.1.11-12	30	75-15	0.75	250
C.2.1	45	80-20	0.35	250
C.2.2	45	80-25	0.41	250
C.2.3	45	80-25	0.51	250
C.2.4	45	80-20	0.56	250
C.2.5	45	80-20	0.73	250
C.2.6	45	80-20	0.85	250
C.2.7	45	80-20	0.70	150
C.2.8	45	80-20	0.90	150

Measurements using an *in-situ* Raman probe were made during selected experiments. The probe was inserted through one of the ports in the lid of the reactor. Due to the enclosed nature of the reactor (see Figure 25) it was not possible to make non-invasive Raman measurements as had been done by Laura Palmer [14] when monitoring crystallisation of LGA in other types of reactors. Details of the Raman measurements are given later on in this chapter.

3.5.2 Isolation and Characterisation of the Product

The product from the suspension was separated by filtration using a Buchner filtration system (Whatman 3 filter paper) and dried in an oven overnight at 50°C.

Crystals were analysed *off-line* using XRPD, laser diffraction (Malvern MasterSizer) and a Motic digital microscope.

3.5.3 The Stirred Tank Reactor and Oscillatory Baffled Reactor Setups

Complimentary crystallisation results were provided by Laura Palmer [14] for the crystallisation of LGA in a stirred tank reactor (STR) and a batch oscillatory baffled reactor (OBR). The STR consisted of a 1 L jacketed glass vessel fitted with a glass paddle impeller, where the jacket temperature was controlled using a circulating water bath. The concentration of L-glutamic acid, temperature range and the agitator speed were the variables changed during the experiments. The summary of the conditions used in a stirred tank reactor are shown in Table 4.

Table 4. Experimental conditions – stirred tank reactor

Experiment	Cooling rate [°C/min]	Concentration [g/L]	Final temperature [°C]	Agitator speed [rpm]
S1	0.5	45	40	200
S2	0.5	45	40	100
S3	0.5	15	10	200
S4	0.5	15	10	100

The oscillatory baffled reactor (OBR) consisted of a jacketed glass vessel holding a total volume of 1 L, where the jacket temperature was controlled using a circulating water bath. Mixing within the OBR was created using a baffled string consisting of two equally spaced PTFE orifice baffles supported by two 5 mm diameter steel rods. The string was connected to an electrical motor which provided oscillation frequencies of 1 and 3 Hz and amplitudes of 10 and 30 mm. The oscillation frequency, amplitude, cooling rates, temperature ranges and L-glutamic acid concentration were the variables changed during the experiments (Table 5) [14].

Table 5. Experimental conditions - OBR

Experiment	Cooling rate [°C/min]	Concentration [g/L]	Final temperature [°C]	Frequency [Hz]	Amplitude [mm]
O1	0.5	15	10	3	30
O2	0.5	45	40	1	10
O3	0.5	45	40	3	30
O4	0.5	15	10	1	10
O5	0.5	45	40	3	10
O6	0.5	45	40	1	30
O7	0.5	45	40	2	10
O8	0.5	15	10	2	10

3.5.4 Conditions for Analytical Measurements

3.5.4.1 Laser diffraction

Laser diffraction measurements were originally carried out using a Mastersizer 2000 (Malvern). Isopropanol was added to the Hydro2000SM cell. Powder samples were added to the cell until the laser obscuration reached 10 %. Isopropanol was used because of L-glutamic acid has poor solubility in this solvent. Because of equipment failure, measurements were repeated using a Malvern Mastersizer 3000. Isopropanol was used again as a dispersant for measurements carried out in a “wet” unit – Hydro3000MV. Measurements were also carried out in a dry unit – Aero S for comparison.

The laser diffraction measurements provided particle size information about the volume distribution, the $d(0,5)$, the $d(4,3)$ and the span were used. $D(0,5)$ is the size of the particle at which 50% of the sample is smaller and 50% is larger than this size; $d(4,3)$ is the volume mean diameter; span is the measurement of the width of the distribution. The smaller the span the narrower the distribution. The width is calculated from the $d(0,9)$ minus the $d(0,1)$ values divided by the $d(0,5)$.

3.5.4.2 X-Ray diffraction

Powder samples were placed on a 28 well plate supported by kapton film (7.5 μm thickness). Data were collected with a Bruker AXS D8Advance transmission

diffractometer equipped with Θ/Θ geometry, primary monochromatic radiation (Cu, $K_{\alpha 1}$), a Braun 1D position sensitive detector (PSD) and an automated multi-position x-y sample stage. Data were collected from 4-35° 2Θ with 0.015° 2Θ step size and 1 s step^{-1} count time.

3.5.4.3 Microscope images

Crystals were observed using a Motic Digital Microscope – with magnifications of 4x and 10x.

3.5.4.4 Raman measurements

Raman measurements were carried out using a Kaiser RXN1 spectrometer with an immersion probe. The spectrometer used a 785 nm class IIIb laser with a power setting of up to 350 mW and a charge coupled device (CCD) detector. The data acquisition software was Hologram. An instrument calibration was carried out using cyclohexane. The spectral data collected was processed in Matlab using a Savitsky-Golay first derivative filter which used a width of 51 data points and a second order polynomial.

3.6 Results

3.6.1 Setup A

Table 6 shows the results of the experiments carried out in the CoFlux reactor. Crystals were only produced in experiments C.1.1-4. The conditions chosen for experiments C1.5-12 did not yield crystallisation in the timeframe of the experiment.

Table 6. Results of the analysis of the obtained product in the CoFlux reactor

Experiment	Polymorph – XRD	d(0,5) [µm]	d(4.3) [µm]	Span [µm]	Yield [%]
C.1.1	α/β	482	518	1.9	79.4
C.1.2	α/β	531	540	1.2	73.4
C.1.3	α/β (α>β)	384	410	1.3	79.1
C.1.4	α/β (α>β)	306	332	1.4	76.4

The yield was calculated from the ratio of the amount of pure product recovered (g) to the amount of crude material used (g) (Equation 62).

Equation 62

$$\%yield = \frac{\text{the amount of pure product recovered (g)}}{\text{amount of crude material used (g)}} \times 100$$

From the table above it was clear that the stirrer speed had a significant impact on the crystal size. The mean particle size was lower at the higher impeller speed. This is due to an increase of particle attrition. Figure 43 shows the crystal size distribution for crystals obtained during experiments no. C.1.1– 4. The plots were obtained based on measurements made with the Mastersizer 2000.

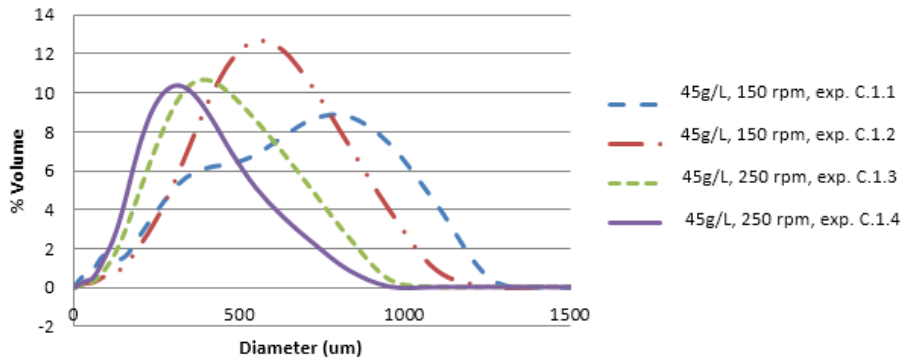


Figure 43. Crystal size distribution for L-glutamic acid crystals obtained during experiments no. C. 1.1 – 4, Mastersizer 2000

As can be observed in Figure 43 the particles obtained during experiments C.1.2-4 had a mono-modal distribution. The drying time for the crystals obtained in the experiment (C.1.1) was shorter than for the rest of the products, which could have resulted in some degree of aggregation which could explain the bi-modal size distribution (blue dashed plot) in Figure 43.

As mentioned in the introduction, the CoFlux reactor system was able to measure the enthalpy, process power and temperature trends. Figure 44 shows typical profiles for each parameter obtained during the cooling crystallisation of LGA (experiment C.1.4).

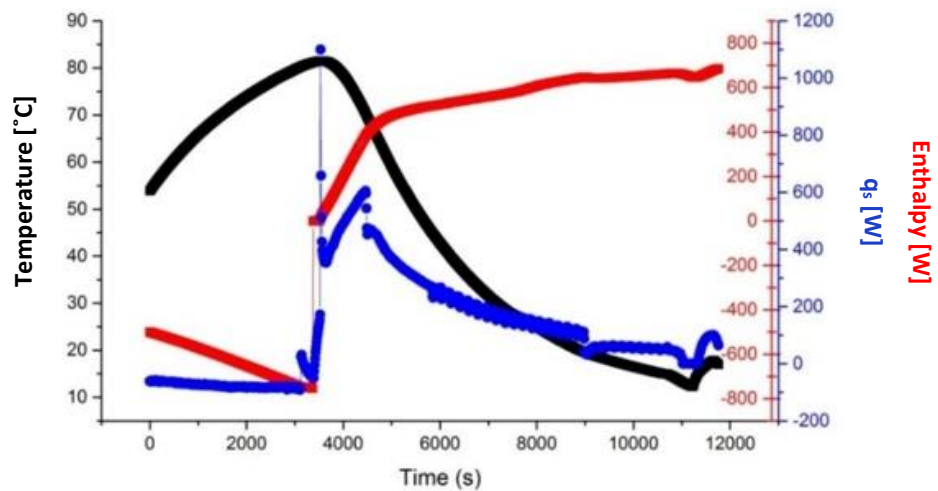


Figure 44. Enthalpy (red line) measured in Watts [W], temperature (black line) measured in Celsius [°C] and process power trend (blue line) measured in Watts [W] for experiment no. C.1. 4

The reactor setup allowed to record the wall temperature as well as reactor temperature throughout the experiment. An example of the relationship between wall and reactor temperature (for experiment C.1.3) is depicted below in Figure 45.

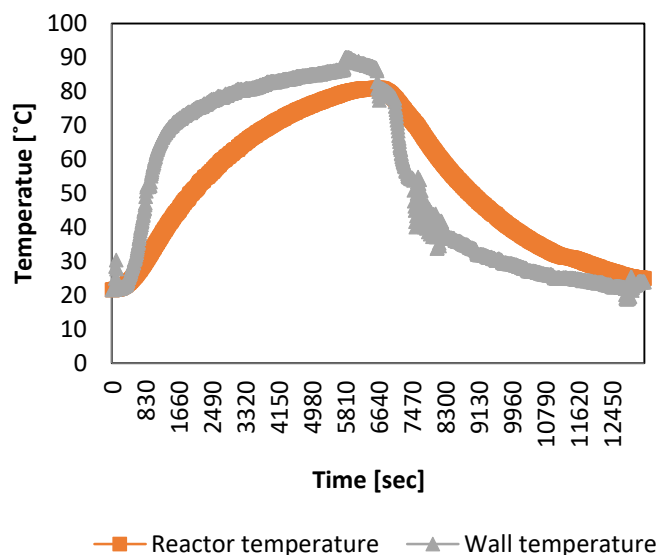


Figure 45. An example of the relationship between wall and reactor temperature during crystallisation of L-glutamic acid (experiment C.1.3.)

One aim of the study was to assess if enthalpy measurement was an advantage of the CoFlux reactor for monitoring the crystallisation of LGA. As can be seen in Figure 44, a significant change in the process power was observed at around 4500 s (65°C) and this peak was suspected as being indicative nucleation. However, based on the solubility curve for L-glutamic acid, this temperature was considered to be too high for the beginning of the nucleation process. Based on information found in [101] the heat of crystallisation is the same as the heat of solution. According to the data in the literature, the heat of solution for organic compounds is between 5 and 20 kJ/mol. Based on this information the power of crystallisation for L-glutamic acid was calculated (assuming the heat of crystallisation was 10 kJ/mol). The equations (Equation 63 and Equation 64) used to calculate the heat of crystallisation are shown below:

Equation 63

$$Q = n * \Delta H [kJ]$$

Equation 64

$$Q[W] = \frac{Q[kJ] * 1000}{t[s]}$$

Where Q is the heat in kilojoules, n is the number of moles, t is time in seconds, and ΔH is the heat of crystallisation in kilojoules per mol. For the calculations it was assumed: the yield of crystallisation was 75%, the time of the process was 5700 s (the time of the process was calculated as a time of cooling from 80°C to 20°C), the volume of the process was 3.4L and concentration of LGA was 45 g/L. The calculations are shown below (Equation 65):

Equation 65

$$n_{LGA} = \frac{153}{147.13} \left[\frac{g}{\frac{g}{mol}} \right] = 1.04 \text{ mol} \quad \text{yield} = 75\%$$
$$n'_{LGA} = 0.75 * 1.04[mol] = 0.78 \text{ mol}$$

$$Q = 10 * 0.78 = 7.8 \text{ kJ in total} \quad \text{time} = 5700 \text{ s}$$

$$Q = \frac{7.8 * 1000}{5700} = 1.4W$$

Based on this calculation it is possible to say that for LGA the heat of crystallisation (power) is too low to be detected using calorimetry in the CoFlux system. To make sure that the broad peak at 65°C was not connected with the crystallisation process, an immersion Raman probe was deployed to obtain spectral measurements. The measurements started while the LGA particles dispensed in the reactor were

dissolved as the temperature was increased to 80°C. Figure 46 shows the Raman spectra for the alpha, beta and solute form of L-glutamic acid.

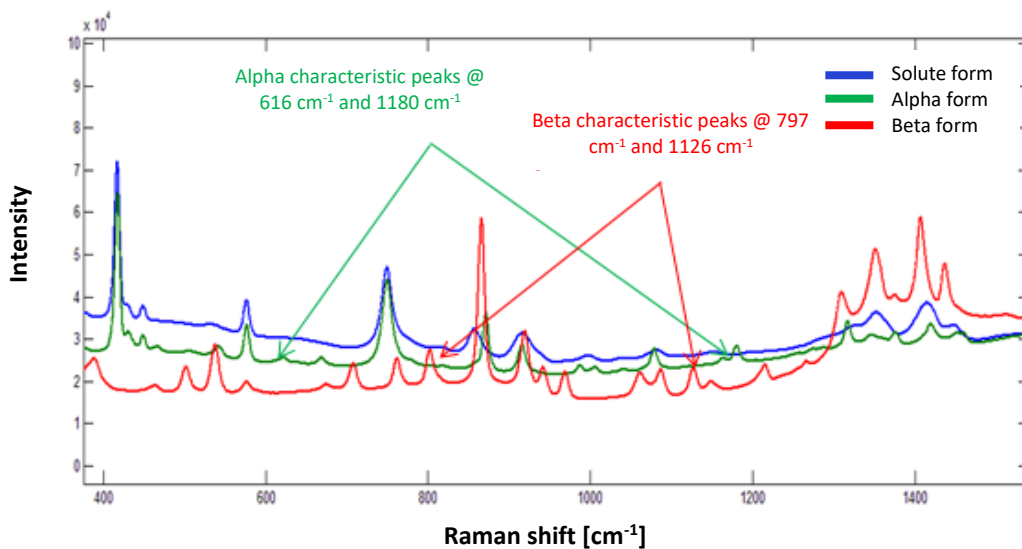


Figure 46. The Raman spectra for alpha (green), beta(red) and solute(blue) form of L-glutamic acid

In Figure 47 real time Raman data is shown. It can be observed at the start of dissolution that the spectra was the beta form (red plot), the spectrum once all the particles had dissolved had peaks that overlapped the particle spectra (blue plot), and the spectrum from the actual crystallisation phase was mainly alpha.

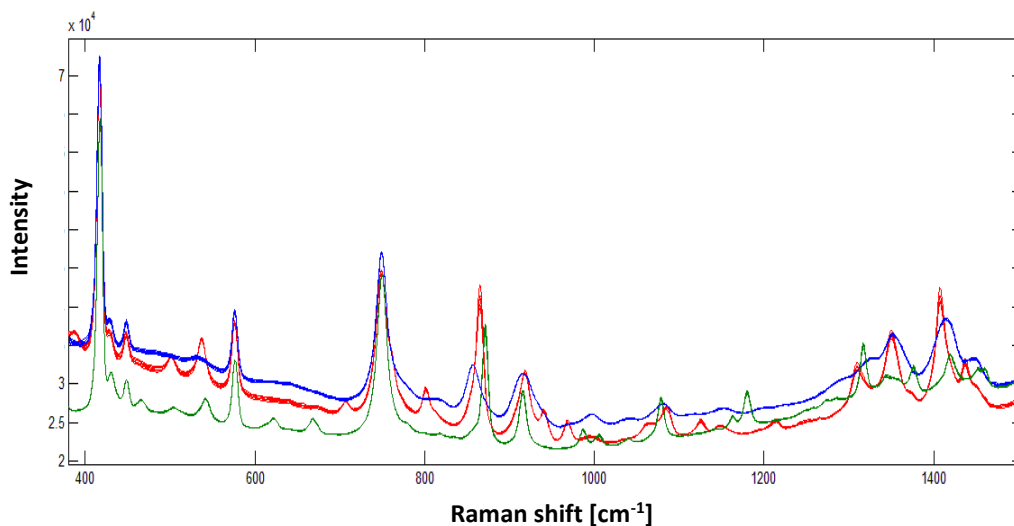


Figure 47. Raman real-time measured spectra of L-glutamic acid for dissolution stage (red plot), fully dissolved stage (blue plot) and crystallisation stage (green plot) (exp. C.1.4)

As mentioned above, the solute form peaks overlapped the particle spectra – for example the characteristic peak for the beta form (at 797 cm^{-1}) was slightly overlapped by a solute peak at the same wavenumber. To highlight the differences between the early stages of dissolution, the fully dissolved state and the plateau of crystallisation the 1st derivative of Raman spectra are shown below (Figure 48).

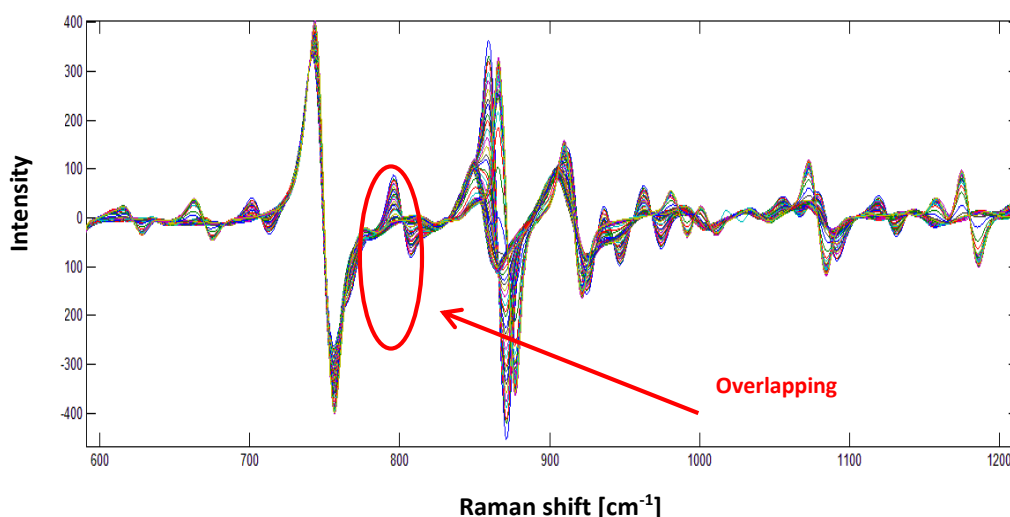


Figure 48. The 1st derivative of Raman spectra of L-glutamic acid (exp. C.1.4)

Based on the Raman data (1st derivative) the dissolution and crystallisation profiles were obtained for experiment C.1.4. The characteristic peaks for the alpha form (peak at 616 cm⁻¹) and beta form (peak at 797 cm⁻¹) were plotted over time (Figure 49). A minus value for the beta form is the result of overlap by the solute form peak.

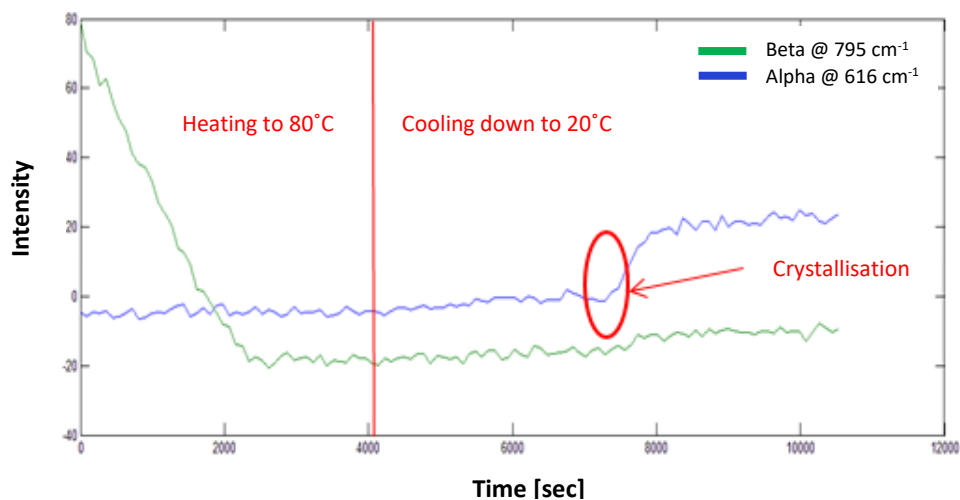


Figure 49. Dissolution and crystallisation profile (exp C.1.4) of L-glutamic acid based on peak @ 616 cm⁻¹ (blue) for alpha form and peak @ 795 cm⁻¹ (green) for beta form based on the 1st derivative of the Raman spectra.

Figure 50 shows the dissolution and crystallisation profile of L-glutamic acid for the conditions listed in Table 3, experiment C.1.4, based on the 1st derivative Raman spectra. In this figure the solute peak was also included.

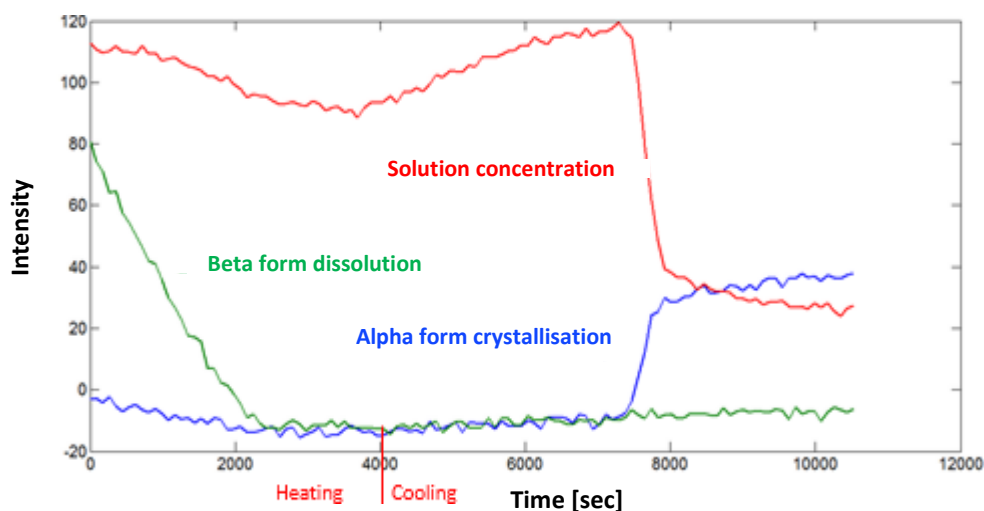


Figure 50. Dissolution and crystallisation profile of L-glutamic acid from experiment C.1.4 based on the 1st derivative spectra for the alpha form at 663 cm⁻¹ (blue plot), for the beta form at 797 cm⁻¹ (green plot) and for the solution at 872 cm⁻¹ (red plot).

From the Raman data it was clear that crystallisation was taking place around 7500 s which corresponds to 35°C. The implementation of the Raman probe suggested that the enthalpy measurements were not a viable option to monitor or control the crystallisation of LGA in the CoFlux reactor. The Raman probe was also implemented to confirm the polymorphic form of the obtained crystals. Figure 50 shows that the raw material was pure beta form of L-glutamic acid while the obtained crystals were a mixture of both the alpha and beta form, however the decrease of signal is more significant for the alpha form than for beta. A dissolution of the beta form in the Raman data (decreasing of the signal) do not correspond clearly with the solute signal – the solute signal does not increase when the beta form signal decreases, which was expected. It was caused by overlapping of the Raman spectra of the solute and the beta form – if the solute peak was free from overlap then the intensity would increase during dissolution, reach a maximum when all the LGA was dissolved and then decrease again as the alpha form precipitated. However, for the conditions used during these experiments it was impossible to find the solute peak without overlap. Analogous analysis was carried out for two different characteristic peaks – the peak at 1180 cm⁻¹ for the alpha form and peak at 1126 cm⁻¹ for the beta form.

Figure 51 depicts the changes in the intensity of the alpha and beta form characteristic peaks (mentioned above) over time.

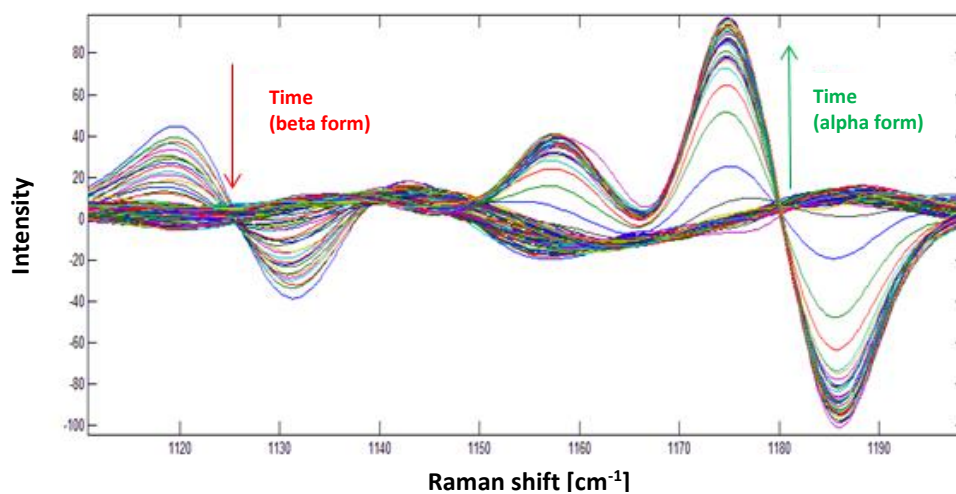


Figure 51. The 1st derivative of the Raman spectra of L-glutamic acid, showing changes in the intensities of the alpha and beta peaks over time

Figure 52 shows the dissolution and crystallisation profile based on the peaks discussed.

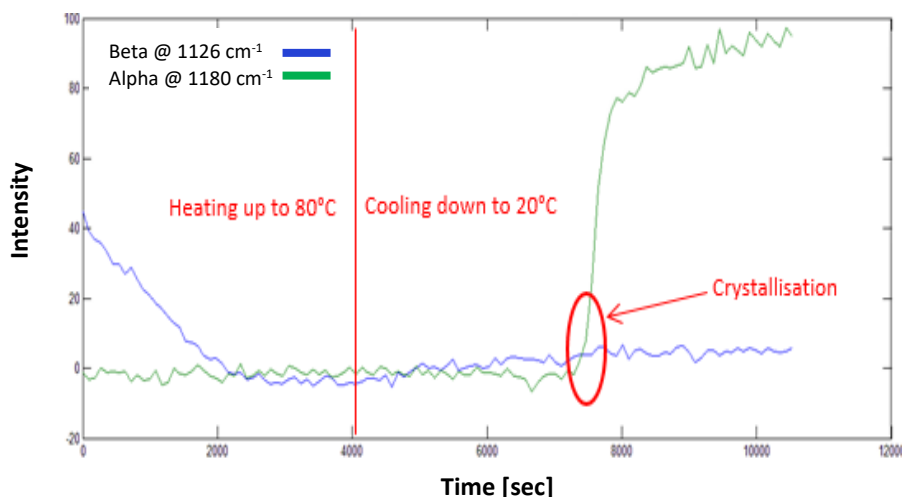


Figure 52. Raman dissolution and crystallisation profile (exp C.1.4) of L-glutamic acid, based on the changes in the intensities of alpha (at 1180 cm^{-1}) – green plot and beta (at 1126 cm^{-1}) – blue plot characteristic peaks.

The most reasonable way to plot the intensity of the characteristic peaks over time was to choose the peak at 1180 cm^{-1} for the alpha form and peak at 1126 cm^{-1} for the beta form due to the fact that they are free from overlap at these wavenumbers.

Using invasive measurements was not ideal as there was the risk that crystals may grow on the probe and fouling will occur. During experiments crystal growth was observed on the probe, which meant that the results obtained were not credible. There was a danger that the plateau in the Raman signals observed in the figures with trend plots was due to material on the probe end and not truly indicative of the process status.

Very similar conclusions can be reached after analysing the X-Ray pattern data of the particles from experiment C.1.4 (Figure 53). The X-Ray pattern shows that the product obtained is a mixture of both polymorphic forms of L-glutamic acid – alpha and beta. However, the intensities of the alpha form peaks are significantly higher than for the beta form, which confirms observation based on the Raman plots that the crystals obtained were mainly the alpha form.

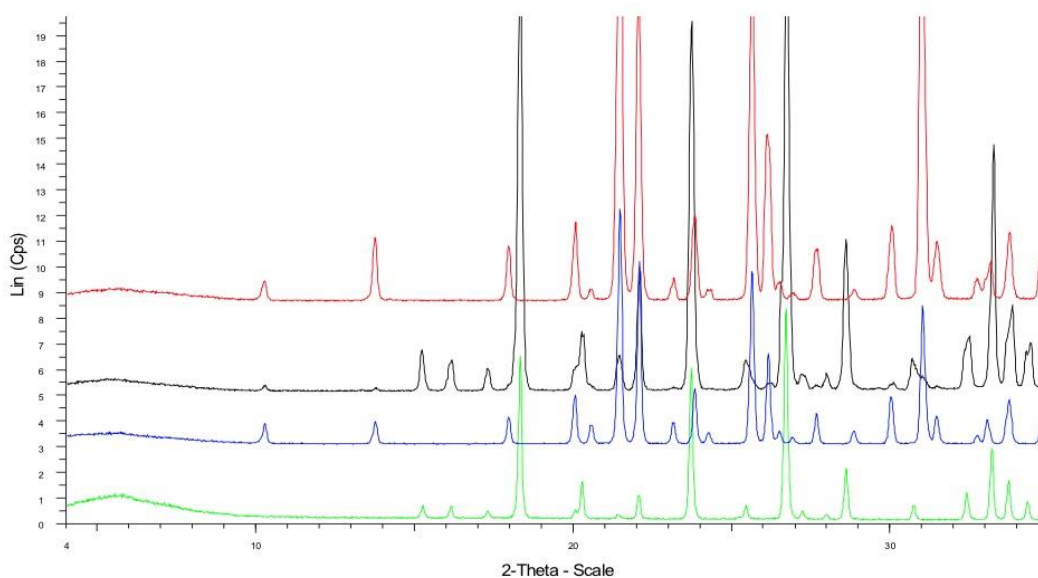


Figure 53. XRPD pattern for the raw material (red plot), crystallisation product (black plot), alpha (green plot) and beta (blue plot) form of L-glutamic acid (experiment no. C.1.4)

The crystals obtained in the experiment no. C.1.4 were also analysed using the microscope. Figure 54 shows a microscope image for those crystals. The microscope image also confirmed that the crystals obtained were predominantly the alpha form.

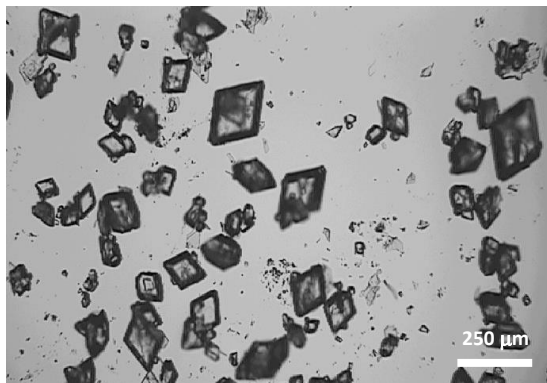


Figure 54. Microscope image of prismatic shape of the alpha crystals obtained during the experiment C.1.4 – magnification 4x.

3.6.2 Setup B

Table 7 shows the results of the experiments carried out in the CoFlux reactor, when operated under slightly different conditions, named here as setup B. In this case particle sizing analysis was carried out using a Malvern Mastersizer 3000, Hydro3000MV unit.

Table 7. Results of the analysis of the obtained product in the CoFlux reactor, setup B

Experiment	Cooling rate [°C/min]	Polymorph - XRD	d(0,5) [µm]	d(4.3) [µm]	Span [µm]	Yield [%]
C.2.1	0.35	α	241	248	1.0	64.2
C.2.2	0.41	α/β	245	268	1.7	67.3
C.2.3	0.51	α/β (α>β)	368	379	1.2	71.0
C.2.4	0.56	α/β	242	245	1.2	76.1
C.2.5	0.73	α	264	273	1.0	75.7
C.2.6	0.85	α	293	320	1.4	73.7
C.2.7	0.90	α	331	352	1.2	68.4
C.2.8	0.80	α	333	364	1.4	64.6

Based on the results shown in Table 7, it is possible to determine that the cooling rate does not significantly affect the particle size. The higher cooling rates of 0.5 – 0.85°C/min gave a higher yield of crystals than for 0.35°C/min and 0.41°C/min, however the differences are not substantial. For the experiments C.2.7 and C.2.8, where the cooling rate was 0.9°C/min and 0.8°C/min the yield was lower, however these results can be explained by the mixing speed – for these two experiments the mixing speed was lower – 150 rpm, than for the rest of the experiments – 250 rpm. The main advantage of the applied temperature loop is, that using the slow cooling rate (0.35°C/min) only produces the alpha form of L-glutamic acid – Figure 55 shows a XRPD pattern to confirm the microscope observation (Figure 56). For the higher cooling rate a mixture of alpha and beta crystals was observed. However, this observation would have to be confirmed by repeating the experiment. To explain this phenomenon, it would be necessary to implement analytical tools, like Focused Beam

Reflectance Measurement (FBRM), to detect the nucleation point and to describe the metastable zone for the system.

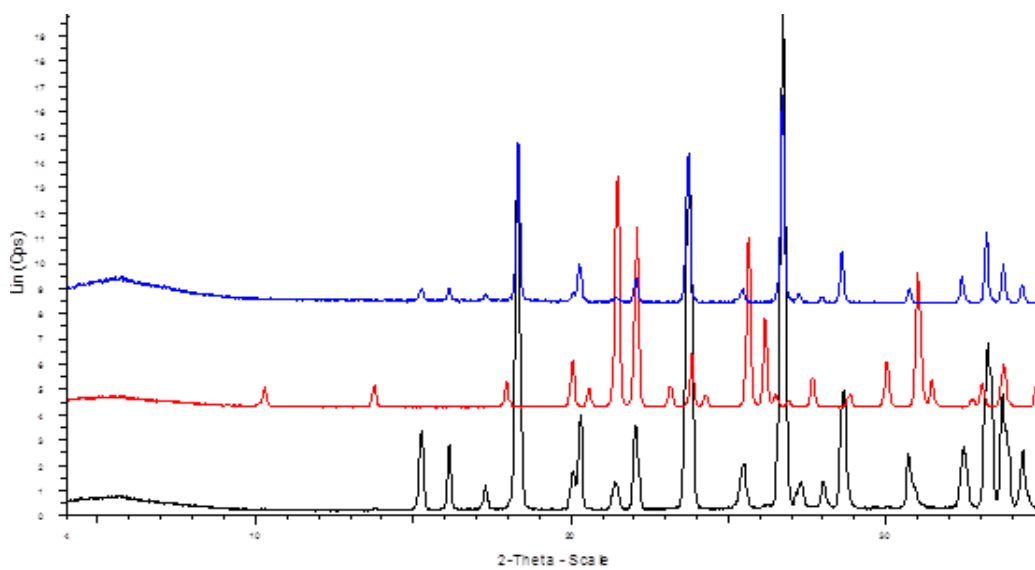


Figure 55. XRPD pattern for crystallisation product (black plot), alpha (blue plot) and beta (red plot) form of L-glutamic acid (experiment no. C.2.3)

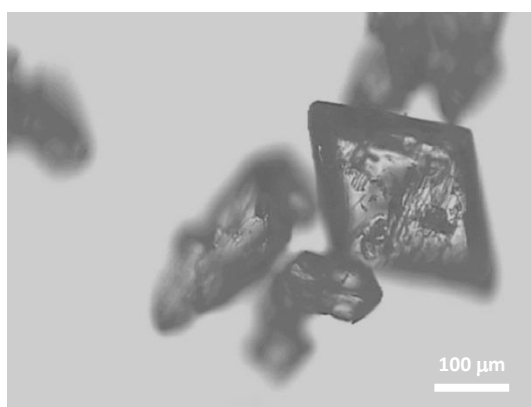


Figure 56. Microscope image – magnification 10x, exp. C.2.1

Table 8 shows the results obtained during measurements of the particle size carried out in the two different Malvern MasterSizer units.

Table 8. Comparison of the results obtained during measurements of the particle size carried out in the two different Malvern MasterSizer units

Sample	Dry Unit - Aero S			Wet Unit – Hydro3000MV		
	d(0,5) [μm]	d(4.3) [μm]	Span [μm]	d(0,5) [μm]	d(4.3) [μm]	Span [μm]
C.1.1	N/A	N/A	N/A	487	484	1.49
C.1.2	359	394	1.57	506	527	1.28
C.1.3	262	287	1.56	323	337	1.18
C.1.4	242	266	1.58	258	269	1.17
C.2.1	224	243	1.59	241	248	0.97
C.2.2	128	142	2.02	245	268	1.75
C.2.3	126	143	2.14	368	379	1.17

For every sample the size of particles is smaller when measured in the dry unit than in the wet unit. This may be a result of the way the dry unit operates – the small ball bearing, which is supposed to move the powder through the cell may cause breakage of the particles. For the wet unit a narrower size distribution (as indicated by the span) is observed. A possible explanation is that the fine particles dissolve in the dispersant and it affects the particle size distribution.

Figure 57 shows the crystal size distribution for crystals obtained during the experiments no.C.2.6-C.2.8. The plots were obtained based on measurements made with Mastersizer 3000.

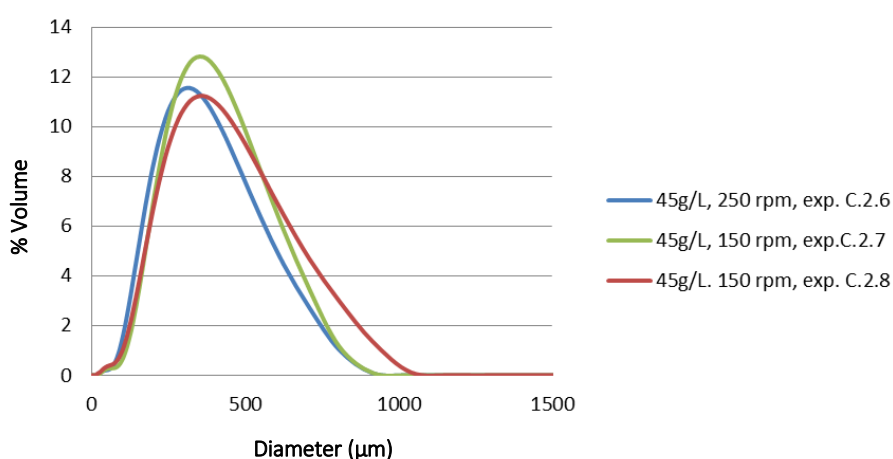


Figure 57. Crystal size distribution for L-glutamic acid crystals obtained during experiments no. C.2.6 – 8, Mastersizer 3000

As mentioned in the description of the experimental conditions, the new CoFlux reactor system (setup B) was able to measure the accumulation or heat shift in the process fluid trend. The accumulation or heat shift in the process fluid trends measurements were a more sensitive way to measure the process power changes. The aim of implementing this kind of measurement was to assess if calorimetry could be a useful method for monitoring and controlling crystallisation.

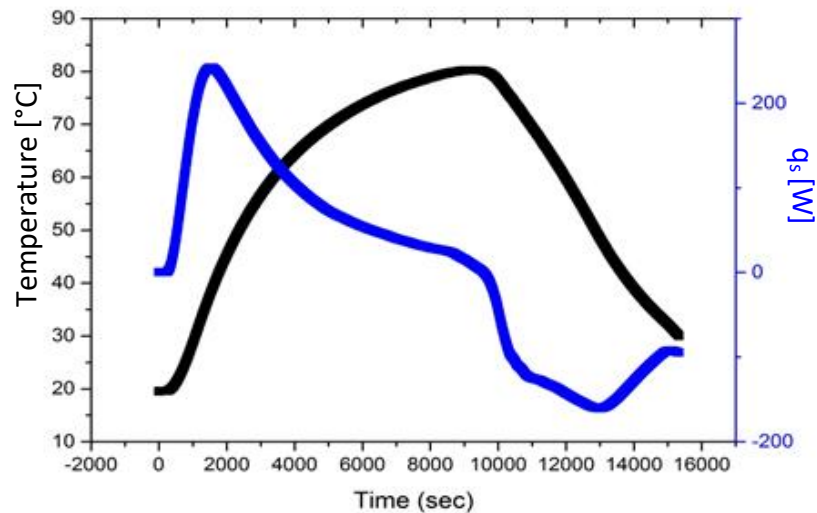


Figure 58. A real time accumulation or heat shift (q_s) in the process fluid [W] (blue plot) and temperature [°C] trend (black plot) for dissolution and crystallisation of L-glutamic acid, exp. C.2.2, cooling rate 0.41°C/min

In Figure 58 two substantial changes are observed - firstly the increase of the signal during the dissolution stage and then the decrease of the signal during cooling. These two changes may indicate when the LGA was being dissolved and when the LGA crystallisation started. To prove these observations, the accumulation or heat shift in the process fluid measurements were carried out for water. A plot for this investigation is shown in Figure 59.

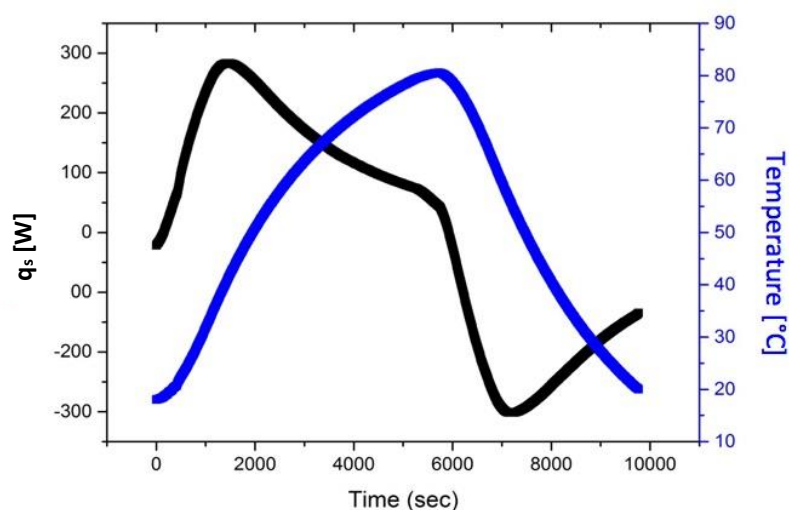


Figure 59. A real time accumulation or heat shift (q_s) in the process fluid [W] (black plot) and temperature trend for heating and cooling water (blue plot), cooling rate $0.75^\circ\text{C}/\text{min}$

Accumulation or heat shift (q_s) in the process fluid trend for heating and cooling water had a very similar shape to the q_s in the process fluid trend for the dissolution and crystallisation of L-glutamic acid. However, a part of q_s in the process fluid trend which corresponds to the cooling profile was different for crystallisation – more disturbances were observed, but this may be connected with the different cooling rates applied for experiment C.2.2 and the experiment with water.

Figure 60 shows plots obtained during the six different experiments. It is possible to say that all plots show the same tendency – an increase of the signal during the dissolution stage and a decrease of the signal when cooling was applied. In Figure 60 C, D and F a red circle indicates the possible signs of crystallisation, however the plots do not seem to be reproducible. The slight plateau observed in Figure 60 C, D and F is not observed in the remaining plots, which makes it almost impossible to decide if these are indicators of crystallisation.

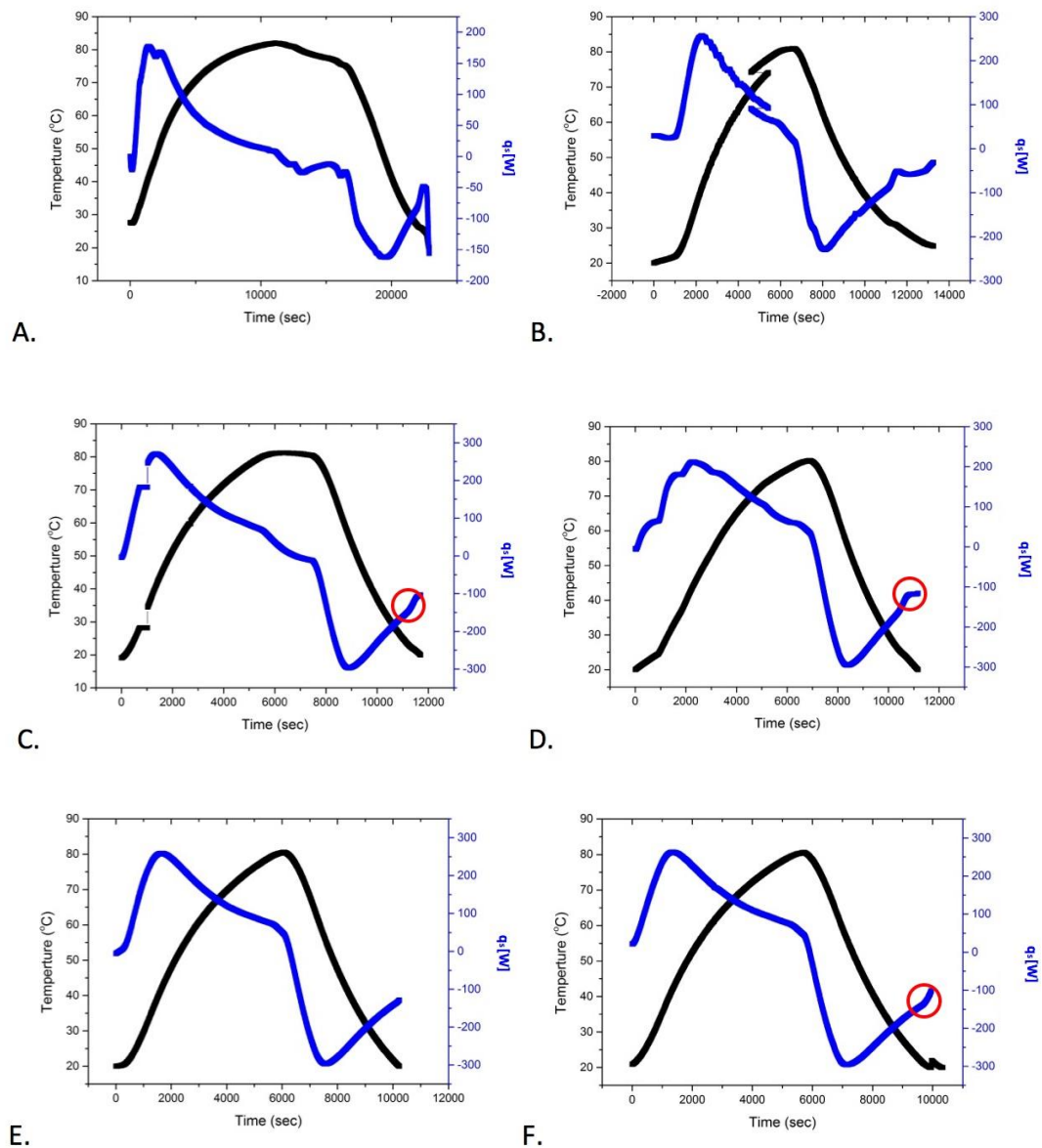


Figure 60. A real time accumulation or heat shift in the process fluid – q_s (blue plots) and temperature trend (black plots) for dissolution and crystallisation of L-glutamic acid, A - exp. C.2.1, B - exp. C.2.3, C - exp. C.2.5, D - exp. C.2.6, E - exp. C.2.7, F - exp. C.2.8

Raman measurements were implemented during experiment C.2.3, where cooling was applied at 6640 seconds. The same type of analysis was carried out for this experiment as for experiment C.1.4.

b.

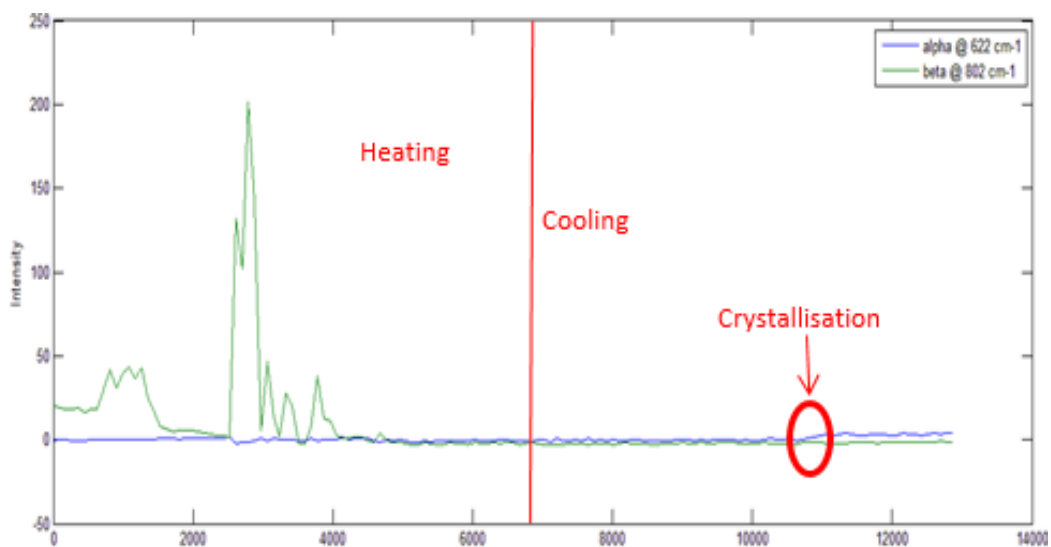


Figure 61a shows the dissolution and crystallisation profile based on the peak at 1181 cm^{-1} for the alpha form and the peak at 1126 cm^{-1} for the beta form. For comparison Figure 61b shows the dissolution and crystallisation profiles (experiment C.2.3) based on the alpha peak at 622 cm^{-1} and the beta peak at 802 cm^{-1} are shown.

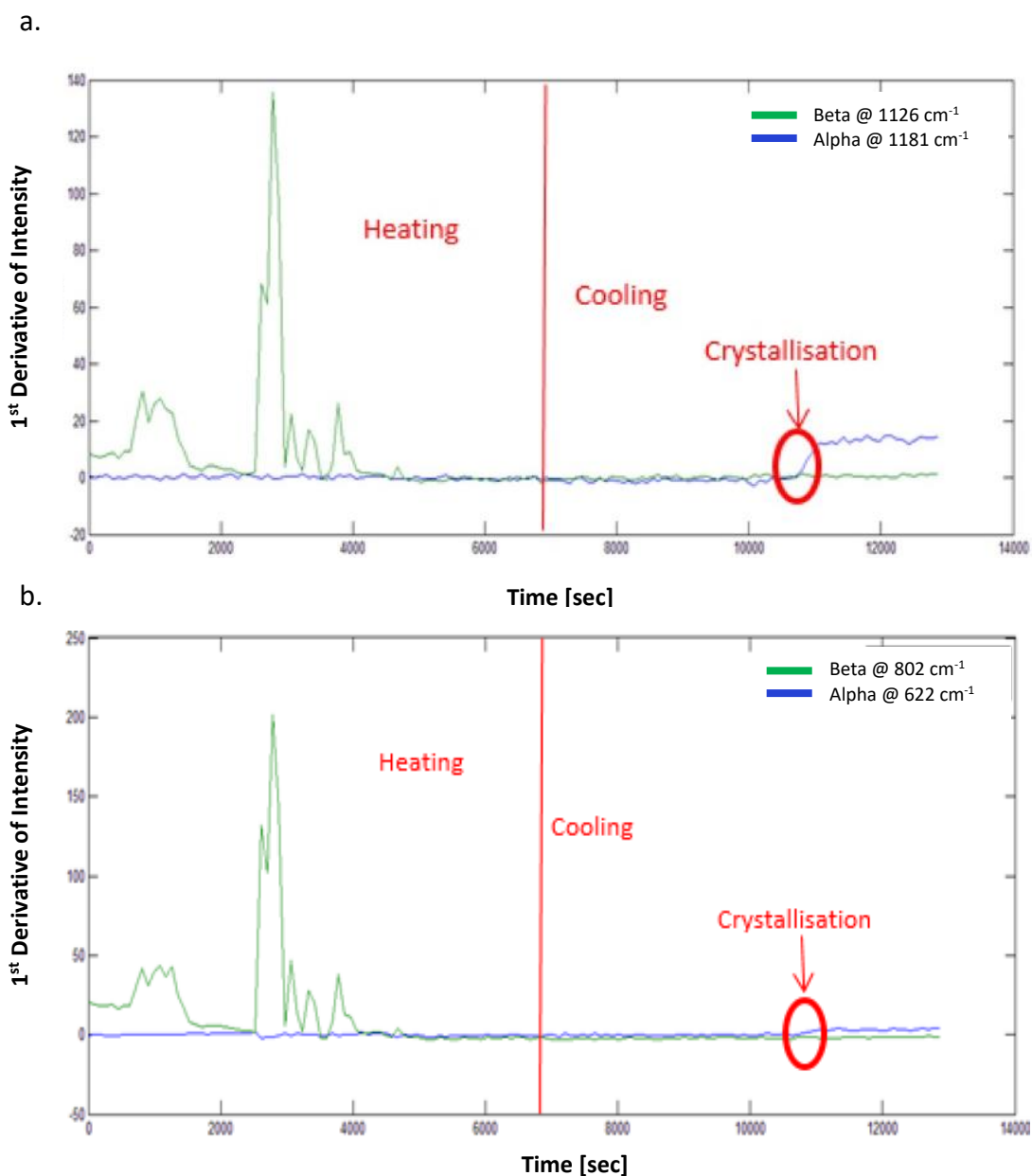


Figure 61. a) Raman dissolution and crystallisation profile (exp C.2.3) of L-glutamic acid, based on the 1st derivative of the intensity changes of alpha characteristic peak at 1181 cm^{-1} (blue plot) and beta characteristic peak at 1126 cm^{-1} (green plot) and b) Raman dissolution and crystallisation profile (exp C.2.3) of the same compound based on the 1st derivative of the intensity changes of alpha characteristic peak at 622 cm^{-1} (blue plot) and beta characteristic peak at 802 cm^{-1} (green plot).

Figure 62a and Figure 62b show only the crystallisation profile for the experiment C.2.3.

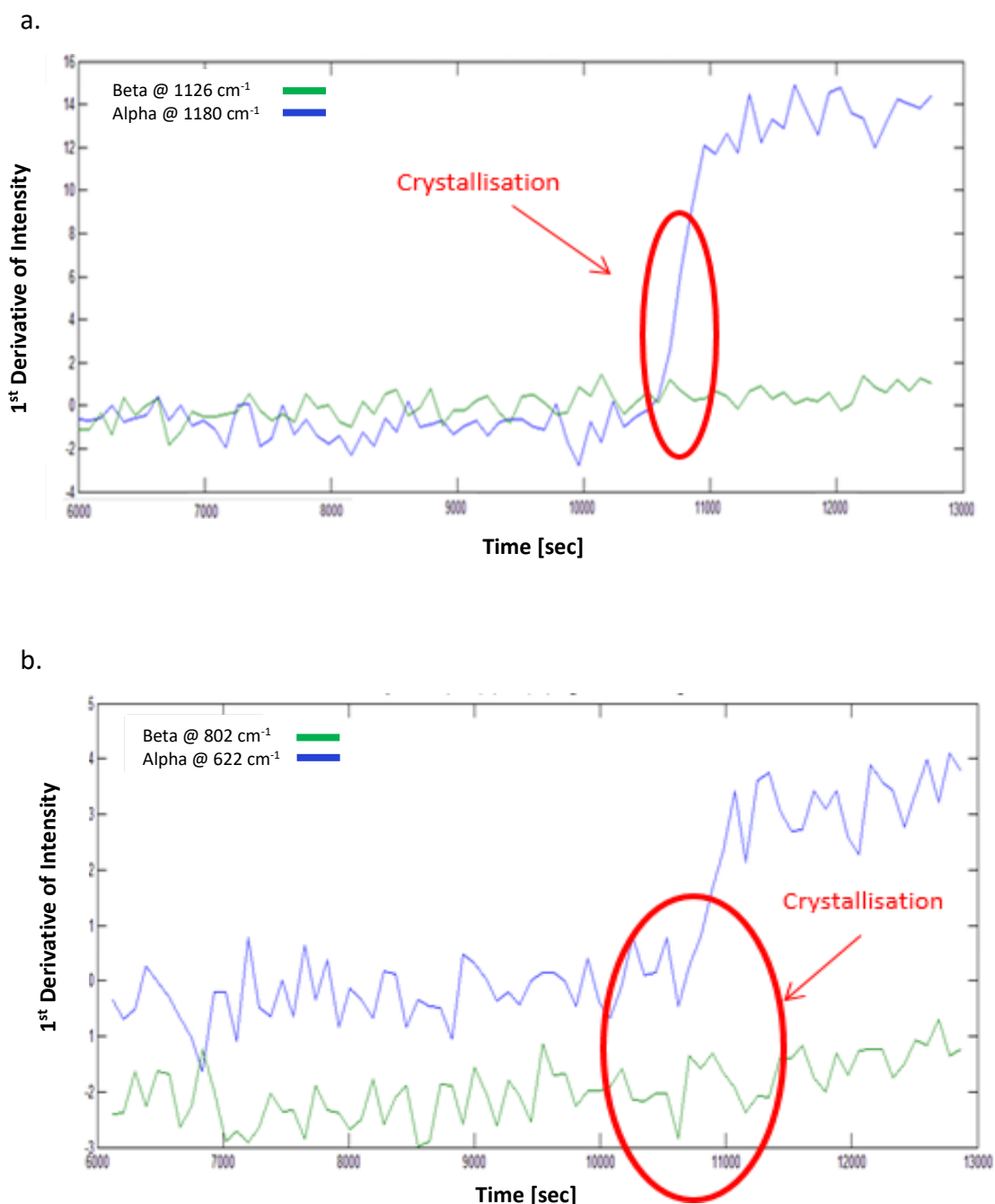


Figure 62. a) Zoomed in Raman crystallisation profile (exp C.2.3) based on the 1st derivative of the intensity changes of alpha characteristic peak at 1181 cm^{-1} (blue plot) and beta characteristic peak at 1126 cm^{-1} (green plot) and b) Zoomed in Raman crystallisation profile (exp C.2.3) based on the 1st derivative of the intensity changes of alpha characteristic peak at 622 cm^{-1} (blue plot) and beta characteristic peak at 802 cm^{-1} (green plot).

Again, as was observed during previous analyses, the peak at 1180 cm^{-1} for the alpha form and the peak at 1126 cm^{-1} for beta form are best for monitoring the crystallisation of LGA in real time. The most significant changes were observed for these two peaks. However, comparison of the data obtained for experiment C.1.4 and C.2.3 showed that for setup A (C.1.4) the changes in Raman intensity were more significant. The yield of the crystals in C.1.4 was 76.42%, slightly higher than that of experiment C.2.3 – 71.04%, however, the difference was not great enough to explain the decrease in the Raman intensity of alpha LGA at 1181 cm^{-1} from 100 to 15. This decrease in the peak intensity may have been caused by a reduction in the output intensity of the laser radiation between the two experiments or a change in the position at which the measurements were made within the reactor contents, which may not be homogenous.

Based on Raman results the crystallisation was taking place at 10500 seconds (Figure 62b). Figure 63 shows enthalpy, temperature and accumulation or heat shift (q_s) in the process fluid trend for experiment no. C.2.3, where 10500 seconds corresponds to 35°C . The accumulation or heat shift (q_s) in the process fluid power trend did not show any significant changes at 10500 seconds, which meant that calorimetry measurements were not useful for monitoring the crystallisation of LGA in the CoFlux reactor.

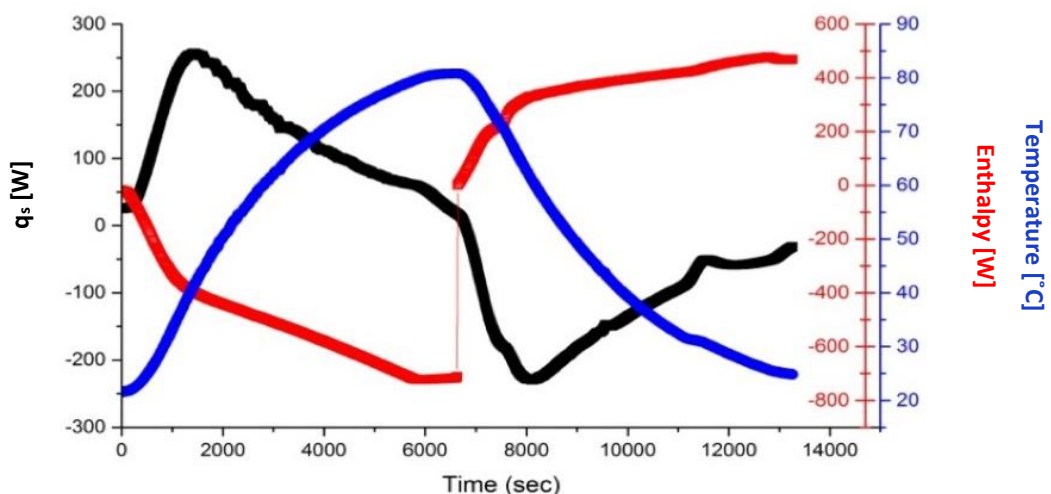


Figure 63. Enthalpy (red plot), temperature (blue plot) and accumulation or heat shift (q_s) in the process fluid [W] (black plot) trend for experiment no. C.2.3

The Raman measurements were again used for experiment no. C.2.8. During this experiment the cooling started at 6100 seconds. As shown before, the best way to monitor the crystallisation of LGA in real time, was to use the peak at 1180 cm^{-1} for the alpha form and the peak at 1126 cm^{-1} for the beta form, and plot for experiment C.2.8 is shown in Figure 64.

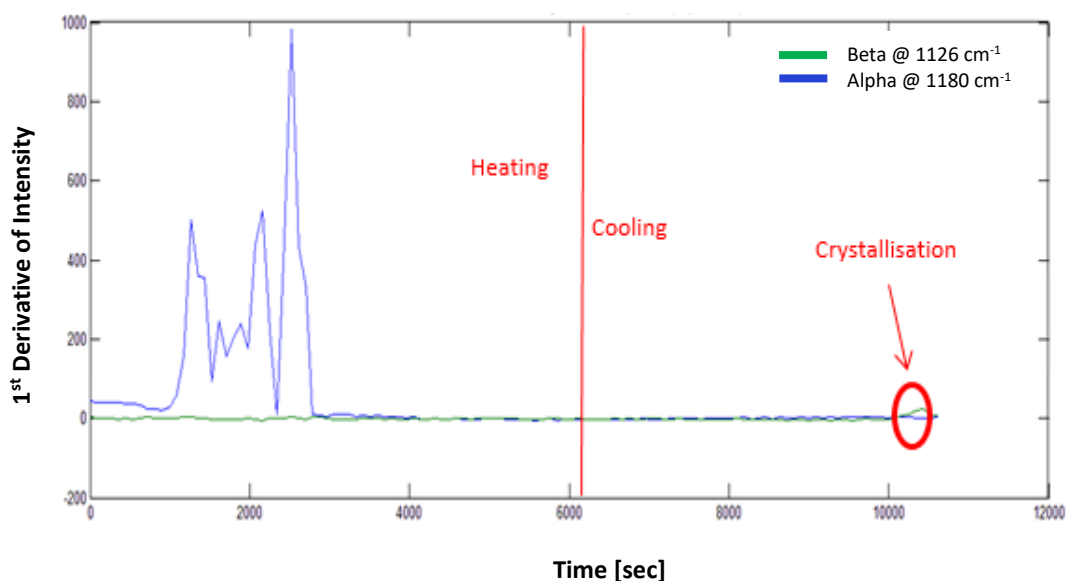


Figure 64. Raman dissolution and crystallisation profile (exp C.2.8) based on the 1st derivative of the intensity changes of alpha characteristic peak at 1181 cm^{-1} (blue plot) and beta characteristic peak at 1126 cm^{-1} (green plot).

Based on the crystallisation profile for this (C.2.8) experiment (Figure 65) crystallisation took place at 10000 seconds. This time corresponds with a temperature of 21.8°C .

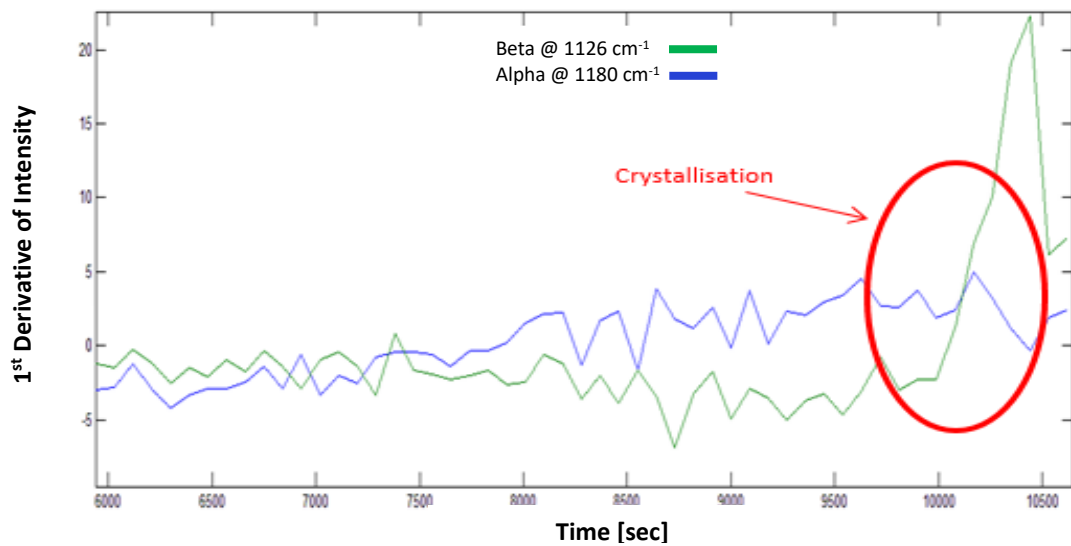


Figure 65. Zoomed in Raman crystallisation profile (exp C.2.8) based on the 1st derivative of the intensity changes of alpha characteristic peak at 1181 cm⁻¹ (blue plot) and beta characteristic peak at 1126 cm⁻¹ (green plot).

In Figure 66 the real time accumulation or heat shift (q_s) in the process fluid, enthalpy and temperature trends are shown. The accumulation or heat shift in the process fluid trend steadily increased to the point where it corresponded with the information obtained from the Raman spectra where an unexpected increase was observed. It may indicate the crystallisation point (as it corresponds with Raman data) however, as was mentioned above, these kinds of changes were not observed during the experiment.

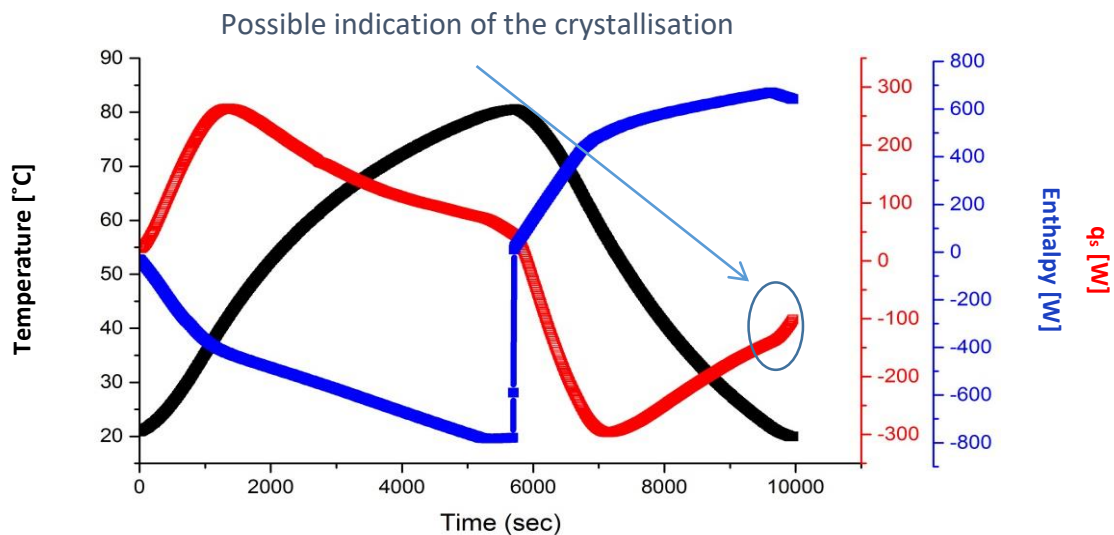


Figure 66. Enthalpy (blue plot), temperature (black plot) and accumulation or heat shift (q_s) in the process fluid (red plot) trend for experiment no. C.2.8

For experiments C.2.3 and C.2.8, the Raman profile at the dissolution stage was varied, which was not observed for experiment C.1.4, where the dissolution profile of the beta particles was a smooth decrease. The possible explanation of this was that beta particles were growing on the probe surface and obscured the results from this analytical tool.

3.7 Discussion

Table 9 and Table 10 summarise the results obtained with the CoFlux reactor and the two other systems used by Dr Laura Palmer [14]. The experiments in the CoFlux reactor were carried out using operating conditions similar to those of the stirred tank reactor (STR) and oscillatory baffled reactor (OBR) to simplify the comparison of the three platforms. The method of temperature control in the CoFlux reactor consistently gave a good yield of crystallisation – around 75%. Using different stirring rates caused a change in particle size – using a higher agitation rate gave smaller $d(0,5)$ values. However, it was believed that the lower particle size was achieved through attrition, which is not necessarily a good method of generating small particles. It was impossible to obtain crystals in the experiments when the lower concentrations of LGA were used (15 g/L and 30g/L), which meant that conditions within the reactor did not reach adequate levels of supersaturation in order for crystals to form at these concentrations. With the relatively low supersaturation level ($S=2.1$ (15 g/L)), crystals were formed only using the oscillatory baffled reactor – but with very poor yield. Results obtained with the CoFlux reactor (C.1.3) were more comparable with results obtained in the OBR (experiments O3, O5, O6) than with the STR. The sizes of crystals formed during experiments with using the CoFlux reactor were comparable with the sizes of crystals formed during OBR experiments. The major polymorphic form obtained during the experiments in the CoFlux reactor was the alpha form. Even when the XRPD pattern suggested that the product was a mixture of the alpha and the beta form, it could be easily observed that the alpha form was the main polymorph produced. The width of particle distribution – the span in the MasterSizer data – was narrower in the case of the CoFlux crystals, which meant that the crystal size was more uniform than crystals obtained in the OBR or STR.

The second CoFlux setup (B) did not significantly affect the crystals size or crystal size distribution. Very slow cooling rate (experiment C.2.1) looked promising for producing the metastable alpha form of L-glutamic acid, which contradicted previous work reported by Borrisova et al. [93], where it was shown that slower cooling rate

favoured the formation of the beta form. The explanation was based on the fact that the alpha form, nucleates first and over the time crystals are converted to the beta form. For the experiments, where the high cooling rate was applied (0.7-0.9°C/min) the pure alpha form was produced, which confirmed what was reported by Borrisova et al. [93]. The application of the temperature loop meant that for many experiments the pure alpha form was the only product of the crystallisation. The system without the temperature loop always yielded a mixture of alpha and beta form. The temperature loop seemed to change the characteristics of the reactor, because in CoFlux setup B, there was no noticeable effect from the cooling rate or mixing speed. The same product properties were observed no matter what the experimental conditions were.

Table 9. Comparison of the results obtained during experiments in stirred tank reactor and oscillatory baffled reactor

Exp.	Initial – final temperature [°C]	Cooling rate [°C/min]	Concentration [g/L]	Agitation [rpm] Frequency[Hz]/ Amplitude[mm]	Polymorph	d(0,5) [μm]	d(4,3) [μm]	Span [μm]	Yield [%]
S1	80-40	0.5	45	200	β	212	285	2.8	55.6
S2	80-40	0.5	45	100	β	285	338	2.4	41.4
S3	80-10	0.5	15	200	-	-	-	-	-
S4	80-10	0.5	15	100	-	-	-	-	-
O1	80-10	0.5	15	3 / 30	α	83	89	1.2	17.9
O2	80-40	0.5	45	1 / 10	α/β	457	559	2.2	54.6
O3	80-40	0.5	45	3 / 30	α/β	312	382	2.3	61.7
O4	80-10	0.5	15	1 / 10	α	46	106	2.8	0.2
O5	80-40	0.5	45	3 / 10	α/β	351	385	1.3	55.8
O6	80-40	0.5	45	1 / 30	α/β	365	388	1.1	55.0
O7	80-40	0.5	45	2 / 10	α/β	395	428	1.6	34.1
O8	80-10	0.5	15	2 / 10	α/β	166	178	1.2	8.7

Table 10. Comparison of the results obtained during experiments in CoFlux reactor

Exp.	Initial – final temperature [°C]	Cooling rate [°C/min]	Concentration [g/L]	Agitation [rpm]	Polymorph	d(0,5) [μm]	d(4,3) [μm]	Span [μm]	Yield [%]
C.1.1	80-20	0.74	45	150	α/β	482	519	1.9	87.4
C.1.2	80-20	0.76	45	150	α/β	531	541	1.2	73.4
C.1.3	80-20	0.75	45	250	α/β (α>β)	385	410	1.3	79.1
C.1.4	80-20	0.74	45	250	α/β (α>β)	306	333	1.4	76.4
C.2.1	80-20	0.35	45	250	α	241	248	1.0	64.2
C.2.2	80-25	0.41	45	250	α/β	245	268	1.7	67.3
C.2.3	80-25	0.51	45	250	α/β (α>β)	368	379	1.2	71.0
C.2.4	80-20	0.56	45	250	α/β	242	245	1.2	76.1
C.2.5	80-20	0.73	45	250	α	264	273	1.0	75.7
C.2.6	80-20	0.85	45	250	α	293	320	1.4	73.7
C.2.7	80-20	0.70	45	150	α	331	352	1.2	68.4
C.2.8	80-20	0.90	45	150	α	333	364	1.4	64.6

3.8 Conclusions

The use of the CoFlux reactor in the crystallisation of L-glutamic acid brought satisfactory results. The cooling profile obtained during the experiments was almost linear and during the process disturbances in the temperature profile were not observed. Excellent temperature control permitted a significantly higher yield to be achieved than in the other types of reactor.

The temperature control also affected the polymorphic form of L-glutamic acid obtained during the experiments. Both for the slow cooling rate (contradiction to the results reported by Borrisova et al. [93]) and for the fast cooling rate the predominant polymorph was the metastable alpha form.

Twelve experiments were carried out in the reactor with cooling rates ranging from 0.35-0.9°C/min. For seven of these experiments the alpha form was either the predominant form produced, or in five cases the only form produced. It is therefore likely that the crystallisation process in this reactor type began far beyond the metastable zone (MSZ), and the cooling profiles were tracing the alpha-solubility curve. This would account for the large number of experiments where the alpha form dominates. The other four experiments were equal mixtures of the alpha and the beta form. The beta polymorph usually prefers to nucleate on the alpha crystals [102].

In a regular stirred tank reactor, the jacket heat transfer fluid is not uniformly mixed as it is in the CoFlux reactor, meaning that there will be no cold spots on the CoFlux reactor wall. Without cold spots, crystallisation can take longer to occur, as the cold areas provide a temperature driving force to initiate nucleation earlier on in the process i.e. creating local areas of high supersaturation. This means, and was verified through observation, that the crystallisation takes place at lower temperatures. If crystallisation takes place at a lower temperature and the initial supersaturation was considerably high, the beta polymorph would be absent because of the available supersaturation depleting very quickly. In turn the beta crystals did not have enough time to nucleate on the surface of the alpha crystals (their preferred method of nucleation).

The experiments carried out with the CoFlux reactor indicate some areas for future work to improve the suitability of the reactor for crystallisation studies:

- The applied cooling and heating rate was relatively slow and it was impossible to control the process temperature rate of change directly. It would be beneficial to change the software to link the heater/chiller unit temperature change with the required change of process temperature
- The Raman immersion probe was implemented during some experiments. Crystal growth was observed on the probe, which created risk that the results obtained were not credible. To apply a *non-invasive* probe, a window into the reactor was required - this problem cannot be resolved – reactor reconstruction would be necessary.
- During the experiments (especially during the cooling process) disturbances in the process power trend line were observed (see Figure 44). It could hinder the observation of changes in the trend and consequently prevent the use of the measurement of enthalpy to monitor and control crystallisation. It was clear that enthalpy measurement did not detect the nucleation point, but the changes in the accumulation or heat shift (q_s) in the process fluid trend may indicate crystallisation. Nevertheless, for control over the particle features this kind of information is not really useful.

Table 11 shows the final comparison of the results produced during the experiments carried out in the two different CoFlux setups – setup A without the temperature loop, setup B with the temperature loop.

Table 11. Final comparison of the results obtained using two different CoFlux setups (A and B)

Crystals properties	Setup A	Setup B
Crystallisation temperature	35°C	Varied - 35°C, 21°C
Polymorphic form	α/β ($\alpha>\beta$)	α , α/β ($\alpha>\beta$)
Crystal size (150 rpm mixing speed)	500 μm	350 μm
Crystal size (250 rpm mixing speed)	350 μm	250 μm
Span value	1.5	1.0
Yield	75-80%	65-70%
Enthalpy measurements	Not useful at all	Accumulation or heat shift (q_s) in the process fluid trend did not indicate the nucleation point, however may be used as an indicator of crystallisation

The idea of the implementing the temperature loop was to stabilize the temperature, which in turn should stabilize the accumulation or heat shift (q_s) in the process fluid trend baseline, and this was achieved. However, the application of the temperature loop changed the reactor characteristics and affected the crystal properties. Using the CoFlux system with the temperature loop favoured the formation of the alpha form of L-glutamic acid. The crystal size was not significantly dependent on the mixing speed and the crystal size distribution is narrower. The yields were slightly lower (however the change was not significant) and using the accumulation or heat shift (q_s) in the process fluid trend measurement may be used as the indicator of the crystallisation.

4 Chromatographic Techniques for Impurity Determination and Quantification During Crystallisation Processes

4.1 Chapter Outline

Metformin (dimethylbiguanide) hydrochloride was chosen as a model compound for this study due to its ionic form and potential of forming salts with different counter ions present in the solution. Metformin hydrochloride is an oral anti-hyperglycemic agent and the first line drug for treating type II diabetes. The physical and chemical properties of this compound are presented in this chapter.

This chapter describes the development and the validation of the liquid - chromatography mass spectrometry (LC-MS) method for determination of five out of six known, organic impurities of metformin. The theory behind the operations of both – chromatography and mass spectrometry and the key parameters to be considered during the method validation are described here.

One of the impurities – dimethylamine – could not be determined using the LC-MS method, therefore an ion chromatography (IC) method was developed and validated. Both the experimental results and the theory behind the principles of this technique are covered in this chapter.

The application for both developed methods is presented, as well as a stability test results of metformin hydrochloride samples.

4.2 Analytical Techniques

4.2.1 Liquid Chromatography

Liquid chromatography is a physicochemical separation technique widely used in pharmaceutical analysis for the quantitation of drugs in formulations. The basic principles are based on the separation of components of homogeneous mixtures as a result of various distributions between the mobile phase (liquid) and a stationary phase (usually stainless steel tube filled with silica gel) in the chromatography system.

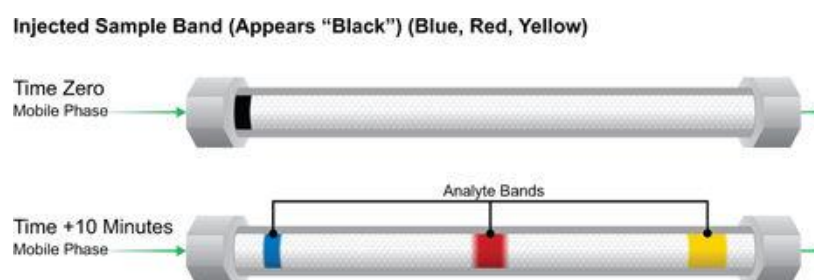


Figure 67. Diagram showing how the process of the chromatographic separation [103]

The mobile phase is the transport method used to pass the analyte through the stationary phase inhibits the migration of different component in the analyte. The separation of the components between the two phases occurs due to the difference in their distribution coefficients (differences in mobility) when the analyte is transported through the stationary phase. The greater the affinity of a compound to the stationary phase the slower it will migrate through the stationary phase, separating it from the rest of the analyte. The efficacy of this process is dependent on the affinity of the compound to the stationary phase. This allows the stationary phase to be tailored to separate a desired component form the analyte within a specific time.

Liquid chromatography has been utilised in many different techniques such as: normal-phase liquid chromatography, reversed-phase liquid chromatography, ion-exchange liquid chromatography, size-exclusion chromatography. However, with equipment available in our lab only normal-phase and reversed-phase liquid chromatography modes are used.

4.2.1.1 Normal Phase Liquid Chromatography

Normal-phase liquid chromatography is also known as adsorption chromatography. The stationary phase is characterised by high polarity and is based on silica gel, alumina or carbon. Silica gel or carbon particles can be modified to change their affinity to a desired/targeted compound (or separation) by possessing different functional groups having varying polarity such as amino (-NH₂), cyano (-CN), or hydroxyl (-OH) groups. The solvents used in the mobile phase can also be tailored to suit a given process. By choosing different solvents (or mixtures) the affinity of the compound to the solvent can be altered - the separation between the mobile and stationary phase will change and therefore the retention of the desired compound will change too. This system is composed of nonpolar organic solvents such as 2-propanol, acetonitrile, ethyl acetate or hexane.

Functional groups present in the solute molecules interact with the functional groups in the mobile phase through polar interactions. The retention time for the individual solute molecules will depend on its polarity. The retention time for more polar molecules will be longer than the retention time for molecules characterised by low polarity.

One of the variants of normal phase chromatography is hydrophilic interaction liquid chromatography (HILIC), which offers a substitution for effective separation small polar molecules on polar stationary phases. However, the separation mechanism used in HILIC is more complicated than in normal phase liquid chromatography mode. HILIC uses the conventional polar stationary phases, but the mobile phases are analogous to those used in the reverse phase liquid chromatography. Using HILIC mode it is also possible to analyse the charged molecules, so this shows the similarity of this mode to ion chromatography.

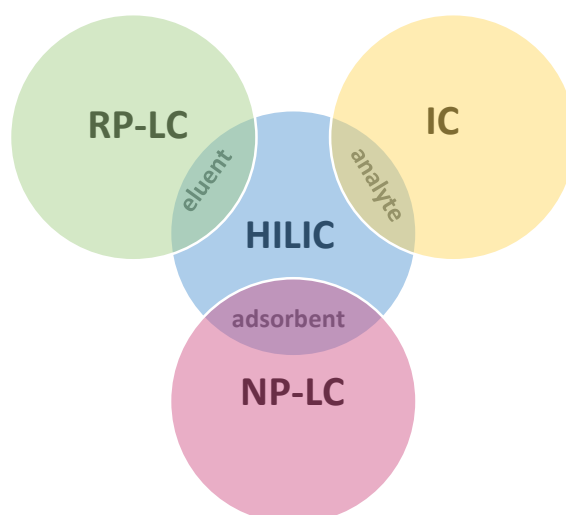


Figure 68. Diagram showing the relationship between hydrophilic interaction liquid chromatography (HILIC) and other chromatographic techniques – reverse phase (RP-LC), normal phase (NP-LC) and ion chromatography (IC).

There are many advantages of HILIC column over conventional normal and reverse phase chromatographic modes:

- 1) Molecules that elute near the void in RP-LC can be analysed using HILIC
- 2) Polar samples well soluble in aqueous/organic mobile phase, which overcomes the solubility issue in NP-LC
- 3) HILIC does not require expensive ion pair reagents
- 4) HILIC became a separation choice for highly hydrophilic and amphiphilic compounds, that cannot be analysed using RP-LC due to their high polarity
- 5) HILIC can be used as a variant of IC, if the analysed compounds have insufficient charge for an effective separation using ion-exchange chromatography [104].

4.2.1.2 Reversed Phase Liquid Chromatography

Reversed-phase liquid chromatography is based on the fact that the stationary phase is less polar than the mobile phase. The most often used column packing material is octadecylsilyl silica (ODS-C18), in which silica is covalently modified by C₁₈H₃₇ alkyl chain (C₁₈) functional groups. Here the solutes partition between the surface coating and the mobile phase can be described as a liquid-liquid extraction. In this system the mobile phase is more polar than the stationary phase, so often the mobile phase consists of water and a water-miscible organic solvent, for example methanol, acetonitrile and tetrahydrofuran (THF).

Figure 69 shows the structure differences between normal-phase and reversed-phase column packing material.

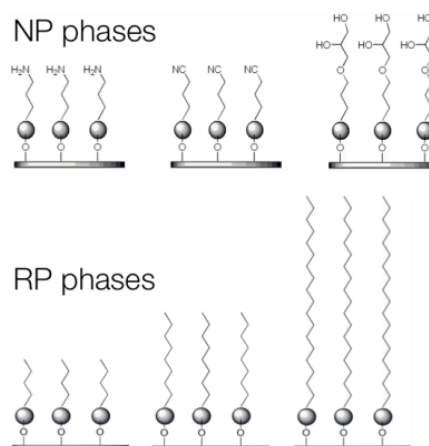


Figure 69. Differences between a normal-phase (NP) and reversed-phase (RP) structure

Figure 70 shows the most commonly used reversed-phase stationary phases and the relationship between the polarity of the stationary phase and the retention time of non-polar analytes.

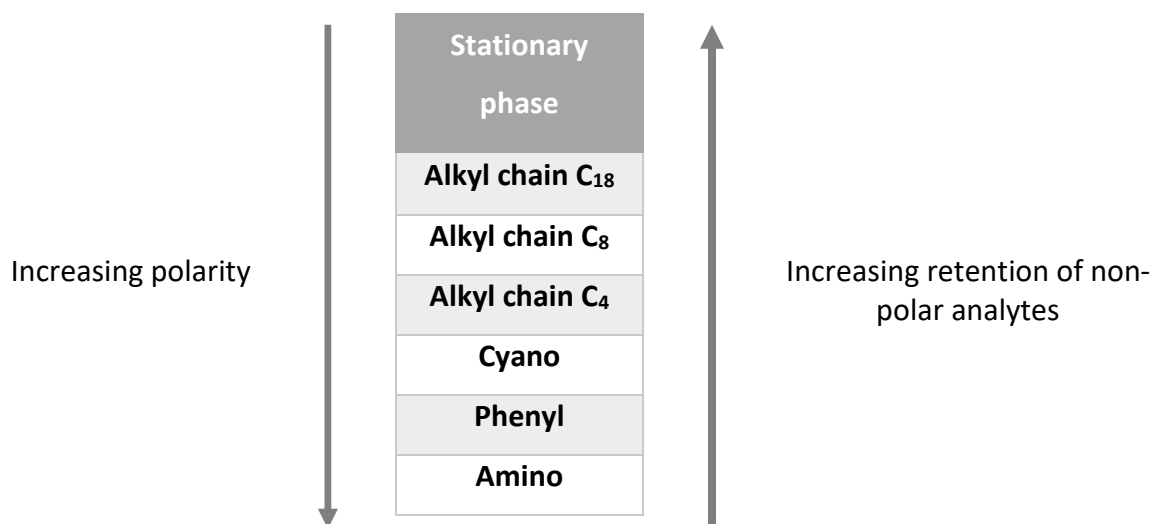


Figure 70. Commonly used reversed-phase stationary phases and their polarity

4.2.1.3 Factors Determining Chromatographic Efficiency

There are several parameters that have to be considered while validating the method – see Figure 71. Some of them will be further described in this section.

Precision	Accuracy	Column efficiency	Capacity factor
Robustness	Peak asymmetry	Signal/Noise Ratio	Selectivity
Resolution	Linearity	Limit of Detection	Limit of Quantification

Figure 71. A typical method validation parameters

4.2.1.3.1 Accuracy

The accuracy of an analytical method is the closeness of test results to the true value.

It can be evaluated by:

- 1) Analysing a reference material of known concentration and comparing the measured value to the true value
- 2) Comparing the obtained test results to the well-known and validated method
- 3) Analysing blank matrix spiked with known amounts of impurities and calculating the recovery
- 4) Analysing samples spiked with known amounts of impurities and calculating the recovery

4.2.1.3.2 Precision

Precision is the degree of agreement among individual test results when an analytical method is used repeatedly to analyse a homogenous sample. It is expressed as the percent relative standard deviation for a minimum of 6 samples.

4.2.1.3.3 Limit of Detection (LOD) and Limit of Quantification (LOQ)

The limit of detection (LOD) is defined as the lowest amount of analyte that can be detected above, typically, three times the noise level.

The limit of quantification (LOQ) is the lowest amount of analyte that can be reproducibly quantified, usually above ten times the noise level.

Both parameters can be estimated based on visual evaluation or based on standard deviation of response and slope as it is shown below:

Equation 66

$$LOD = 3\sigma/s$$

Equation 67

$$LOQ = 10\sigma/s$$

where σ is standard deviation of the response based on either the standard deviation of the blank, the residual standard deviation of the regression line, or the standard deviation of y-intercepts of the calibration line, and s is the slope of the calibration curve.

4.2.1.3.4 Capacity factor (K')

The components of the sample are retained on the column for different length of the time, depending on their properties. A parameter, which allows prediction of the retention time of the individual component, is called the retention or capacity factor (K'). This factor is a measure of the degree to which that component is retained by the column and can be described as follows

Equation 68

$$K' = \frac{V_r - V_0}{V_0} = \frac{t_r - t_0}{t_0}$$

where V_r and t_r are the retention volume and retention time of the component respectively, while V_0 and t_0 are the void volume of the column and the time for an unretained molecule to pass through the column.

A schematic diagram of chromatographic separation on the HPLC column is shown below in Figure 72.

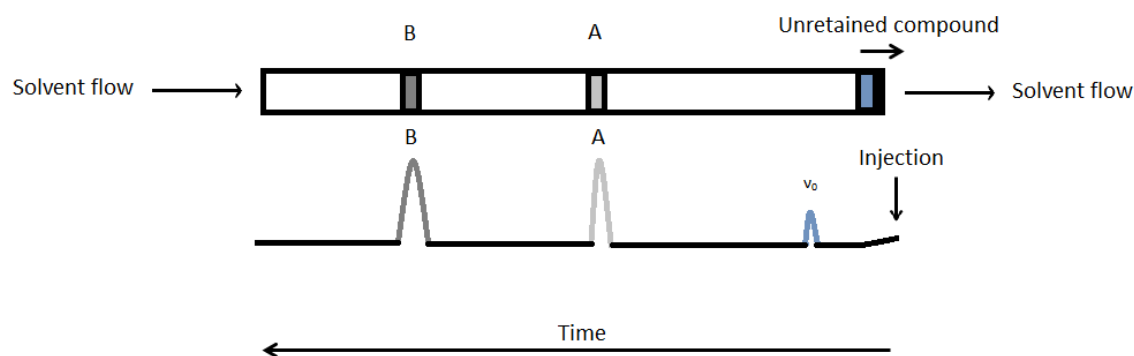


Figure 72. Schematic diagram of chromatographic separation on the HPLC column: A and B are two components, V_0 is the void time

The higher K' value the more retained the sample is on the column, what that means is that the interaction between the analyte and the stationary phase is stronger, changing its peak position in the chromatograph (it's retention time).

4.2.1.3.5 Column efficiency

Column efficiency can be evaluated using the width of the peak at half its height ($W_{1/2}$) and its retention time (t_r) using the equation shown below.

Equation 69

$$n = 5.54 * \left(\frac{t_r}{W_{1/2}} \right)^2$$

In the equation above n is the number of theoretical plates. Usually the column efficiency is described as a number of theoretical plates per meter (in the equation below L is the column length in cm).

Equation 70

$$n \times 100/L$$

4.2.1.3.6 Peak asymmetry

Very often chromatographic peak tails to a certain degree and this leads to peak asymmetry. The exact definition of peak asymmetry says that a peak will be described as asymmetrical when it deviates from the ideal symmetrical shape of a Gaussian peak. An example is shown below (Figure 73).

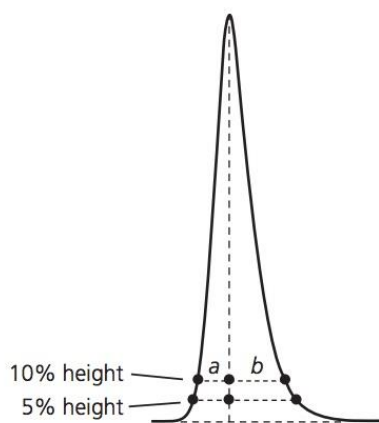


Figure 73. An example of asymmetric peak. In the scheme above a and b are the front and back half widths at 5% (or 10%) of peak height [105]

Asymmetry factor is defined as the ratio of the trailing half of the peak (b) to the leading half of the peak (a) – both measured at 10% of the peak height.

Equation 71

$$\text{Asymmetry factor (AF)} = \frac{b}{a}$$

The acceptable value of the asymmetry factor is between 0.9 and 1.2 [105].

4.2.1.3.7 Separation factor/selectivity

The selectivity parameter, α , is a measure of the spacing between two peaks and is defined as follows:

Equation 72

$$\alpha = \frac{K'_2}{K'_1}$$

K'_1 and K'_2 are the capacity factors for compound 1 and compound 2. Capacity factor was defined in Equation 68.

4.2.1.3.8 Resolution

The resolution between two peaks – A and B (Figure 74) can be calculated as follows:

Equation 73

$$R_s = 2 \frac{t_{R2} - t_{R1}}{W_1 + W_2}$$

where t_{R1} and t_{R2} are the retention time of peaks A and B respectively, and W_1 and W_2 are the widths of peaks A and B measured at baseline.

A resolution value of 1.2 and greater between two peaks will guarantee that the sample components are separated completely.

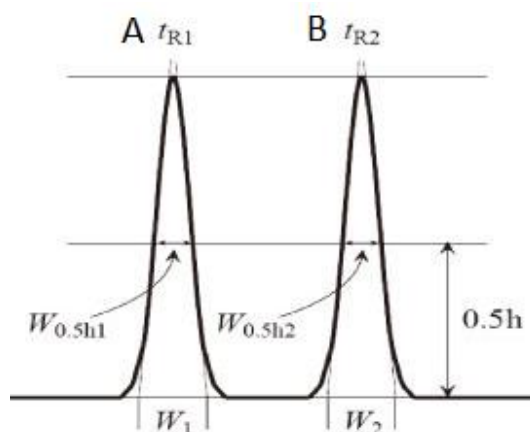


Figure 74. A schematic diagram showing the retention time (t_{R1} and t_{R2}) and the widths of peaks A and B measured at baseline (W_1 and W_2) as well as the widths of peaks A and B measured at 50% of peak height ($W_{0.5h1}$ and $W_{0.5h2}$). All these parameters are required to calculate the peak resolution.

4.2.2 Ion Chromatography

4.2.2.1 Salt formation

Salt formation is a very effective method of increasing bioavailability and solubility of drug molecules. Approximately 50% of all drugs on the market are developed in salt forms by pairing a basic or acidic drug molecule with a counter ion [106]. There has to be an ionisable functional group in the molecular structure of the drug for this to be possible, as it will therefore interact with the salt former through ionic interactions

[106]. The choice of counter ion is dictated by the range of conditions that the salt is expected to exist in. The type of formulation will play a significant role in salt former selection – for suspensions, fairly insoluble counter ions (embonate, estylate, tosylate) are chosen, while for solid dosage forms, injectables and oral solutions, highly soluble salts such as hydrochlorides and mesylates are suitable. The molecular weight of the counter ion needs to be considered when the high-dose are designed – it is preferable to pair low-potency drugs with counter ions of a low molecular mass. It is not important when potent drugs are designed. Large and fairly insoluble counter ions are preferable when slow drug release is expected. The choice of the counter ion is limited by the therapeutic indications of the drug, e.g. sodium intake should be controlled in conditions such as hypertension and diabetes. Another critical parameter to be considered during the salt selection is the degree of ionisation. The difference between the pK_a of the counter ion and the pK_a of the drug should be at least 2 pH units (lower for salt forms of basic drugs, higher for salt forms of acidic drugs) to ensure that the proton transfer is energetically favourable [106].

In 1994, Morris et al. [107], proposed a multi-staged approach for effective salt screening. The crystallinity assessment was the first stage of this methodology – crystalline structure was thought to be more stable and therefore easier to handle, store and use. In the next stage, the hygroscopic profile was assessed to test the physicochemical stability of the product under different humidity conditions. Afterwards, polymorphism of the salt form was studied and the following properties of the accepted forms were then tested: corrosiveness, taste, wettability and flowability. The final stage of the approach proposed by Morris et al. was the pharmacological properties assessment for selected salt, including onset and the duration of activity, drug release profile and safety studies.

Transformation of drugs into their salt forms can significantly increase solubility and dissolution rate as well as change other physicochemical properties, such as thermo-stability, photo-stability, organoleptic properties and compatibility.

Regardless of the many advantages of salt formation there is a list of potential undesirable effects that have to be faced during production. Counter ions are

therapeutically inactive, therefore the produced capsules and tables might be bigger and in consequence cause problems at administration. Production of salts increases the risk of hydrate and polymorph formation, which can affect the drug stability. Using hydrochlorides, for example, may cause problems with corrosion of the production machinery. Due to ionic properties of salts a reduced permeability of drugs through biological membranes (limited partitioning into lipophilic phases) is observed. It may cause a reduction in drug absorption and bioavailability.

Producing the correct salt form of APIs has become a significant problem for the pharmaceutical industry – the wrong salt puts the patient in a potential risk. In relation to the crystallisation process the presence of impurities might have a significant effect on primary and/or secondary nucleation, solubility, crystal shape and morphology [108], [109].

4.2.2.2 Ion Chromatography Principles

It has been observed that organic impurities can appear during the synthesis of a drug, during the purification steps or as the degradation product during the storage of the API. Inorganic impurities can be introduced in to a product during the manufacturing process, which makes necessary to assess the inorganic impurities content in order to meet the pharmacopeia standards and toxicity levels.

Ion chromatography is the most widely used technique to separate organic and inorganic ions. It is a separation technique, where the differences in the affinity of ions and polar molecules to the ion exchanges are used. This process can significantly change suboptimal physicochemical and biopharmaceutical properties of APIs and change the solubility, stability or bioavailability of the drug. Using this technique, it is possible to identify and quantify a wide range of cations and anions. In this type of chromatography, the column is packed with anion or cation exchange resin – typically polymers with cationic or anionic groups attached to the surface, while the mobile phase contains aqueous sodium hydroxide – in anion exchange mode and aqueous methane sulfonic acid in cation exchange mode.

The basic process of chromatography using ion exchange can be represented in following steps:

- eluent loading – in this step the resin surface becomes saturated with the eluent anion or cation;
- sample injection;
- separation of sample – based on the fact that the strength of the interaction with the surface will be different for different ions. The greater the charge of the ion or the ionic radius the longer will be the elution time;
- elution of individual analytes.

Figure 75 shows the process described above.

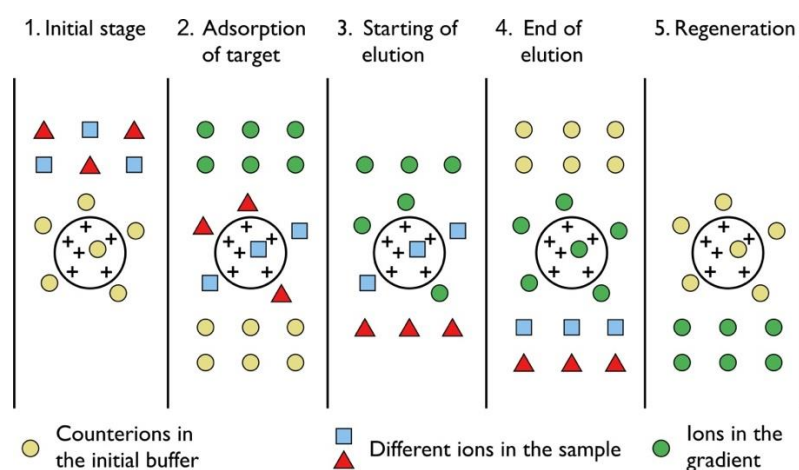


Figure 75. Basic principles of the ion chromatographic separation [110]

Ion chromatography with suppressed conductivity detection plays an important role in the salt selection process to establish correct molecular mass of the entity in the early stages of drug development. Ion chromatography can also be used in quality control to verify identity, strength, and purity of ionic APIs. Due to its high sensitivity, stability, efficiency and robustness, the suppressed conductivity detector is the main choice for the separation of counter ions in pharmaceuticals. The possibility of the use of the solvents with low conductivity, such as water or carbonic acid, increases

the sensitivity of the suppressed conductivity detector – by reduction of the baseline it is possible to detect counter ions at levels of low ppm.

In this project ion chromatography was used to determine the counter ions present in metformin hydrochloride samples.

4.2.3 Gas Chromatography

This chromatographic technique uses the ability of a substance to vaporize and analyse volatile compounds without decomposition. If the compound is not itself volatile, it may through a chemical reaction form a suitable, thermally stable derivative, making it viable for gas chromatography (GC) analysis. In this system the sample is transported through the column by the flow of an inert, gaseous mobile phase – usually helium.

Though the popularity of the GC has been declining for a number of years, due to improvements in HPLC, it still crucial in pharmaceutical analysis. Currently the gas chromatography is mainly used for quantitative and qualitative analyses for drugs that do not have a chromophore in their structure. However, what is often overlooked is the fact that capillary GC can provide better separation of many compounds when compared to methods such as HPLC.

4.2.4 Mass Spectrometry

Mass spectroscopy (MS) is an analytical technique which provides information about the molecular mass of the sample. Using a high vacuum region immediately prior to a sample entering a high vacuum a mass spectrometer generates charged molecules or molecular fragments. By generation of the ions in the gas phase it is possible to manipulate by the application of magnetic or electric field to the generated ions and allow the determination of their molecular weights.

4.2.4.1 *Ion generation methods*

There are a number of ion generation methods such as electrospray ionisation (ESI), electron impact ionisation (EI), atmospheric pressure chemical ionisation (APCI) or

matrix assisted laser desorption ionisation (MALDI). Due to the fact, that in this project electrospray ionisation has been used, only this ionisation method will be described [31].

4.2.4.1.1 Electrospray ionisation

Electrospray ionisation was popularised around 20 years ago and its main advantage is the direct compatibility with high-pressure liquid chromatography. Figure 76 shows the electrospray ionisation process. The transfer of ionic species from solution into the gas phase can be described in three steps:

- production of highly charged droplets with the same polarity as the capillary voltage – the eluent from LC system passes through a stainless steel or quartz silica capillary to which a high voltage (2.5-6.0 kV) is applied
- solvent evaporation - using a coaxial flow of nebulising gas (usually nitrogen) the solvent evaporates and enhances a higher sample flow rate.
- due to internal charge repulsion charged droplets break up to give gas phase ions, which are transported to a heated capillary (to which an opposite charge is applied) inlet to the mass spectrometer, which operates under high vacuum. The ion injection from the highly charged droplets is the last step [31, 32].

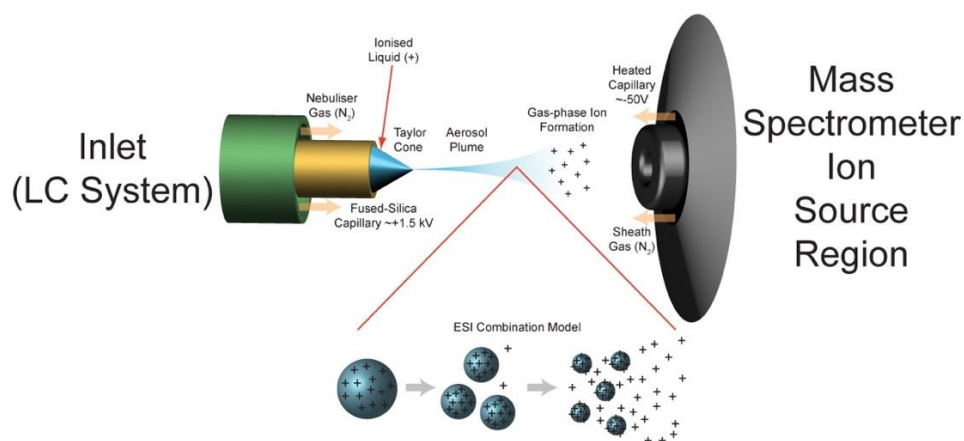


Figure 76. Electrospray Ionisation (ESI) and Ion Source Overview [33]

4.2.4.2 Mass analysers

Generated ions need to be analysed. Mass analysers separate the ions travelling through a magnetic or electrical field, according to their mass-to-charge ratio. There are six general types of mass analysers that can be used for the separation of ions in a mass spectrometry: Quadrupole Mass Analyser, Time of Flight Mass Analyser (TOF), Magnetic Sector Mass Analyser, Electrostatic Sector Mass Analyser, Orbitrap, Ion Cyclotron Resonance (ICR). For the purposes of this work only Time of Flight Mass Analyser (TOF) will be described in detail.

4.2.4.2.1 Time of flight (TOF) mass analyser

Time of flight (TOF) mass analyser measures the mass-dependent time it takes ions of different masses to move from the ion source to the detector. Ions are given a defined kinetic energy (Equation 74) and allowed to drift through a field-free region.

Equation 74

$$T = eV = \frac{mv^2}{2}$$

The ion velocity (v) is defined by the length of the flight path L and the flight time (t) as shown in Equation 75.

Equation 75

$$v = \frac{L}{t}$$

The time at which ions arrive at the detector is measured and related to the m/z ratio and it can be calculated based on equation below (Equation 76).

Equation 76

$$t = L \sqrt{\frac{m}{e} \frac{1}{2V}}$$

Linear theory assumes ions formed at rest, at the same time, and all at the same position in the source. In reality, ions are formed throughout the source at various times, in various locations, with a range of initial kinetic energies. To compensate for these differences a new design of time of flight analyser was developed by Alikhanov in 1957 [111]. The new design contained a reflectron, which is an ion optic device in which ions in a time-of-flight mass spectrometer pass through a "mirror" or "reflectron" and their flight is reversed. A linear-field reflectron allows ions with greater kinetic energies to penetrate deeper into the reflectron than ions with smaller kinetic energies. The ions that penetrate deeper will take longer to return to the detector. If a packet of ions of a given mass-to-charge ratio contains ions with varying kinetic energies, then the reflectron will decrease the spread in the ion flight times, and therefore improve the resolution of the time-of-flight mass spectrometer. A curved-field reflectron ensures that the ideal detector position for the time-of-flight mass spectrometer does not vary with mass-to-charge ratio. This also results in improved resolution for time-of-flight mass spectrometers.

Due to its high specificity mass spectrometry is used for determination or identification of produced active pharmaceutical ingredients or raw materials during the manufacturing process. Coupling mass spectroscopy with liquid or gas chromatography makes these systems very reliable tools for detecting impurities in drugs and formulation excipients due to their high sensitivity and specificity. For the same reasons LC/MS and GC/MS systems are widely used for determination of drugs and their metabolites in biological samples.

The main limitation of mass spectrometry is the cost of the instrumentation and the difficulty of maintenance.

4.3 Model Compound

4.3.1 Introduction to Metformin Hydrochloride

Metformin (dimethylbiguanide) hydrochloride is an oral anti-hyperglycemic agent and the first line drug for choice for the treatment of type II diabetes. The chemical structure of metformin can be described as a biguanide derivative in which two hydrogen atoms at the N1 nitrogen have been substituted with methyl groups. Currently metformin is the only biguanide derivative used in the medicine [112].

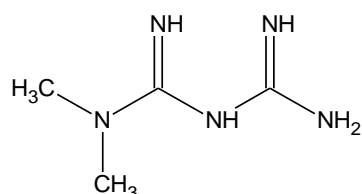


Figure 77. A chemical structure of metformin

The molecular weight of metformin is 129.16 g/mol and its molecular formula is C₄H₁₁N₅. The structure of this compound was shown above in Figure 77. At room temperature metformin hydrochloride exists as colourless and odourless crystals. The melting point has been reported as 218-220°C [113].

Metformin hydrochloride is practically insoluble in ether, chloroform, but highly soluble in water and 95% alcohol [113]. It has been reported that when metformin hydrochloride is heated to decomposition it emits toxic fumes of nitric oxides [114]. The usual synthesis of metformin, which was originally described in 1922 [115] involves the reaction of dimethylamine hydrochloride and 2-cyanoguanidine (dicyandiamide) with heating (Figure 78).

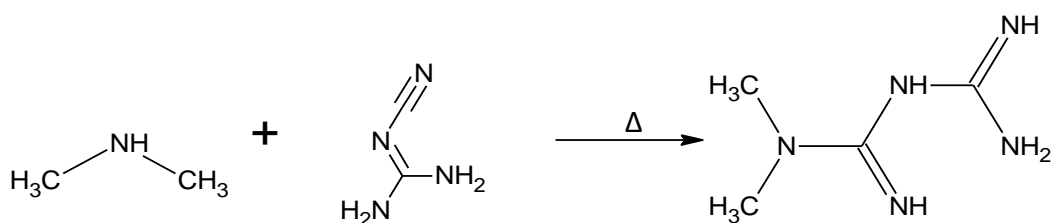


Figure 78. Metformin synthesis route

The actual procedure has been described in Pharmaceutical Manufacturing Encyclopedia [116]. According to it, equimolar amounts of dimethylamine and 2-cyanoguanide are dissolved in toluene with cooling to make a concentrated solution. Afterwards an equimolar amount of hydrochloric acid is slowly added, and this causes spontaneous boiling of the prepared solution. After cooling, metformin hydrochloride crystallises with a 96% yield. Due to the fact that metformin is a highly hygroscopic compound it causes a lot of stability problems, and this consequently affects the ability to form tablets. As a result, it is necessary to use additional excipients to change (improve) flow and compaction properties of the drug in a tableting mix [117]. It has been already reported, that addition of impurities can change the crystal habit, which in turn will change the tableting behaviour of the drug. Dramatic changes in crystal size and shape have been also observed, when in the solution the polymeric additives are included in the crystallising solution [117]. Metformin hydrochloride exists in two polymorphic forms – form A (thermodynamically stable, needle shape) and form B (metastable form, prismatic shape) [117]. Both forms are shown in the Figure 79.

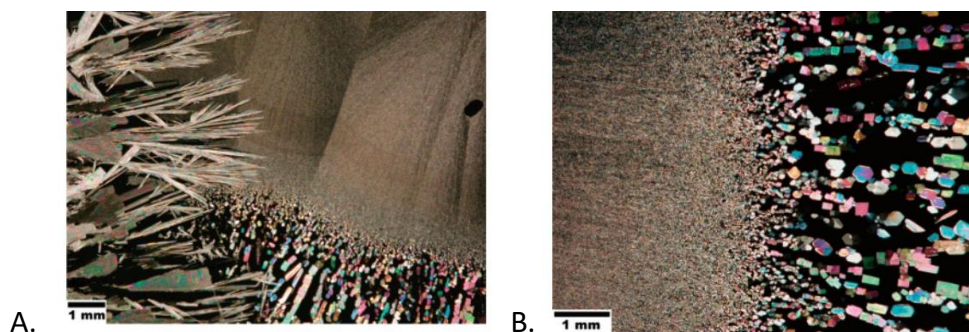


Figure 79. (A) Needle shape form A crystals of metformin hydrochloride growing with the loss of (B) form B [117]

Childs et al. carried out work to isolate and characterise a metastable form of metformin hydrochloride using capillary crystallisation and thermal microscopy techniques [117]. Authors carried out a polymorph screen in capillary tubes for 28 solvents and 8 evaporation conditions – for most of conditions form A has been

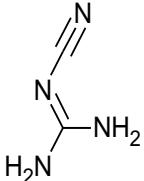
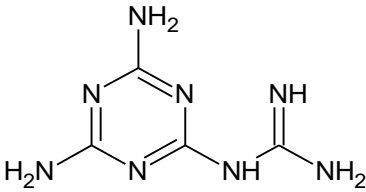
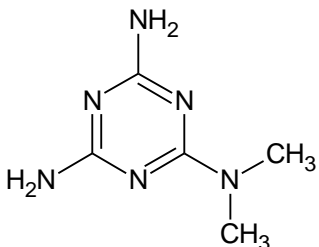
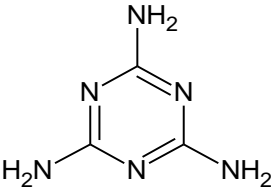
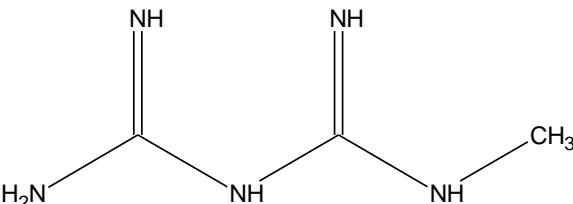
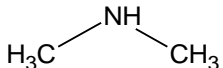
produced, however for about 45% of all experiments the XPRD pattern showed the presence of form B. It also has been found that the higher temperature favours the formation of form B, while crystallisation at room temperature favours the formation of form A. Unfortunately, samples of form B were only stable when left unattended - any actions, like grinding or removing the solids from the capillary result in transformation to form A. For Raman analysis the authors prepared samples of form B metformin hydrochloride by evaporating to dryness at 60°C the mixture of metformin hydrochloride in 3:1 acetone/water (concentration of 200 mg/mL) placed in a 0.7 mm diameter capillary tube.

4.3.2 Potential Impurities and their Determination

Six potential impurities have been reported in the literature [112] and they are listed below (Table 12).

All impurities listed in Table 12 (A-F) have been listed in British Pharmacopoeia (BP) [118]. The monograph for metformin hydrochloride provides an HPLC method for determination all of the impurities (Figure 80).

Table 12. Potential impurities in metformin hydrochloride samples

Impurity	IUPAC Name	Structure
A	Cyanoguanidine	
B	(4,6-diamino-1,3,5-triazin-2-yl)guanidine	
C	N,N-dimethyl-1,3,5-triazine-2,4,6-triamine	
D	Melamine	
E	1-methylbiguanide	
F	Dimethylamine	

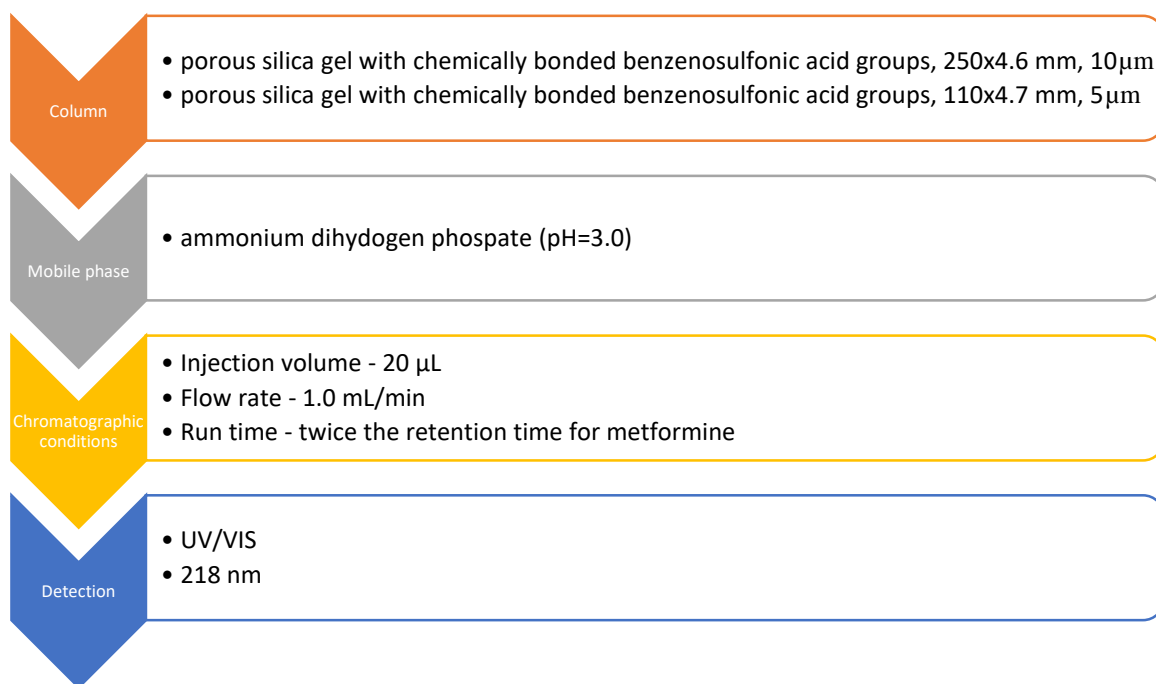


Figure 80. HPLC method for determination of metformin hydrochloride impurities [37]

For the cyanoguanidine BP provides a definite limit which is 1 μ g/ml (0.02% w/w) and for the rest of the impurities the level is 5 μ g/ml (0.1% w/w).

The literature provides a few examples of chromatographic methods, which have been used to determine impurities in metformin hydrochloride tablets. The most common chromatographic method was high performance liquid chromatography with UV detection. Examples of the application of HPLC-UV for determination metformin hydrochloride and its impurities are presented below.

Al-Rimawi [119] developed a simple HPLC-UV method for the analysis of metformin hydrochloride and 1-cyanoguanidine. For this method Nova-Pac silica column, 150mm x 3.9 mm, 4 μ m column was used and the column was kept at room temperature. Isocratic elution of a mixture of ammonium dihydrogen phosphate buffer (0.01 M, pH=5.0) and methanol (21/79, v/v) has been used and the flow rate was set at 1.0 ml/min. UV detection was performed at 232 nm and the run time was 5 minutes. The author provides a limit of detection for 1-cyanoguanidine at 5 μ g/ml and a limit of quantification at 10 μ g/ml. The full validation of the method was

performed and the provided method can be described as precise, selective and accurate.

Kłaczko and Anuszevska [112] published an HPLC-UV method for determination cyanoguanidine, melamine, (4,6-diamino-1,3,5-triazin-2-yl)guanidine and N,N-dimethyl-1,3,5-triazine-2,4,6-triamine in medical products containing metformin hydrochloride. Authors used 1.7% (w/v) ammonium dihydrogen phosphate water solution (pH=3.1) with a flow rate set at 1.5 mL/min. The injection volume was 40 μ L and the column (PARTISPHERE SCX 250x4.6 mm) was kept at 40°C. Spectrophotometric detection was performed at 218 nm. The method which has been published allows detection of cyanoguanidine at level of 0.01 μ g/mL, melamine at 0.04 μ g/mL, (4,6-diamino-1,3,5-triazin-2-yl)guanidine at 0.15 μ g/mL and N,N-dimethyl-1,3,5-triazine-2,4,6-triamine at 0.50 μ g/mL. Limits of quantification for all compounds were approximately three times limit of detection. This method was successfully applied to the analysis of medical products containing metformin hydrochloride.

Another paper, published by Ali et al. [120], describes the Mixed-Mode HILIC method for determination two the most common impurities in metformin hydrochloride products – cyanoguanidine and melamine. In this case the mobile phase was a mixture of acetonitrile and phosphate buffer (84:16 v/v ratio). A hydrophilic interaction liquid chromatography (HILIC) was used, so the chosen column was 250x4.6 mm, 5 μ m, Atlantis HILIC-Si. The flow rate was constant at 2 mL/min and the run time was 13 minutes. All compounds were detected at 218 nm using a UV detector. The authors carried out a full validation of the method to meet all the requirements of the International Conference on Harmonisation (ICH) guidelines. The limits of detection for cyanoguanidine, melamine and metformin hydrochloride were defined at 5 ng/mL for cyanoguanidine, 25 ng/mL for melamine and 100 ng/mL for metformin hydrochloride. The levels of quantification were not straight forward calculations from the limit of detection. For cyanoguanidine the limit of quantification was defined at 25 ng/mL, for melamine at 75 ng/mL and for metformin hydrochloride at 350 ng/mL. All statistical calculations to validate the method were

done and all values fit well within acceptable limits. This method could be successfully applied to the analysis of the commercially available products containing metformin hydrochloride.

Tache and Albu [121] proposed an algorithm which demonstrates the specificity of the analytical method for an analyte and allows the differentiation of an analyte of interest from its degradation products. As an example they used metformin hydrochloride and five of its impurities (cyanoguanidine, [(4,6-diamino-1,3,5-triazine-2-yl)-guanidine], N,N-dimethyl-1,3,5-triazine-2,4,6-triamine, 1,3,5-triazine-2,4,6-triamine, 1-methylbiguanide hydrochloride). Each of the impurities was a result of degradation in different environmental conditions (thermal degradation and photolysis, photolytic-hydrolysis, acidic-, alkaline- and neutral-oxidation). For their experiments the authors used a mixture of 10 mM aqueous octane-1-sulfonic acid sodium salt (pH=3.0) and acetonitrile (80/20 v/v ratio) as a mobile phase, setting the flow rate at 1.2 mL/min and run time of 30 minutes. The injection volume was 5 μ L and the column was kept at 30°C. 218 nm was selected as the UV absorption wavelength for all the compounds. All analysed compounds were well separated from each other, which showed the usefulness of the method for routine analysis.

There are not many methods for determination of dimethylamine (DMA) reported in the literature. Tsikas et al. [122] developed the gas chromatography – mass spectrometry method for quantification of dimethylamine (DMA) in human urine. Authors used pentafluorobenzoyl chloride as the derivatising agent in order to transform dimethylamine to its pentafluorobenzamide derivative. The method developed was proved to be rapid, precise and accurate.

Chobanyan et al. [123] used the same derivative of DMA to determine it in human plasma and serum using GC-MS and GC-tandem MS. The proposed method allows to determine DMA at the level of 100 nM with good accuracy (81%) and precision (0.3%).

Thermo Scientific in one of their application notes [124] presented an ion chromatography method for determination of dimethylamine in metformin hydrochloride samples. Five different DMA concentrations were tested within the

range of 0.1 – 2.0 mg/mL. Dionex IonPac CS10 Analytical Column (4x250 mm) was chosen for this study and the gradient elution was applied. The column was kept at 40°C and the injection volume was 20 µL. Suppressed conductivity detection was used during the study. Limit of detection for the method was 1.5 µg/L. Using this method, it was possible to separate dimethylamine and six common cations – lithium, sodium, ammonium, potassium, magnesium and calcium, that can be present in drug products.

4.4 Materials and Methods

4.4.1 Liquid Chromatography - Mass Spectrometry Method Development

Liquid Chromatography – Mass Spectrometry was selected as an analytical technique to determine and quantify organic impurities in metformin hydrochloride samples due to its high sensitivity and robustness.

The LC/MS system used in this study was the Agilent 1290 Infinity Quaternary system, equipped with the 1290 Infinity Diode Array Detector, 1290 Infinity Autosampler, 1290 Infinity Quaternary Pump and the Agilent 6530 Accurate-Mass Quadrupole Time-of-Flight Detector. The data were acquired using Agilent MassHunter Workstation Data Acquisition software and analysed using Agilent MassHunter Qualitative Analysis B.07.00 software.

A Merck, ZIC-HILIC, 200 Å, 3.5 µm, 4.6x50 mm column was used. Two different mobile phase compositions – both used in gradient mode - were tested:

- 1) Mobile phase A: 10 mM ammonium acetate in water with 5% methanol
Mobile phase B: 10 mM ammonium acetate in acetonitrile with 5% methanol
- 2) Mobile phase A: 0.1% formic acid in water
Mobile phase B: 0.1% formic acid in acetonitrile

Both of these mobile phase compositions were found to provide promising results, however due to difficulties caused by ammonium acetate present in method 1 – blockage in the capillaries in the mass spectrometer, method 2 was selected for this work.

As mentioned before, the gradient program was selected for this work - Table 13 shows detailed information about the mobile phase composition through the run.

Table 13. LC/MS method gradient program

Time [min]	A [%]	B[%]	Flow rate [mL/min]
0	30	70	0.4
1.5	30	70	
5	80	20	
9	80	20	
9.1	30	70	
12	30	70	

The flow rate was set to 0.4 mL/min and the oven temperature to 30°C. The injection volume was 10 µL and two detection wavelengths were chosen – 210 nm and 254 nm. Once the elution was optimised, several MS parameters were tested to achieve the best possible detection. Those parameters were: drying gas temperature (DG), drying gas flow (DF), fragmentor voltage (Frag), VCap voltage (VCap) and the nebuliser pressure (Neb). Table 14 summarises all tested parameters and those, highlighted in green were chosen as the final parameters for the developed method. It was found that under those parameters the highest intensity and the best peak shape was achieved for all investigated compounds.

Table 14. MS detector optimisation parameters, with final values highlighted in green

DF [L/min]	DG [°C]	Frag [V]	VCap [V]	Neb [psig]
4	150	80	1000	15
6	200	100	2000	35
8	250	120	3000	45
10	300	140	4000	60
12	350	160	5000	
		180		

All compounds were detected using the positive ion polarity, the acquisition mass range was set up as 30-1005 m/z, the acquisition rate was chosen to be 2 spectra per second with the acquisition time of 5000 ms per spectrum.

Final retention times of all detected impurities and metformin hydrochloride are presented below in Table 15.

Table 15. Retention times for metformin hydrochloride and its impurities

Impurity	IUPAC Name	Material supplier	Retention time [min]
A	Cyanoguanidine	Sigma Aldrich	1.994
B	(4,6-diamino-1,3,5-triazin-2-yl)guanidine	LGC Standards	4.930
C	N,N-dimethyl-1,3,5-triazine-2,4,6-triamine	LGC Standards	3.714
D	Melamine	Sigma Aldrich	4.956
E	1-methylbiguanide	LGC Standards	5.828
	Metformin hydrochloride	Sigma Aldrich	4.749

4.4.1.1 Liquid Chromatography – Mass Spectrometry Calibration Curves Preparation

Each of determined compounds was weighed out accurately (5 mg of each compound) and added to a 50 mL volumetric flask before being dissolved in the mixture of water and acetonitrile (30/70 v/v). Chosen composition of solvents matched the initial mobile phase composition used in the chromatographic method. The stock solution had concentration of 100 µg/mL.

Standard solutions for the evaluation of the metformin hydrochloride calibration curve were prepared, using a dilution by a required factor, over a concentration range of 15.0-5.0 µg/mL. Standard solutions for the evaluation of cyanoguanidine calibration curve were prepared, using a dilution by a required factor, over a concentration range of 550.0-50.0 ng/mL. Standard solutions for the evaluation of

the melamine, 1-methylbiguanide, (4,6-diamino-1,3,5-triazin-2-yl) guanidine and N,N-dimethyl-1,3,5-triazine-2,4,6-triamine calibration curve were prepared, using a dilution by a required factor, over a concentration range of 25.0-1.0 ng/mL.

4.4.2 Gas Chromatography Sample Preparation and Measurement Conditions

Gas chromatography was the first choice analytical technique for determination of dimethylamine (DMA). The initial measurements of dimethylamine as its hydrochloride salt were unsuccessful and therefore it was necessary to derivatise dimethylamine hydrochloride to dimethylacetamide. Several trials were carried out in order to find the best derivatisation route and they are described below:

- 1) 100 µg of DMA was dissolved in 1 mL of 1% sodium orthophosphoric acid monohydrate aqueous solution, then two portions of 10µL of acetic anhydride were added and the solution was extracted with 1 mL of ethyl acetate. 200 µL of organic layer was therefore transferred into a GC/MS vial and analysed.
- 2) 500 µg of DMA was treated with 200 µL of a 1:1 (v/v) mixture of pyridine and acetic anhydride for 30 minutes at 60°C. In the next step almost all the reagents were blown off using nitrogen and the residue was dissolved in 1 mL of ethyl acetate and analysed using GC/MS.
- 3) 500 µg of DMA was dissolved in 1 mL of water and then basified with few drops of ammonia solution. Afterwards the solution was treated in the same way as in trial 2.
- 4) 100 µg of DMA was dissolved in 1 mL of 5% sodium orthophosphoric acid monohydrate aqueous solution and subsequently treated as described for trial 2.

1 µL of each prepared sample was injected in splitless mode at 200°C into the GC-MS (Focus GC-DSQ2) system from Thermo Fisher Scientific (Bremen, Germany), equipped with InertCap 1 MS (30m, 0.25 mm i.d. and 0.25 µm film thickness) capillary column (GL Sciences, Japan). The temperature gradient was programmed as follows: initially holding at 50°C for 2 min, linearly increasing to 200°C at the rate of 5°C/min and

holding at 200°C for 5 minutes. The temperature in the ionisation source was set at 250°C and the ionisation voltage was 70 eV for EI-MS in positive mode.

4.4.3 Ion Chromatography Conditions

All measurements were carried out using the Reagent-Free Capillary HPIC system of an ICS-5000+ instrument (Thermo Fisher Scientific, Hemel Hempstead UK). The system contains a methanesulfonic acid electrolytic eluent generation module, an anion capillary eluent suppressor (EGC MSA), an AS-AP Autosampler and a conductivity detector. All eluents were generated as methanesulfonic solution using a diluent of ultrapure water (ICW 3000) purification system with a resistivity of 18.2 MΩ.cm ((ICW 3000), Millipore, Watford, UK). A Dionex IonPac CS19, 0.4x250 mm capillary column was used in the separations.

The data were collected and analysed using Chromeleon 6.8 software (Thermo Fisher Scientific).

4.4.3.1 *Ion Chromatography Calibration Curve for Dimethylamine Preparation*

Dimethylamine (Sigma Aldrich) was weighed out accurately (5 mg) and added to a 50 mL volumetric flask before being dissolved in deionised water. A stock solution had concentration of 100 µg/mL. Standard solutions for the evaluation of dimethylamine calibration curve were prepared over a concentration range of 20.0-1.0 µg/mL

4.4.3.2 *Sample Preparation for Ion Chromatography Analysis*

Metformin hydrochloride (Molecula) was weighed out accurately (50 mg) and added to a 50 mL volumetric flask before being dissolved in deionised water. A final concentration of metformin hydrochloride was 1 mg/mL.

4.4.4 Temperature Stability Test Conditions

Temperature stability test of metformin hydrochloride was carried out in order to investigate whether or not the chosen compound was stable under the desired temperature conditions which might be used for crystallisation. As was mentioned,

this project was carried out to provide the required information for designing the continuous crystallisation process of metformin hydrochloride.

A sample of metformin at 10% w/w in 80:20 ethanol:water was kept at 65°C for 10 days. During this period samples were taken twice a day. Those samples were diluted then run using the LC/MS to track the metformin hydrochloride and impurity concentrations over the time period of 10 days. Figure 81 shows a schematic diagram of the setup used during this test.

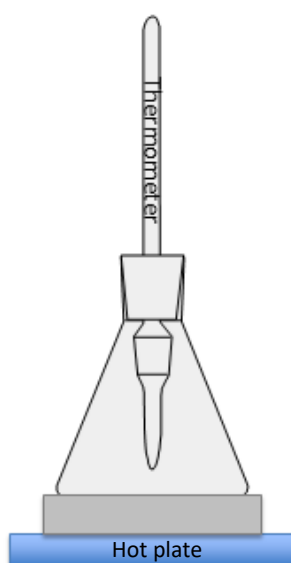


Figure 81. A schematic diagram of the setup used during the temperature stability test

4.5 Results

4.5.1 Calibration Curves and Method Validation Results

4.5.1.1 Calibration curves

Each concentration of standard solution was injected three times and the results are shown in Table 16. An example of the extracted ion chromatogram for concentration of 10 µg/mL is shown in Figure 129 (Appendix, Chapter 7).

Table 16. Calibration curve results of metformin hydrochloride, including regression coefficient and the equation

Concentration [µg/mL]	Average Peak Area (n=3)	Peak Area RSD [%]
15.0	232982069.1	1.04
12.5	210974952.8	0.22
10.0	188437251.9	0.18
7.5	164838591.8	0.55
5.0	132432287.3	0.43
Correlation coefficient: $R^2 = 0.9932$ Regression line: $y = 9889436.98x + 87038660.76$		

For melamine each concentration of standard solutions was injected three times and the results are shown in Table 17. An example of the extracted ion chromatogram for concentration of 10 ng/mL is shown in Figure 133 (Appendix, Chapter 7).

Table 17. Calibration curve results of melamine, including regression coefficient and the equation

Concentration [ng/mL]	Average Peak Area (n=3)	Peak Area RSD [%]
25.0	621372.27	0.75
10.0	292552.83	1.36
5.0	160547.09	1.51
2.5	81567.21	0.60
1.0	44205.34	1.74
Correlation coefficient: $R^2 = 0.9961$ Regression line: $y = 23940.24x + 31768.82$		

For 1-methylbiguanide each concentration of standard solutions was injected three times and the results are shown in Table 18. An example of the extracted ion chromatogram for concentration of 10 µg/mL is shown in Figure 134 (Appendix, Chapter 7).

Table 18. Calibration curve results of 1-methylbiguanide, including regression coefficient and the equation

Concentration [µg/mL]	Average Peak Area (n=3)	Peak Area RSD [%]
25.0	731757.40	1.13
10.0	238570.79	1.52
5.0	135792.29	0.89
2.5	29681.00	1.17
1.0	8252.22	1.36
Correlation coefficient: $R^2= 0.9954$		
Regression line: $y=30326.80x - 35032.42$		

For (4,6-diamino-1,3,5-triazin-2-yl) guanidine each concentration of standard solutions was injected three times and the results are shown in Table 19. An example of the extracted ion chromatogram for concentration of 10 µg/mL is shown in Figure 131 (Appendix, Chapter 7).

Table 19. Calibration curve results of (4,6-diamino-1,3,5-triazin-2-yl) guanidine, including regression coefficient and the equation

Concentration [µg/mL]	Average Peak Area (n=3)	Peak Area RSD [%]
25.0	2952957.35	1.43
10.0	1541588.79	1.04
5.0	913960.00	0.73
2.5	592905.22	1.23
1.0	348868.92	1.30
Correlation coefficient: $R^2=0.9925$		
Regression line: $y=106634.94x+324332.08$		

For N,N-dimethyl-1,3,5-triazine-2,4,6-triamine each concentration of standard solutions was injected three times and the results are shown in Table 20. An example of the extracted ion chromatogram for concentration of 10 µg/mL is shown in Figure 132 (Appendix, Chapter 7).

Table 20. Calibration curve results of N,N-dimethyl-1,3,5-triazine-2,4,6-triamine, including regression coefficient and the equation

Concentration [µg/mL]	Average Peak Area (n=3)	Peak Area RSD [%]
25.0	5199994.48	1.01
10.0	2938138.69	0.46
5.0	1939696.09	0.55
2.5	1383356.09	1.58
1.0	1015050.08	1.22
Correlation coefficient: $R^2 = 0.9919$		
Regression line: $y = 171620.70x + 1002146.99$		

For cyanoguanidine each concentration of standard solutions was injected three times and the results are shown in Table 21. An example of the extracted ion chromatogram for concentration of 10 µg/mL is shown in Figure 130 (Appendix, Chapter 7).

Table 21. Calibration curve results of cyanoguanidine, including regression coefficient and the equation

Concentration [µg/mL]	Average Peak Area (n=3)	Peak Area RSD [%]
550.0	364302.99	0.41
400.0	275032.08	0.36
250.0	171479.39	1.53
100.0	81157.15	1.14
50.0	39883.76	0.90
Correlation coefficient: $R^2 = 0.9990$		
Regression line: $y = 646.0x + 11950.64$		

4.5.1.2 Precision studies

The precision of the method was determined by repeat analysis (intraday precision) of standard solutions. Precision was determined in six replicates on the same day for three different concentrations. The results are expressed as %RSD of the measurement for both retention time and peak area. The acceptable value of %RSD is below 2% - in tables below green indicates that the results were below this value and orange indicate that the results were just above the 2% limit. Table 22, Table 23 and Table 24 show the results obtained to demonstrate the precision of the LC/MS method for metformin hydrochloride determination at three different concentrations – 15 µg/mL, 10 µg/mL and 5 µg/mL.

Table 22. Demonstration of the precision of the LC/MS method for metformin hydrochloride as shown by the results on 6 replicate injections of one solution of 15 µg/mL concentration

Injection number	RT [min]	Peak Area
1	4.734	228624063.15
2	4.714	230913932.71
3	4.732	230320522.99
4	4.722	233774040.75
5	4.733	229276898.39
6	4.711	232792541.28
Mean	4.724	230950333.21
RSD [%]	0.22	0.87

Table 23. Demonstration of the precision of the LC/MS method for metformin hydrochloride as shown by the results on 6 replicate injections of one solution of 10 µg/mL concentration

Injection number	RT [min]	Peak Area
1	4.756	190768132.20
2	4.740	191376092.05
3	4.730	191332134.39
4	4.753	192883076.76
5	4.749	191508568.28
6	4.750	193984388.41
Mean	4.746	191975398.68
RSD [%]	0.19	0.63

Table 24. Demonstration of the precision of the LC/MS method for metformin hydrochloride as shown by the results on 6 replicate injections of one solution of 5 µg/mL concentration

Injection number	RT [min]	Peak Area
1	4.780	134116948.03
2	4.773	133338849.38
3	4.775	134250804.05
4	4.780	131681181.45
5	4.775	133966661.58
6	4.771	134254678.56
Mean	4.776	133601520.51
RSD [%]	0.08	0.75

Table 25, Table 26 and Table 27 show the results obtained to demonstrate the precision of the LC/MS method for melamine determination at three different concentrations – 25 ng/mL, 5 ng/mL and 1 ng/mL.

Table 25. Demonstration of the precision of the LC/MS method for melamine as shown by the results on 6 replicate injections of one solution of 25 ng/mL concentration

Injection number	RT [min]	Peak Area
1	4.953	628732.11
2	4.946	613842.26
3	4.953	611570.68
4	4.951	626615.15
5	4.945	618047.13
6	4.950	619454.53
Mean	4.950	619710.31
RSD [%]	0.06	1.10

Table 26. Demonstration of the precision of the LC/MS method for melamine as shown by the results on 6 replicate injections of one solution of 5 ng/mL concentration

Injection number	RT [min]	Peak Area
1	4.959	163266.14
2	4.964	161767.35
3	4.955	161607.02
4	4.960	159148.77
5	4.955	159154.96
6	4.952	164937.23
Mean	4.958	161646.91
RSD [%]	0.09	1.41

Table 27. Demonstration of the precision of the LC/MS method for melamine as shown by the results on 6 replicate injections of one solution of 1 ng/mL concentration

Injection number	RT [min]	Peak Area
1	4.964	43391.41
2	4.965	44924.82
3	4.947	44299.79
4	4.972	44635.95
5	4.980	43520.58
6	4.942	42175.41
Mean	4.962	43911.31
RSD [%]	0.29	2.30

Table 28, Table 29 and Table 30 show the results obtained to demonstrate the precision of the LC/MS method for 1-methylbiguanide determination at three different concentrations – 25 ng/mL, 5 ng/mL and 1 ng/mL.

Table 28. Demonstration of the precision of the LC/MS method for 1-methylbiguanide as shown by the results on 6 replicate injections of one solution of 25 ng/mL concentration

Injection number	RT [min]	Peak Area
1	5.856	747498.34
2	5.855	732062.10
3	5.859	743685.78
4	5.859	744658.47
5	5.856	748946.13
6	5.853	752447.68
Mean	5.856	744883.08
RSD [%]	0.04	0.94

Table 29. Demonstration of the precision of the LC/MS method for 1-methylbiguanide as shown by the results on 6 replicate injections of one solution of 5 ng/mL concentration

Injection number	RT [min]	Peak Area
1	5.880	134742.86
2	5.889	129483.96
3	5.882	134978.27
4	5.874	132007.62
5	5.873	132771.53
6	5.875	131952.83
Mean	5.879	132656.18
RSD [%]	0.10	1.54

Table 30. Demonstration of the precision of the LC/MS method for 1-methylbiguanide as shown by the results on 6 replicate injections of one solution of 1 ng/mL concentration

Injection number	RT [min]	Peak Area
1	5.914	8126.36
2	5.907	8541.42
3	5.916	8692.88
4	5.900	8286.91
5	5.894	8707.07
6	5.895	8343.40
Mean	5.904	8449.67
RSD [%]	0.16	2.78

Table 31, Table 32 and Table 33 show the results obtained to demonstrate the precision of the LC/MS method for (4,6-diamino-1,3,5-triazin-2-yl) guanidine determination at three different concentrations – 25 ng/mL, 5 ng/mL and 1 ng/mL.

Table 31. Demonstration of the precision of the LC/MS method for (4,6-diamino-1,3,5-triazin-2-yl) guanidine as shown by the results on 6 replicate injections of one solution of 25 ng/mL concentration

Injection number	RT [min]	Peak Area
1	4.922	2979567.16
2	4.917	2976767.16
3	4.921	2912205.48
4	4.912	2910546.58
5	4.916	3010367.02
6	4.912	2947590.68
Mean	4.917	2956174.01
RSD [%]	0.08	1.35

Table 32. Demonstration of the precision of the LC/MS method for (4,6-diamino-1,3,5-triazin-2-yl) guanidine as shown by the results on 6 replicate injections of one solution of 5 ng/mL concentration

Injection number	RT [min]	Peak Area
1	4.939	901252.49
2	4.933	915012.68
3	4.928	921989.49
4	4.924	916284.59
5	4.927	921276.42
6	4.923	915788.81
Mean	4.929	915267.41
RSD [%]	0.12	0.82

Table 33. Demonstration of the precision of the LC/MS method for (4,6-diamino-1,3,5-triazin-2-yl) guanidine as shown by the results on 6 replicate injections of one solution of 1 ng/mL concentration

Injection number	RT [min]	Peak Area
1	4.949	354215.96
2	4.947	354500.30
3	4.943	360626.52
4	4.935	347119.93
5	4.942	359050.72
6	4.942	363334.61
Mean	4.943	356474.67
RSD [%]	0.10	1.62

Table 34, Table 35 and Table 36 show the results obtained to demonstrate the precision of the LC/MS method for N,N-dimethyl-1,3,5-triazine-2,4,6-triamine determination at three different concentrations – 25 ng/mL, 5 ng/mL and 1 ng/mL.

Table 34. Demonstration of the precision of the LC/MS method for N,N-dimethyl-1,3,5-triazine-2,4,6-triamine as shown by the results on 6 replicate injections of one solution of 25 ng/mL concentration

Injection number	RT [min]	Peak Area
1	3.694	5239365.58
2	3.694	5252928.85
3	3.687	5238382.99
4	3.691	5269384.10
5	3.690	5220791.00
6	3.688	5214820.70
Mean	3.691	5239278.87
RSD [%]	0.07	0.38

Table 35. Demonstration of the precision of the LC/MS method for N,N-dimethyl-1,3,5-triazine-2,4,6-triamine as shown by the results on 6 replicate injections of one solution of 5 ng/mL concentration

Injection number	RT [min]	Peak Area
1	3.714	1959070.71
2	3.713	1972926.03
3	3.713	1986161.82
4	3.703	1964175.42
5	3.716	1955578.29
6	3.708	1959541.96
Mean	3.711	1966242.37
RSD [%]	0.13	0.58

Table 36. Demonstration of the precision of the LC/MS method for N,N-dimethyl-1,3,5-triazine-2,4,6-triamine as shown by the results on 6 replicate injections of one solution of 1 ng/mL concentration

Injection number	RT [min]	Peak Area
1	3.740	1084512.73
2	3.740	1111027.05
3	3.746	1118880.67
4	3.742	1137717.89
5	3.742	1110752.07
6	3.737	1139956.04
Mean	3.741	1117141.08
RSD [%]	0.08	1.83

Table 37, Table 38 and Table 39 show the results obtained to demonstrate the precision of the LC/MS method for cyanoguanidine determination at three different concentrations – 550 ng/mL, 250 ng/mL and 50 ng/mL.

Table 37. Demonstration of the precision of the LC/MS method for cyanoguanidine as shown by the results on 6 replicate injections of one solution of 550 ng/mL concentration

Injection number	RT [min]	Peak Area
1	1.997	365376.59
2	1.994	362608.75
3	1.996	364923.62
4	1.988	363598.11
5	2.000	370022.71
6	1.987	363986.09
Mean	1.994	365085.98
RSD [%]	0.24	0.71

Table 38. Demonstration of the precision of the LC/MS method for cyanoguanidine as shown by the results on 6 replicate injections of one solution of 250 ng/mL concentration

Injection number	RT [min]	Peak Area
1	1.998	177054.62
2	1.991	175208.11
3	1.995	178890.34
4	1.990	174524.15
5	1.992	178668.74
6	1.993	177813.21
Mean	1.993	177026.53
RSD [%]	0.15	1.02

Table 39. Demonstration of the precision of the LC/MS method for cyanoguanidine as shown by the results on 6 replicate injections of one solution of 50 ng/mL concentration

Injection number	RT [min]	Peak Area
1	1.999	40277.94
2	1.996	39803.57
3	1.992	39569.78
4	1.993	39560.07
5	1.992	39729.66
6	1.999	39420.43
Mean	1.995	39726.91
RSD [%]	0.17	0.76

4.5.1.3 Accuracy studies

The accuracy of the method was demonstrated by preparing samples of three known concentrations in six replicates. The results were expressed as a mean value and the error was expressed as %RSD.

Table 40. Demonstration of the accuracy of the LC/MS method for metformin hydrochloride as shown by the results on 6 replicate injections of three solutions of 15, 10 and 5 µg/mL concentrations respectively

Injection Number	Calculated Concentration [µg/mL]	Expected Concentration [µg/mL]	Accuracy [%]	RSD [%]
1	14.32	15	95.45	1.39
2	14.55		96.99	
3	14.49		96.59	
4	14.84		98.92	
5	14.38		95.89	
6	14.74		98.26	
		Average:	97.01	
7	10.49	10	104.89	1.15
8	10.55		105.50	
9	10.55		105.46	
10	10.70		107.03	
11	10.56		105.64	
12	10.81		108.14	
		Average:	106.11	
13	4.76	5	95.21	2.15
14	4.68		93.64	
15	4.77		95.48	
16	4.51		90.28	
17	4.75		94.91	
18	4.77		95.49	
		Average:	94.17	

Table 41. Demonstration of the accuracy of the LC/MS method for melamine as shown by the results on 6 replicate injections of three solutions of 25, 5 and 1 ng/mL concentrations respectively

Injection Number	Calculated Concentration [ng/mL]	Expected Concentration [ng/mL]	Accuracy [%]	RSD [%]
1	24.94	25	99.74	1.16
2	24.31		97.25	
3	24.22		96.87	
4	24.85		99.39	
5	24.49		97.96	
6	24.55		98.19	
		Average:	98.23	
7	5.49	5	109.85	1.75
8	5.43		108.60	
9	5.42		108.47	
10	5.32		106.41	
11	5.32		106.42	
12	5.56		111.25	
		Average:	108.50	
13	0.49	1	48.55	8.37
14	0.55		54.95	
15	0.52		52.34	
16	0.54		53.75	
17	0.49		49.09	
18	0.43		43.47	
		Average:	50.36	

Table 42. Demonstration of the accuracy of the LC/MS method for 1-methylbiguanide as shown by the results on 6 replicate injections of three solutions of 25, 5 and 1 ng/mL concentrations respectively

Injection Number	Calculated Concentration [ng/mL]	Expected Concentration [ng/mL]	Accuracy [%]	RSD [%]
1	25.80	25	103.21	0.90
2	25.29		101.18	
3	25.68		102.71	
4	25.71		102.84	
5	25.85		103.40	
6	25.97		103.87	
		Average:	102.87	
7	5.60	5	111.96	1.21
8	5.42		108.50	
9	5.61		112.12	
10	5.51		110.16	
11	5.53		110.66	
12	5.51		110.12	
		Average:	110.59	
13	1.42	1	142.31	0.54
14	1.44		143.68	
15	1.44		144.18	
16	1.43		142.84	
17	1.44		144.23	
18	1.43		143.03	
		Average:	143.38	

Table 43. Demonstration of the accuracy of the LC/MS method for (4,6-diamino-1,3,5-triazin-2-yl) guanidine as shown by the results on 6 replicate injections of three solutions of 25, 5 and 1 ng/mL concentrations respectively

Injection Number	Calculated Concentration [ng/mL]	Expected Concentration [ng/mL]	Accuracy [%]	RSD [%]
1	24.73	25	98.93	1.53
2	24.71		98.82	
3	24.10		96.40	
4	24.08		96.34	
5	25.02		100.08	
6	24.43		97.73	
		Average:	98.05	
7	5.24	5	104.83	1.30
8	5.37		107.41	
9	5.44		108.72	
10	5.38		107.65	
11	5.43		108.58	
12	5.38		107.56	
		Average:	107.46	
13	0.11	1	11.14	40.92
14	0.11		11.41	
15	0.17		17.16	
16	0.04		4.49	
17	0.16		15.68	
18	0.20		19.70	
		Average:	13.26	

Table 44. Demonstration of the accuracy of the LC/MS method for N,N-dimethyl-1,3,5-triazine-2,4,6-triamine as shown by the results on 6 replicate injections of three solutions of 25, 5 and 1 ng/mL concentrations respectively

Injection Number	Calculated Concentration [ng/mL]	Expected Concentration [ng/mL]	Accuracy [%]	RSD [%]
1	24.69	25	98.76	0.48
2	24.77		99.07	
3	24.68		98.73	
4	24.86		99.46	
5	24.58		98.32	
6	24.55		98.19	
		Average:	98.76	
7	5.58	5	111.52	1.19
8	5.66		113.13	
9	5.73		114.67	
10	5.61		112.11	
11	5.56		111.11	
12	5.58		111.57	
		Average:	112.35	
13	0.48	1	47.99	17.78
14	0.63		63.44	
15	0.68		68.02	
16	0.79		78.99	
17	0.63		63.28	
18	0.80		80.30	
		Average:	67.00	

Table 45. Demonstration of the accuracy of the LC/MS method for cyanoguanidine as shown by the results on 6 replicate injections of three solutions of 550, 250 and 50 ng/mL concentrations respectively

Injection Number	Calculated Concentration [ng/mL]	Expected Concentration [ng/mL]	Accuracy [%]	RSD [%]
1	547.10	550	99.47	0.74
2	542.81		98.69	
3	546.40		99.35	
4	544.35		98.97	
5	554.29		100.78	
6	544.95		99.08	
		Average:	99.39	
7	255.58	250	102.23	1.10
8	252.72		101.09	
9	258.42		103.37	
10	251.66		100.66	
11	258.08		103.23	
12	256.75		102.70	
		Average:	102.21	
13	43.85	50	87.70	1.09
14	43.12		86.23	
15	42.75		85.51	
16	42.74		85.48	
17	43.00		86.00	
18	42.52		85.05	
		Average:	85.99	

4.5.1.4 Column Efficiency, Peak Asymmetry and Capacity Factor Studies

Toluene was chosen as the non-retained compound, since it has no affinity for the stationary phase and therefore elutes with the solvent front at time t_0 (dead time). This parameter was calculated as an average from the three injections and was found to be 1.559 minute.

The capacity factor was calculated based on Equation 68 and the results are presented in Table 46.

Table 46. Capacity factors for all individual compounds

Compound	Capacity Factor (K')
Metformin hydrochloride	0.672
Melamine	0.685
Cyanoguanidine	0.218
1-methylbiguanide	0.732
(4,6-diamino-1,3,5-triazin-2-yl) guanidine	0.684
N,N-dimethyl-1,3,5-triazine-2,4,6-triamine	0.580

Equation 69 and Equation 70 were used to calculate the column efficiency and Equation 71 was used to estimate the peak asymmetry. The results are summarised in Table 47.

Table 47. Summary of two validation parameters: peak asymmetry and column efficiency for all analysed compounds

Compound	Concentration [µg/mL]	Peak Asymmetry Factor (AF) ± %RSD	Column Efficiency (n) [m] ± %RSD
Metformin hydrochloride	15	1.81±3.85%	40421±0.66%
	10	1.69±5.62%	50718±0.88%
	5	1.53±4.12%	66580±0.42%
Compound	Concentration [ng/mL]	Peak Asymmetry Factor (AF)	Column Efficiency (n) [m]
Melamine	25	1.38±4.84%	150708±3.97%
	5	1.35±5.44%	170381±5.02%
	1	1.01±5.05%	147338±4.75%
Cyanoguanidine	550	1.26±3.38%	88159±1.16%
	250	1.26±4.30%	93922±1.22%
	50	1.24±5.03%	98085±3.70%
1-methylbiguanide	25	1.74±1.76%	337774±1.29%
	5	1.41±5.03%	319629±2.12%
	1	0.98±5.01%	1322454±4.28%
(4,6-diamino-1,3,5-triazin-2-yl) guanidine	25	1.18±2.81%	131045±1.43%
	5	1.01±3.22%	176233±3.39%
	1	0.87±3.22%	198331±3.62%
N,N-dimethyl-1,3,5-triazine-2,4,6-triamine	25	1.24±2.39%	69662±0.55%
	5	1.25±3.01%	75574±0.58%
	1	1.22±3.63%	78393±1.16%

4.5.1.5 Limit of Detection and Limit of Quantification

Limit of Detection (LOD) and Limit of Quantification (LOQ) for all individual components were calculated based on Equation 66 and Equation 67 respectively. The slope value was taken from the calibration curve equation and standard deviation of the response was taken as the standard deviation of the lowest point in calibration curve. The results are shown below in Table 48.

Table 48. Limit of Detection and Limit of Quantification for all individual compounds

Compound	Slope	Standard Deviation	LOD [$\mu\text{g/mL}$]	LOQ [$\mu\text{g/mL}$]
Metformin hydrochloride	9889436.98	570505.31	0.19	0.58
Compound	Slope	Standard Deviation	LOD [ng/mL]	LOQ [ng/mL]
Melamine	23940.24	771.06	0.11	0.32
1-methylbiguanide	30326.80	112.60	0.01	0.04
cyanoguanidine	646.00	360.83	1.84	5.56
(4,6-diamino-1,3,5-triazin-2-yl) guanidine	106634.94	4518.76	0.14	0.42
N,N-dimethyl-1,3,5-triazine-2,4,6-triamine	171620.70	12363.53	0.24	0.72

4.5.2 Stability Test Results

Stability test results are presented below in Figure 82. It shows the concentration change over 241 hours. Three samples were taken at each time point and each sample was analysed three times, giving the total number of repetitions of nine. As it can be seen, the level remained constant at the level of approximately 10 µg/mL.

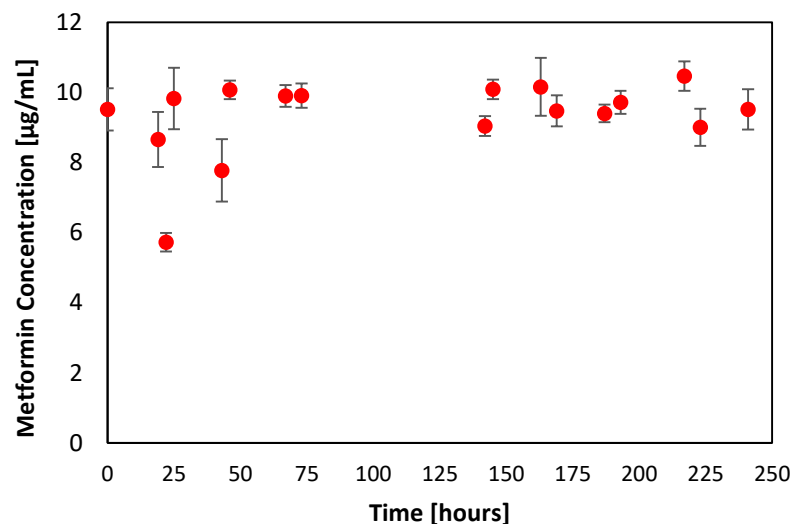
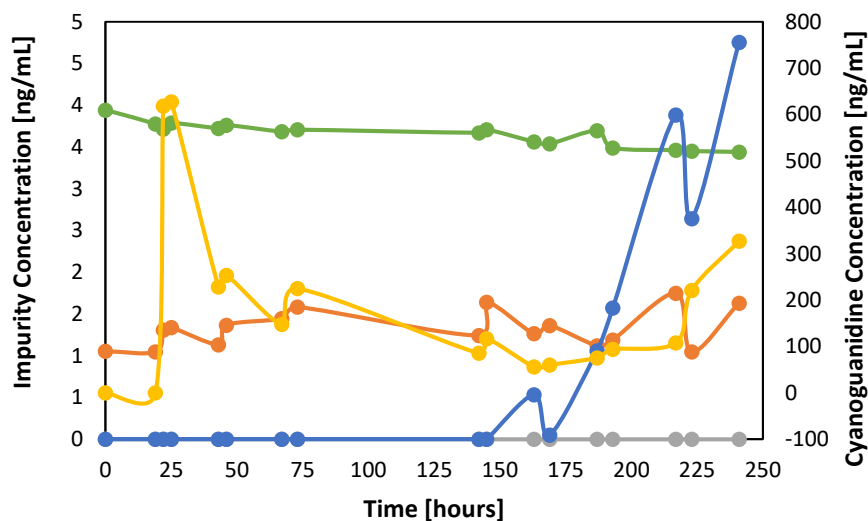


Figure 82. Metformin hydrochloride stability test results, showing the changes in its concentration over time

The concentration changes for all studied impurities are shown in Figure 83. No melamine was detected in the samples. The levels of 1-methylbiguanide, (4,6-diamino-1,3,5-triazin-2-yl) guanidine and cyanoguanidine were stable throughout the stability test. N,N-dimethyl-1,3,5-triazine-2,4,6-triamine started forming at the time of 163 hours and continue to increase until the end of the experiment. A proposed mechanism of formation is shown in Figure 84, however needs to be further investigated.



● (4,6-diamino-1,3,5-triazin-2-yl)guanidine ● 1-methylbiguanide
● Melamine ● N,N-dimethyl-1,3,5-triazine-2,4,6-triamine
● Cyanoguanidine

Figure 83. Stability test results, showing the changes in the impurities concentrations over time: green – (4,6-diamino-1,3,5-triazin-2-yl) guanidine, grey – melamine, yellow – cyanoguanidine, orange – 1-methylbiguanide, blue – N,N-dimethyl-1,3,5-triazine-2,4,6-triamine

Table 49 shows relative impurity concentration (% w/w) in relation to metformin hydrochloride in the initial solution (t=0 hr) and in the final solution (t=241 hr).

Table 49. Relative impurity concentrations (%w/w relative to metformin hydrochloride) in the initial solution (t=0) and final solution (t=241 hr).

Impurity	Relative impurity concentration [%w/w] t=0 [hr]	Relative impurity concentration [%w/w] t=241 [hr]
Cyanoguanidine	0	3.43
Melamine	0	0
1-methylbiguanide	0.01	0.02
4,6-diamino-1,3,5-triazin-2-yl) guanidine	0.04	0.04
N,N-dimethyl-1,3,5-triazine-2,4,6-triamine	0	0.05

4.5.3 Results for Dimethylamine Determination

4.5.3.1 *Gas Chromatography Results*

Unfortunately, none of the attempted methods for derivatisation of dimethylamine to dimethylacetamide were successful. The derivatisation involved many steps, which resulted in many residual materials being left in the sample. Those residuals had a negative effect on the GC/MS results – solvent residuals overlapped dimethylamine peak and therefore it was impossible to track DMA in the samples.

4.5.3.2 *Ion Chromatography Calibration Curve*

Standard solutions for the evaluation of dimethylamine calibration curve were prepared over a concentration range of 20.0-1.0 µg/mL in triplicate and the results are shown in Table 50.

Table 50. Calibration curve results for dimethylamine

Concentration (µg/ml)	Injection No.	Peak area [µSmin]	Average Peak Area [µSmin]	RSD (%)
1	1	0.2420	0.2409	0.68
	2	0.2397		
	3			
2.5	1	0.6289	0.6084	2.93
	2	0.5990		
	3	0.5972		
5	1	1.2503	1.2319	1.29
	2	1.2238		
	3	1.2217		
7.5	1	1.9183	1.8341	4.38
	2	1.7581		
	3	1.8260		
10	1	2.5066	2.5319	0.88
	2	2.5406		
	3	2.5485		
15	1	3.7533	3.7166	0.86
	2	3.6951		
	3	3.7013		
20	1	4.8190	4.7673	1.45
	2	4.6889		
	3	4.7941		
Correlation coefficient: $R^2=0.99867$ Regression line: $y=0.2411x + 0.0318$				

4.5.3.3 Application of the Ion Chromatography Method for Dimethylamine

Due to equipment failure when the stability test was carried out, the levels of dimethylamine were not quantified.

In order to test whether the dimethylamine can be detected in real samples, the raw material of metformin hydrochloride was analysed. Figure 84 shows that dimethylamine can be detected in real samples. It demonstrates the advantage of an impurity eluting before the studied API, in this case metformin hydrochloride. The concentration of dimethylamine in raw material metformin hydrochloride sample calculated based on calibration curve was 1.26 µg/mL, equivalent to 1260 ppm relative to the metformin hydrochloride sample.

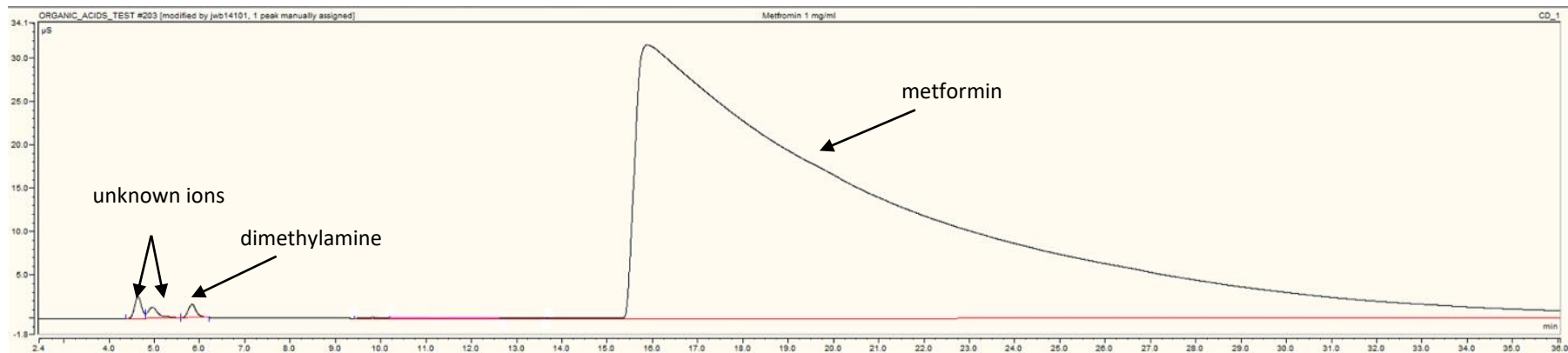


Figure 84. An example of ion chromatogram, for dimethylamine (5.827 min) present in metformin hydrochloride sample

4.6 Discussion

The calibration curves given in this chapter all demonstrated good fits into the regression model with the R^2 value being greater than 0.99. This shows the excellent relationship between the peak area values and the concentration for all analysed compounds.

The precision studies for the retention time and peak area for six injections at three different concentrations showed that for metformin hydrochloride, (4,6-diamino-1,3,5-triazin-2-yl) guanidine, N,N-dimethyl-1,3,5-triazine-2,4,6-triamine and cyanoguanidine, the RSD values were less than 2% for both parameters. This was true for all concentrations that were studied, showing that the method was highly reproducible and reliable. Melamine and 1-methylbiguanide had RSD values under 2% for their retention times but over 2% for the peak area of the lowest concentration. This means that the method is reproducible and reliable for these compounds, however the error increases as the concentration decreases and this was as expected.

The accuracy of the LC/MS method was tested at three different concentrations and for six injections. Metformin hydrochloride and cyanoguanidine had accuracy percentages which differed by < 10% from the expected values for all concentrations and the RSD value was less than 2%. Melamine, 1-methylbiguanide, (4,6-diamino-1,3,5-triazin-2-yl)guanidine, N,N-dimethyl-1,3,5-triazine-2,4,6-triamine had accuracy percentages which differed by < 10% from the expected values for 25 and 5 ng/mL. There was a larger error for the 1 ng/mL concentration which was close to the LOD and therefore this was expected.

The capacity factor showed that the order of elution was (from first to elute to last):

- 1) Cyanoguanidine
- 2) N,N-dimethyl-1,3,5-triazine-2,4,6-triamine
- 3) Metformin hydrochloride
- 4) 4,6-diamino-1,3,5-triazin-2-yl) guanidine
- 5) Melamine
- 6) 1-methylguanide

The reasons for this order are due to two factors: the polarity of the molecule and the number of sites available for hydrogen bonding interactions. The more polar the molecule and the more sites for hydrogen bonding then the longer the analyte will spend in the column due to the increase in favourable interactions. The order of the elution backs this up as the molecule with the lowest polarity and fewest sites is cyanoguanidine and the molecule with the most sites and most defined polarity is 1-methylbiguanide.

When investigating the peak asymmetry, cyanoguanidine, 4,6-diamino-1,3,5-triazin-2-yl) guanidine and N,N-dimethyl-1,3,5-triazine-2,4,6-triamine had values within the range of 0.8 – 1.2. Melamine and 1-methylbiguanide had good peak asymmetry for 1 ng/mL and the values for the other two concentrations of melamine were just above the accepted values. For 1-methylbiguanide, the values were acceptable for 5 ng/mL but there was significant asymmetry for the 25 ng/mL concentration. Metformin also had significant peak asymmetry, however the peaks were acceptable as the AF value was less than 2. The reasons behind the variation in peak asymmetry could be that the injection volume was too large however with smaller injections the sensitivity would have been compromised. The analyte could have been adsorbed onto active sites within the column meaning that the molecules would spend more time and not all elute simultaneously. Peak asymmetry was calculated in the software of the instrument and the algorithm used determined the start and end of the peak and so there could be different points used for different injections and this would generate an error contributing to the asymmetry. Potential solutions to this peak tailing issue is that a more acidic mobile phase could be used with pH less than three or to decrease the injection volume, whilst making sure that the sensitivity is retained.

The column efficiency for all compounds that were analysed was larger than 2000. The LOD and LOQ values were obtained via the calibration curves due to equipment failure. All the calibration curve points were above the LOD and LOQ.

During the stability test, it was found that the levels of metformin hydrochloride and the impurities were stable over the course of the experiment with the exception of

N,N-dimethyl-1,3,5-triazine-2,4,6-triamine which was being formed. It was proposed that this impurity was formed via reaction between cyanoguanidine and metformin hydrochloride during the stability test experiment. The possible reaction route is given below in Figure 85.

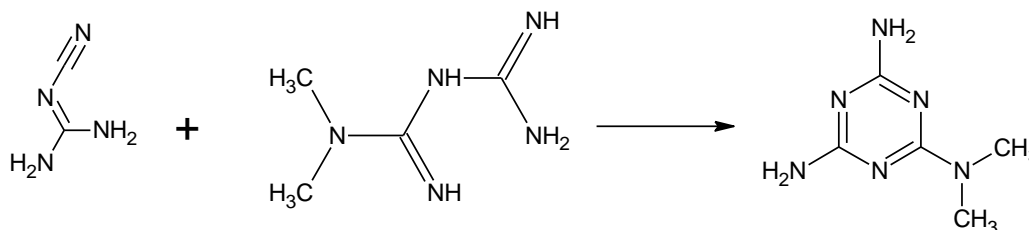


Figure 85. Potential route of formation of N,N-dimethyl-1,3,5-triazine-2,4,6-triamine

The relative impurity concentration (% w/w in relation to metformin hydrochloride) was calculated in the initial and final solutions used for the stability test. Melamine, 1-methylbiguanide and 4,6-diamino-1,3,5-triazin-2-yl were below the reporting threshold suggested by ICH (see Table 1 in Chapter 1). Relative concentration of N,N-dimethyl-1,3,5-triazine-2,4,6-triamine in the final solution was 0.05%, which means that this impurity should be reported. Cyanoguanidine was an impurity, which relative concentration was well above the qualification threshold – 3.43%. It means that this impurity should always be quantified as well as its toxicity should be assessed in details.

While the experiment was being run there were two observations in that a strong smell developed over time, likely due to the formation of dimethylamine and this was accompanied by a colour change from colourless to pale yellow as can be seen in the photograph in Figure 86.

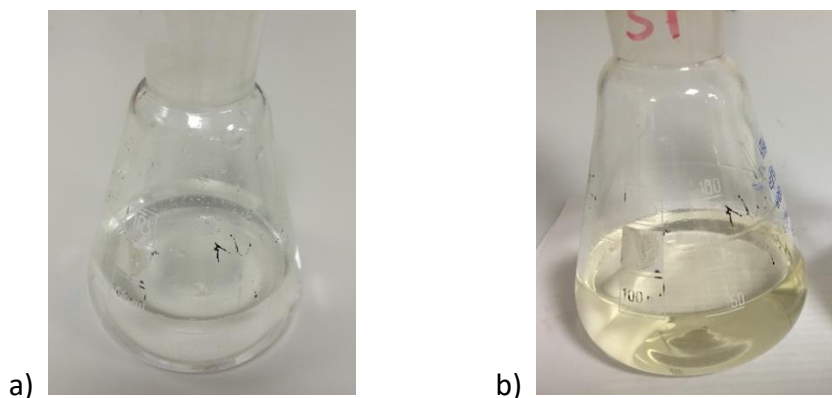


Figure 86. Photograph showing the colour difference between a) a freshly made sample of metformin hydrochloride and b) a sample collected at the end of the stability test

Application of gas chromatography for determination of dimethylamine was impossible due to high residuals of solvents that were used during the derivatisation process. Therefore, ion chromatography was chosen as the analytical method for the determination of DMA.

The calibration curve obtained for dimethylamine using ion chromatography had a very high regression coefficient of 0.99867, which shows the calibration model is suitable for this compound. The application of this method was presented for the raw metformin hydrochloride material, which contained dimethylamine. This proved that detection of dimethylamine was possible using this method, despite not being used during the stability test, as a result of equipment failure.

4.7 Conclusions

Calibration curves obtained in this project were successfully fitted with high regression coefficients for the relationship between the peak area and the concentration. The precision of the developed LC/MS method, for the majority of injections had %RSD less than 2% for the retention time and the peak area. This shows that the method developed was highly reliable and reproducible. In general, the accuracy of the method was within acceptable values, but performed best for metformin hydrochloride and cyanoguanidine. Peak asymmetry was within the accepted range, however metformin hydrochloride exhibited higher asymmetry factor, probably due to the too large injection volume. The column efficiency was much larger than the accepted value in literature, showing that the separation of analytes was highly satisfactory. The calibration curves were used to calculate the LOD and LOQ values, which were reasonable and the lowest point in the calibration curves was above these parameters.

Metformin hydrochloride was found to be stable over time during heating, however N,N-dimethyl-1,3,5-triazine-2,4,6-triamine was generated after 163 hours. This was proposed that this could happen via a reaction between cyanoguanidine and metformin hydrochloride.

The method outlined for dimethylamine could be used in future work for determination of this compound in real samples.

In conclusion the work carried out in this chapter would allow the concentrations of metformin hydrochloride and its associated impurities to be determined off-line using LC/MS and IC during the continuous crystallisation.

5 Determination of the Effect of Ammonium Sulfate on the Nucleation Rate of Metformin Hydrochloride

5.1 Chapter Outline

This chapter details the procedure and results for all experiments that were carried out in order to determine the effect of ammonium sulfate on the nucleation rate of metformin hydrochloride. The experimental work was carried out in order to assess:

- 1) The impurity content in raw metformin hydrochloride – determination of the number of impurities and identification of those impurities.
- 2) The effect of impurity on metformin hydrochloride induction time. This was carried out in two parts:
 - a. Induction time experiments were conducted in the Crystalline reactor and therefore the data obtained were fitted into two models: the ter Horst model – based on probability distributions of induction times and the classical nucleation theory model in order to determine the crystal nucleation rates.
 - b. Dynamic light scattering measurements were carried out using the Malvern Zetasizer to examine the effect of the sulfate anions on the nucleation rate of metformin hydrochloride. The presence of different sizes of the prenucleation clusters was investigated as a potential reason for the different behaviour of samples containing impurities compared with pure metformin hydrochloride samples.

5.2 Materials Used in the Study

Metformin hydrochloride was used as the model compound and ammonium sulfate was chosen as the source of sulfate anions. Sulfate was found to be an existing impurity in metformin hydrochloride samples following analysis by anion chromatography (results shown in section 5.2.2).

5.2.1 Metformin Hydrochloride

The detailed information about metformin hydrochloride and why it was used is given in section 4.3.

5.2.2 Ammonium Sulfate

Ammonium sulfate has molecular mass 132.14 g/mol and the molecular structure given below (Figure 87).

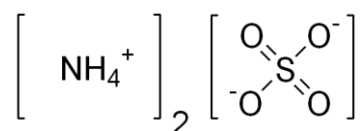


Figure 87. Molecular structure of ammonium sulfate

The decision behind using ammonium sulfate as the model impurity for studying impurity effects on metformin hydrochloride is illustrated here. Initial experiments involved re-crystallisation of metformin hydrochloride from ethanol:water mixture of 80:20 w/w% in several crystallisation platforms and under different stirring speeds and cooling rates. In order to identify which inorganic impurities were present in significant amounts, ion chromatography was carried out.

Due to ionic nature of metformin, it is possible for this compound to form salts. Salt forms of drugs have a large effect on the drugs' quality, safety, and performance. The properties of salt-forming species (i.e., counterions) significantly affect the pharmaceutical properties of a drug (like solubility or physicochemical stability). Commercially available metformin exists as hydrochloride salt. To determine if

metformin forms different salts during the crystallisation process is one of the project aims.

It was appropriate whilst doing this to compare the results of several crystallisation platforms and their capabilities to test whether or not these parameters had an influence on the impurities present and the properties of the crystals themselves.

All measurements were carried out using the Reagent-Free Capillary HPIC system of an ICS-5000+ instrument (Thermo Fisher Scientific, Hemel Hempstead UK). The system contains a potassium hydroxide electrolytic eluent generation module, an anion capillary eluent suppressor (ACES), an AS-AP Autosampler and a conductivity detector. All eluents were generated as potassium hydroxide using a diluent of ultrapure water (ICW 3000) purification system with a resistivity of 18.2 MΩ.cm ((ICW 3000), Millipore, Watford, UK). A Dionex IonPac AS11-HC 4 μm (250 × 0.4 mm) capillary column was used in the separations. The gradient program was used in order to separate the ions – see Table 51.

Table 51. Gradient program and measurement conditions for Ion Chromatography

	Time [min]	KOH Concentration (mM)	Flow rate [μL/min]	Injection volume [μl]	Back pressure [psi]	Column Temperature [°C]
1	0	1	10	1	3200	15
2	10	1 – 30				
3	30	30 – 40				
4	40	60				
5	50	60				

Analysing the samples obtained during the experiments described in Table 52 with Ion Chromatography provided an overview on the ion in the samples – see Figure 88. The results are qualitative at this preliminary stage.

Table 52. Sample description and experimental conditions

Sample name	Reactor	Cooling rate	Mixing speed
		[°C/min]	[rpm]
1	Crystalline	0.5	350
2			700
3		5	350
4			700
5	EasyMax	0.5	350
6			700
7		5	350
8			700
9	OptiMax	0.5	350
10			700
11		5	350
12			700
13	Raw material	-	-

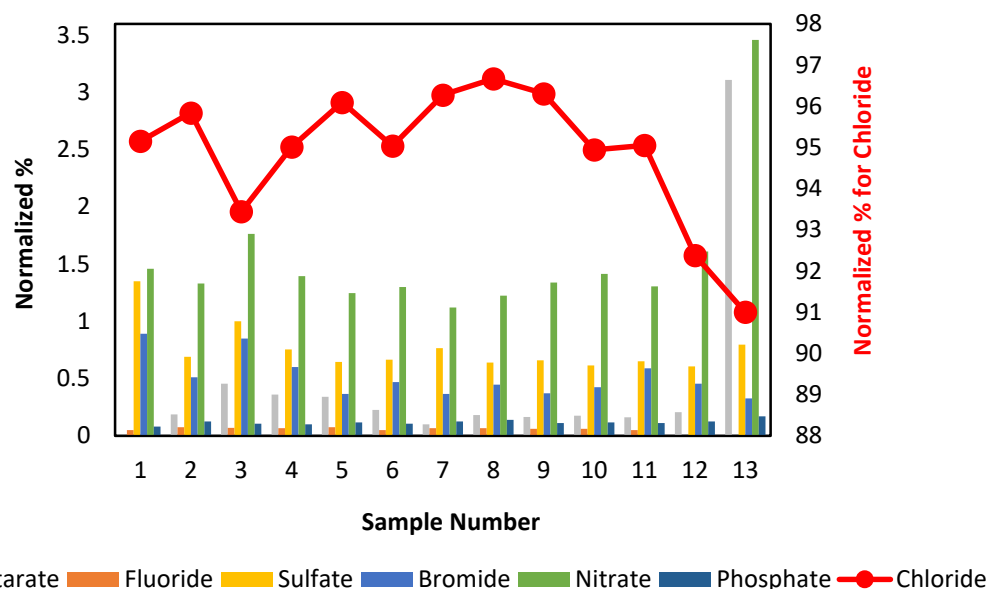


Figure 88. A summary of the results obtained for samples of metformin hydrochloride crystallised in three different reactors - Crystalline, OptiMax and EasyMax (sample description and experimental conditions are provided below – Table 55).

Metformin is commonly used as its hydrochloride salt, which explains the very high content of the chloride. After re-crystallisation of the raw material it was observed that the content of two ions – bromide and sulfate increased. A high content of the nitrate ions was also detected – even after re-crystallisation. On this basis, these three ions were selected for further investigation of the effect of the ion content on induction time and crystal morphology.

The results obtained can be used to illustrate the use of crystallisation as a purification technique. Despite the increase in concentrations of the three ions that were mentioned earlier – nitrate, bromide and sulfate, the general purity of the product after re-crystallisation is much higher than the raw material. The content of chloride ions for most of the obtained crystals oscillates between 95 and 97%, while raw material contained only 91% of these ions. This is consistent with an effective purification from the crystallisation. Ammonium sulfate was chosen as the source of sulfate (SO_4^{2-}) ions. Due to time limitations, the other ions (nitrate and bromide) were unable to be investigated.

5.2.3 Solvent Choice

The solvent system used was an 80:20 %w/w mixture of ethanol and water respectively. Metformin hydrochloride has a high solubility in water therefore vast amounts of material would be needed to generate a successful crystallisation process and so ethanol yielded a more practical working solubility.

5.3 Equipment and Techniques Used in the Study

5.3.1 Crystallisation Platforms

Two types of reactors that were used while conducting this study will be described below.

5.3.1.1 *Crystalline*

Crystalline (Technobis SE) shown in Figure 89 is a multiple reactor station that functions as a parallel crystalliser on 8 mL volume scale.



Figure 89. Crystalline Equipment Photograph

It combines turbidity measurements with independent real time particle visualization (PV). Each reactor is independent, which means that the crystallisation can be monitored independently in each vial using the high quality digital visualisation probes and the turbidity measurements and the temperature profile can be different for each independent reactor. The Crystalline can hold 8 vials, each with 8 mL volume. A unit consists of 8 independently heated reactor blocks and these blocks are

temperature controlled by a microprocessor controlling a heat and Peltier element (temperature range of -25 to 145°C with heat/cool rate of 0 to 20°C/min). The Peltier element is cooled by heat transfer with cooling liquid from an external cryostat set at 18°C. Crystalline provides an inlet for a dry purge gas (typically nitrogen) to prevent condensation on the reactor blocks and electronics.

5.3.1.2 *Optimax and Easymax*

OptiMax (Figure 90) is a powerful synthesis workstation designed by Mettler Toledo.



Figure 90. OptiMax reactor photograph

The unique design gives the possibility of working with temperatures ranging from -40 to 180°C without oil or ice baths. It has an interface which is easy to learn and has no training requirements. All of this makes OptiMax a perfect tool for process development experiments. The reactor works in a way that offers high traceability and reproducibility of the results. The OptiMax platform consists of a thermostat system, screen control panel, stirrer motor, temperature probe, 1000 mL two-piece glass reactor, pitched blade stirrer, Alloy C-22 Bar type baffle. A number of ports in the reactor lid allows many PAT tools to be used to fully monitor the process.

Easymax is the equivalent of the Optimax but at 100 mL scale.

5.3.2 Analytical Techniques

5.3.2.1 Scanning Electron Microscope

Scanning Electron Microscope (SEM) is a type of microscope that uses a focused beam of high-energy electrons instead of light to form an image - when the electrons in the beam interact with the sample, various signals are being produced and therefore transformed into an image. Figure 91 shows a schematic diagram of SEM microscope. An electron gun located at the top of the instrument produces a beam of electrons, which follows a vertical path through the anode and magnetic lens – the microscope is held within a vacuum. Electromagnetic fields and lenses present in the microscope concentrate the beam before it illuminates the sample. Electrons and X-rays are ejected from the sample when the focused electron beams go in the contact with the sample.

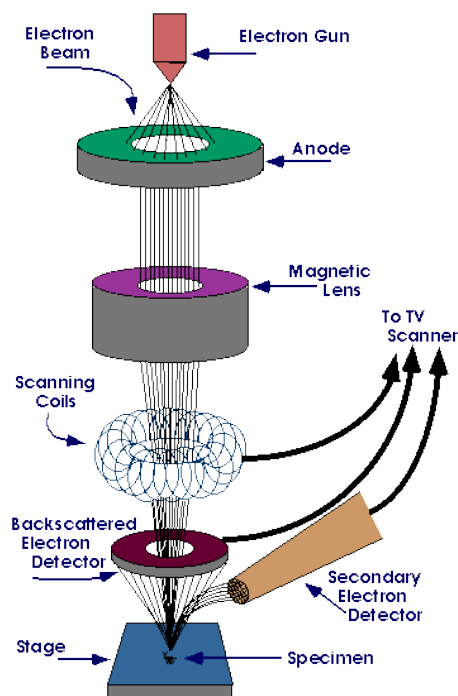


Figure 91. A schematic diagram of a scanning electron microscope [125]

Detectors, located further down in the SEM, collect secondary electrons, backscattered electrons and X-rays (see Figure 92) and convert them into a signal and produce the final image.

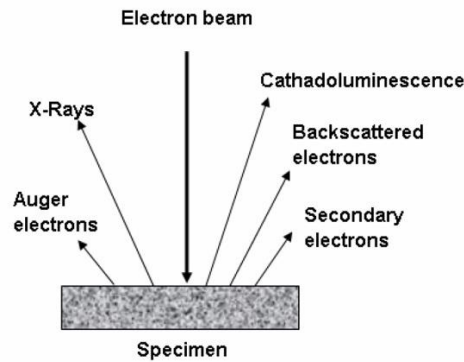


Figure 92. Types of electrons ejected from the sample, when the focused electron beam hits the sample [126]

Using this technique information such as: sample morphology, chemical composition, crystalline structure and orientation of materials forming the sample can be revealed.

SEM is mainly used to:

- generate high-resolution images of shapes of objects,
- discriminate phases based on mean atomic number using back-scatter detector,
- identify phases based on qualitative chemical analysis and/or crystalline structure – when energy – dispersive X-ray microanalysis (EDX) is coupled with SEM,
- precise measurements of very small objects,
- examine microfabric and crystallographic orientation in many materials – SEMs equipped with diffracted backscattered electron detectors.

As with all analytical techniques, SEM has strengths and limitations. SEM is well known for its very broad application in characterisation and imaging of solid materials. Instruments are easy to operate and quite often the sample preparation procedure is very simple and the data acquisition is relatively rapid (5 minutes per image). SEM limitations are associated with a sample nature required for the measurements. The sample needs to be solid, containing no solvent, it must be stable

under vacuum conditions and be relatively small. Instruments using energy-dispersive X-Ray Spectroscopy detectors are unable to detect elements with atomic numbers less than 11 (Na) [127].

5.3.2.2 Time-of-Flight Secondary Ion Mass Spectrometry

Time-of-Flight Secondary Ion Mass Spectrometry is a very sensitive surface analytical technique, that provides elemental, chemical state and molecular information from surfaces of solid material. A solid surface is bombarded by primary ions with defined keV energy. This energy is used to target atoms via atomic collisions and to generate a so-called 'collision cascade' [128]. Part of the energy is transported back to the surface and therefore surface atoms and molecules are able to overcome the surface binding energy and are ejected. The energy of the collision cascade is low enough to allow molecules with masses up to 10000 u to escape without or with minimal fragmentation. Most of the emitted particles do not have any charge, but those negatively or positively charged will be subsequently transferred in to the time-of-flight analyser and the data obtained provides detailed information on the elemental and molecular composition of the surface. The principles of TOF mass spectrometry were described in detail in Section 4.2.4. SIMS penetrates only one or two monolayers, which explains why this technique is widely used for surface analysis.

There are several applications of TOF-SIMS:

- Surface spectrometry – used for investigation of the original, non-modified surface composition. The output of this analysis is a mass spectrum.
- Surface imaging – provides a mass resolved secondary image of the surface.
- Depth Profiling – using two ion beams – one for sputtering a crater and one for analysing the crater bottom it is possible to analyse more layers than the top two, which are being analysed during the standard measurement.
- 3D analysis – can be obtained by combining spectral, imaging and depth information. This type of analysis is suitable for the investigation of complex and unknown structures or defects.

The TOF-SIMS is a very sensitive technique, that provides very detailed information about the elemental and chemical composition of the surface with a very high mass resolution, allowing distinction between species of similar nominal mass. Along with many advantages there are also a few limitations of this technique, such as:

- quantitative analyses are not possible
- limited optical capabilities
- an image shift between positive and negative ion data collection mode – almost impossible to obtain both modes ion data on exactly the same spot [128].

Hence here the interest is to investigate its potential application for crystal surface analysis.

5.3.2.3 Differential Scanning Calorimetry

Differential Scanning Calorimetry (DSC) monitors heat changes associated with phase transitions (melts, glass transition, phase changes) or chemical reactions as a function of temperature. This technique provides qualitative and quantitative information on exothermic (heat evolution) and endothermic (heat absorption) processes [129].

This technique can be used as an analytical tool for the determination of the purity of organic compounds through determination of a melting point. DSC purity determination is established on the fact that eutectic impurities lower the melting point of a eutectic system, what can be described by the Van't Hoff equation (see Equation 77) or its simplified version (see Equation 78):

Equation 77

$$T_f = T_0 - \frac{RT_0 T_{fus}}{\Delta H_f} \ln\left(1 - x_{2.0} \frac{1}{F}\right)$$

Equation 78

$$T_f = T_0 - \frac{RT_0^2}{\Delta H_f} x_{2.0} \frac{1}{F}$$

where T_f is the melting temperature, T_0 is the melting point of the pure substance, R is the gas constant, ΔH_f is the molar heat of fusion (based on the peak area), $x_{2.0}$ is the concentration (mole fraction of the impurity), T_{fus} is the clear melting point of the impure substance, F is the fraction melted and $1/F$ is the reciprocal of the fraction melted and can be expressed as:

Equation 79

$$\frac{1}{F} = \frac{A_{tot} + c}{A_{part} + c}$$

where A_{tot} is the total area of the peak, A_{part} is the partial area of the peak and c is the linearization factor.

Non-eutectic impurities also affect the melting point and sometimes may cause its increase [130].

5.3.2.4 Dynamic Light Scattering

There are two potential effects of contact between light and particles/molecules. Firstly, absorption of the energy, when the wavelength of incident light corresponds to an energy transmission within the molecule or atoms. Secondly, light scattering, when the wavelength of incident light does not correspond to an energy transmission within the molecule or atoms. Sample homogeneity is an essential condition for light scattering to happen. In aqueous solutions the scattered light is a result of a difference in optical properties in the solution, such as the refractive index difference between detected particles and the bulk solution [131]. Figure 93 shows the setup for dynamic light scattering experiments.

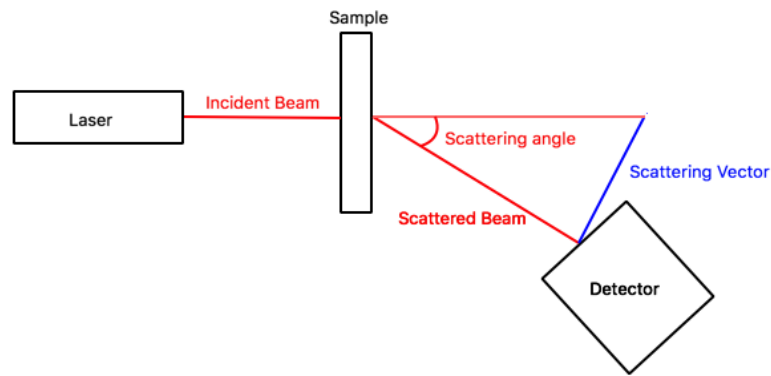


Figure 93. Dynamic light scattering diagram

The position of the scattering vector, $q(m)$, and the scattering angle (θ) are shown in the Figure 93. In order to calculate the scattering vector, it is necessary to assume that q has the same magnitude as the vector associated with the incident beam. Therefore, the scattering vector can be expressed as the difference between the incident and the scattered wave vectors as is given in Equation 80.

Equation 80

$$q = \frac{4\pi n}{\lambda} \sin \frac{\theta}{2}$$

In the equation above n is the refractive index of the solution and λ is the wavelength of the laser beam [131]. The results obtained during the lab scattering experiments are based on intensity (I), which is a function of the scattering angle (θ) and the observation time (t): ($I(\theta, t)$). During the dynamic light scattering measurements, the speed at which the particles are diffusing due to Brownian motion is measured by recording the rate at which the intensity of the scattered light fluctuates - smaller particles cause the intensity to fluctuate more rapidly than large particles. If the diffusion coefficient of the moving particles is known, then it is possible to estimate a particle size [131]. The function obtained from intensity fluctuations in the light scattered by the sample is called an autocorrelation function.

5.3.2.4.1 Autocorrelation Function

A graphical representation of the scattered intensity over time is called the autocorrelation function and can be expressed as it is shown in Equation 81.

Equation 81

$$G_2(\tau) = \langle (I(t) \cdot I(t + \tau)) \rangle$$

where $I(t)$ is the average intensity recorded at time t and $I(t + \tau)$ is the intensity recorded after a time delay, τ . The autocorrelation function is a decaying function of time delay when Brownian motion in a solution is studied [131]. The general trend is being observed – the larger are the decay times, the larger particles are present in the solution. The decay rate Γ (s^{-1}) of the autocorrelation function can be related to the diffusion coefficient D (m^2s^{-1}) of the particles in solution and the scattering vector $q(m)$ and can be defined as:

Equation 82

$$\Gamma = Dq^2$$

5.3.2.4.2 Decay Rate

The decay rate can be obtained from the autocorrelation function by fitting a third order polynomial to the plot of the natural log of $G_2(\tau)$ vs. the lag time, which operation is called cumulant analysis. When the sample is monodispersed the cumulant analysis would yield a linear plot of $\ln(G_2(\tau))$ vs. lag time. However, the polydispersity of the samples is often observed and then several decay rates may be present in one autocorrelation function.

The decay rate is equal to the coefficient on the first order term in the equation.

5.3.2.4.3 Hydrodynamic Diameter

A theoretical diameter of a hard sphere, which diffuses in the same manner as the particles in the sample is called the hydrodynamic diameter (d_H) and it can be estimated based on Stokes-Einstein equation given in Equation 83:

Equation 83

$$d_H = \frac{k_B T}{3\pi\eta D}$$

where k_B is the Boltzman constant with value 1.38×10^{-23} J/K; T is the temperature in Kelvin, η is the sample viscosity in Pa.s and d_H is in meters and D is the diffusion coefficient D (m^2s^{-1}). The hydrodynamic diameter is an approximate value, due to assumption that the particles present in the sample are hard spheres. This technique allows to determine the polydispersity of the sample and the hydrodynamic diameter for a wide range of particle sizes (1-1000 nm) without a complicated sample preparation procedure. However, when the DLS measurement is carried out for a highly polydispersed samples there is a chance of providing a false information about the sample content. The intensity of scattered light is directly proportional to the diameter of the species in the sample raised to the 6th power ($I \propto d^6$) and therefore the presence of small particles can be masked by the large particles.

5.3.2.5 Data Analysis of Autocorrelation Functions

Samples studied during this project were characterised by high polydispersity and therefore the autocorrelation functions consisted of several exponential decays, so in some cases 2 or 3 exponential decay had to be fitted to one function. It was possible to do using Matlab, using the formula shown in Equation 84:

Equation 84

$$G_2(\tau) = Q_1 e^{-\frac{1}{Q_2}\tau} + Q_3 e^{-\frac{1}{Q_4}\tau} + Q_5 e^{-\frac{1}{Q_6}\tau}$$

where Q_1 , Q_3 and Q_5 are coefficients which indicate the contributions of each decay as part of the whole function and $-1/Q_2$, $-1/Q_4$ and $-1/Q_6$ are the decay rates referring to each individual decay. An interactive curve fitting tool [132] allowed the calculation all the parameters described above automatically from the obtained data. An example of the interface is depicted in Figure 94.

The tool was designed in a way that the initial guess values to fit the experimental data to Equation 84 were used and then the interactive cursors represented in red, green and blue in Figure 94 could be moved on the graph to change the guess values. The best possible fit was achieved when the lowest error was observed. For the filtered data only two decays had to be fitted to the model, so the Matlab script was modified accordingly.

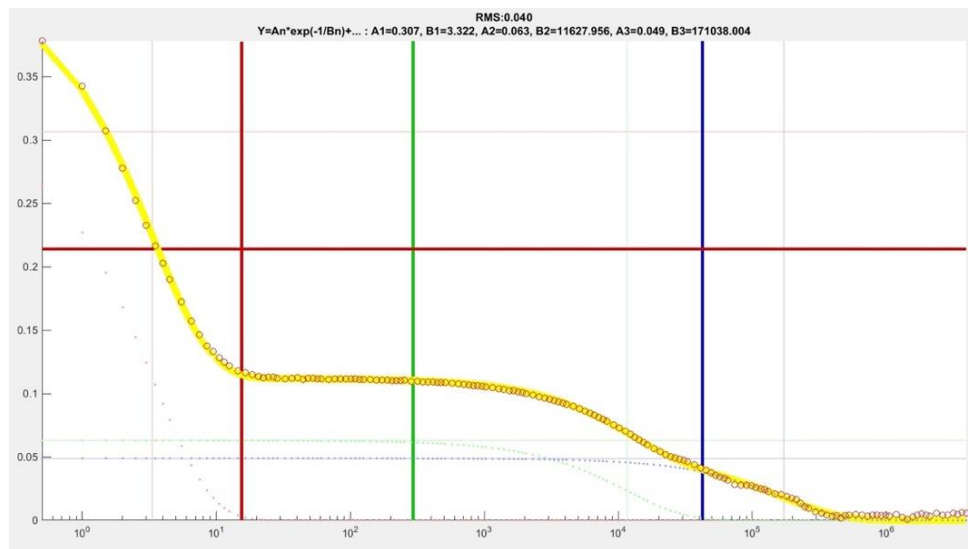


Figure 94. Screenshot of the interactive curve fitting tool created by Dr. Jerzy Dziewierz. Interactive cursors are indicated in red - corresponding with the 1st decay, green – the 2nd decay and blue - the 3rd decay.

5.4 Methods Used in the Study

5.4.1 Methods for Induction Time Effects

5.4.1.1 *Induction Time Experimental Conditions*

Several conditions, including different supersaturations and filtration treatment, were explored during these experiments including supersaturation (which was altered by changing the final temperature in the reactor). Table 52 summarises all conditions which were used.

The same mass of metformin hydrochloride (6.3225 g) was weighed each time to create each solution. These supersaturations were determined based on the solubility curve given in Figure 95. The supersaturations chosen were conditions that had been selected for the practical design of a continuous crystallisation of metformin hydrochloride to provide relevants. The purpose of this work was therefore to investigate these conditions further before the continuous campaign would be carried out.

Different %w/w of ammonium sulfate were chosen to study the effect of impurity concentrations on the induction time for primary nucleation. The mass of ammonium sulfate (based on %w/w of the mass of metformin hydrochloride) was added to the solution in the Crystalline as unfiltered or filtered (with polyethersulfone (PES) syringe filters with pore diameters of 0.22 μm). The stock solution of metformin hydrochloride and the desired mass of ammonium sulfate was prepared in 75 ml of the ethanol:water mixture and left to stir in a water bath until completely dissolved. Once dissolved, 5 ml of the solution was pipetted into 8 Crystalline vials which were closed and placed inside the Crystalline chambers at which point the experiment was started.

Table 53. Experimental Conditions for Induction Time Experiments

Supersaturation	Final Temperature (°C)	Ammonium Sulfate Concentration (w/w%)	No. of repetitions	Filtration Treatment
1.38	38	0.0	16	Unfiltered
		0.1		
		0.5		
		1.0		
1.55	34	0.0	40	Unfiltered + Filtration with 0.22 µm PES
		0.01		
		0.1		
		0.25		
		0.5		
		0.75		
		1.0		
1.64	32	0.0	16	Unfiltered + Filtration with 0.22 µm PES
		0.1	(unfiltered)	
		0.5	8	
		1.0	(filtered)	
1.73	30	0.0	16	Unfiltered + Filtration with 0.22 µm PES
		0.1	(unfiltered)	
		0.5	8	
		1.0	(filtered)	

Each experiment experienced the same temperature profile during the induction time study. Initially the solution was heated to 65°C and held for 30 minutes to ensure all solutes were completely dissolved, which was confirmed via imaging. The temperature was then reduced to the final temperature which to achieve the desired supersaturation at a rate of 5 °C per minute (the highest cooling rate achievable using the Crystalline platform). The solution was then held at the final temperature for 24 hours. The stirring rate for all experiments was 700 rpm and this was created by magnetic stirrer bar.

5.4.1.2 SEM Measurement Conditions

The images were captured using an SEM Keysight U9320B, where 1000 volts was applied.

5.4.1.3 ToF-SIMS Sample Preparation and Measurement Conditions

Samples crystallised during the induction time experiments were collected, filtered and washed twice using 1 mL of diethyl ether each time. Then samples were dried overnight in the oven. Prior the analysis they were ground using pestle and mortar to homogenise the sample.

The ToF-SIMS experiments were performed with a ToF-SIMS V mass spectrometer (ION-TOF GmbH, Münster, Germany) based at Wolfson Foundation “Pharmaceutical Surfaces Laboratory” within the National CMAC Centre and equipped with a Bismuth Liquid Metal Ion Gun (LMIG). Spectra were acquired in positive and negative ion mode over the mass range of 1-855 u, using Bi³⁺ as primary ion source, with a 30 kV applied voltage, a 0.6 pA aperture current, and 3 minutes acquisition time. A low electron energy flood gun was used to prevent sample surface charging. Images were collected over a 100 µm x 100 µm area, with a delivered primary ion dose density (PIDDD) of approximately 7.0×10^{12} (primary ions/cm²).

5.4.1.4 DSC Sample Preparation and Measurement Conditions

Samples were ground and well dispersed prior to measurements. The solid material was weighed out in an aluminium sample pan. Then the pan containing sample was placed in the sample press. Aluminium lid was then pierced with a pin to allow venting of lost solvent during the heating stage and any gas that could be produced during the sample decomposition. All the measurements were carried out using a Mettler Toledo DSC214. Samples were heated up from room temperature to 250°C and then cooled down to room temperature using two cooling rates – 10°C/min and 1°C/min.

5.4.1.5 DLS Sample Preparation and Measurement Conditions

When unfiltered solutions were analysed using DLS, two supersaturations were chosen – SS=0.9 at 20 °C and SS=1.55 at 34°C. Solutions were prepared by weighing out the desired amount of powder into a 100 mL glass bottle and dissolving it in 75 mL of ethanol:water mixture. It was left to stir in the water bath for an hour then the solution was transferred into a quartz cuvette with path length 1 cm and analysed in the Malvern Zetasizer in backscattering mode.

Only supersaturated solutions (SS=1.55) were filtered using 0.22 µm PES syringe filters and measured using DLS. The reason behind this was that only supersaturated solutions were studied during the induction time experiments, therefore it was crucial to investigate the effect of the prenucleation cluster formation on nucleation induction time. Undersaturated solutions were therefore not studied here.

Dynamic light scattering (backscattering angle of 173°) was used on the Malvern Zetasizer. The experimental conditions are listed in Table 54:

Table 54. DLS experimental conditions summary

Supersaturation	Ammonium sulfate content (w/w%)	Filtration	Temperature [°C]	Viscosity [Pa.s]	Refractive index [133]
0.9	0	Unfiltered	20	0.001186 [134]	1.576
	0.01				
	0.1				
	0.5				
	1.0				
1.55	0	Unfiltered	34	0.000983 [135]	1.576
	0.01				
	0.1				
	0.5				
	1.0				
1.55	0	PES	34	0.000983	1.576
	0.1				
	0.5				
	1.0				

The viscosity used for the measurements was taken to be that of ethanol since it made up 80% w/w of the solvent mixture and therefore had the strongest influence. The water contribution to the viscosity value was therefore ignored.

5.4.1.6 Ion Chromatography Sample Preparation and Measurement Conditions

Prior the analysis approximately 5 mg of the sample was dissolved in 50 mL of the deionized water and diluted afterwards 5 times. Prepared in this was sample was then subjected to analysis. For the filtrate samples, 1 mL of the filtrate was diluted with 4 mL of deionized water and then measured.

Two anions of interest – chloride and sulfate, were measured in the media using a 883 Basic IC Plus (Metrohm, UK), equipped with a peristaltic pump, an 863 Compact Autosampler, a Metrohm A sup 5 250/4.0mm column, and a 850 Professional IC conductivity Detector. The eluent was 3.2 mM sodium carbonate and 1 mM sodium bicarbonate per L of deionized water (dH₂O). A MSM Suppressor, operated at 10 MPa was used to suppress the eluent, using 0.1 M H₂SO₄, 0.1 M oxalic acid, and 5% (v/v) acetone per L of dH₂O as the regenerant. Blanks and internal standards were analysed periodically to ensure that the IC was performing adequately.

Due to equipment failure samples were analysed in the Environmental Engineering Institute for Infrastructure and Environment at University of Edinburgh. I would like to express my special gratitude and thanks to Michael Ross and Andrea Semiao for their help with running and analysing samples.

5.4.1.7 pH Investigation Experimental Conditions

The OptiMax reactor mentioned previously was used as the platform to test whether or not pH was an important factor in the change in induction time. The pH probe could be inserted into this reactor and that is why it was used, despite it being a much larger volume than the Crystalline vials. The conditions chosen for this experiment set were analogous to those used for Crystalline experiments but scaled up to 1 L.

84.3 g of metformin hydrochloride was added to 1 L of the ethanol:water solvent mixture along with the required mass of ammonium sulfate and heated to 70°C in a

water bath until dissolved. The solution was then transferred to the OptiMax vessel where the solution was again heated back up to 70°C and held for 30 minutes to ensure all material was dissolved. The solution was then cooled at 5°C per minute to the final temperatures stated previously. In total 5 experiments were carried out with pure metformin, 0.01, 0.1, 0.5 and 1.0 ammonium sulfate %w/w addition. The stirring was carried out with an overhead polytetrafluoroethane (PTFE) agitator at speed 350 rpm. 700 rpm could not be achieved here due to equipment limitations. The pH probe was inserted during the experiment as was a temperature probe which recorded data throughout. The final temperature was held until the solution crystallised. Experiments were not held for longer than 4 hours.

5.4.1.8 The Effect of Impurity Concentration on Solubility of Metformin Hydrochloride – Experimental Conditions

The solubility of metformin hydrochloride containing different amounts of ammonium sulfate in the 80:20 solvent mixture of ethanol:water was determined in the Crystalline platform.

Eight different concentrations of metformin hydrochloride were chosen to build a solubility curve, which are summarised in Table 55. Five different ammonium sulfate concentrations were used during the study – 0.0, 0.01, 0.1, 0.5 and 1.0 (%w/w).

Table 55. Concentrations used in solubility study of metformin hydrochloride

Sample	Concentration [mg/mL]
1	31.51
2	42.55
3	49.75
4	56.88
5	74.3
6	94.71
7	118.25
8	144.81

During each experiment the same temperature profile was used. Initially the solution was heated to 65°C and held for 30 minutes to ensure the solutes were completely

dissolved. The temperature was then reduced to the final temperature set at -10°C at a rate of 0.5°C per minute. The solution was then held at the final temperature for an hour and the cycle was repeated 3 times. The stirring rate for all experiments was 700 rpm and this was created by magnetic stirrer bars.

5.5 Results and Discussion

5.5.1 Determining Solubility of Metformin Hydrochloride in Solvent System Results

Prior to the nucleation study, the solubility of metformin hydrochloride in the 80:20 solvent mixture of ethanol:water was determined in the Crystalline platform. This provided the equilibrium solubility to enable control of the driving force for nucleation (Equation 13).

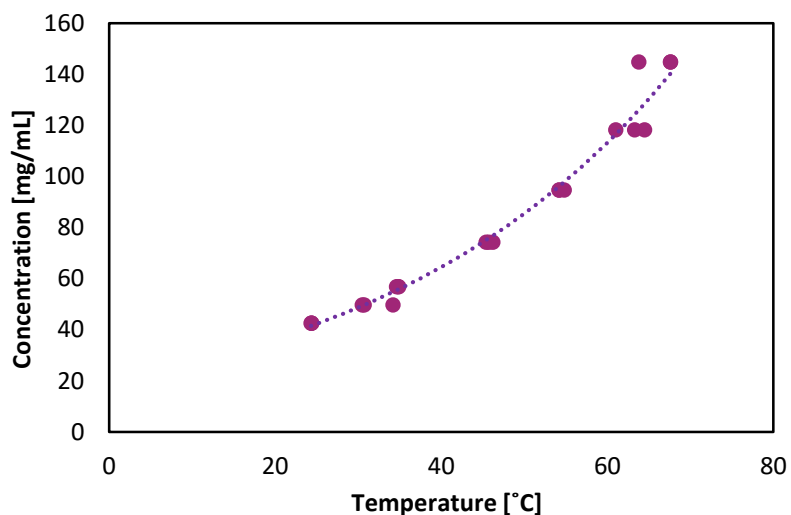


Figure 95. Solubility curve for pure metformin hydrochloride

5.5.2 Induction Time Experiments

5.5.2.1 Results from Induction Time Experiments

Figure 96 shows the summary of the induction times for metformin hydrochloride samples containing 0.0, 0.01, 0.1, 0.25, 0.5, 0.75 and 1.0 %w/w of ammonium sulfate at supersaturation 1.55. The results are sorted to show the increase in the induction time depending on the amount of ammonium sulfate added to the solution.

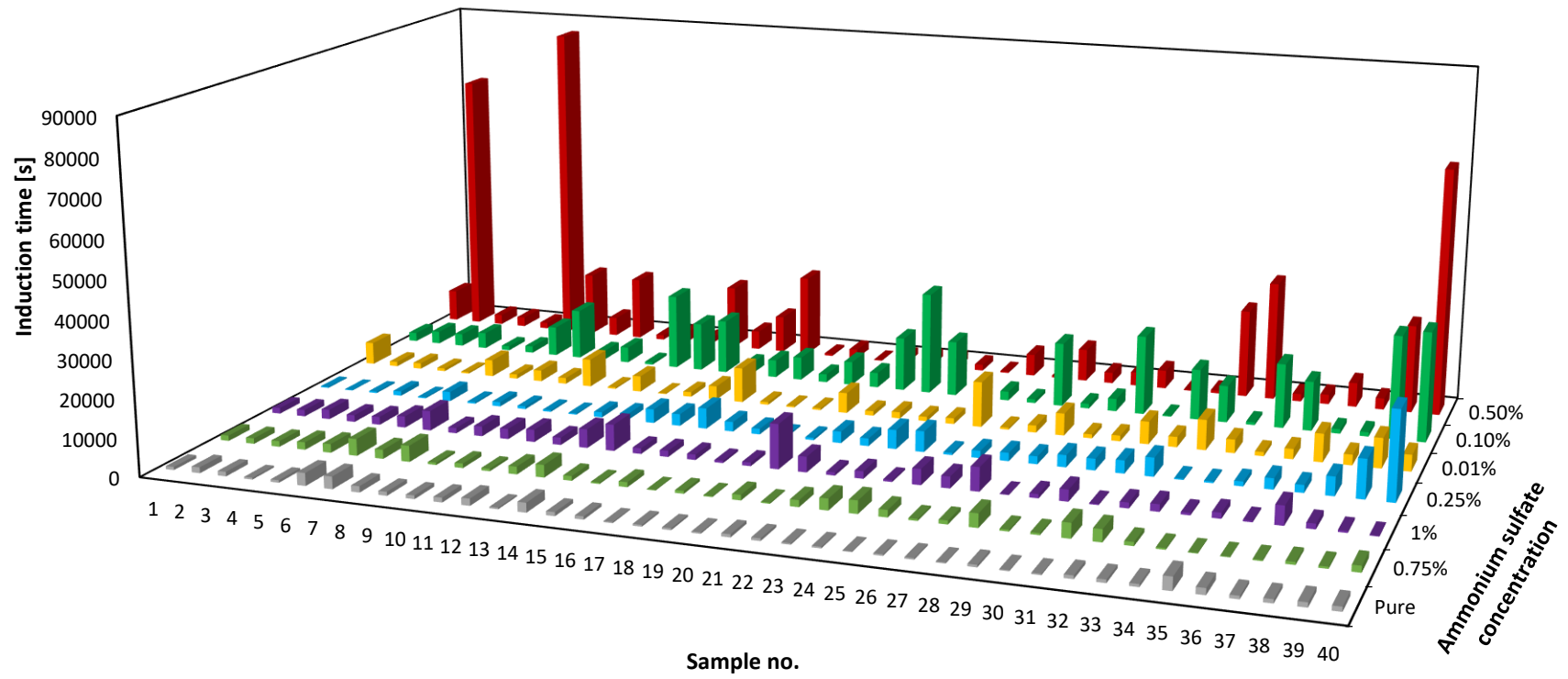


Figure 96. The summary of the induction times for metformin hydrochloride samples containing different concentrations of ammonium sulfate at SS=1.5

Figure 97 and Figure 98 depict the summary of all induction times obtained during all experiments for filtered and unfiltered solution. As it was expected, the higher the supersaturation, the shorter the induction times, both for filtered and unfiltered solutions. However, filtration caused a significant lengthening of nucleation times, due to the reduction in heterogeneous nucleation rates.

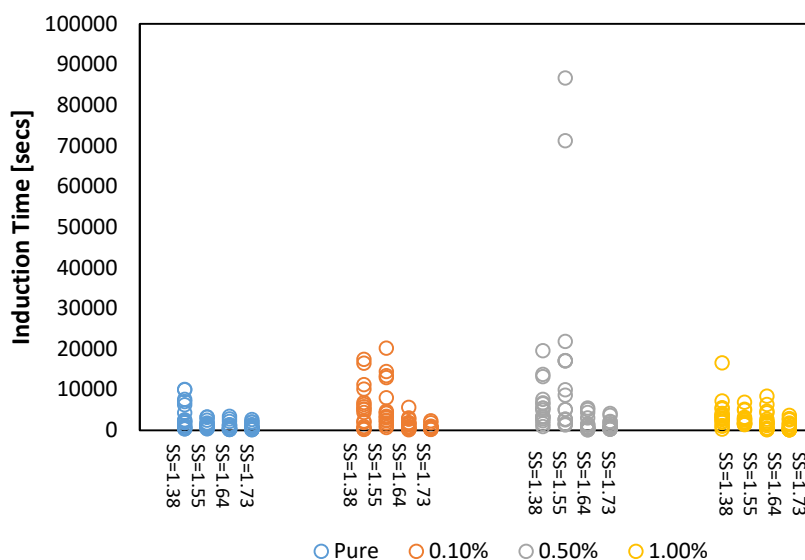


Figure 97. Summary of all induction times obtained during all experiments carried out with unfiltered solution: [○] represents pure metformin hydrochloride samples, [○] represents metformin hydrochloride samples doped with 0.10 %w/w of ammonium sulfate, [○] 0.50 %w/w of ammonium sulfate and [○] 1.00 %w/w of ammonium sulfate.

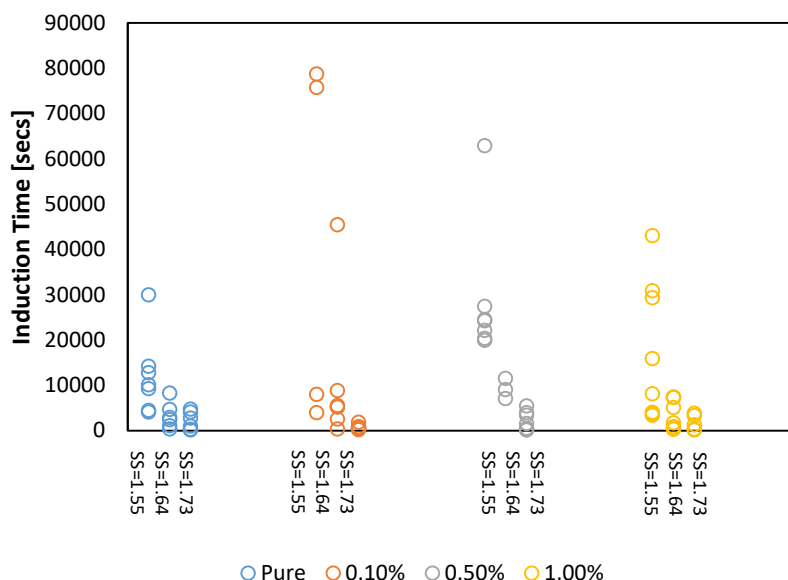


Figure 98. Summary of all induction times obtained during all experiments carried out with filtered solution: [○] represents pure metformin hydrochloride samples, [○] represents metformin hydrochloride samples doped with 0.10 %w/w of ammonium sulfate, [○] 0.50 %w/w of ammonium sulfate and [○] 1.00 %w/w of ammonium sulfate

5.5.2.1.1 Model-Based Analysis

In order to analyse the results obtained from the induction time experiments, model analysis was carried out using both the model based on the cumulative probability distribution of induction times and a model based on classical nucleation theory.

5.5.2.1.1.1 Crystal Nucleation Rates from Probability Distributions of Induction Times
 As described in section 2.4.3.1.2 through using the cumulative probability distribution of induction times, the growth time and the nucleation rate under the conditions used can be determined. The cumulative probability distribution is given in Figure 99 and Figure 100 with logarithmic time scale.

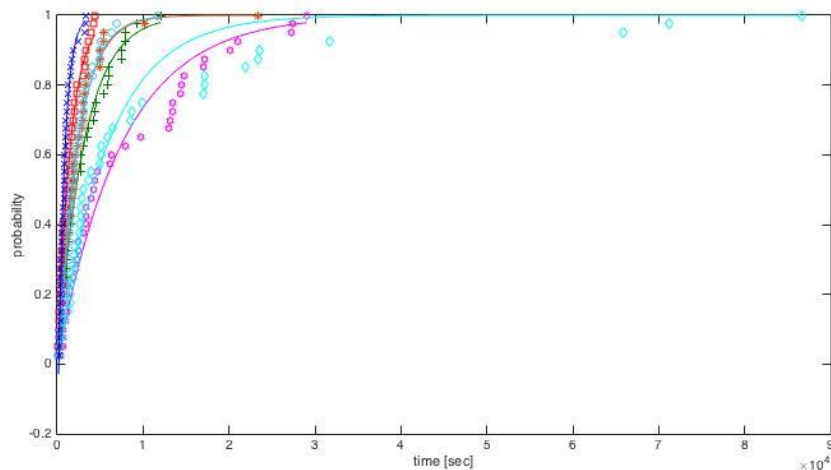


Figure 99. Cumulative probability distributions of induction times for metformin hydrochloride samples: [x] pure metformin hydrochloride, [+] metformin hydrochloride doped with 0.01 %w/w ammonium sulfate, [O] 0.1 %w/w ammonium sulfate, [O] 0.25 %w/w ammonium sulfate, [D] 0.5 %w/w ammonium sulfate, [□] 0.75 %w/w ammonium sulfate and [*] 1.0 %w/w ammonium sulfate.

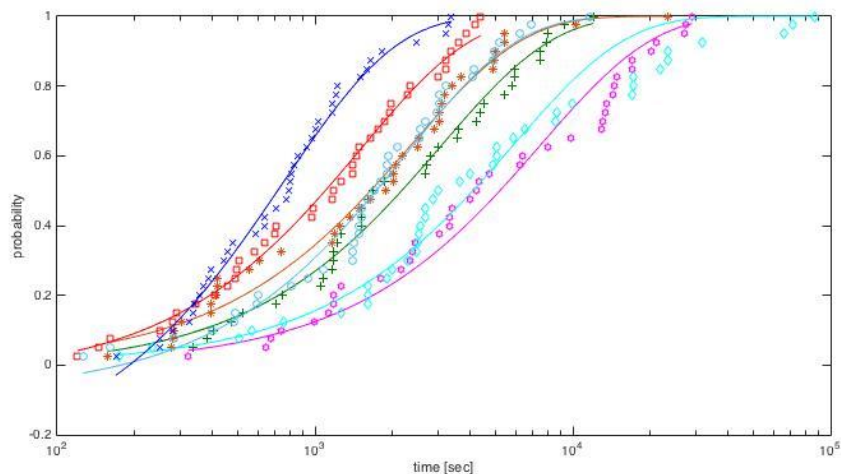


Figure 100. Cumulative probability distributions of induction times for metformin hydrochloride samples with logarithmic time scale: [x] pure metformin hydrochloride, [+] metformin hydrochloride doped with 0.01 %w/w ammonium sulfate, [O] 0.1 %w/w ammonium sulfate, [O] 0.25 %w/w ammonium sulfate, [D] 0.5 %w/w ammonium sulfate, [□] 0.75 %w/w ammonium sulfate and [*] 1.0 %w/w ammonium sulfate.

The results are presented in Figure 101 and show the growth time in seconds and nucleation rate in $\text{m}^{-3}\text{s}^{-1}$ for each experimental set.

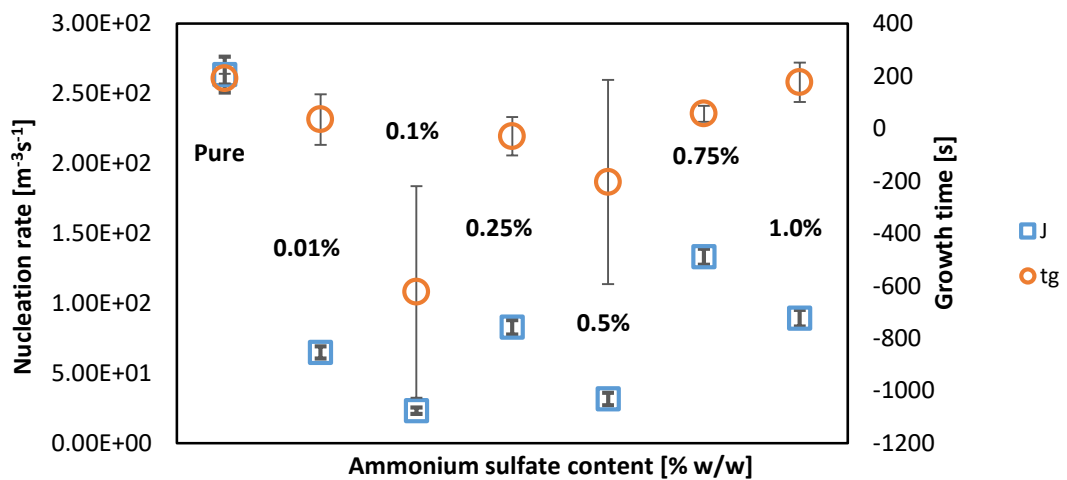


Figure 101. Summary of results ($n=40$) from fitting the ter Horst model to the cumulative probability distributions of all induction time experiments for all unfiltered conditions. In the graph blue \square represents nucleation rate - J and orange \circ represents growth time - t_g .

The analysis yielded negative growth time results, which were physically meaningless. The potential reason behind this is that the model was being over-fitted. The nucleation rate decreased for samples containing up to 0.5 %w/w ammonium sulfate and then increased again with the increased amount of ammonium sulfate addition. However, due to negative growth time values, the obtained physical means of the nucleation rate is questionable.

5.5.2.1.1.2 Classical Nucleation Theory

The Classical Nucleation Theory model was described in section 2.4.3.1 and the results obtained for the nucleation rate in $\text{m}^{-3}\text{s}^{-1}$ are presented in Figure 102 for unfiltered samples and in Figure 103 for filtered samples.

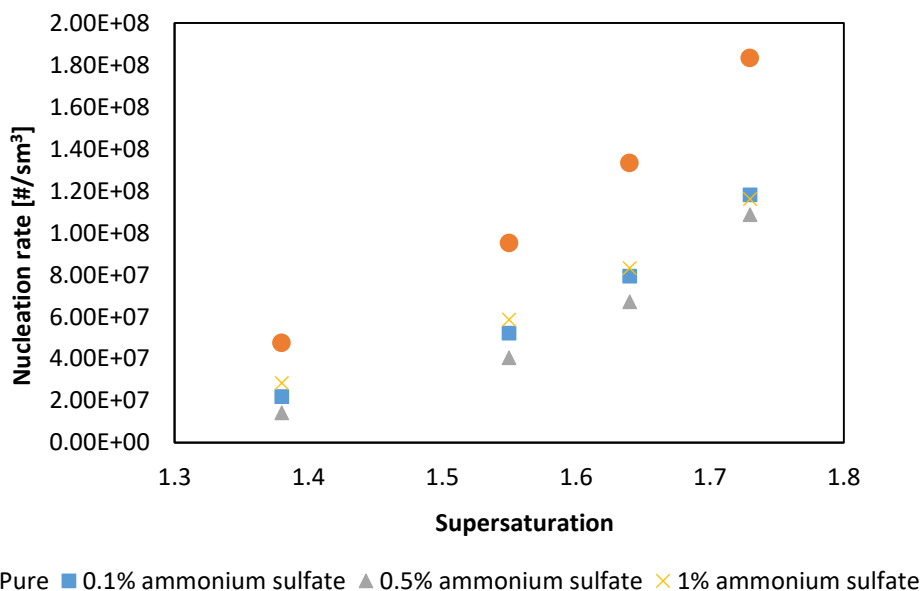


Figure 102. Summary of results from fitting the Classical Nucleation Theory model to the cumulative probability distributions of all induction time experiments for all unfiltered conditions: [●] represents pure metformin hydrochloride samples, [■] represents metformin hydrochloride samples doped with 0.10 %w/w of ammonium sulfate, [▲] 0.50 %w/w of ammonium sulfate and [×] 1.00 %w/w of ammonium sulfate

Classical Nucleation Theory model (based on Kubota's approach [27]) results showed an increase in nucleation rate with supersaturation. The nucleation rates for all doped samples are lower than for pure metformin hydrochloride. The nucleation rate (J) for 1 %w/w ammonium sulfate (e.g. $SS=1.55$, $J= 5.86E+07$ [#/ sm^3]) is in general larger than for 0.1 %w/w (e.g. $SS=1.55$, $J= 5.22E+07$ [#/ sm^3]). The biggest effect though was observed for samples containing 0.5 %w/w ammonium sulfate, where this produced the lowest nucleation rate (e.g. $SS=1.55$, $J= 4.05E+07$ [#/ sm^3]) and did not fit the general trend.

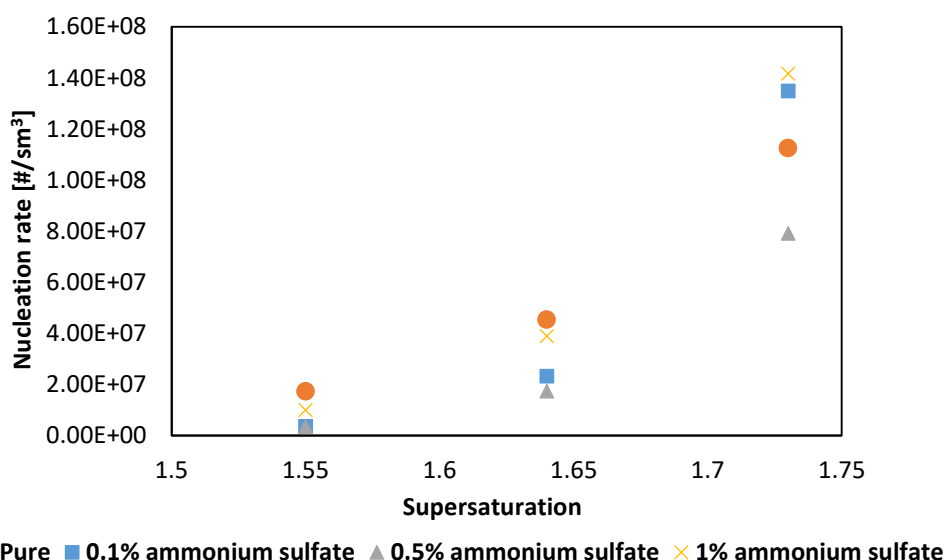


Figure 103. Summary of results from fitting the Classical Nucleation Theory model to the cumulative probability distributions of all induction time experiments for all filtered conditions: [●] represents pure metformin hydrochloride samples, [■] represents metformin hydrochloride samples doped with 0.10 %w/w of ammonium sulfate, [▲] 0.50 %w/w of ammonium sulfate and [×] 1.00 %w/w of ammonium sulfate

For filtered samples a similar trend was observed, however rates with addition of the 0.1 and 1.0 %w/w ammonium sulfate for 1.74 are larger than expected from the unfiltered experiments.

5.5.2.2 Induction Time Experiments Discussion

Using the Crystalline platform, induction time experiments were carried out for metformin hydrochloride samples containing different amounts of ammonium sulfate to investigate its effect on nucleation time. The concentrations of ammonium sulfate added to the metformin hydrochloride samples were 0.0, 0.01, 0.1, 0.25, 0.5, 0.75 and 1.0 %w/w. Addition of 1.0 %w/w was chosen as a maximum due to the low solubility of ammonium sulfate in the ethanol:water mixture. Based on the raw data (8-40 experiments per each condition), the addition of ammonium sulfate up to 0.5 %w/w caused an increase of the induction time and a broadening of the distribution of induction times, while addition of 1.0 % w/w of ammonium sulfate lost its effect

and induction times were comparable to the pure system. These points were true for all supersaturations of metformin hydrochloride that were used (1.38, 1.55, 1.64, 1.73).

The results from the ter Horst model showed a decrease in nucleation rate, when up to 0.5 %w/w ammonium sulfate was added to metformin hydrochloride solution, which agrees with the raw data. However, the negative growth time obtained brings the validity of the model into question in this case. When a smaller number of points were put into the model, the results were more realistic, indicating that the model was being over-fitted. However, the loss of physical meaning meant that this model was not suitable for this set of experiments.

The Classical Nucleation Theory model yielded a fit to the described data that was more promising and showed the trends that were observed in the raw data for the nucleation rate. On this basis, the classical nucleation theory model was explored further. The pure system demonstrated the highest nucleation rates across all four supersaturations and the 0.5 %w/w ammonium sulfate had the lowest nucleation rates. Out of all of the samples containing impurities, the 1.0 %w/w ammonium sulfate had the shortest induction times. This again backs up the raw data, showing that this model is suitable for this system. Filtration with 0.22 μm PES syringe filters was employed for the induction time experiments to see if ammonium sulfate effects became clearer after the solution was purified. In general, induction times were much longer and the distribution was wider. This was due to the solutions being more homogenous i.e. less dust contaminants were present, reducing the nucleation sites and prolonging observed nucleation time. Several samples did not crystallise over a period of 24 hours, therefore some conditions had a smaller number of repetitions. The filtered samples, despite having longer induction periods, agree with the unfiltered sample data. The supersaturation 1.73 was the only exception, where the pure system did not follow the trend and had lower nucleation rate than expected. It could be due to sample aging, increasing the amount of impurity already in the sample. The classical nucleation model explains the variation in terms of interfacial energy, which is discussed in section 5.5.3.

The comparison of the nucleation rate values obtained from both models for experiments, where supersaturation of 1.55 was chosen is shown below in Table 56.

Table 56. The comparison of the nucleation rate values obtained from the two studied models - Classical Nucleation Theory and ter Horst Model, for the experiments, where supersaturation of 1.55 was chosen.

Impurity content [%]	CNT	ter Horst
0.0	9.51E07	2.64E02
0.1	5.22E07	2.32E01
0.5	4.05E07	3.17E01
1.0	5.86E07	8.93E01

The much higher values observed from the Classical Nucleation Theory are caused by the assumption made by Mitchell et al. [27] about the number of derived particles taken into account during the calculations of the nucleation rate – 100000000000 (10E11) was assumed for a detectable number density. However, a general agreement between the two models is observed.

There were several areas of further investigation that were carried out in order to explain why the addition of 0.5 %w/w had the biggest effect on nucleation rate and why samples containing 1.0 %w/w were behaving similarly to pure metformin hydrochloride samples.

5.5.3 Investigation of Impurity Concentration Effect on Induction Time

The results from the induction time experiments revealed that the 0.5 %w/w concentration of ammonium sulfate had the greatest influence over the induction time of metformin hydrochloride. In order to probe this effect, it was thought that several reasons could be responsible for this:

- 1) A pH change in the solution because of the presence of two salts in the solution
- 2) The solubility of metformin hydrochloride was being altered by the presence of the ammonium sulfate in solution
- 3) The interfacial energy of metformin hydrochloride nuclei was being altered by the presence of ammonium sulfate

5.5.3.1 Results and Discussion from pH Investigation

The graph given in Figure 104 shows the change in pH with decreasing temperature for all experiments. The pH ranged from 5.4 to 6.2 for the initial conditions and 6.2 to 6.7 for the crystallisation point. The error of the pH probe, when using a non-aqueous solvent can be as high as ± 0.5 pH [136].

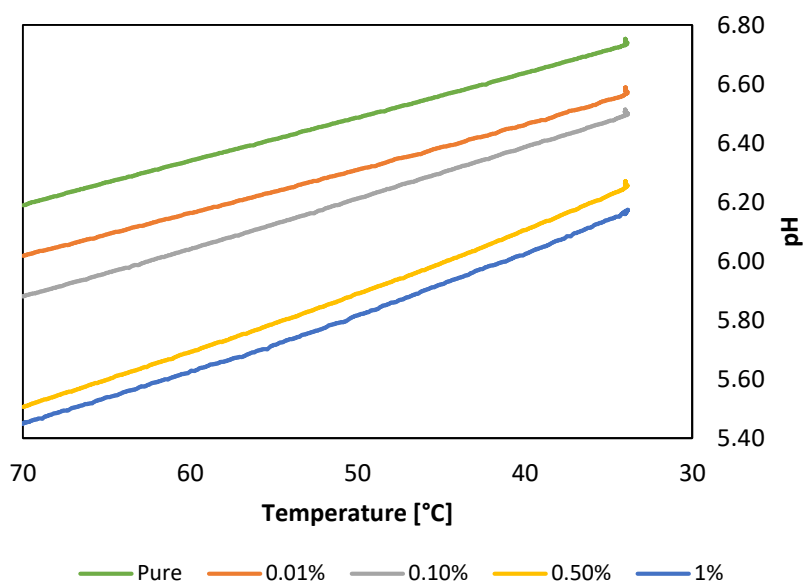


Figure 104. pH investigation results showing changes with decreasing temperature in the Optimax reactor during crystallisation of metformin hydrochloride. Green represents pure metformin hydrochloride samples, orange represents metformin hydrochloride samples doped with 0.01 %w/w of ammonium sulfate, grey samples doped with 0.10 %w/w of ammonium sulfate, yellow samples doped with 0.50% of ammonium sulfate and blue samples doped with 1.00 %w/w of ammonium sulfate.

The initial pH of the solution containing ammonium sulfate and metformin hydrochloride dissolved in the ethanol:water mixture showed a clear relationship between the amount of ammonium sulfate added and the pH of the solution – the pH decreased as the concentration of ammonium sulfate increased. The measured pH values were as follows: pure metformin hydrochloride – 6.73, sample containing 0.01 %w/w ammonium sulfate – 6.51, 0.1 %w/w ammonium sulfate – 6.49, 0.5 %w/w ammonium sulfate – 6.25, 1.0 %w/w ammonium sulfate – 6.16. The ammonium sulfate is an acidic salt and this was increasing the content of protons in the mixture. The final pH of the solution after crystallisation took place followed the same trend, therefore showing that the pH was not the reason for changing the nucleation behaviour of samples containing 0.5 %w/w ammonium sulfate. However, it needs to be noted, that in alcoholic solution the pH measurement is not fully reliable. This means that comparing the plots is not possible and only the general trend of each individual plot can be stated [137].

5.5.3.2 Results and Discussion from Solubility Investigation

The next stage of the investigation was to test the solubility of metformin hydrochloride under each concentration of ammonium sulfate. Solubility curves obtained are given in Figure 105 along with the exponential fits. The pure metformin hydrochloride solubility curve is plotted for comparison.

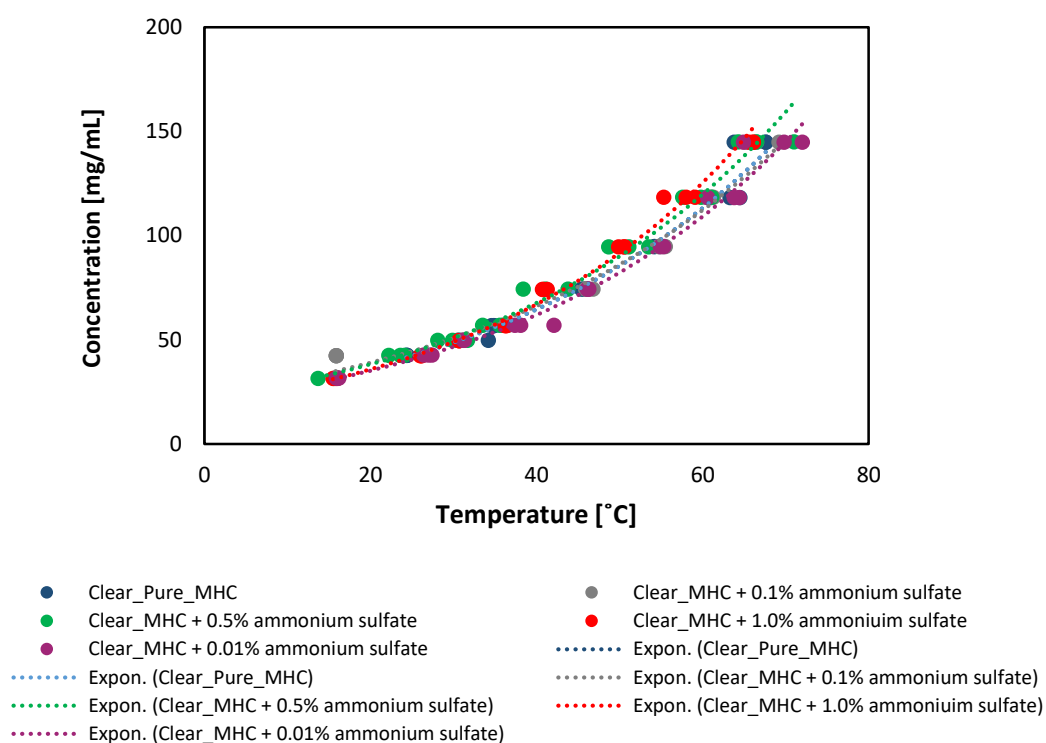


Figure 105. Solubility curves obtained in the Crystalline platform for all unfiltered experiments with pure metformin (blue) and metformin doped with different ammonium sulfate concentrations: 0.01 %w/w (purple), 0.1 %w/w (grey), 0.5 %w/w (green) and 1.0 %w/w (red).

Solubility curves obtained were comparable to one another, showing that ammonium sulfate did not significantly affect the solubility, and hence the interactions between metformin and the solvent molecules. Solubility was then ruled out as a cause of the difference of induction time between conditions.

5.5.3.3 Results and Discussion from the Interfacial Energy Calculations

The interfacial energy values in mJ/m^2 were calculated using classical nucleation theory described in section 2.5.1. Equation 85 (shown previously as Equation 8) presents the relationship between the interfacial energy (γ) and the free energy change (ΔG) for nucleation.

Equation 85

$$\Delta G = \frac{-4\pi r^3 \Delta\mu}{3v} + 4\pi r^2 \gamma$$

$$\frac{d\Delta G}{dr} = \frac{-4\pi r^2 \Delta\mu}{v} + 8\pi r \gamma = 0$$

The interfacial energy was calculated to try and answer why the 0.5% ammonium sulfate concentration had the biggest effect on the nucleation parameters.

The plot in Figure 106 shows the results of the interfacial energy calculations for all experimental conditions. As it can be seen the highest value was obtained for samples containing 0.5 %w/w of metformin hydrochloride. The errors included in the graph were calculated based on the regression model in the Matlab curve fitting tool for the slope and y-intercept parameters.

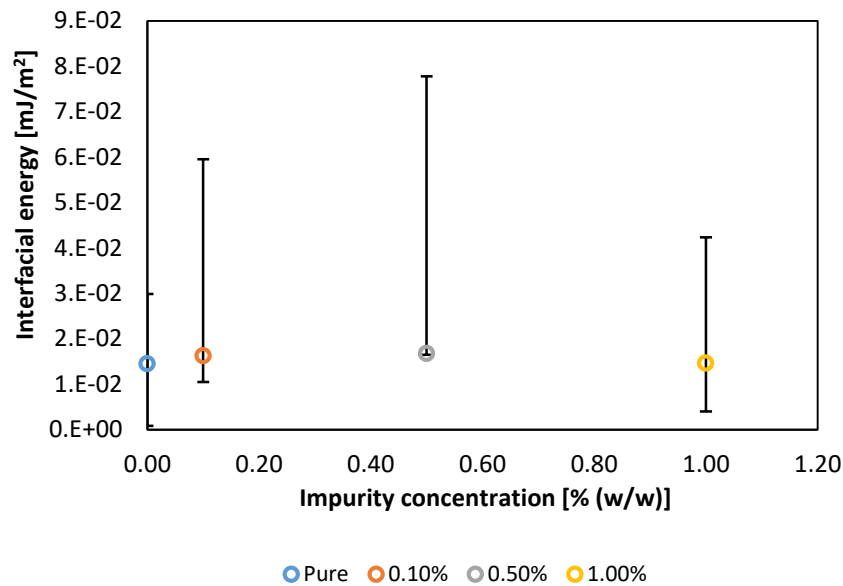


Figure 106. Graph showing results obtained for the interfacial energy determination for pure metformin hydrochloride (blue) and metformin hydrochloride doped with 0.1 %w/w (orange), 0.5 %w/w (grey) and 1.0 (yellow) %w/w ammonium sulfate

The interfacial energy calculations showed that the highest value was achieved for 0.5 %w/w ammonium sulfate samples with a value of $1.68 \cdot 10^{-2}$ mJ/m². All other conditions had values lower than this. From the free energy relationship, given in Equation 8, ΔG required for nucleation becomes less negative and hence less favourable. The results from the pure metformin hydrochloride samples and from the 1.0 %w/w ammonium sulfate samples were $1.45 \cdot 10^{-2}$ mJ/m² and $1.472 \cdot 10^{-2}$ mJ/m² respectively. This reinforced the fact, that the induction times for those conditions were similar, suggesting that the effect disappears at the 1.0% ammonium sulfate concentration.

The difficulties in comparing the results calculated based on CNT result from the assumption made by Morris et al. [107], about the number of derived particles taken into account during the calculations of the nucleation rate and consequently the interfacial energy. However, the general trends observed during this study can be compared with general trends already published in the literature. Shanmugham et al. [52] investigated the effect of soluble impurities (potassium carbonate, potassium sulfate, potassium oxalate, potassium chromate and sodium borate) on nucleation

rates and interfacial energy of potassium dihydrogen orthophosphate. They concluded that the presence of the impurities caused a decrease of the interfacial energy, which contradicts the results obtained during the investigation of the ammonium sulfate effect on metformin hydrochloride nucleation kinetics. Peng et al. [59] observed that the presence of Cl^- and SO_4^{2-} caused an increase of interfacial energy, when the crystallisation of borax dehydrate was studied. Similar results were reported by Rahman [57] who investigated the effect of potassium chloride (KCl) on the interfacial energy of potassium acid phthalate (KAP). Almost a twofold increase in the interfacial energy value was reported, however, further investigation revealed that in this case KCl was incorporated into the KAP crystal lattice, which was not observed for ammonium sulfate and metformin hydrochloride.

5.5.3.4 Results and Discussion from SEM Analysis

The following images in Figure 107 show the SEM results for re-crystallised metformin hydrochloride, the raw material and metformin hydrochloride doped with 0.1, 0.5, 1.0 %w/w ammonium sulfate respectively.

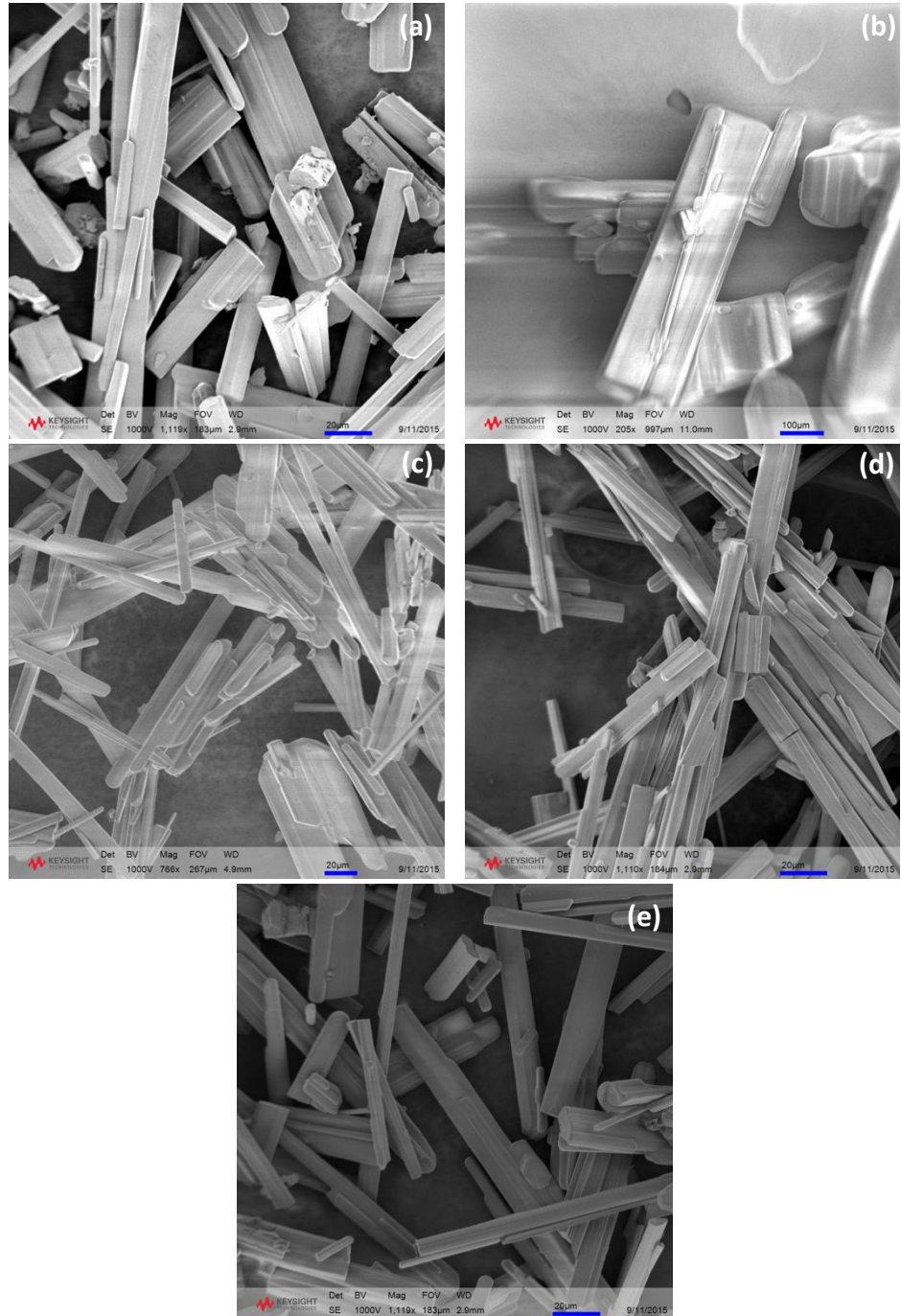


Figure 107. SEM image taken at (a) 1119x magnification of recrystallised metformin (b) 205x magnification of the metformin raw material (c) 766x magnification of metformin crystals produced in the presence of 0.1 %w/w ammonium sulfate (d) 1110x magnification of metformin crystals produced in the presence of 0.5 %w/w ammonium sulfate (e) 1119x magnification of metformin crystals produced in the presence of 1.0 %w/w ammonium sulfate

The SEM images showed that the morphology was the same for all re-crystallised samples and that the raw material has larger crystals size than the re-crystallised material. The ammonium sulfate does not alter the crystal shape and the smaller crystal size was expected after recrystallization. Therefore, the results suggest that impurities were not present in final washed crystals and the effect observed from ammonium sulfate seems to be a solvent-cluster interaction rather than a crystal structure alteration. This is backed up by the interfacial energy calculations, as they describe the solute-solvent interactions prior to nucleation and growth.

5.5.3.5 Results and Discussion from ToF-SIMS Analysis

Figure 108 shows the differences in the peak intensity between samples containing 0.1, 0.5 and 1.0 %w/w of ammonium sulfate.

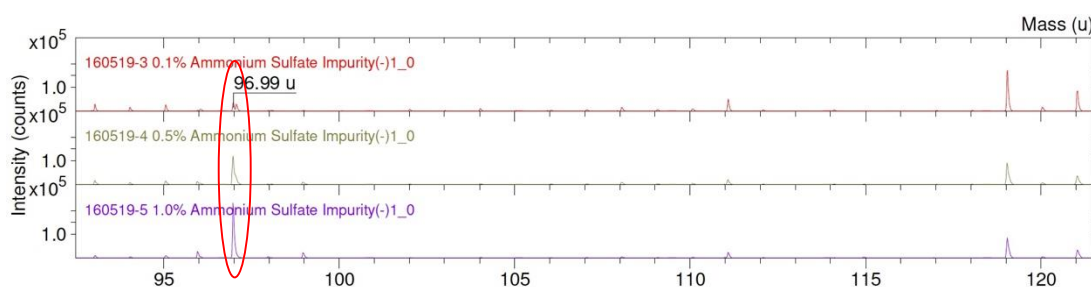


Figure 108. Results obtained from TOF-SIMS showing the increase in the peak area corresponding to ammonium sulfate in the crystals produced when the doping concentration was increased – highlighted in red.

Figure 109 below presents the peak area of the peaks highlighted in Figure 108.

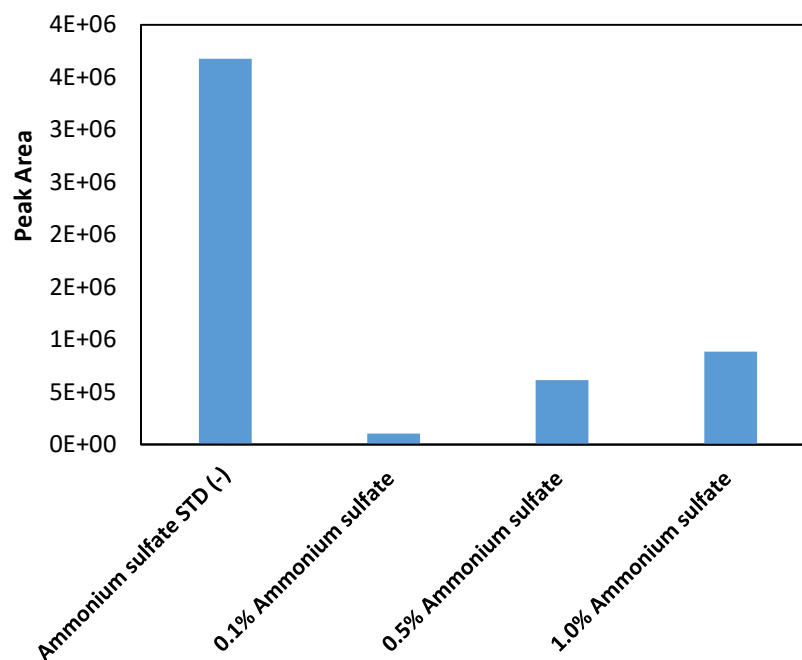


Figure 109. Peak area results from TOF-SIMS for the ammonium sulfate standard and the metformin crystals doped with 0.1, 0.5 and 1.0 %w/w ammonium sulfate in the solution

TOF-SIMS results suggested that the sulfate ion concentration increased, as the ammonium sulfate added to the solution was increased. There could be three possible explanations for this:

- 1) Some residual crystallisation solution could still remain on the crystal surface, even after washing.
- 2) The sulfate anions could be incorporated into the crystal structure, without altering the morphology.
- 3) The sulfate picked up was the inherent sulfate from the raw material.

Point number two seems unlikely, as it would be expected that the solubility would drastically change the solubility of metformin hydrochloride, but this was not found from the solubility investigation (see section 5.5.3.2).

5.5.3.6 Results and Discussion from DSC Analysis

Thermal traces for all analysed samples where a 10°C/min cooling rate was applied are shown in Figure 110.

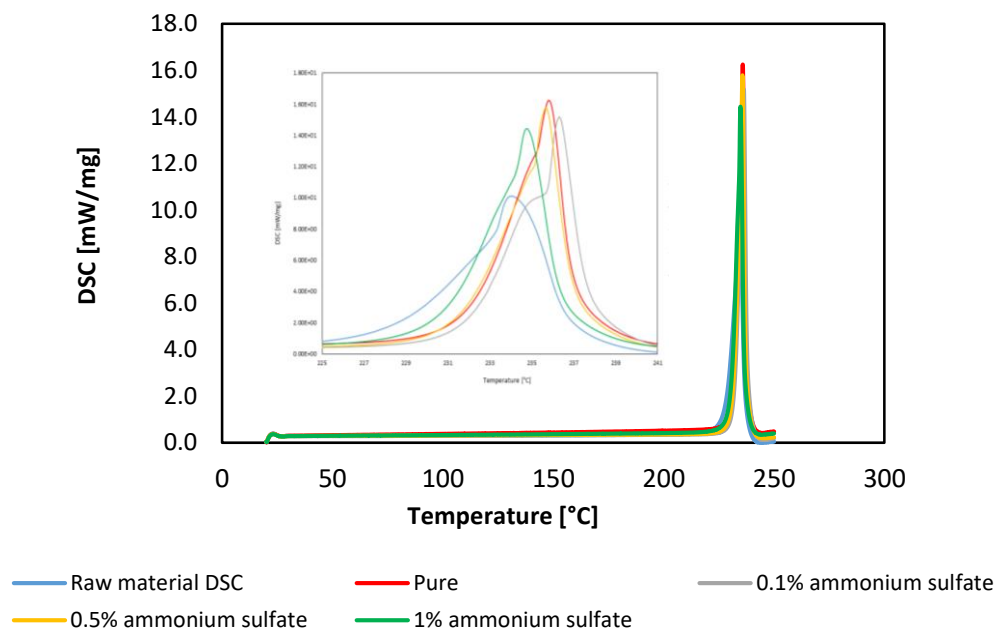
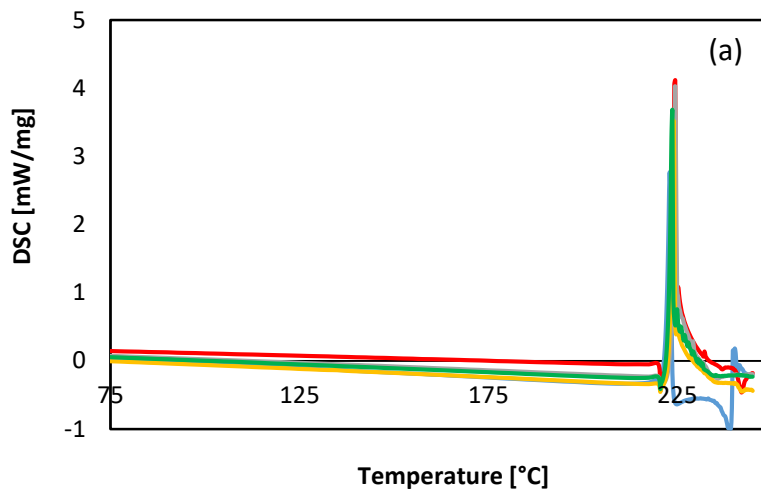
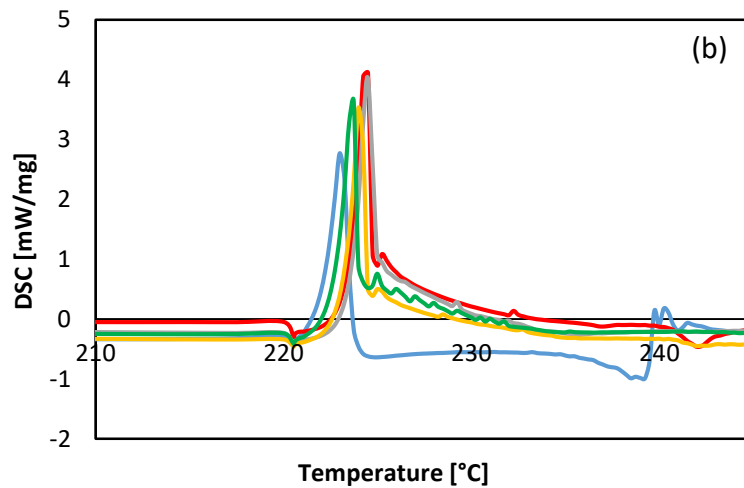


Figure 110. Thermal traces for metformin hydrochloride raw material (blue), pure material (red), sample containing 0.1 %w/w of ammonium sulfate (grey), 0.5 %w/w of ammonium sulfate (yellow) and 1.0 %w/w of ammonium sulfate (green), 10°C/min cooling rate.

Thermal traces for all analysed samples where 1°C/min cooling rate was applied are shown in Figure 111.



— Raw material DSC — Pure — 0.1% ammonium sulfate
 — 0.5% ammonium sulfate — 1% ammonium sulfate



— Raw material DSC — Pure — 0.1% ammonium sulfate
 — 0.5% ammonium sulfate — 1% ammonium sulfate

Figure 111. Thermal traces for metformin hydrochloride raw material (blue), pure material (red), sample containing 0.1 %w/w of ammonium sulfate (grey), 0.5 %w/w of ammonium sulfate (yellow) and 1.0 %w/w of ammonium sulfate (green), 1°C/min cooling rate: a) full profile and b) zoomed in profile

The Differential Scanning Calorimetry results revealed that the raw material had the lowest melting point and therefore was the most impure sample. For the remaining

samples, it was observed that the melting point increased as the addition of ammonium sulfate decreased, which is consistent with the theoretical assumption of DSC application for impurity determination.

5.5.3.7 Results and Discussion from Ion Chromatography Analysis

Figure 112 shows the summary of the results obtained during the ion chromatography measurements for the re-dissolved crystals. It can be seen that both blanks – for deionized water (dH₂O) and the solvent mixture contained trace amounts of sulfate ions. Obtained results revealed that the concentration of sulfate in all samples was at the level of about 0.5 µg/mL. Slightly higher concentration of sulfate ions is observed for samples containing 0.5 %w/w of ammonium sulfate, however the difference is not significant.

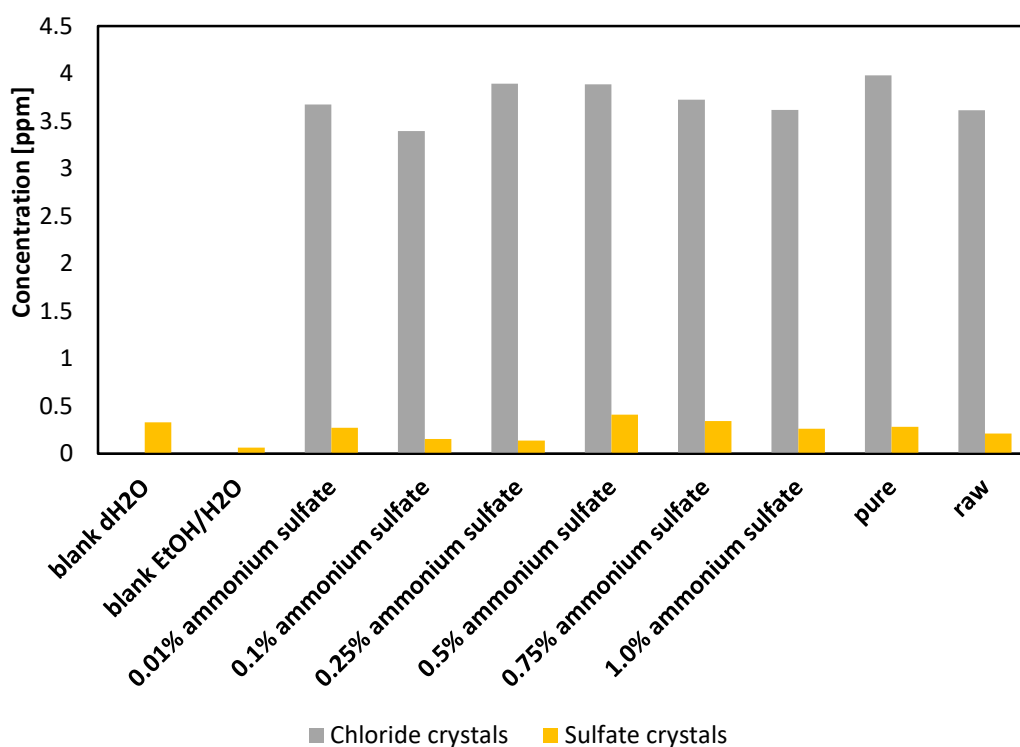


Figure 112. Results from ion chromatography showing the concentration of chloride (grey) and sulfate (yellow) in the metformin hydrochloride crystals produced under different doping concentrations of ammonium sulfate (0.01, 0.1, 0.25, 0.5, 0.75, 1.0 %w/w) as well as blank distilled water and blank solvent

Figure 113 shows the summary of the results obtained during the ion chromatography measurements for the filtrates. Obtained results show a good correlation between the concentration of ammonium sulfate added to the crystallising solution and the concentration calculated based on ion chromatography results. As it can be seen the ammonium sulfate concentration increases with the concentration obtained from the ion chromatography results.

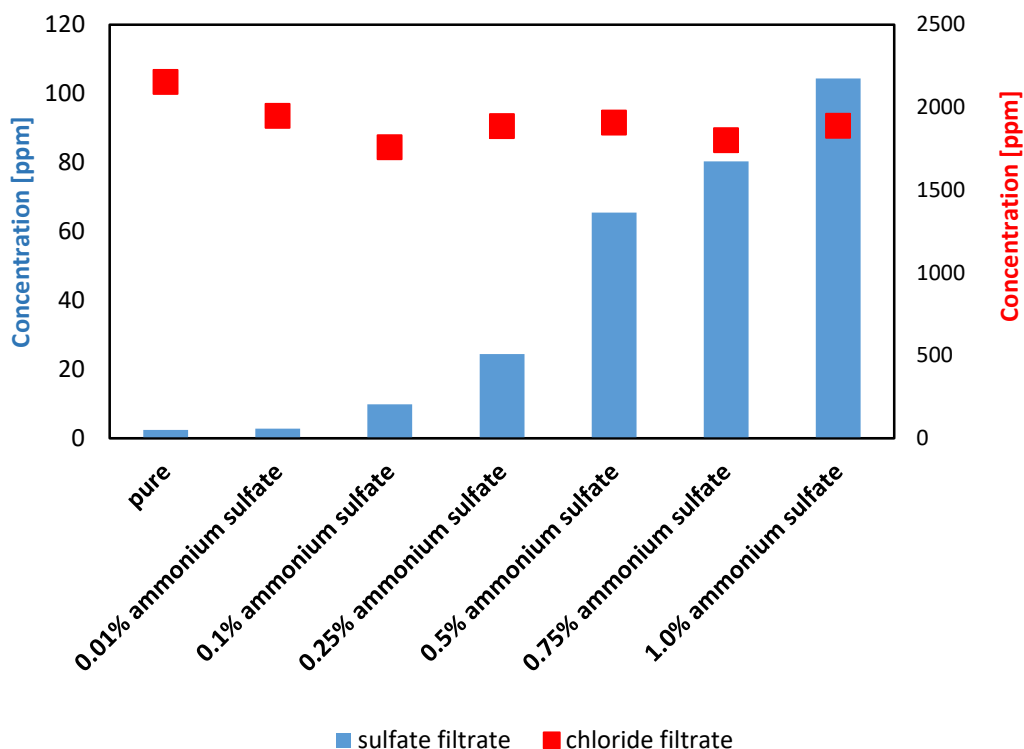


Figure 113. Results from ion chromatography showing the concentration of chloride (red) and sulfate (blue) in the metformin hydrochloride filtrate produced under different doping concentrations of ammonium sulfate (0.01, 0.1, 0.25, 0.5, 0.75, 1.0 %w/w)

The Ion Chromatography investigation showed that the crystals produced during the 0.5 %w/w ammonium sulfate experiments had the largest concentration of sulfate anions at 0.41 ppm. The lowest concentration of the sulfate anions came from the 1.0 %w/w ammonium sulfate experiment samples with the concentration of 0.26 ppm. The blank distilled water contained 0.33 ppm of sulfate ions. From this the sulfate added in the doping stage was not incorporated into the crystal. The trace

amounts of sulfate could be attributed to the solvent residuals from the washing process or from the inherent sulfate in the raw material, which contained 0.28 ppm. The analysis carried out for the liquor samples revealed an increasing amount of the sulfate ions as the addition of ammonium sulfate increased. This indicated that all the sulfate was left in the solution, which confirms that ammonium sulfate alters solvent-solute interactions in the solution.

5.5.3.8 Results and Discussion from Dynamic Light Scattering Experiments

Dynamic Light Scattering was used to probe the solution properties prior to nucleation, under the conditions used during the induction time experiments. Undersaturated solutions were also analysed to investigate the clustering ability of the system. In this section the graphs obtained from the DLS results are given in the form unprocessed autocorrelation functions, mean count rates and calculated hydrodynamic diameters.

5.5.3.8.1 Autocorrelation Functions

The autocorrelation functions for metformin hydrochloride at supersaturation 0.9 for unfiltered solution and the repetition of this condition are given in Figure 114. Each graph has the result for the pure metformin hydrochloride plus the results for when the crystallising solution was doped with various concentrations of ammonium sulfate. The concentrations were the same as were used during the induction time experiments mentioned previously: 0.01, 0.1, 0.5 and 1.0 %w/w ammonium sulfate.

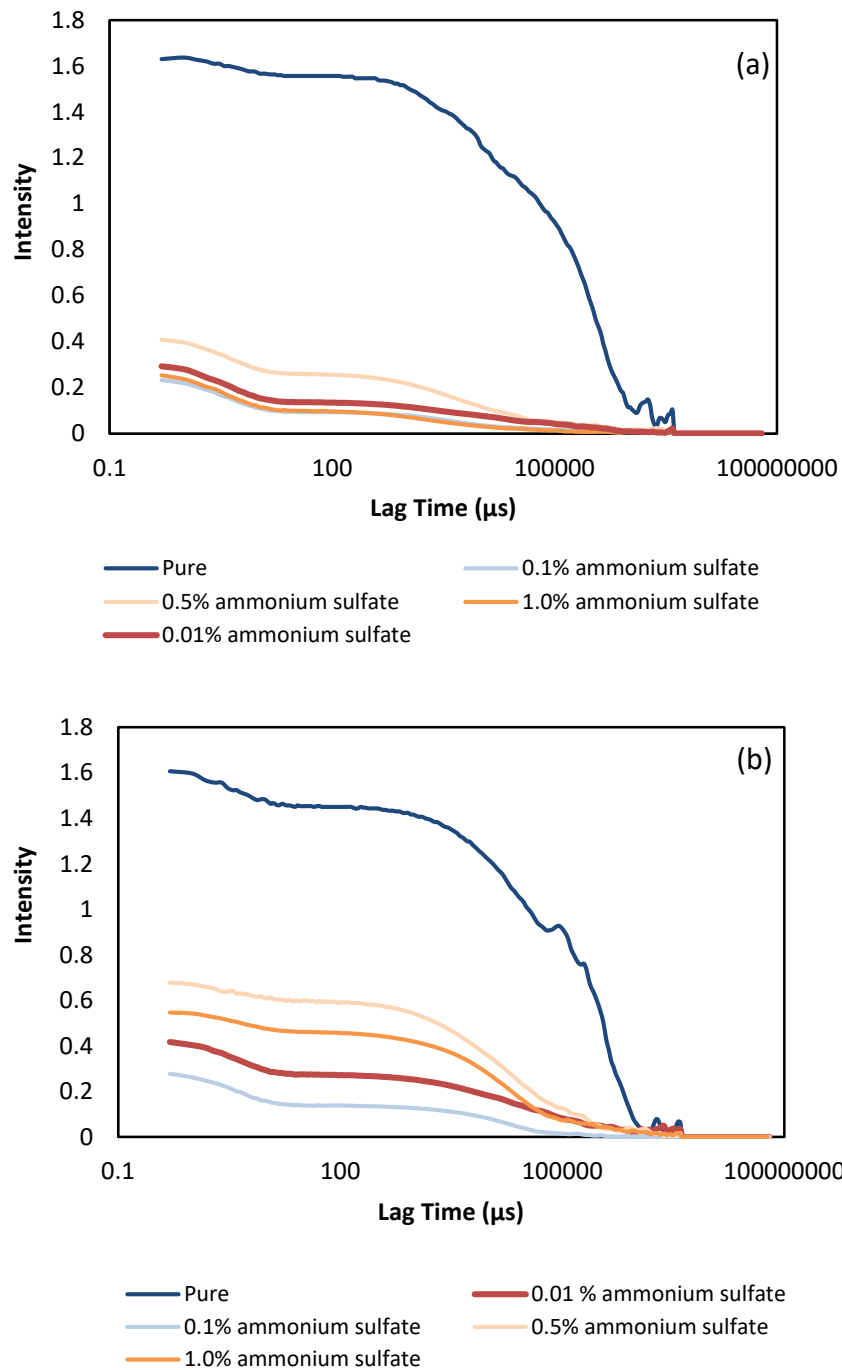


Figure 114. Autocorrelation functions from dynamic light scattering measurements (angle 173°) for undersaturated solution of metformin hydrochloride (SS=0.9) first (a) and second experimental run (b)

The graph below in Figure 115 depicts the mean count rate results with each experimental condition. It can be seen that the first experimental run had lower count rates.

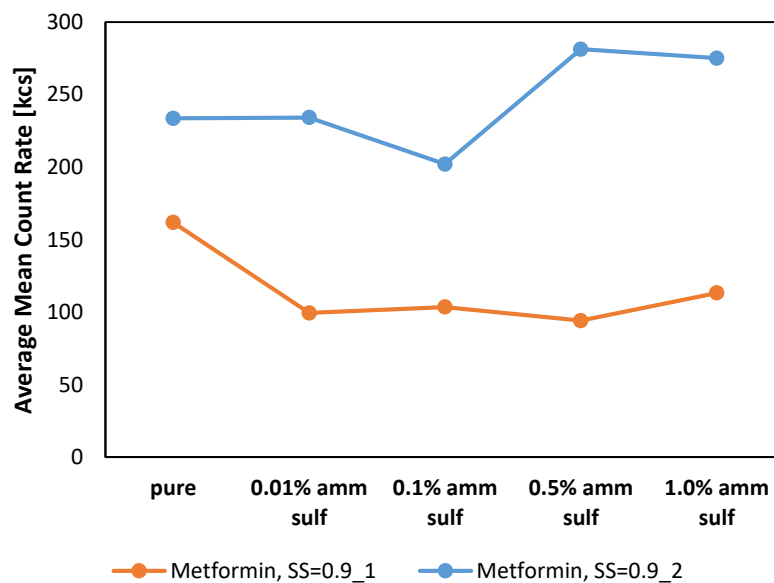


Figure 115. Mean count rate recorded in kilo counts per second for each impurity concentration during the dynamic light scattering measurements for undersaturated solution of metformin hydrochloride (SS=0.9) for repetition 1 (blue) and repetition 2 (orange).

Figure 116 shows the autocorrelation functions for the unfiltered supersaturated condition of 1.55 for the first and second experimental run. The supersaturated solution shows different trends in that it is not always the pure system with the largest intensity. The intensities for the second run are lower than the first.

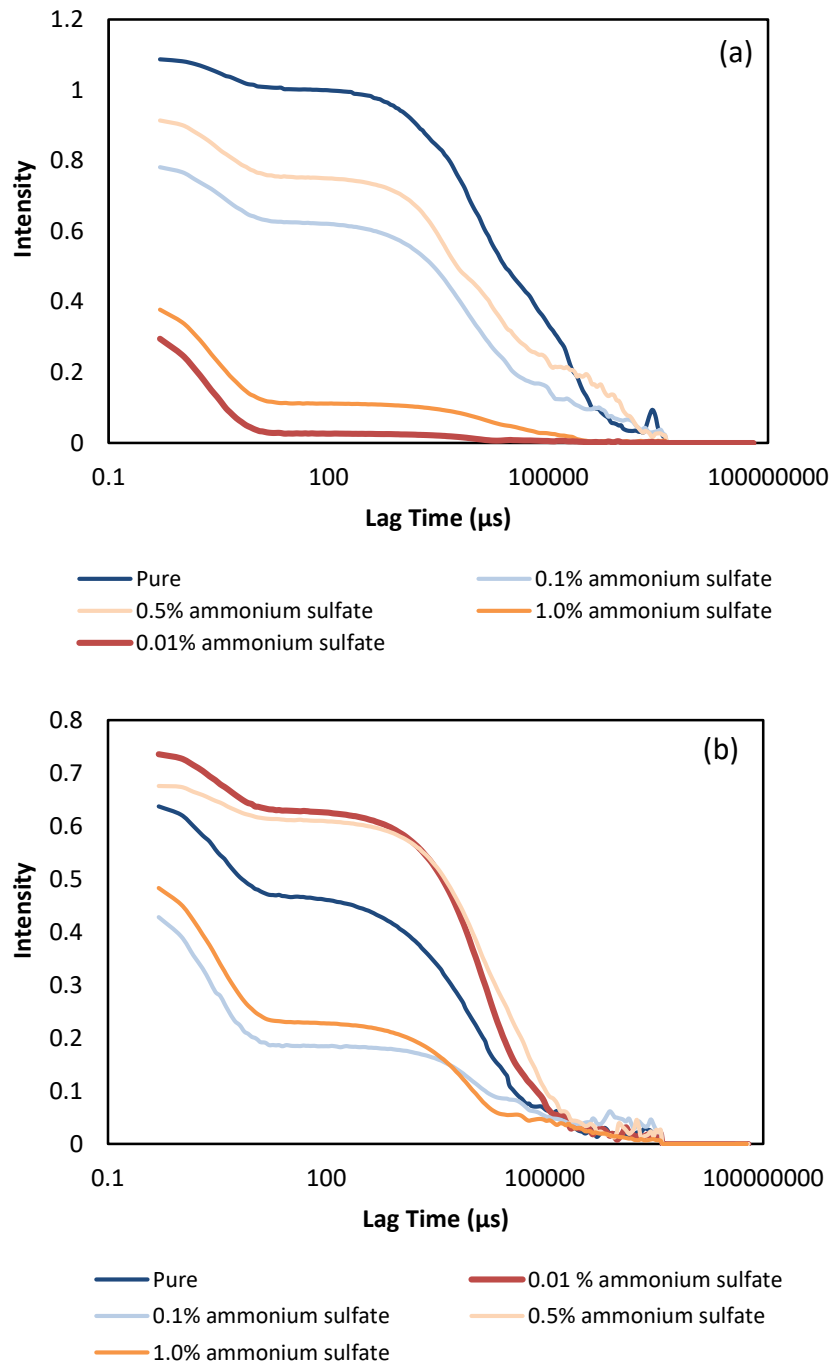


Figure 116. Autocorrelation functions from dynamic light scattering measurements (angle 173°) for unfiltered supersaturated solution of metformin hydrochloride ($SS=1.55$) first (a) and second experimental run (b)

The mean count rates for the higher supersaturation, for both experimental runs, are shown below in Figure 117. The second experimental run had higher mean count rate values than the first run.

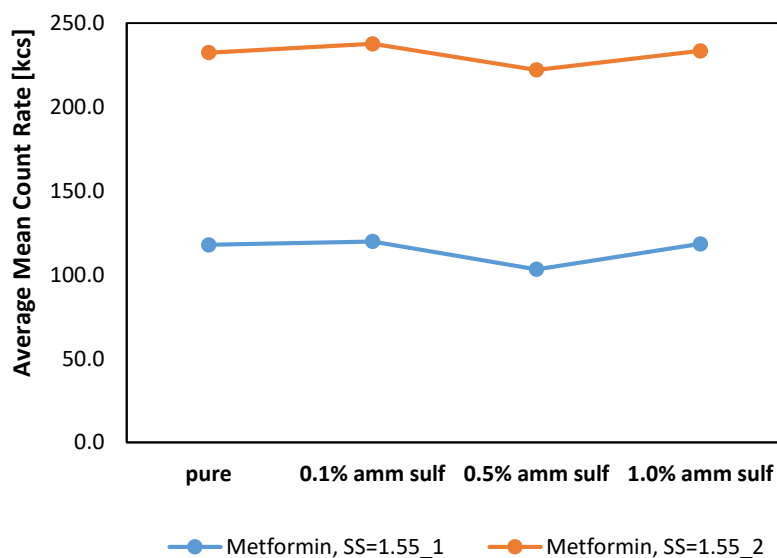


Figure 117. Mean count rate recorded in kilo counts per second for each impurity concentration during the dynamic light scattering measurements for supersaturated solution of metformin hydrochloride (SS=1.55) for repetition 1 (blue) and repetition 2 (orange).

The autocorrelation functions for filtered metformin hydrochloride doped with different ammonium sulfate concentrations are given in Figure 118. The filtered samples have much lower intensity and no clearly visible decays present in the autocorrelation functions for both experimental runs.

The baselines in the second experimental run are slightly irregular compared to the first run and is emphasized in the zoom section in the figure.

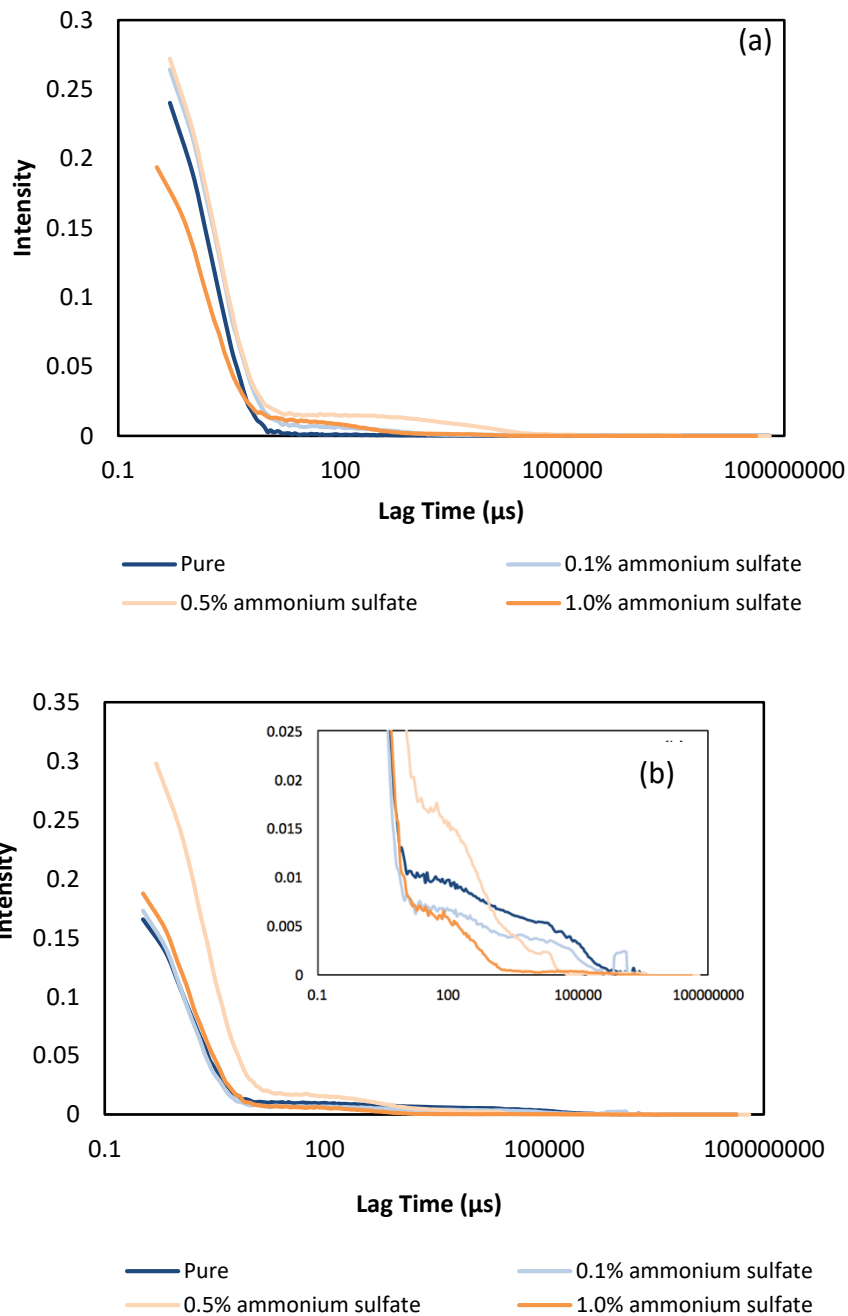


Figure 118. Autocorrelation functions from dynamic light scattering measurements (angle 173°) for filtered supersaturated solution of metformin hydrochloride ($SS=1.55$) first (a) and second experimental run (b)

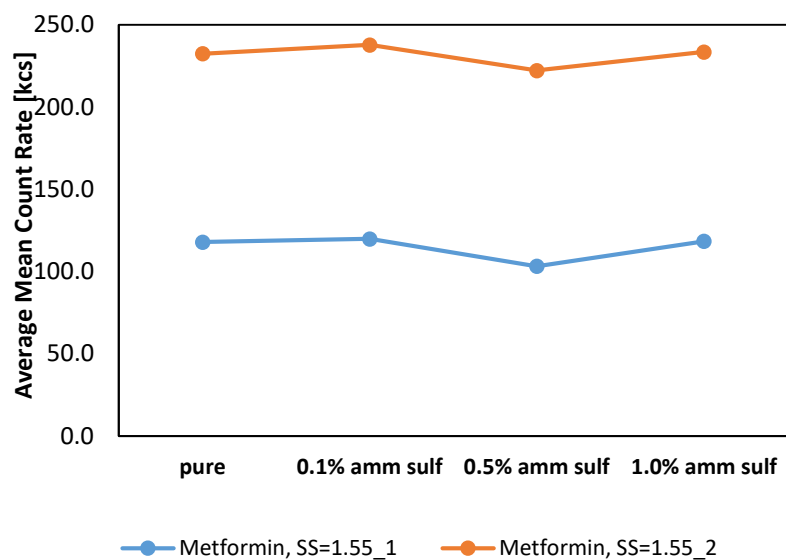


Figure 119. Mean count rate recorded in kilo counts per second for each impurity concentration during the dynamic light scattering measurements for supersaturated solution of metformin hydrochloride (SS=1.55) for repetition 1 (blue) and repetition 2 (orange).

5.5.3.8.2 Hydrodynamic Diameter

Figure 120, Figure 121 and Figure 122 are plots showing all the calculated hydrodynamic diameters from all DLS experiments using the Stokes-Einstein equation. All conditions show that there are species in the solution present with diameters ranging from 10 to 6000 nm.

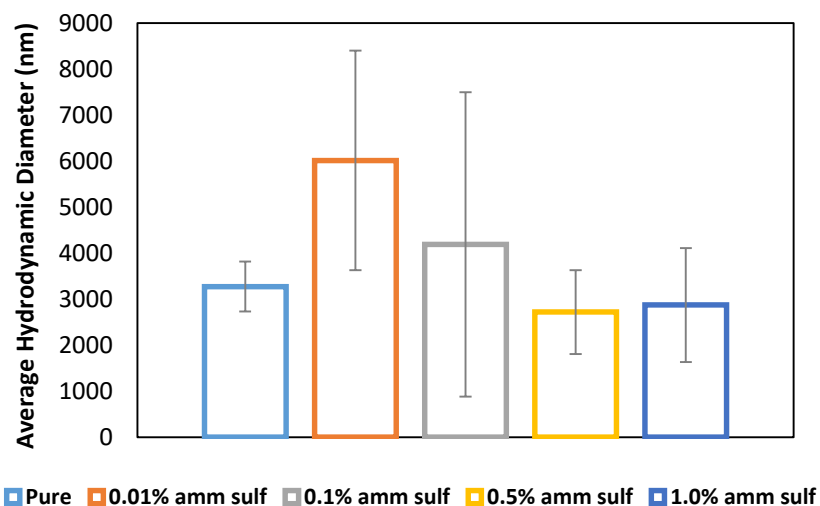


Figure 120. Average Diameter (nm) from 2nd Decay vs. Impurity Concentration for undersaturated solution of metformin hydrochloride (SS=0.9): pure metformin hydrochloride (light blue), samples doped with 0.01 %w/w of ammonium sulfate (orange), 0.1 %w/w (grey), 0.5 %w/w (yellow) and 1.0 %w/w (dark blue).

The largest average diameters of the prenucleation clusters are always present in a doped sample. For the undersaturated unfiltered solutions it was 0.01 %w/w ammonium sulfate, for the supersaturated unfiltered solutions it was 0.1 %w/w and for the filtered supersaturated samples it was the 0.5 %w/w.

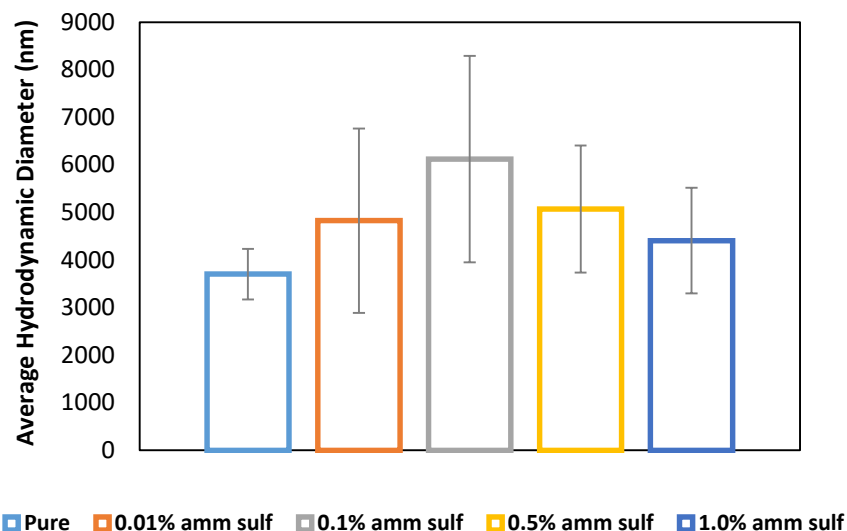


Figure 121. Average Diameter (nm) from 2nd Decay vs. Impurity Concentration for unfiltered supersaturated solution of metformin hydrochloride (SS=1.55): pure metformin hydrochloride (light blue), samples doped with 0.01 %w/w of ammonium sulfate (orange), 0.1 %w/w (grey), 0.5 %w/w (yellow) and 1.0 %w/w (dark blue).

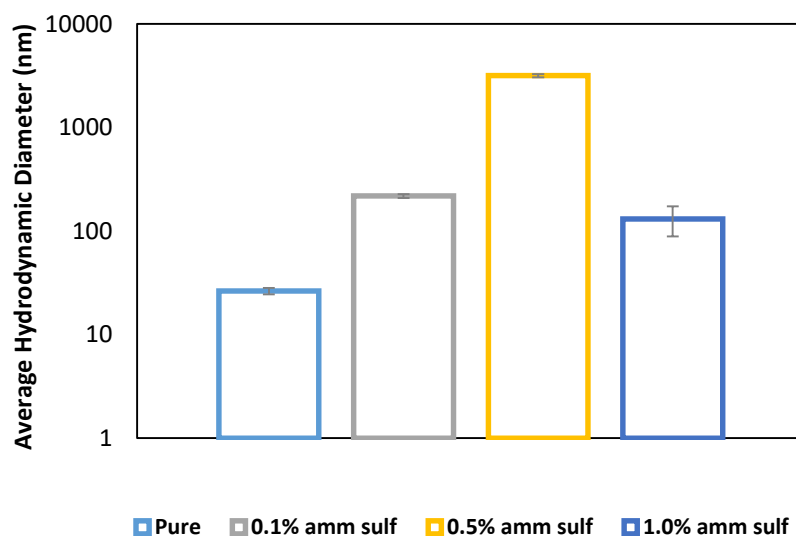


Figure 122. Average Diameter (nm) from 2nd Decay vs. Impurity Concentration for filtered supersaturated solution of metformin hydrochloride (SS=1.55). The y-axis is presented in logarithmic scale: pure metformin hydrochloride (light blue), samples doped with 0.1 %w/w (grey) of ammonium sulfate 0.5 %w/w (yellow) and 1.0 %w/w (dark blue).

5.5.3.8.3 Discussion from Dynamic Light Scattering Experiments

When analysing the autocorrelation function for $SS=0.9$ the pure sample had the highest intensity compared to all other conditions with ammonium sulfate being added. This showed that the presence of ammonium sulfate does have an effect on the solution structure, even at the lowest concentration of 0.01 %w/w. All functions for $SS=0.9$ and $SS=1.55$ have decays present showing that the pure system and doped systems all have internal structure in the solution.

The mean count rates were lower for the first experimental run. This could have been due to the solvent mixture in this case having fewer impurities. The mean count rates were higher in the second run of $SS=1.55$. This may explain why the second experimental run autocorrelation for the pure sample does not reflect the first. If the metformin hydrochloride used in this case had higher initial impurities due to being kept for too long in the laboratory, then it would have a higher concentration of initial impurities. After doping with ammonium chloride, the impurity effect would be increased even further, causing the large difference between the first and second run of supersaturation 1.55.

In the second experimental run of the filtered $SS=1.55$ experiments, the baselines of the autocorrelation functions were irregular. This resulted in the mean count rates for the second experimental run being higher than the first as can be seen from Figure 119. Not only this, the zoomed section also shows that the solution still has a decay present, at very low intensity. This is the same for the first and second run. The hydrodynamic diameters in Figure 122 show that there are still species present in the sample that are larger than the pore diameter (0.22 μm) of the syringe filter. This backs up the presence of prenucleation clusters being a fundamental property of solution. The filter only reduces their concentration but does not eliminate their presence.

The count rates for the conditions that were filtered with the PES syringe filter are more consistent across all the different ammonium sulfate concentrations. If the filtration step changes or even partly removes the effect that the ammonium sulfate has on the nucleation of metformin hydrochloride, then this would give a reason

behind the longer induction period for these samples. However, the pure samples were also found to have longer induction periods so the filtration is also affecting the pure metformin hydrochloride before it nucleates. This could suggest that the longer induction time was not purely down to removing dust and other foreign substances from solution, but perhaps the nucleation mechanism was being altered by the filtration step by reducing the number and/or size of the prenucleation clusters. Considering the hydrodynamic diameter values obtained, there were always diameters of significant value. From the results it was clear that the presence of impurity altered the diameter of the prenucleation clusters when compared to the pure system. The 1.0% w/w ammonium sulfate experiments always produced prenucleation clusters with the lowest diameter out of all the doped experiments. This backed up data obtained from the induction time experiments where these samples had induction times which were more comparable to the pure system. Prenucleation clusters of similar diameters would be assumed to create crystal nuclei at the same rate and hence have similar induction times.

5.6 Conclusions

Metformin hydrochloride was found to have many inherent inorganic impurities, which were detected in the preliminary stage. The inorganic impurity effect on crystallisation was not altered by mixing rate, scale of reactor or cooling rate. The presence of ammonium sulfate affected the induction period of metformin hydrochloride, but was dependent on the concentration of ammonium sulfate. Induction times were longer in the presence of ammonium sulfate than when pure apart from for 1.0 %w/w ammonium sulfate, which was similar to pure system. The ter Horst model was not suitable for this system, but the Classical Nucleation Theory model yielded sensible values for the nucleation rates under each experimental condition. pH was not a contributing factor to the changes in induction time and neither was the solubility. Interfacial energy was higher for 0.5 %w/w ammonium sulfate and pure system and 1.0% w/w ammonium sulfate were similar, indicating that an interfacial energy effect was responsible. SEM showed no morphology change, but TOF-SIMS showed an increase in sulfate on crystal surfaces with increasing ammonium sulfate concentration. However, with no change in solubility this was deemed to be residual solvent. The effect of ammonium sulfate on melting point was as expected – the bigger addition of the impurity the lower melting point of metformin hydrochloride.

The IC results revealed that sulfate was not a significant component in the crystal structure, but was retained in the filtrate after crystal collection. Filtering the solution prior to crystallisation resulted in longer induction times, due to removing dust particles in the solution. DLS showed that solutions had internal structure with and without impurity present and with and without filtration. Prenucleation clusters were present as filtration did not remove all species from solution with diameters larger than the pore diameter. The results showed that the 1.0 %w/w ammonium sulfate and the pure system behaved similarly prior to nucleation.

In conclusion, the evidence collected suggests that the alteration of the nucleation process is from the interaction of the ammonium sulfate with the metformin hydrochloride/solvent interactions. The addition of ammonium sulfate prolongs the

induction time in some cases, but when it reaches a critical concentration it loses its effect. The reverse effect of the 1.0 %w/w ammonium sulfate could be due to an increase in ionic interaction between the ammonium sulfate ions – for the lower concentration the strength will be reduced, making it easier for the individual ions to block the growth and the interaction between the metformin hydrochloride clusters. This would then increase the induction time. As a doubly charged anion sulfate will associate strongly with metformin than chloride and this might disrupt the formation of prenucleation clusters, although it is difficult to explain why the effect does not increase with increasing sulfate concentrations.

The reversed effect of the sulfate on crystallisation of metformin hydrochloride is very interesting and seems to be a phenomenon that has not been previously described in the literature. The extensive literature review presented in this thesis shows many examples, where the effect of impurities on crystallisation kinetics was studied, however none of them reported a reversed effect.

6 Overall Conclusions and Future Work

6.1 Conclusions from This Study

The conclusions outlined here cover of three experimental chapters with respect to the original project outline, stated in section 1.2. This project dealt with the topic of impurity characterisation, whether this was in the form of organic and inorganic molecules or an undesired polymorph. The work carried out aimed to quantify the presence of impurities as well as investigate their effects on nucleation and growth. From the CoFlux reactor experiments the excellent temperature control gave a much higher yield of L-glutamic acid crystals when compared to other types of reactors used in our laboratories. Enhanced temperature control was the reason behind this as this was the only major difference between this reactor and others. Polymorphic form was influenced greatly by the temperature control in this reactor and in most cases it was the metastable alpha polymorph that was produced. This was contrary to the products obtained in other reactor used. When the temperature loop was introduced the formation of the alpha form was even more prevalent. Crystal size distribution was found not to be influenced by the mixing speed but a narrower distribution was obtained with the improved temperature control. This project revealed that the trend in the accumulation or heat shift of the process fluid can be an indicator of the onset of crystallisation. It was clear from this work that more effective temperature control was the key factor in the polymorphic outcome.

The work conducted using LC/MS yielded a method, whereby metformin hydrochloride and its impurities could be analysed during the routine metformin hydrochloride characterisation. It was necessary to implement the ion chromatography, because dimethylamine could not be detected using the developed LC/MS method. The method developed here could be implemented in a continuous crystallisation of metformin hydrochloride to monitor changes in impurity concentration during the process.

Several inorganic impurities were detected in the raw material of metformin hydrochloride. The effect of mixing rate, scale and cooling rate did not affect the impurity level detected in the metformin hydrochloride crystals. Ammonium sulfate

altered the induction time of metformin hydrochloride crystals and the concentration of ammonium sulfate added changed the average induction time. The results from this project show that this was likely to be a result of molecular interaction between the ammonium sulfate and the metformin hydrochloride at the solution level. The induction time was delayed by doping with ammonium sulfate until a critical concentration was reached at which point the effect was reversed. This is an important observation since it might be that the most important impurities affecting crystallisation for a drug which is an acid or base are inorganic counter ions. Most drug substances contain a range of inorganic counter ions accumulated during manufacture. The reversed effect of the sulfate on crystallisation of metformin hydrochloride is a phenomenon that has not been previously described in the literature. The extensive literature review presented in this thesis shows many examples, where the effect of impurities on crystallisation kinetics was studied, however none of them reported a reversed effect. Many potential explanations of this phenomenon were tested during this study, however none of them explained the results.

6.2 Suggestions for Future Work

This project has provided tools and insight into the effects impurities can have on crystal nucleation. There is no evidence in the literature of using light scattering techniques in a doped system to study nucleation mechanisms. The evidence of prenucleation clusters in both undersaturated and supersaturated solutions of metformin hydrochloride was provided during this project, however the experimental procedure was not designed to its optimum, so potential changes could improve the quality and repeatability of the results obtained. Also, implementing Nanoparticle Tracking Analysis, could back up the results obtained from the Dynamic Light Scattering Experiments.

It could be useful to develop a derivatisation method for dimethylamine, which would not affect the other organic impurities present in the sample and therefore all known, organic impurities could be analysed using only LC/MS, without the implementation of IC.

Further research into the effects different inorganic impurities have on the nucleation of metformin hydrochloride could also be undertaken.

7 Appendix

7.1 LC - MS Calibration Curves

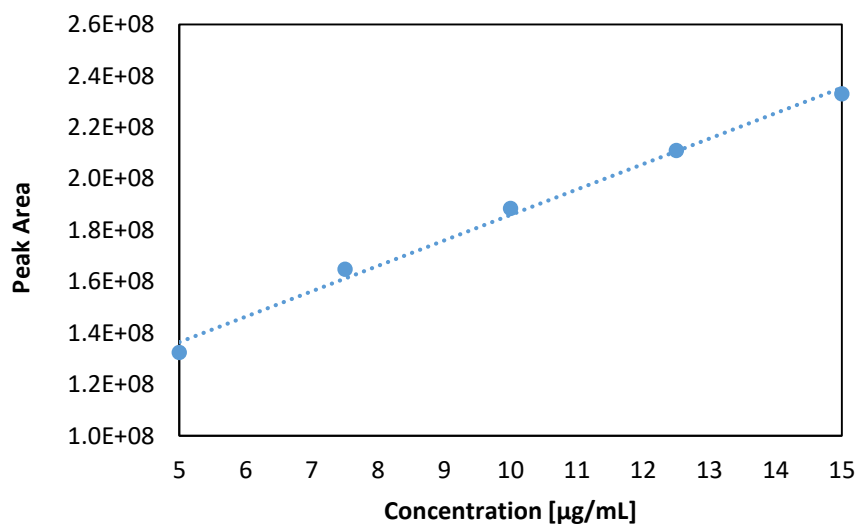


Figure 123. LC - MS calibration curve for metformin hydrochloride

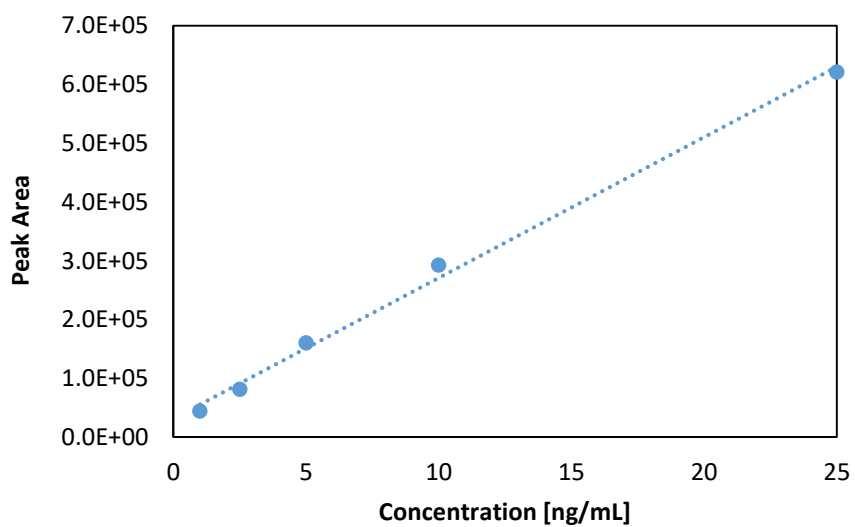


Figure 124. LC - MS calibration curve for melamine

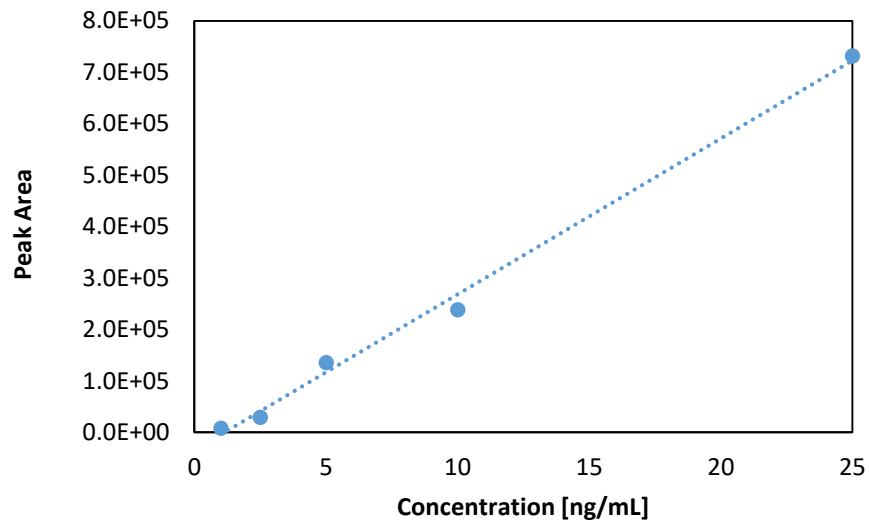


Figure 125. LC - MS calibration curve for 1-methylbiguanide

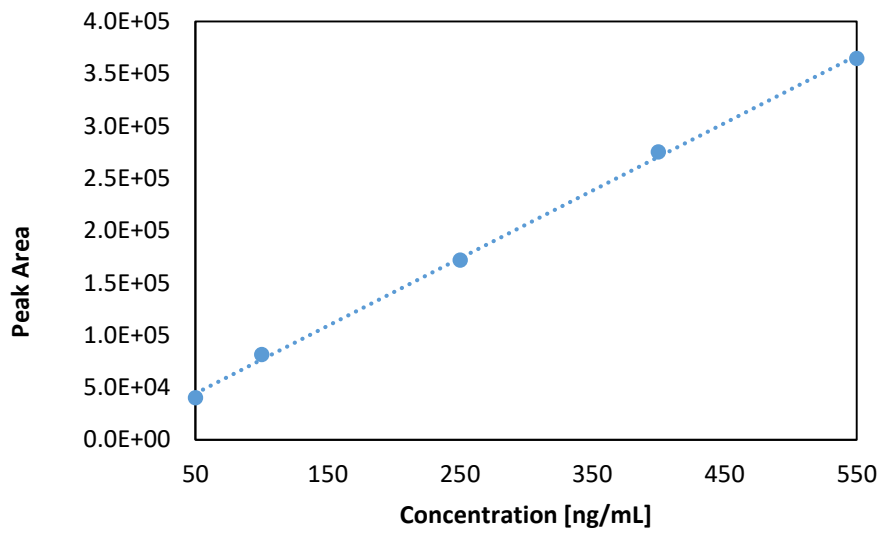


Figure 126. LC - MS calibration curve for cyanoguanidine

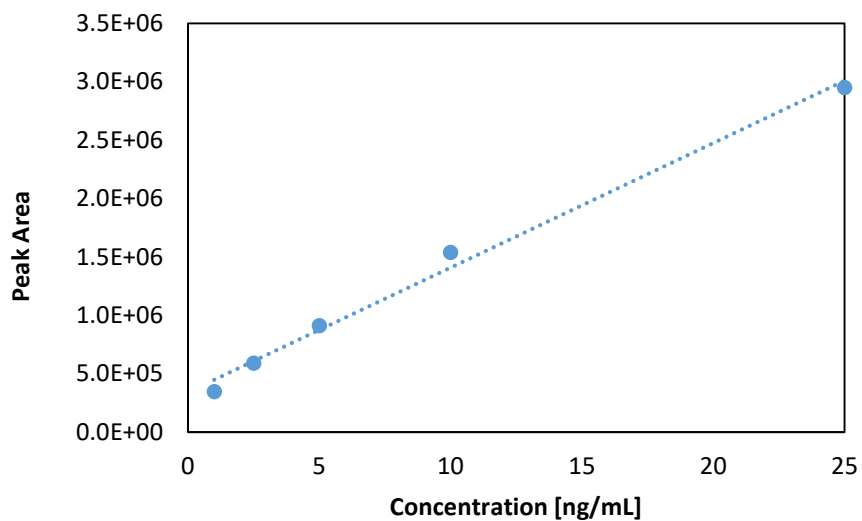


Figure 127. LC - MS calibration curve for (4,6-diamino-1,3,5-triazine-2-yl)-guanidine

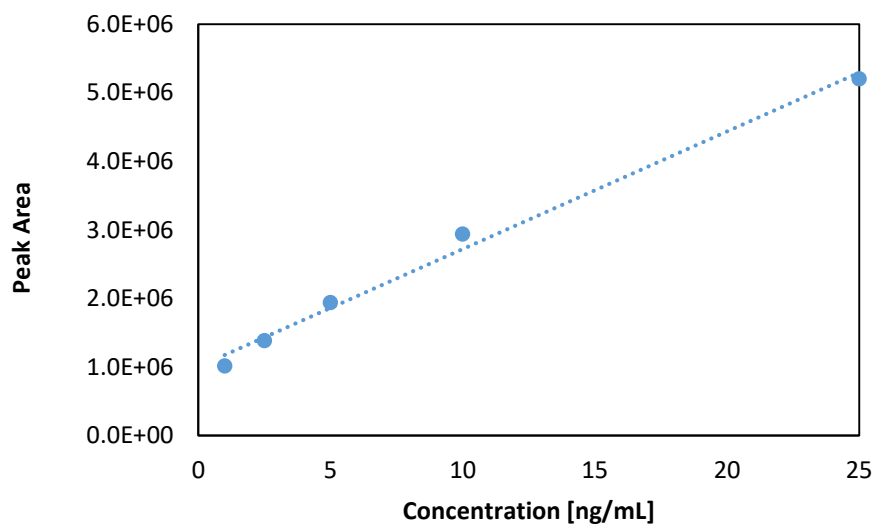


Figure 128. LC - MS calibration curve for N,N-dimethyl-1,3,5-triazine-2,4,6-triamine

7.2 Examples of Extracted Ion Chromatograms for Metformin Hydrochloride and Its Impurities

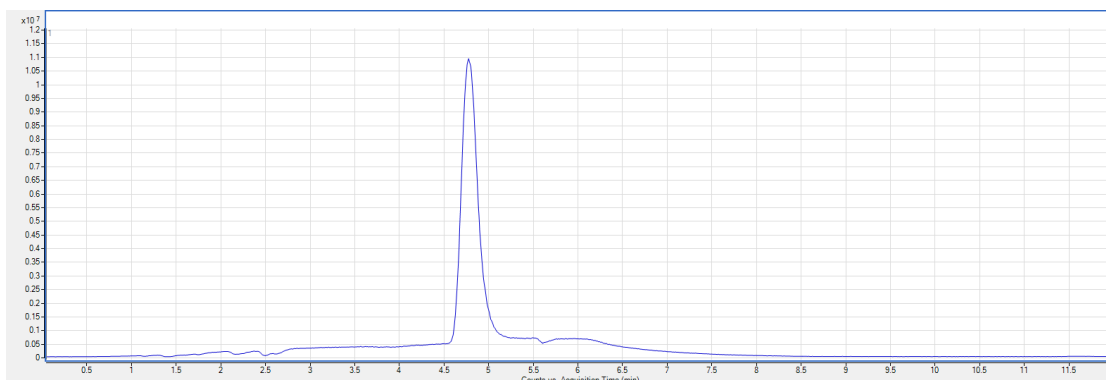


Figure 129. Extracted Ion Chromatogram of Metformin Hydrochloride at concentration of 5 mg/mL

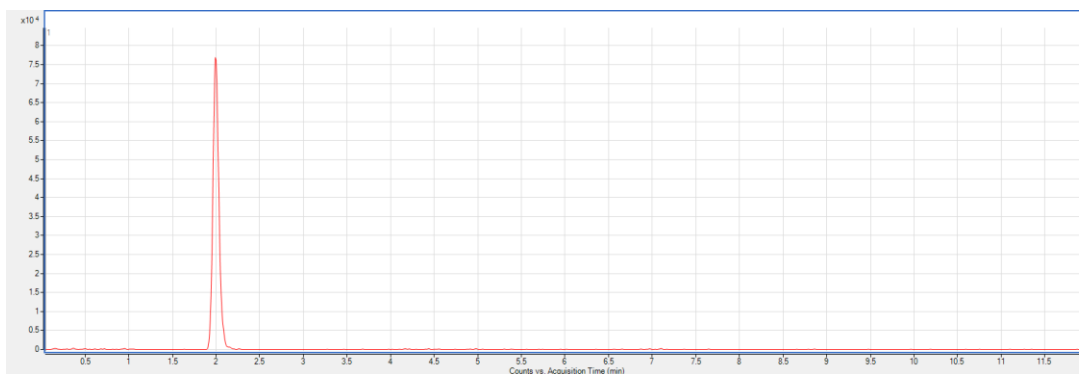


Figure 130. Extracted Ion Chromatogram of Cyanoguanidine at concentration of 550 ng/mL

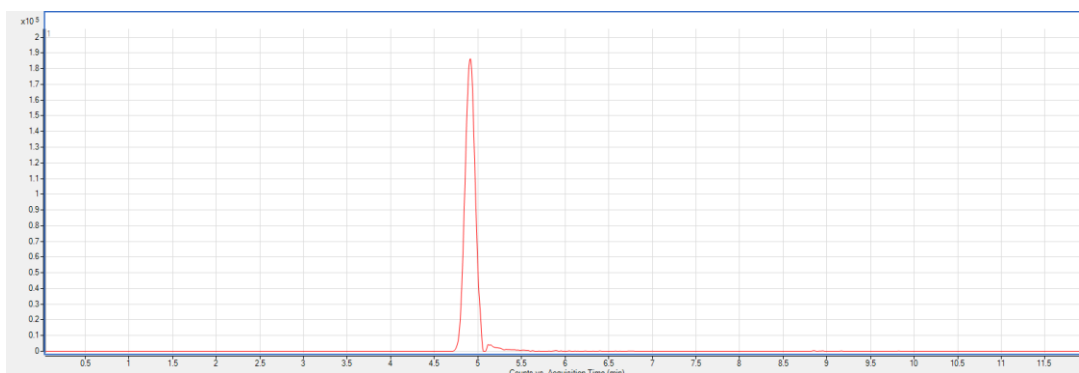


Figure 131. Extracted Ion Chromatogram for (4,6-diamino-1,3,5-triazine-2-yl)-guanidine at concentration of 10 ng/mL

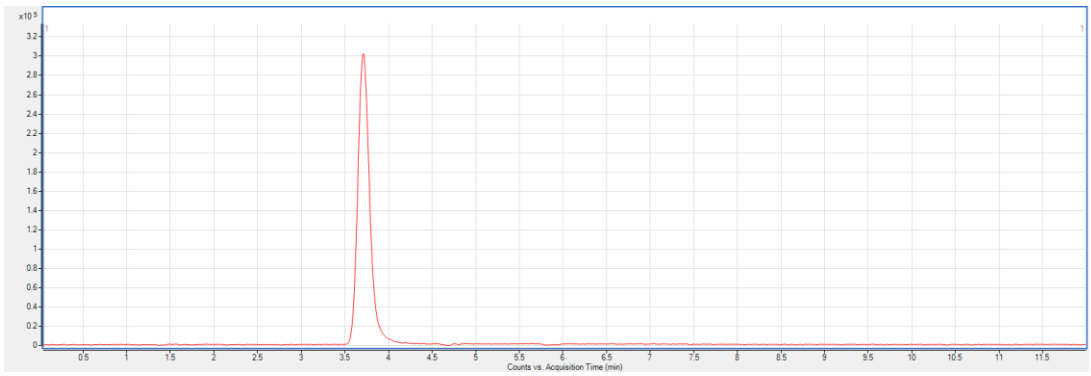


Figure 132. Extracted Ion Chromatogram of N,N-dimethyl-1,3,5-triazine-2,4,6-triamine at concentration of 10 ng/mL

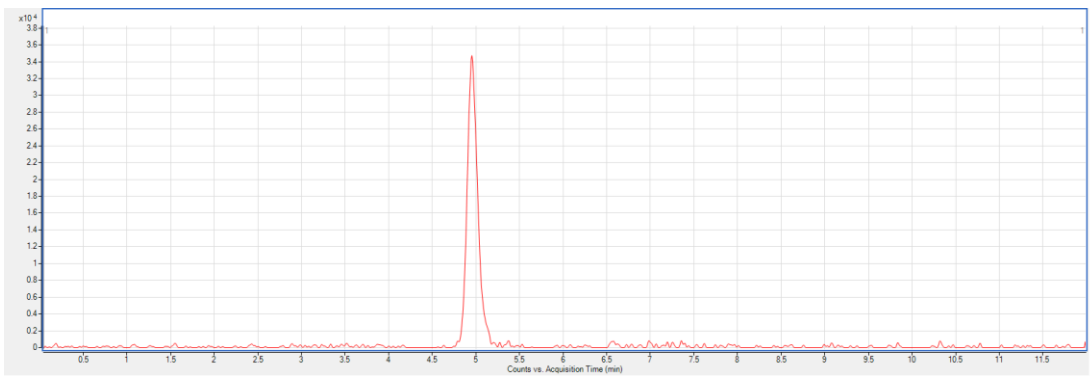


Figure 133. Extracted Ion Chromatogram for Melamine at concentration of 10 ng/mL

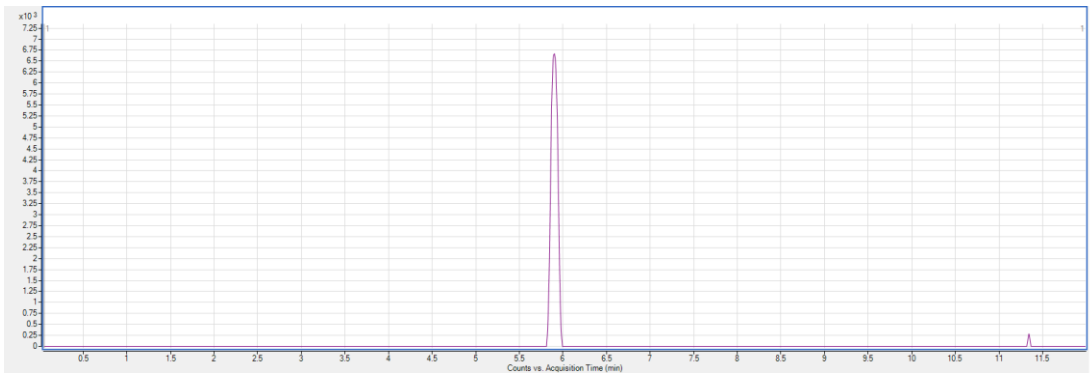


Figure 134. Extracted Ion Chromatogram for 1-methylbiguanide at concentration of 10 ng/mL

7.3 Dimethylamine Calibration Curve for Ion Chromatography

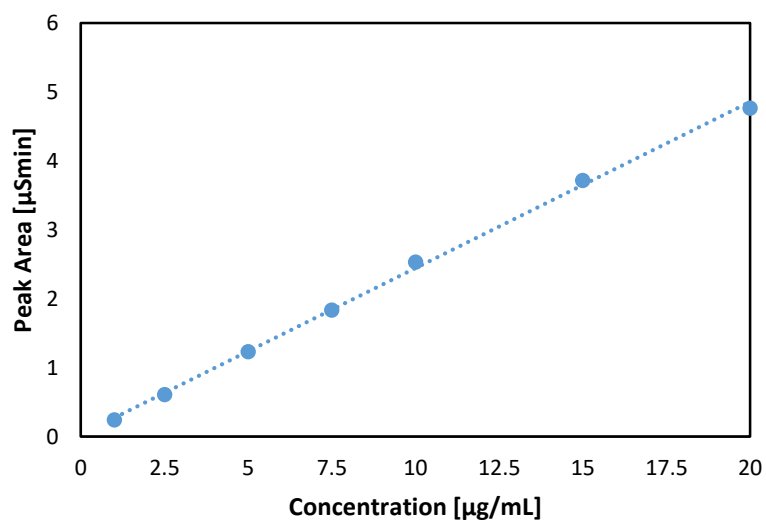


Figure 135. Calibration curve for dimethylamine

7.4 Ion Chromatogram Example for Dimethylamine Standard

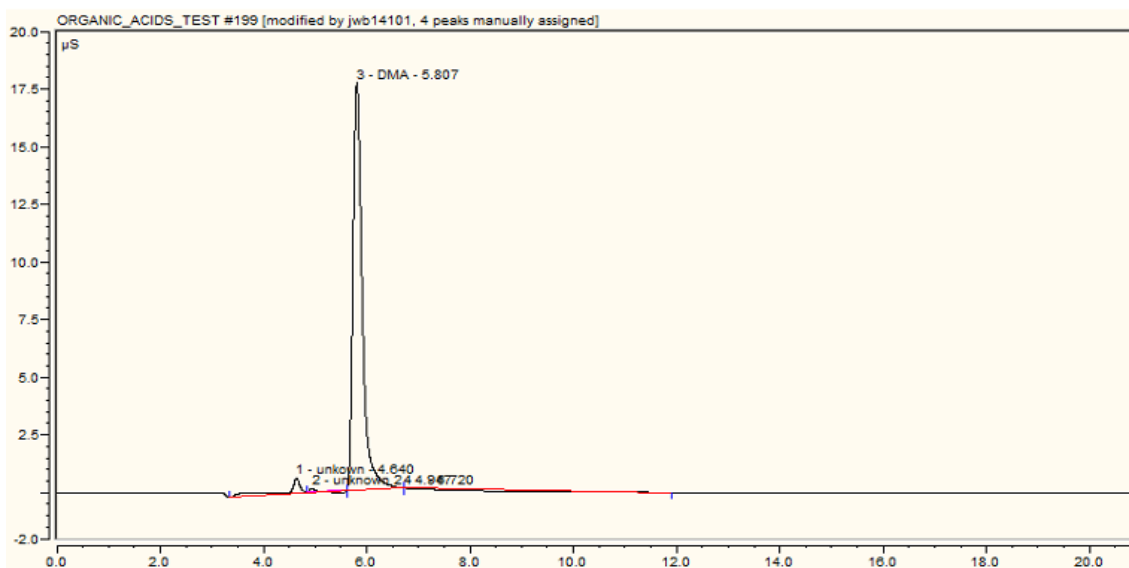


Figure 136. An example of ion chromatogram, for 15 µg/mL dimethylamine standard solution

7.5 Ion Chromatogram Example for Chloride and Sulfate Ions

Figure 137 shows an example ion chromatogram, for re-crystallised 0.1% w/w ammonium sulfate sample.

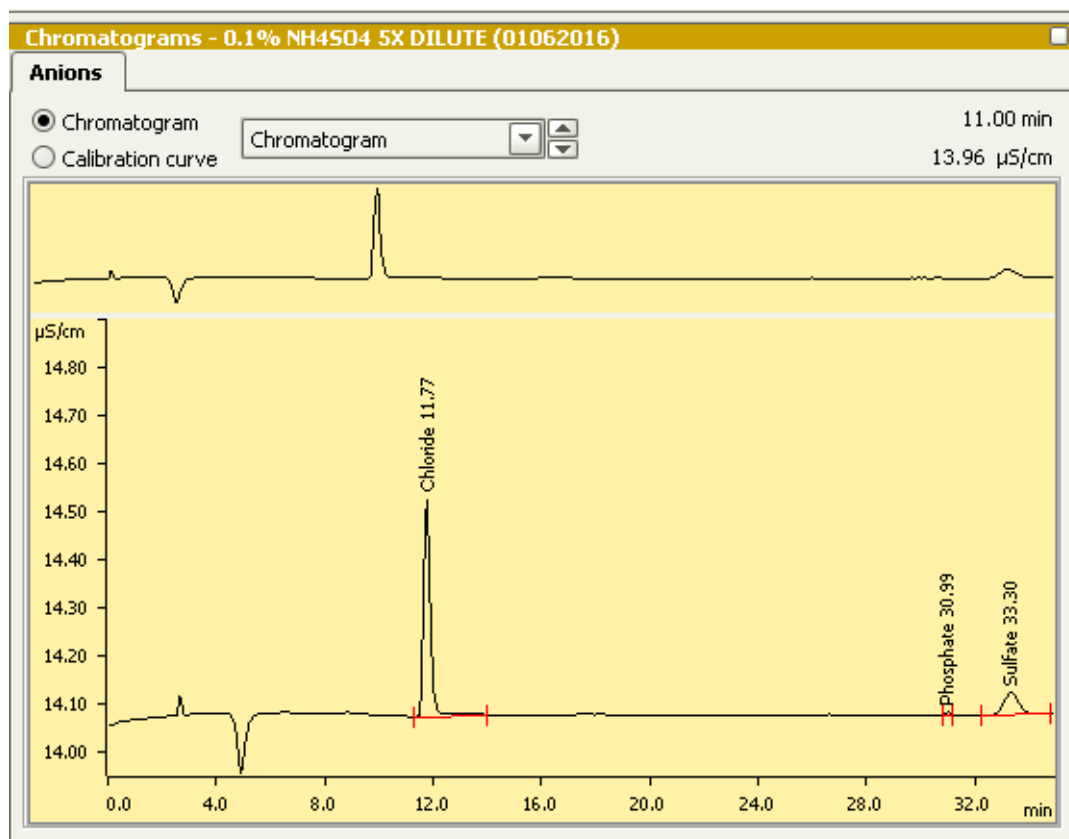


Figure 137. An example of ion chromatogram, for 0.1% w/w ammonium sulfate crystals from the re-crystallised sample

7.6 Ion Chromatography Calibration Curves

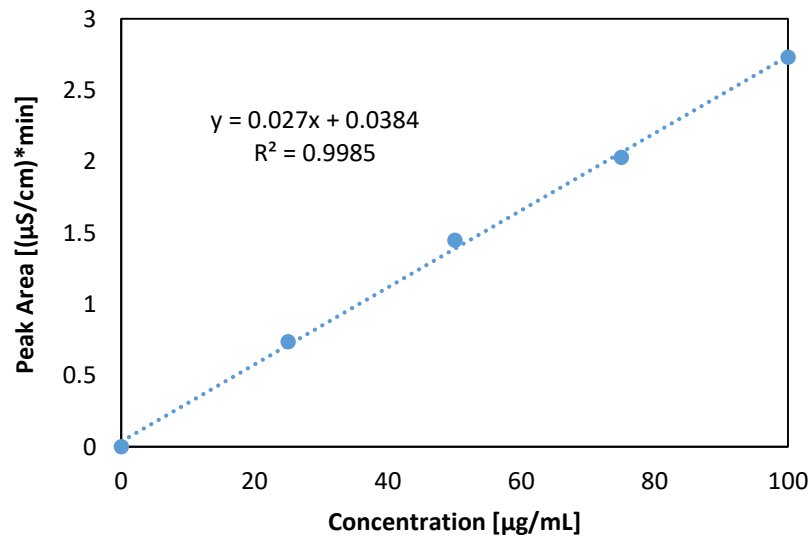


Figure 138. Ion chromatography calibration curve for sulfate anions showing the equation of the line

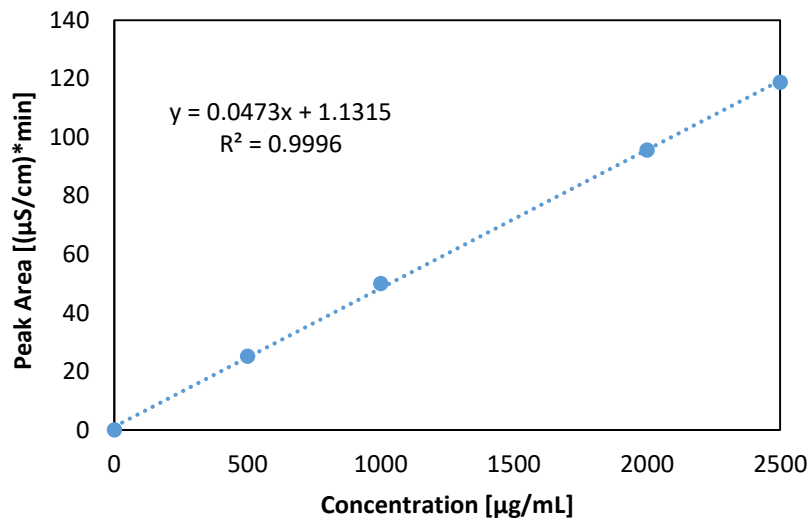


Figure 139. Ion chromatography calibration curve for chloride anions in the filtrate showing the equation of the line

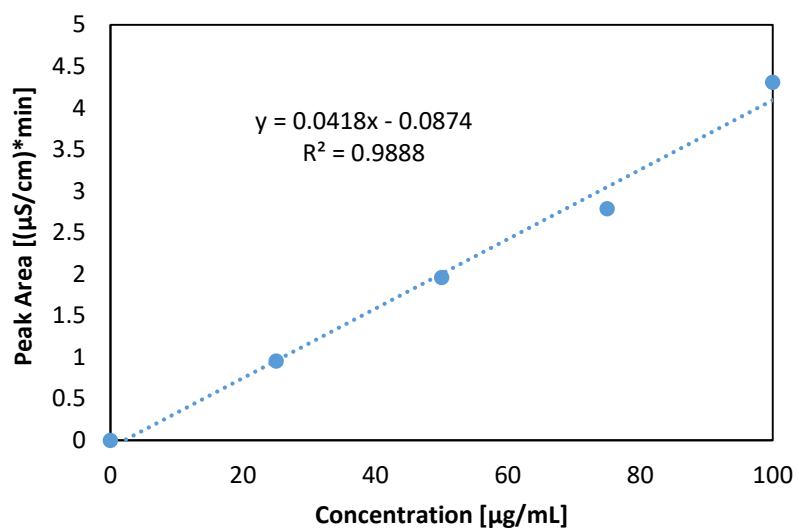


Figure 140. Ion chromatography calibration curve for chloride anions in the crystals showing the equation of the line

7.7 Dynamic Light Scattering Parameter Tables

Table 57. SS=0.9 Unfiltered

	Decay 1		Decay 2		Decay 3		RMS	Diffusion	Diffusion	Diffusion	Hydrodynamic Diameter (nm)		
	A1	B1	A2	B2	A3	B3		Coefficient 1 (m ² /s)	Coefficient 2 (m ² /s)	Coefficient 3 (m ² /s)	Decay 1	Decay 2	Decay 3
pure	0.088	5.63	0.39	8183.209	1.167	436820.799	0.332	1.82018E-10	1.25227E-13	8.78115E-10	1.988379012	2890.110307	0.412156005
0.01% amm sulf	0.174	4.753	0.073	5268.89	0.061	380453.164	0.055	2.15603E-10	1.94493E-13	1.67994E-08	1.678643951	1860.843747	0.021543716
0.1% amm sulf	0.155	4.445	0.07	5245.417	0.023	664691.523	0.034	2.30542E-10	1.95363E-13	4.45548E-08	1.569865845	1852.553654	0.00812304
0.5% amm sulf	0.166	5.247	0.18	5868.721	0.075	439676.666	0.103	1.95304E-10	1.74614E-13	1.36635E-08	1.853112731	2072.689461	0.026488175
1.0% amm sulf	0.111	2.769	0.05	774.212	0.005	106964.228	0.013	3.70083E-10	1.32362E-12	2.04952E-07	0.977943425	273.4328405	0.001765878

Table 58. SS=0.9 Repetition Unfiltered

	Decay 1		Decay 2		Decay 3		RMS	Diffusion Coefficient 1 (m ² /s)	Diffusion Coefficient 2 (m ² /s)	Diffusion Coefficient 3 (m ² /s)	Hydrodynamic Diameter (nm)		
	A1	B1	A2	B2	A3	B3					Decay 1	Decay 2	Decay 3
pure	0.169	4.535	0.35	10353.268	1.103	424064.319	0.304	2.25967E-10	9.89794E-14	9.29067E-10	1.601651655	3656.522344	0.389552762
0.01% amm sulf	0.163	5.976	0.207	28805.503	0.055	6097173.784	0.164	1.71479E-10	3.55752E-14	1.8632E-08	2.110577793	10173.40277	0.019424662
0.1% amm sulf	0.154	4.892	0.126	18490.56	0.01	2319508.349	0.041	2.09477E-10	5.54207E-14	1.02476E-07	1.727735369	6530.415884	0.003531757
0.5% amm sulf	0.082	8.453	0.35	9528.527	0.237	184342.489	0.166	1.2123E-10	1.07547E-13	4.32388E-09	2.985393924	3365.243891	0.083702633
1.0% amm sulf	0.096	8.371	0.35	15498.41	0.1	508635.196	0.119	1.22418E-10	6.61204E-14	1.02476E-08	2.956433519	5473.661308	0.035317567

Table 59. SS=1.55 Unfiltered

	Decay 1		Decay 2		Decay 3		RMS	Diffusion Coefficient 1 (m ² /s)	Diffusion Coefficient 2 (m ² /s)	Diffusion Coefficient 3 (m ² /s)	Hydrodynamic Diameter (nm)		
	A1	B1	A2	B2	A3	B3					Decay 1	Decay 2	Decay 3
pure	0.256	4.174	0.31	7451.204	0.066	400420.281	0.164	2.4551E-10	1.3753E-13	1.55267E-08	1.863524096	3326.664637	0.029466361
0.01% amm sulf	0.319	2.686	0.021	7743.472	0.007	820583.328	0.017	3.81519E-10	1.32339E-13	1.46394E-07	1.199191596	3457.150612	0.00312522
0.1% amm sulf	0.18	4.497	0.449	10275.312	0.169	972023.126	0.165	2.27876E-10	9.97304E-14	6.06367E-09	2.00773068	4587.515933	0.075451742
0.5% amm sulf	0.185	4.238	0.469	9240.46	0.281	8903329.043	0.195	2.41803E-10	1.10899E-13	3.64683E-09	1.892097537	4125.495895	0.125455264
1.0% amm sulf	0.307	3.322	0.063	11627.956	0.049	171038.004	0.064	3.08477E-10	8.8129E-14	2.09135E-08	1.483140164	5191.417391	0.021876541

Table 60. SS=1.55 Repetition Unfiltered

	Decay 1		Decay 2		Decay 3		RMS	Diffusion Coefficient 1 (m ² /s)	Diffusion Coefficient 2 (m ² /s)	Diffusion Coefficient 3 (m ² /s)	Hydrodynamic Diameter (nm)		
	A1	B1	A2	B2	A3	B3					Decay 1	Decay 2	Decay 3
pure	0.195	4.884	0.337	9140.099	0.12	208977.001	0.152	2.0982E-10	1.12117E-13	8.53967E-09	2.180510705	4080.688721	0.053575202
0.01% amm sulf	0.124	4.362	0.477	13879.806	0.149	181492.322	0.145	2.34929E-10	7.3831E-14	6.87759E-09	1.947458578	6196.778372	0.066522542
0.1% amm sulf	0.28	3.164	0.132	17147.025	0.053	5978555.264	0.073	3.23881E-10	5.97632E-14	1.93351E-08	1.412599482	7655.46101	0.023662381
0.5% amm sulf	0.079	4.139	0.357	13469.75	0.253	136729.82	0.147	2.47587E-10	7.60787E-14	4.05044E-09	1.847897995	6013.704765	0.112954383
1.0% amm sulf	0.288	3.723	0.179	8110.732	0.051	676918.633	0.136	2.75251E-10	1.26346E-13	2.00933E-08	1.66217063	3621.117517	0.022769461

Table 61. SS=1.55 Filtered

	Decay 1		Decay 2		RMS	Diffusion Coefficient 1 (m ² /s)	Diffusion Coefficient 2 (m ² /s)	Hydrodynamic Diameter (nm)	
	A1	B1	A2	B2				Decay 1	Decay 2
pure	0.300	2.130	0.002	71.0002	0.005	4.81108E-10	1.44332E-11	0.752264173	25.07554308
0.1% amm sulf	0.308	2.523	0.008	596.971	0.013	4.06167E-10	1.7166E-12	0.891062211	210.8356318
0.5% amm sulf	0.314	2.402	0.015	8727.21	0.013	4.26628E-10	1.17421E-13	0.848327955	3082.238224
1.0% amm sulf	0.217	1.822	0.013	285.721	0.011	5.62437E-10	3.58658E-12	0.643486068	100.9097051

Table 62. SS=1.55 Repetition Unfiltered

	Decay 1		Decay 2		RMS	Diffusion Coefficient 1 (m ² /s)	Diffusion Coefficient 2 (m ² /s)	Hydrodynamic Diameter (nm)	
	A1	B1	A2	B2				Decay 1	Decay 2
pure	0.188	1.729	0.009	64384.967	0.017	578368.9994	15.53157587	5.9269E-10	1.59161E-14
0.1% amm sulf	0.205	1.575	0.006	53885.252	0.015	634920.6349	18.55795348	6.50642E-10	1.90175E-14
0.5% amm sulf	0.333	2.651	0.018	1155.366	0.02	377216.1449	865.526595	3.86556E-10	8.86957E-13
1.0% amm sulf	0.213	1.827	0.008	456.105	0.011	547345.3749	2192.477609	5.60898E-10	2.24676E-12

8 Bibliography

- [1] A. K. El-Zhry El-Yafi and H. El-Zein, "Technical crystallization for application in pharmaceutical material engineering: Review article," *Asian Journal of Pharmaceutical Sciences*, vol. 10, no. 4, pp. 283-291, 2015.
- [2] R. Davey and J. Garside, *From Molecules to Crystallizers: An Introduction to Crystallization*, New York: Oxford University Press, 2002.
- [3] J. W. Mullin, "Crystallisation and Precipitation," in *Ullmann's Encyclopedia of Industrial Crystallisation*, 6th ed., Wiley, 2003.
- [4] A. W. Jones, *Crystallisation Process Systems*, Oxford: Butterworth-Heinemann, 2002.
- [5] J. W. Mullin, *Crystallisation*, 4th ed., Oxford: Butterworth-Heinemann, 2001.
- [6] A. S. Myerson, *Handbook of Industrial Crystallisation*, 2nd ed., Oxford: Butterworth-Heinemann, 2001.
- [7] J. Ulrich and C. Strege, "Some aspects of the importance of metastable zone width and nucleation in industrial crystallizers," *Journal of Crystal Growth*, Vols. 237-239, no. 1, pp. 2130-2135, 04 2002.
- [8] H. Qu, H. Alatalo, H. Hatakka, J. Kohonen, M. Louhi-Kultanen, S.-P. Reinikainen and J. Kallas, "Raman and ATR FTIR spectroscopy in reactive crystallization: Simultaneous monitoring of solute concentration and polymorphic state of the crystals," *Journal of Crystal Growth*, vol. 311, no. 13, pp. 3466-3475, 2009.
- [9] G. Févotte, "In Situ Raman Spectroscopy for In-Line Control of Pharmaceutical Crystallization and Solids Elaboration Processes: A Review," *Chemical Engineering Research and Design*, vol. 85, no. 7, pp. 906-920, 2007.
- [10] U. Pillaniya, K. Pilaniya, H. K. Chandrawanshi, P. Manchandani, P. Jain and N. Singh, "Recent trends in the impurity profile of pharmaceuticals," *Journal of Advanced Pharmaceutical Technology & Research*, vol. 1, no. 3, pp. 302-310, 2010.

- [11] "Impurities in New Drug Products Q3B(R2)," 2006.
- [12] R. N. Rao and V. Nagaraju, "An overview of the recent trends in development of HPLC methods for determination of impurities in drugs," *Journal of Pharmaceutical and Biomedical Analysis*, vol. 33, pp. 335-377, 2003.
- [13] M. S. Charde, J. Kumar, A. S. Welankiwar and R. D. Chakole, "Recent approaches for impurity profiling of pharmaceuticals," *International Journal of Advances in Pharmaceutics*, vol. 2, no. 3, pp. 25-33, 2013.
- [14] L. Palmer, "Investigation of batch and continuous crystallisation processes using non-invasive Raman and acoustic emission spectrometries," 2013.
- [15] D. Kashchiev, "Nucleation," in *Science and Technology of Crystal Growth*, J. P. van der Eerden and O. S. Bruinsmo, Eds., Kluwer Academic Publishers, 1995, pp. 53-66.
- [16] R. Davey and J. Garside, *From Molecules to Crystallizers: An Introduction to Crystallization*, Oxford: Oxford University Press, 2000.
- [17] W. Omar and J. Ulrich, "Application of Ultrasonics in the On-line Determination of Supersaturation," *Crystal Research & Technology*, vol. 34, no. 3, pp. 379-389, 1999.
- [18] K. Sangwal, "Recent developments in understanding of the metastable zone width of different solute-solvent systems," *Journal of Crystal Growth*, vol. 318, no. 1, pp. 103-109, 2011.
- [19] J. W. Mullin, *Crystallisation*, 4th ed., Oxford: Butterworth-Heinemann, 2001.
- [20] J. Ulrich and C. Strege, "Some aspects of the importance of metastable zone width and nucleation in industrial crystallizers.," *Journal of Crystal Growth*, Vols. 237-239, no. Part 3, pp. 2130-2135, 2002.
- [21] A. Jawor-Baczynska, "Nucleation Mechanism of Crystal Formation During Antisolvent or Cooling Induced Crystallisation," 2010.

- [22] D. Erdemir, A. Y. Lee and A. S. Myerson, "Nucleation of crystals from solution: Classical and Two-Step Models," *Accounts of chemical research*, vol. 42, no. 5, pp. 621-629, 2009.
- [23] V. M. Fokin and E. D. Zanotto, "Crystal nucleation in silicate glasses: the temperature and size dependence of crystal/liquid surface energy," *Journal of Non-Crystalline Solids*, vol. 265, no. 1-2, pp. 105-112, 2000.
- [24] D. W. Oxtoby and D. Kashchiev, "A general relation between the nucleation work and the size of the nucleus in multicomponent nucleation," *Journal of Chemical Physics*, vol. 100, pp. 7665-7771, 1994.
- [25] D. Erdemir, A. Y. Lee and A. S. Myerson, "Nucleation of crystals from solution: Classical and Two-Step Models," *Accounts of Chemical Research*, pp. 621-629, 6 October 2008.
- [26] S. G. Agrawal and H. J. Paterson, "Secondary Nucleation: Mechanisms and Models," *Chemical Engineering Communications*, vol. 202, no. 5, pp. 698-706, 205.
- [27] N. A. Mitchell and P. J. Frawley, "Nucleation kinetics of paracetamol-ethanol solutions from metastable zone widths," *Journal of Crystal Growth*, vol. 312, pp. 2740-2746, 2010.
- [28] S. Jiang and J. H. ter Horst, "Crystal Nucleation Rates from Probability Distributions of Induction Times," *Crystal Growth & Design*, vol. 11, pp. 256-261, 2011.
- [29] H. Vehkamäki, *Classical Nucleation Theory in Multicomponent Systems*, Springer, 2006, pp. 113-114.
- [30] J. Drenth and C. Haas, "Nucleation in Protein Crystallisation," *Acta Crystallographica Section D: Biological Crystallography*, vol. 54, pp. 867-872, September 1998.
- [31] J. Merikanto, A. Lauri, E. Zapadinsky and H. Vehkamäki, "An Insight into the Failure of Classical Nucleation Theory," Springer, 2007.

- [32] P. R. ten Wolde and D. Frenkel, "Enhancement of Protein Crystal Nucleation by Critical Density Fluctuations," *Science*, vol. 277, pp. 1975-1978, 1997.
- [33] M. Sedlak, "Large-Scale Supramolecular Structure in Solutions of Low Molar Mass Compounds and Mixtures of Liquids: I. Light Scattering Characterization," *Journal of Physical Chemistry*, pp. 4329-4388, 2006.
- [34] M. Sedlak, "Large-Scale Supramolecular Structure in Solutions of Low Molar Mass Compounds and Mixtures of Liquids: II. Kinetics of the Formation and Long-Time Stability," *Journal of Physical Chemistry*, pp. 4339-4345, 2006.
- [35] M. Sedlak, "Large-Scale Supramolecular Structure in Solutions of Low Molar Mass Compounds and Mixtures of Liquids: III. Correlation with Molecular Properties and Interactions," *Journal of Physical Chemistry*, pp. 13976-13984, 2006.
- [36] A. Jawor-Baczynska, J. Sefcik and B. D. Moore, "250 nm Glycine-Rich Nanodroplets Are Formed on Dissolution of Glycine Crystals But Are Too Small To Provide Productive Nucleation Sites," *Crystal Growth & Design*, vol. 13, pp. 470-478, 2013.
- [37] A. Jawor-Baczynska, B. D. Moore, H. S. Lee, A. V. McCormick and J. Sefcik, "Population and size distribution of solute-rich mesospecies within mesostructured aqueous amino acid solutions," *Faraday Discussions*, vol. 167, pp. 425-440, 2013.
- [38] A. Jawor-Baczynska, B. D. Moore and J. Sefcik, "Effect of mixing, concentration and temperature on the formation of mesostructured solutions and their role in the nucleation of DL-valine crystals," *Faraday Discussions*, vol. 179, pp. 141-154, 2015.
- [39] S. Karthika, T. K. Radhakrishnan and P. Kalaichelvi, "A Review of Classical and Nonclassical Nucleation Theories," *Crystal Growth and Design*, vol. 16, pp. 6663-6681, 2016.
- [40] P. G. Vekilov, "The two-step mechanism of nucleation of crystals in solution," *Nanoscale*, vol. 2, pp. 2346-2357, 2010.

- [41] R. Harrison, O. Rapaud, N. Pradeilles, A. Maitre and W. E. Lee, "On the Fabrication of ZrC_xN_y From ZrO_2 via two-Step Carbothermic Reduction-Nitridation," *Journal of the European Ceramic Society*, vol. 35, no. 5, pp. 1413-1421, 2015.
- [42] N. Cabrera and D. A. Vermilyea, "The Growth of Crystal from Solution," in *Growth and Perfection of Crystals*, R. H. Doremus, B. W. Roberts and D. Turnbull, Eds., London, Chapman & Hall, 1958.
- [43] N. Kubota and J. W. Mullin, "A kinetic model for crystal growth from aqueous solution in the presence of impurity," *Journal of Crystal Growth*, vol. 152, no. 3, pp. 203-208, 1995.
- [44] N. Kubota, M. Yokota and J. W. Mullin, "Supersaturation dependence of crystal growth in solutions in the presence of impurity," *Journal of Crystal Growth*, vol. 182, no. 1-2, pp. 86-94, 1997.
- [45] M. C. van der Leeden, D. Kashchiev and G. M. van Rosmalen, "Effect of additives on nucleation rate, crystal growth rate and induction time in precipitation," *Journal of Crystal Growth*, vol. 130, no. 1-2, pp. 221-232, 1993.
- [46] C. Gahn and A. Mersmann, "Brittle fracture in crystallization processes Part B. Growth of fragments and scale-up of suspension crystallizers," *Chemical Engineering Science*, vol. 54, no. 9, pp. 1283-1292, 1999.
- [47] M. Rauls, K. Bartosch, M. Kind, S. Kuch, R. Lacmann and A. Mersmann, "The influence of impurities on crystallisation kinetics - a case study on ammonium sulfate," *Journal of Crystal Growth*, vol. 213, pp. 116-128, 2000.
- [48] M. M. Akl, M. M. Nassar and S. A. Sayed, "Influence of Impurities and Suspension Density on the Crystallization Kinetics of Potassium Chloride," *Chemie Ingenieur Technik*, vol. 63, no. 9, pp. 935-939, 1991.
- [49] S. R. Dash and S. Rohani, "Effect of mangesium and sulfata ions on KCl crystallisation in a continuous cooling MSMMPR crystalliser," *Chemical Engineering Communications*, vol. 125, no. 1, pp. 211-216, 1993.

- [50] R. Belhamri and M. Mathlouthi, "Effect of impurities on sucrose crystal shape and growth," *Current Topics in Crystal Growth Research*, vol. 7, pp. 63-70, 2004.
- [51] M. Sultana and K. F. Jensen, "Microfluidic Continuous Seeded Crystallization: Extraction of Growth Kinetics and Impact of Impurity on Morphology," *Crystal Growth & Design*, vol. 12, pp. 6260-6266, 2012.
- [52] M. Shanmugham, F. D. Gnanam and P. Ramasamy, "Nucleation studies in supersaturated potassium dihydrogen orthophosphate solution and the effect of soluble impurities," *Journal of Materials Science*, vol. 19, pp. 2837-2844, 1984.
- [53] M. Rauls, K. Bartosch, M. Kind, S. Kuch, R. Lacmann and A. Mersmann, "The influence of impurities on crystallization kinetics – a case study on ammonium sulfate," *Journal of Crystal Growth*, vol. 213, no. 1-2, pp. 116-128, 2000.
- [54] K. V. Prasad, R. I. Ristic, D. B. Sheen and J. N. Sherwood, "Crystallisation of paracetamol from solution in the presence and absence of impurity," *International Journal of Pharmaceutics*, vol. 215, pp. 29-44, 2001.
- [55] C. Thompson, M. C. Davies, C. J. Roberts, S. J. Tendler and M. J. Wilkinson, "The effects of additives on the growth and morphology of paracetamol (acetaminophen) crystals.," *International Journal of Pharmaceutics*, vol. 280, no. 1-2, pp. 137-150, 2004.
- [56] J. Podder, "The study of impurities effect on the growth and nucleation kinetics of potassium dihydrogen phosphate," *Journal of Crystal Growth*, Vols. 237-239, pp. 70-75, 2002.
- [57] M. A. Rahman and M. M. Rahman, "Determination of the Metastable Zone Width, Nucleation Kinetics, Structural and Optical Properties of KCl Doped KAP Crystal," *Journal of Crystallization Process and Technology*, vol. 5, pp. 31-42, 2015.

- [58] X. Y. Zhang, G. Fevotte, L. Zhong, G. Qian, X.-G. Zhoua and W.-K. Yuan, "Crystallization of zinc lactate in presence of malic acid," *Journal of Crystal Growth*, vol. 312, pp. 2747-2755, 2010.
- [59] J. Peng, Y. Dong, L. Wang, L. Li, W. Li and H. Feng, "Effect of Impurities on the Solubility, Metastable Zone Width, and Nucleation Kinetics of Borax Decahydrate," *Industrial & Engineering Chemistry Research*, vol. 53, pp. 12170-12178, 2014.
- [60] L. Li, D. Lechuga-Ballesteros, B. A. Szkudlarek and N. Rodriguez-Hornedo, "The Effect of Additives on Glycine Crystal Growth Kinetics," *Journal of Colloid and Interface Science*, vol. 168, pp. 8-14, 1994.
- [61] M. C. van der Leeden, D. Kashchiev and G. M. van Rosmalen, "Precipitation of Barium Sulfate: Induction Time and the Effect of an Additive on Nucleation and Growth," *Journal of Colloid and Interface Science*, vol. 152, no. 2, pp. 338-350, 1992.
- [62] J. Schöll, D. Bonalumi, L. Vicum and M. Mazzotti, "In Situ Monitoring and Modeling of the Solvent-Mediated Polymorphic Transformation of L-Glutamic Acid," *Crystal Growth & Design*, vol. 6, no. 4, pp. 881-891, 2006.
- [63] H. Qu, H. Alatalo, H. Hatakka, J. Kohonen, M. Louhi-Kultanen, S.-P. Reinikainen and J. Kallas, "Raman and ATR FTIR spectroscopy in reactive crystallization: Simultaneous monitoring of solute concentration and polymorphic state of the crystals," *Journal of Crystal Growth*, vol. 311, no. 13, pp. 3466-3475, 2009.
- [64] K. Srinivasan and P. Dhanasekaran, "Nucleation control and crystallization of L-glutamic acid polymorphs by swift cooling process and their characterization," *Journal of Crystal Growth*, vol. 318, no. 1, pp. 1080-1084, 2011.
- [65] R. Ashe, D. Littlejohn, A. Nordon and P. Allan, "Sensing change in batch reactor," *Chemical Engineering*, vol. 115, no. 3, pp. 56-59, 2008.
- [66] P. Allan, "Studies in Raman, Infrared and Acoustic Emission Spectrometries and Reaction Calorimetry for Process Analysis".

- [67] R. Ashe, "Precision heating," *The Chemical Engineer*, vol. 7, pp. 44-46, 2006.
- [68] M. S. Abbott, A. P. Harvey, G. Valente Perez and M. K. Theodorou, "Biological processing in oscillatory baffled reactors: operation, advantages and potential," *Interface Focus*, vol. 3, no. 1, pp. 1-13, 2013.
- [69] L. X. Yu, R. A. Lionberger, A. S. Raw, R. D'Costa, H. Wu and A. S. Hussain, "Applications of process analytical technology to crystallization processes," *Advanced Drug Delivery Reviews*, vol. 56, no. 3, pp. 349-369, 2004.
- [70] S. Wartewig and R. H. Neubert, "Pharmaceutical applications of Mid-IR and Raman spectroscopy," *Advanced Drug Delivery Reviews*, vol. 57, no. 8, pp. 1144-1170, 2005.
- [71] G. Févotte, J. Calas, F. Puel and C. Hoff, "Applications of NIR spectroscopy to monitoring and analyzing the solid state during industrial crystallization processes.," *International Journal of Pharmaceutics*, vol. 273, no. 1-2, pp. 159-169, 2004.
- [72] L. Zhao, V. Raval, N. Briggs, A. J. Florence, R. M. Bhardwaj, I. D. Oswald and T. McGlone, "From discovery to scale-up: α -lipoic acid: Nicotinamide co-crystals in a continuous oscillatory baffled crystalliser," *CrystEngComm*, vol. 16, no. 26, pp. 5769-5780, 2014.
- [73] Y. Zhang, Y. Jiang, D. Zhang, K. Li and Y. Qian, "On-line concentration measurement for anti-solvent crystallization of β -artemether using UV-vis fiber spectroscopy," *Journal of Crystal Growth*, vol. 314, no. 1, pp. 185-189.
- [74] T. Ono, J. H. ter Horst and P. J. Jansens, "Quantitative Measurement of the Polymorphic Transformation of L-Glutamic Acid Using In-Situ Raman Spectroscopy.," *Crystal Growth & Design*, vol. 4, no. 3, pp. 465-469, 2004.
- [75] J. Cornel, C. Lindenberg and M. Mazzotti, "Quantitative Application of in Situ ATR-FTIR and Raman Spectroscopy in Crystallization Processes," *Industrial & Engineering Chemistry Research*, vol. 47, no. 14, pp. 4870-4882, 2008.

- [76] T. Ono, H. J. Kramer, J. H. ter Horst and P. J. Jansens, "Process Modeling of the Polymorphic Transformation of L-Glutamic Acid," *Crystal Growth & Design*, vol. 4, no. 6, pp. 1161-1167, 2004.
- [77] P. Atkins, *Physical Chemistry*, 8th ed., New York, 2006.
- [78] R. L. McCreery, "Raman Spectroscopy for Chemical Analysis," *Chemical Analysis*, vol. 157, pp. 1-24, 2000.
- [79] D. Wolverson, "Raman Spectroscopy," in *An Introduction to Laser Spectroscopy*, D. L. Andrews and A. A. Demidov, Eds., New York, Kluwer Academic/Plenum Publishers, 2002.
- [80] A. Rawle, *Basic Principles of Particle Size Analysis*, Malvern Instruments Limited.
- [81] Z. Stojanovic and S. Markovic, "Determination of particle size distributions by Laser Diffraction," *Technics - New Materials*, vol. 21, pp. 11-20, 2012.
- [82] G. Sympatec. [Online]. Available: <http://www.sympatec.com/EN/LaserDiffraction/LaserDiffraction.html>. [Accessed 09 2014].
- [83] G. B. de Boer, C. de Weerd, D. Thoenes and H. W. Goossens, "Laser Diffraction Spectrometry: Fraunhofer Diffraction Versus Mie Scattering," *Particle & Particle Systems Characterisation*, vol. 4, no. 1-4, pp. 14-19, 1987.
- [84] N. Stevens, J. Shrimpton, M. Palmer, D. Prime and B. Johal, "Accuracy assessments for laser diffraction measurements of pharmaceutical lactose," *Measurement Science and Technology*, vol. 18, no. 12, pp. 3697-3706, 2007.
- [85] A. H. de Boer, D. Gjaltema, P. Hagedoorn and H. W. Frijlink, "Characterization of inhalation aerosols: a critical evaluation of cascade impactor analysis and laser diffraction technique," *International Journal of Pharmaceutics*, vol. 249, no. 1-2, pp. 219-231, 2002.
- [86] M. Naito, O. Hayakawa, K. Nakahira, H. Mori and J. Tsubaki, "Effect of particle shape on the particle size distribution measured with commercial equipment," *Powder Technology*, vol. 100, no. 1, pp. 52-60, 1998.

- [87] H. Muhlenweg and D. E. Hirleman, "Laser Diffraction Spectroscopy: Influence of Particle Shape and a Shape Adaptation Technique," *Particle and Particle Systems Characterization*, vol. 15, no. 4, pp. 163-169, 1998.
- [88] N. Gabas, N. Hiquily and C. Laguerie, "Response of Laser Diffraction Particle Sizer to Anisometric Particles.," *Particle & Particle Systems Characterization*, vol. 11, no. 2, pp. 121-126, 1994.
- [89] B. Fultz and J. Howe, *Transmission Electron Microscopy and Diffractometry of Materials*, 4th ed., Springer, 2013.
- [90] R. B. Hammond, X. Lai and K. J. Roberts, "Application of In-Process X-ray Powder Diffraction for the Identification of Polymorphic Forms during Batch Crystallization Reactions," *Crystal Growth & Design*, vol. 4, no. 5, pp. 943-948, 2004.
- [91] S. D. MacMillan, K. J. Roberts, A. Rossi, M. A. Wells, M. C. Polgreen and I. H. Smith, "In Situ Small Angle X-ray Scattering (SAXS) Studies of Polymorphism with the Associated Crystallization of Cocoa Butter Fat Using Shearing Conditions," *Crystal Growth & Design*, vol. 2, no. 3, pp. 221-226, 2002.
- [92] P. Barnes, S. Jacques and M. Vickers, "Powder diffraction," [Online]. Available: <http://pd.chem.ucl.ac.uk/pdnn/diff2/kinemat2.htm>. [Accessed 5 2015].
- [93] A. Borrisova, S. Khan, T. Mahmud, K. J. Roberts, J. Andrews, P. Dallin, Z.-P. Chen and J. Morris, "In Situ Measurement of Solution Concentration during the Batch Cooling Crystallization of L-Glutamic Acid using ATR-FTIR Spectroscopy Coupled with Chemometrics," *Crystal Growth & Design*, vol. 9, no. 2, pp. 692-706, 2008.
- [94] X.-W. Ni, A. Valentine, A. Liao, S. B. Sermage, G. B. Thomson and K. J. Roberts, "On the Crystal Polymorphic Forms of L-Glutamic Acid Following Temperature Programmed Crystallization in a Batch Oscillatory Baffled Crystallizer.," *Journal Growth & Design*, vol. 4, no. 6, pp. 1129-1135, 2004.
- [95] S. Dharmayat, J. C. De Anda, R. B. Hammond, X. Lai, K. J. Roberts and X. Z. Wang, "Polymorphic transformation of L-glutamic acid monitored using

- combined on-line video microscopy and X-ray diffraction," *Journal of Crystal Growth*, vol. 294, pp. 35-40, 2006.
- [96] M. Kitamura, "Polymorphism in the crystallization of L-glutamic acid," *Journal of Crystal Growth*, vol. 96, no. 3, pp. 541-546, 1989.
- [97] C. Cashell, D. Corcoran and B. K. Hodnett, "Control of polymorphism and crystal size of L-glutamic acid in the absence of additives," *Journal of Crystal Growth*, vol. 273, no. 1-2, pp. 258-265, 2004.
- [98] S. Liang, X. Duan, X. Zhang, G. Qian and X. Zhou, "Supersaturation-dependent polymorphic outcome and transformation rate of L-glutamic acid," *RSC Advances*, vol. 6, pp. 74700-74703, 2016.
- [99] S. Liang, X. Duan, X. Zhang, G. Qian and X. Zhou, "Insights into Polymorphic Transformation of L-Glutamic Acid: A Combined Experimental and Simulation Study," *Crystal Growth and Design*, vol. 15, pp. 3602-3608, 2015.
- [100] M. T. Ruggiero, J. Sibik, J. A. Zeitler and T. M. Korter, "Examination of L-Glutamic Acid Polymorphs by Solid-State Density Functional Theory and Terahertz Spectroscopy," *The Journal of Physical Chemistry A*, vol. 120, pp. 7490-7495, 2016.
- [101] J. W. Mullin, *Crystallisation*, 4th ed., Oxford: Butterworth-Heinemann, 2002.
- [102] N. C. Kee, R. B. Tan and R. D. Braatz, "Selective Crystallization of the Metastable α -Form of L-Glutamic Acid using Concentration Feedback Control," *Crystal Growth & Design*, vol. 9, no. 7, pp. 3044-3051, 2009.
- [103] Waters, Waters, [Online]. Available: http://www.waters.com/waters/en_GB/How-Does-High-Performance-Liquid-Chromatography-Work%3F/nav.htm?cid=10049055&locale=en_GB. [Accessed June 2016].
- [104] B. Buszewski and S. Noga, "Hydrophilic interaction liquid chromatography (HILIC)—a powerful separation technique," *Analytical and Bioanalytical Chemistry*, vol. 402, pp. 231-247, 2012.

- [105] J. W. Dolan, "LC Troubleshooting," BASi Northwest Laboratory, [Online]. Available:
http://images.alfresco.advanstar.com/alfresco_images/pharma/2014/08/22/db291f1a-f9e7-48d1-9b96-8801d4514acf/article-69793.pdf. [Accessed 4 June 2016].
- [106] P. Makary, "Principles of salt formation," *UK Journal of Pharmaceutical and Biosciences*, vol. 2, no. 4, pp. 1-4, 2014.
- [107] K. R. Morris, M. G. Fakes, A. B. Thakur, A. W. Newman, A. K. Singh, J. J. Venit, C. J. Spangnolo and A. T. Serajuddin, "An integrated approach to the selection of optimal salt form for a new drug candidate," *International Journal of Pharmaceutics*, vol. 105, no. 3, pp. 209-217, 1994.
- [108] R. J. Bastin, M. J. Bowker and B. J. Slater, "Salt Selection and Optimisation Procedures for Pharmaceutical New Chemical Entities," *Organic Process Research & Development*, vol. 4, pp. 427-435, 2000.
- [109] A. T. Serajuddin, "Salt formation to improve drug solubility," *Advanced Drug Delivery Reviews*, vol. 59, pp. 603-616, 2007.
- [110] G. Hegyi, J. Kardos, M. Kovacs, A. Malnasi-Csizmadia, L. Nyitray, G. Pal, L. Radnai, A. Remenyi and I. Venekei, "Introduction to Practical Biochemistry," [Online]. Available: http://tktamop.elte.hu/online-tananyagok/introduction_to_practical_biochemistry/ch06s02.html. [Accessed June 2016].
- [111] S. G. Alikhanov, "A new impulse technique for ion mass measurement," *Soviet Physics JETP*, vol. 31, pp. 517-518, 1957.
- [112] G. Klaczkow and E. L. Anuszevska, "Determination of impurities in medical products containing metformin hydrochloride," *Acta Poloniae Pharmaceutica*, vol. 67, no. 6, pp. 593-598, 2010.
- [113] M. J. O'Neil, *An Encyclopedia of Chemicals, Drugs, and Biologicals*, 13th ed., RSC Publishing, 2001.

- [114] Sax's Dangerous Properties of Industrial Materials., 9th ed., New York: John Wiley and Sons, 1996.
- [115] E. A. Werner and J. Bell, "The preparation of methylguanidine, and of $\beta\beta$ -dimethylguanidine by the interaction of dicyanodiamide, and methylammonium and dimethylammonium chlorides respectively," *Journal of the Chemical Society*, vol. 121, pp. 1790-1794, 1922.
- [116] Pharmaceutical Manufacturing Encyclopedia, 3rd ed., William Andrew Publishing, 2007.
- [117] S. L. Childs, L. J. Chyall, J. T. Dunlap, D. A. Coates, B. C. Stahly and G. P. Stahly, "A Metastable Polymorph of Metformin Hydrochloride: Isolation and Characterization Using Capillary Crystallization and Thermal Microscopy Techniques," *Crystal Growth & Design*, vol. 4, no. 3, pp. 441-449, 2004.
- [118] British Pharmacopoeia Commission, British Pharmacopoeia, London: TSO.
- [119] F. Al-Rimawi, "Development and validation of an analytical method for metformin hydrochloride and its related compound (1-cyanoguanidine) in tablet formulations by HPLC-UV," *Talanta*, vol. 79, no. 5, pp. 1368-1371, 2009.
- [120] M. S. Ali, S. Rafiuddin, M. Ghori and A. R. Khatri, "Simultaneous Determination of Metformin Hydrochloride, Cyanoguanidine and Melamine in Tablets by Mixed-Mode HILIC.," *Chromatographia*, vol. 67, no. 7, pp. 517-525, 2008.
- [121] F. Tache and M. Albu, "Specificity of an analytical HPLC assay method of metformin hydrochloride," *Revue Roumaine de Chimie*, vol. 52, no. 6, pp. 603-609, 2007.
- [122] D. Tsikas, T. Thum, T. Becker, V. V. Pham, K. Chobanyan, A. Mitschke, B. Beckmann, F.-M. Gutzki, J. Bauersachs and D. O. Stichtenoth, "Accurate quantification of dimethylamine (DMA) in human urine by gas chromatography–mass spectrometry as pentafluorobenzamide derivative: Evaluation of the relationship between DMA and its precursor asymmetric dimethylarginine (ADMA) in health and disease," *Journal of Chromatography B*, vol. 851, pp. 229-239, 2007.

- [123] K. Chobanyan, A. Mitschke, F.-M. Gutzki, D. O. Stichtenoth and D. Tsikas, "Accurate quantification of dimethylamine (DMA) in human plasma and serum by GC–MS and GC–tandem MS as pentafluorobenzamide derivative in the positive-ion chemical ionization mode," *Journal of Chromatography B*, vol. 851, pp. 240-249, 2007.
- [124] S. Tukkeeree, T. Phesatcha and J. Rohrer, "Determination of Dimethylamine in Metformin HCl Drug Product Using IC with Suppressed Conductivity Detection".
- [125] Purdue University, "Scanning Electron Microscopy," [Online]. Available: <https://www.purdue.edu/ehps/rem/rs/sem.htm>. [Accessed June 2016].
- [126] B. Hafner. [Online]. Available: http://www.charfac.umn.edu/sem_primer.pdf.
- [127] S. Swapp, "Geochemical Instrumentation and Analysis," [Online]. Available: http://serc.carleton.edu/research_education/geochemsheets/techniques/SEM.html. [Accessed June 2016].
- [128] J. C. Vickerman and D. Briggs, TOF-SIMS: Surface Analysis by Mass Spectrometry, Second ed., Manchester: IM Publications, 2013.
- [129] "User Com," Mettler Toledo, [Online]. Available: https://www.mt.com/dam/mt_ext_files/Editorial/Generic/2/dsc_purity_determ_0x00024947000254740008078d_files/dsc_purity_determ.pdf. [Accessed 15 May 2016].
- [130] M. E. Brown, "Determination of Purity by Differential Scanning Calorimetry (DSC)," *Journal of Chemical Education*, vol. 56, no. 5, pp. 310-313, 1979.
- [131] R. Finsy, "Particle Sizing by Quasi-Elastic Light Scattering," in *Advances in Colloid and Interface Science*, Elsevier Science, 1994.
- [132] J. Dziewierz, "Interactive curve fitting tool, Matlab," jerzy.dziewierz@strath.ac.uk.
- [133] "Chemspider," [Online]. Available: <http://www.chemspider.com/Chemical-Structure.3949.html>. [Accessed June 2016].

- [134] [Online]. Available: <http://www.celsius-process.com/pdf/ethanol.pdf>. [Accessed June 2016].
- [135] "Viscopedia," [Online]. Available: <http://www.viscopedia.com/viscosity-tables/substances/ethanol/>. [Accessed June 2016].
- [136] Advanced Sensor Technologies, Inc, "MINIMIZING USER ERRORS IN pH MEASUREMENTS," [Online]. Available: http://www.astisensor.com/minimizing_user_errors_ph.pdf. [Accessed June 2016].
- [137] J. Quitmeyer, "pH Measurement in aqueous and non-aqueous solutions: When used in combination with titration, pH measurement is a simple method to monitor bath concentration," *Metal Finishing*, vol. 106, no. 10, pp. 21-24, 2008.
- [138] E. H. Lee, "A practical guide to pharmaceutical polymorph screening & selection," *Asian Journal of Pharmaceutical Sciences*, vol. 9, pp. 163-175, 2014.